



HAL
open science

Exploring the nano-transport paths across spintronic devices for information encoding and energy harvesting.

Bhavishya Chowrira Poovanna

► To cite this version:

Bhavishya Chowrira Poovanna. Exploring the nano-transport paths across spintronic devices for information encoding and energy harvesting.. Physics [physics]. University of Strasbourg, 2021. English. NNT: . tel-03548320

HAL Id: tel-03548320

<https://theses.hal.science/tel-03548320v1>

Submitted on 30 Jan 2022

HAL is a multi-disciplinary open access archive for the deposit and dissemination of scientific research documents, whether they are published or not. The documents may come from teaching and research institutions in France or abroad, or from public or private research centers.

L'archive ouverte pluridisciplinaire **HAL**, est destinée au dépôt et à la diffusion de documents scientifiques de niveau recherche, publiés ou non, émanant des établissements d'enseignement et de recherche français ou étrangers, des laboratoires publics ou privés.



UNIVERSITÉ DE STRASBOURG

ÉCOLE DOCTORALE de Physique, chimie-physique
Institute de Physique et Chimie des Matériaux de Strasbourg

**Exploring the nano-transport paths across spintronic devices
for information encoding and energy harvesting.**

THÈSE présentée par :

Bhavishya Chowrira Poovanna

soutenue le : 14 April 2021

pour obtenir le grade de : **Docteur de l'université de Strasbourg**

Discipline/Spécialité : **Physique**

THÈSE dirigée par :

Mr. Martin Bowen Directeur de recherche, Université de Strasbourg

RAPPORTEURS :

Mr. Henning Sirringhaus Professeur, Université de Cambridge

Mr. Jean-Baptiste Moussy HdR, CEA, Paris Saclay

Examineur :

Mme. Roberta Sessoli Professeur, Université de Florence

*To my parents,
for always supporting and believing in me.*

Acknowledgements

Countless people have supported my effort on this thesis. Firstly, I would like to thank my thesis supervisor Dr. Martin Bowen for his continued guidance and an endless supply of fascinating projects. Your unassuming approach to research and wealth of knowledge is a source of inspiration. This approach is reflected by his simple but clear writing style, which is something I hope to carry forward throughout my career. Thanks Martin for this incredible learning journey and I am extremely grateful to have been a part of your dynamic multicultural team.

I extend my acknowledgments to Mr. Jacek Arabski who played a vital role in my training of hybrid vacuum chambers at IPCMS. I thoroughly enjoyed our teamwork in revamping the purification setup. I will always cherish your contagious enthusiasm, team spirit as well as regular encouragement. I was very fortunate to have shared my thesis years with you, thank you for your unconditional support and positive energy.

I am thankful to the ever energetic team of scientists who nurtured new ideas, gave helpful advice and timely support in my projects specifically Dr. Daniel Lacour, Dr. Wolfgang Weber, Dr. Samy Boukari and team in IJL. I am grateful for their feedback, excellent encouragement, and for their assistance at every stage of the research project. It was a pleasure interacting with cross-department chemistry teams. Thanks to Dr. Damien Metz for our interesting meetings which widened my understanding of surface chemistry.

The man behind-the-scenes in my thesis is Mr. Guy Schmerber. He always welcomed me with a smile and never turned my request down when I ran to him with

my complicated samples for X-ray reflectometry, X-ray diffraction, UV-visible spectroscopy, AGFM measurements. His constructive criticism accelerated my work.

The cleanroom facility STnano is one of the strong pillars of this research work. I am thankful to Mr. Hicham Majjad for always accommodating my requests and sharing his insights on lithography and mask design. I would like to extend my sincere thanks to Mr. Romain Bernard for his unwavering support and belief in me. I also appreciate all the support I received from Mrs. Sabine Siegwald. It is their kind help and guidance that have made my study and life in the IPCMS a wonderful time.

I am deeply grateful to Mr. Christophe Kieber for his timely assistance and words of encouragement that helped me progress in my thesis work. I will forever cherish our teamwork in venting chambers, shared organization skills. Many thanks for always lending a helping hand and teaching me tricks in handling electrical equipment. Many thanks to Mr. Daniel Spor and Mr. Fabrice Scheurer for their ready support in countless occasions.

My heartfelt thanks to Dr. Loic Joly, for his constant support and guidance not only limited to DEIMOS beamtimes but also data analysis and discussions at IPCMS. I would like to extend my thanks to the DEIMOS beamline manager Dr. Philippe Ohresser and his team for all the encouragement and interest in guiding me whenever I was in the beamline. It was a pleasure to work with HERMES beamline manager Dr. Rachid Belkhou and his team whose passion and energy will stay with me forever. I am proud to have been collaborating with two technologically advanced beamlines. Thanks to both DEIMOS and HERMES beamline for financially supporting my thesis. Special thanks for providing us with top-notch experimental end-stations and round the clock support during our beamtimes.

It was wonderful to work with Dr. Benoit Gobaut who recently joined the Hybrid Spintronics team. I am thankful for his pearls of wisdom which made me feel that writing a thesis is fun, thanks for always boosting my energy. My special thanks to Mr. Gilles Versini who was very kind to support our work in the purification of

molecules, thank you for our long conversations on varied topics. I want to thank Dr. Victor Da Costa for showing interest in our work and always ready to help no matter how occupied he is.

My extended thanks to all my distinguished Ph.D defense jury members - Prof. Henning Sirringhaus, Prof. Roberta Sessoli and Dr. Jean-Baptiste Moussy for evaluating my thesis and for a stimulating discussion. My sincere gratitude to Mr. Yves Henry, DMONS department head who leads by example in leadership. Thanks to Mme. Veronique Wernher who kept administrative work at bay and helped me focus more on research. Special thanks to Mme. Catherine Bonnin who made a hassle-free onboarding process to CNRS while I was still in India.

I acknowledge our industry collaborators Mr. Arnel Bahouka and Mr. Samuel Stuber from IREPA laser company for their timely assistance. I would like to thank Dr. Guillaume Rogez and Dr. Silviu Colis for training me on SQUID and AGFM magnetometers. I would like to thank Jose-Francis Radmacher, Dris Ihiawakrim, the team at the Mechanic shop at IPCMS for always helping with a smile, IT team who troubleshoot problems and make life smooth at IPCMS.

The three pillars for a smooth Ph.D. life are scientific support, technical support, and moral support. Thanks to all my dear colleagues for their selfless support and open discussions which expanded my horizon on topics not limited to Science. I cherish all the interactions and the lessons learned from you all - Gladice Magnifouet, Garen Avedissian, Kostantine Katcko, Senthil Kumar Kuppusamy, Shyam Kanta Sinha, Khaled Rassoul, Franck Ngassam Nyakam, Suvidyakumar Homkar, Filip Schleicher, Sambit Mohapatra, Ulrich Noumbe, Lalit-Mohan Kandpal. Thank you folks for all the time spent together in the lab, and in social settings.

The biggest contributors to the success of this thesis are my parents - Mr. Poovanna, Mrs. Sunitha and my dear brother Mr. Bhavin. I'm forever indebted for your sacrifices, trust, and support. Big thanks to Prof. Moodera Jagadeesh, Prof. Berera Geetha and all my beloved teachers who laid a strong foundation for my career.

Contents

Thesis Outline	1
1 Introduction	3
1.1 Spintronics and its role in the microelectronic industry	3
1.2 Giant magneto-resistance (GMR)	4
1.3 Tunneling Magnetoresistance (TMR)	6
1.4 Advancement in MTJs	8
2 Nano transport path in MgO MTJs	11
2.1 Crystalline structure of MgO	11
2.1.1 Point defects within MgO	12
2.1.2 Structure of Fe/MgO	13
2.2 Symmetry filtering in crystalline barrier FM/MgO/FM MTJs	14
2.3 Bloch states and wave function symmetries:	15
2.4 MgO magnetic tunnel junctions	17
2.5 Magneto-crystalline anisotropy at FM/MgO interface	18
2.6 Role of defects in MgO tunnel barrier	20
2.7 “Device Operando” with X-rays	27
2.8 Partial summary	30
3 Nano transport path in molecular MTJs	31
3.1 Contrast between organic and inorganic materials used in MTJs	32
3.2 Salient features of organic semiconductors	33
3.3 Metal-Phthalocyanine	35
3.3.1 General properties of metal phthalocyanine molecules	35
3.3.1.1 Cobalt phthalocyanine	37
3.3.1.2 Spin flip spectroscopy and microscopy	39

3.4	Spin-dependent hybridization at FM/molecule interface	41
3.5	Effects of hybridization at FM/AFM molecular interface	44
3.5.1	Interface spin polarization	44
3.5.2	Exchange Bias	45
3.6	Partial summary	50
4	Thermoelectric energy generators	51
4.1	Classical thermal devices	51
4.1.1	Classical vs quantum thermal devices	53
4.2	Quantum thermal devices	54
4.2.1	Quantum heat engine	55
4.2.1.1	Quantum Particle exchange heat engines	55
4.2.2	Spin Engines	59
4.2.2.1	Quantum Spin Heat Engines	59
4.2.3	Spintronic engines	61
4.2.4	Partial summary	65
4.3	Conclusion	67
	State of the Art	69
5	Thin film engineering	71
5.1	Physics of thin film growth	71
5.1.1	Atomistic mechanisms on surfaces	73
5.2	Instrumentation and thin film metrology techniques	74
5.2.1	Physical vapor deposition (PVD)	75
5.2.1.1	Magnetron sputtering	76
5.2.1.1.1	Working of magnetron sputtering	76
5.2.1.2	Organic molecular beam epitaxy (OMBE)	79
5.3	Molecular stacks	80
5.4	MgO stacks	82
5.4.1	Fabrication of MgO stacks using Nancy Sputtering	82
5.4.1.1	Annealing of MgO stacks	83
5.5	Characterization techniques	84

5.5.1	Super conducting quantum interference device (SQUID)	84
5.5.2	Electron microscope:	86
5.5.3	Transmission Electron Microscopy (TEM)	86
5.5.3.1	TEM specimen preparation	87
5.5.4	Scanning electron microscope (SEM)	87
5.5.5	X-ray reflectometry and X-ray diffraction	89
6	From thin film stacks to magnetic tunnel junction devices	93
6.1	Front-end process	93
6.1.1	MgO thin films patterning	93
6.1.2	Processing of MgO stacks	95
6.1.2.1	Step I : Defining micro pillars	96
6.1.2.2	Step II : Bottom electrode	99
6.1.2.3	Step III : Passivation	100
6.1.2.4	Step IV : Metallization	101
6.1.3	Processing of organic thin films	102
6.1.3.1	Step I : Nano-sphere lithography	102
6.1.3.2	Step II: Patterning nano-pillar MTJs	102
6.1.3.3	Step III : Passivation	104
6.1.3.4	Step IV: Metallization	105
6.2	Back-end process	106
6.2.1	Electrical characterization of magnetic tunnel junctions	106
6.2.1.1	Point probe (2-pp/ 4-pp):	106
6.2.2	Cutting and wire bonding	108
7	Magnetotransport and Operando measurement set-ups	109
7.1	Introduction to magneto-transport Fert bench	109
7.1.1	Operation cycles of the cryostat	110
7.1.2	The group's magneto-transport bench	111
7.2	Synchrotron based experiments	114
7.2.1	Introduction to synchrotron facility:	114
7.2.2	Physics of X-ray absorption spectroscopy (XAS)	116
7.2.2.1	The absorption coefficient $\mu(E)$	118

7.2.2.2	Information extracted from XAS	119
7.2.2.3	Detection methods of XAS	121
7.2.2.3.1	Transmission mode	121
7.2.2.3.2	Fluorescence yield	122
7.2.2.3.3	Total electron yield	124
7.2.2.4	X-ray magnetic circular dichroism (XMCD)	125
7.2.2.4.1	One electron theory	126
7.2.2.4.2	Sum Rules	128
7.3	Beamline DEIMOS	131
7.3.1	Device operando at DEIMOS beamline	134
7.3.2	Device mapping using x-rays	136
7.4	Beamline HERMES	140
7.4.1	Experimental procedure	141
7.4.2	Device operando at HERMES beamline	143
8	Encoding information on the excited state of a molecular spin chain	149
8.1	Device architecture	150
8.2	Impact of in-plane magnetic field cooling	151
8.3	Effect of applied bias voltage on device transport.	155
8.3.1	Bias dependence of magnetoresistance:	155
8.3.2	Bias dependence of differential conductance:	157
8.4	Device characteristics as a function of temperature	160
8.4.1	Temperature dependence of conductance	160
8.4.2	Temperature dependence of magnetoresistance	161
8.5	Additional CoPc based devices exhibiting MR	163
8.6	The three macro-spin transport model	166
8.7	Magnetic anisotropies along CoPc nano-transport path	172
8.8	Study of structural and magnetic properties of Fe/CoPc spinterface using DFT calculations	177
8.9	Summary	181

9 Large spintronic harvesting of thermal fluctuations using paramagnetic molecular centers	183
9.1 Design and operation of the spintronic engine	185
9.1.1 Structural and magnetic characterization of stacks	188
9.2 Magnetotransport results across nanodevices	191
9.2.1 Semiconducting device - A	193
9.2.2 Metallic device - B	198
9.2.3 Metallic device - C	201
9.3 Summary	203
10 General conclusion and perspectives	207
A Nano sphere lithography	211
B Imaging the silica nano spheres	213
Bibliography	217

Résumé en français

L'idée du spin était bien connue depuis des décennies, mais en raison des limites technologiques, son utilisation n'avait pas beaucoup progressé. La découverte pionnière de la magnétorésistance géante (GMR) par Albert Fert et Peter Grünberg a révolutionné l'industrie du stockage de données [1, 2]. Depuis peu, on utilise des têtes de lecture basées sur la magnétorésistance à effet tunnel (TMR). Les dispositifs spintroniques basés sur la TMR sont devenus très populaires et continuent d'étendre leurs capacités dans les domaines des capteurs, de l'IoT, de l'énergie, etc. Voir l'image 1 pour la chronologie de la spintronique. Dans les dispositifs à base de TMR, la barrière tunnel est un isolant extrêmement fin (quelques nm) pris en sandwich entre des électrodes ferromagnétiques. Grâce à cette fine barrière isolante, les électrons passent d'une électrode FM à l'autre par effet tunnel et la magnétorésistance tunnel est donc un effet de mécanique quantique [3]. L'origine de l'effet TMR est la conservation du spin pendant l'effet tunnel. Les dispositifs basés sur le TMR sont communément appelés jonctions magnétiques à effet tunnel (MTJ).

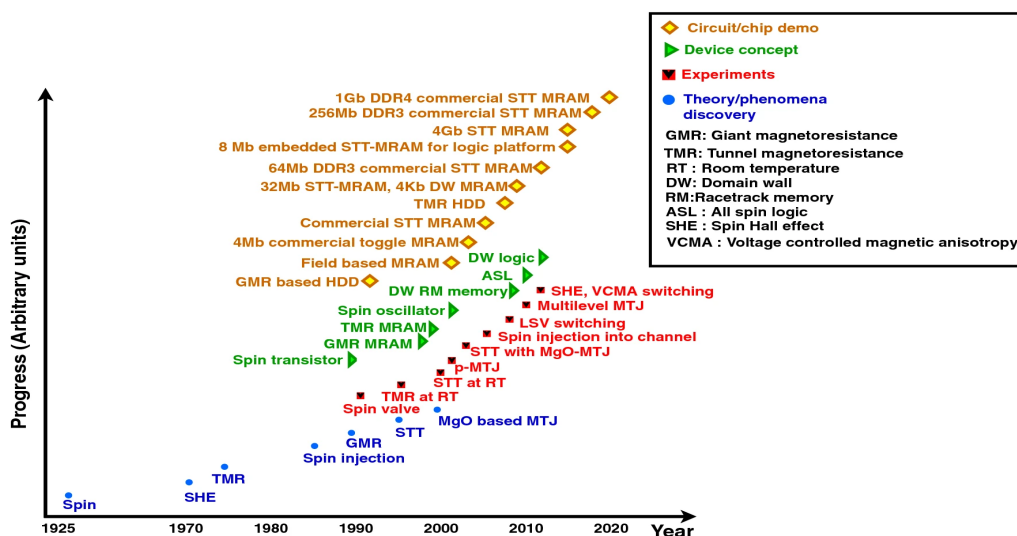


FIGURE 1: L'évolution de la spintronique. Image adaptée du [4]

Cette thèse explore trois voies de nanotransport dans les dispositifs spintroniques, à savoir les lacunes d'oxygène dans les MTJs à base de MgO, les molécules de CoPc dans les MTJs à base de molécules et les centres paramagnétiques de Co dans un nouveau dispositif à l'état solide de moteur spintronique. Nous explorons la voie du nanotransporteur spintronique présentée par deux nano-objets, les lacunes d'oxygène dans le MgO et les centres paramagnétiques moléculaires dans le CoPc, en nous concentrant sur le développement de techniques *operando* basées sur le rayonnement synchrotron.

Nanocanal de transport dans les MgO MTJ : lacunes d'oxygène

Les barrières tunnel cristallines en MgO utilisent le mécanisme de filtrage de symétrie ainsi que des électrodes choisies avec soin pour générer des valeurs élevées de magnétorésistance par effet tunnel. Les amplitudes élevées de la magnétorésistance par effet tunnel rendent les MTJ de MgO attrayantes sur le plan industriel pour le codage de l'information. La théorie et l'image combinée *ab-initio* du paysage énergétique des défauts de l'oxygène montrent que les centres M ont une hauteur de barrière de 0,4eV pour la dominante $T > 250K$. De même, les techniques de dépôt théoriques et expérimentales, comme l'oxydation post-dépôt du Mg métallique, peuvent donner lieu à des vacances d'oxygène à l'interface inférieure de la MTJ à base de MgO. De plus, le post-recuit de l'échantillon donne lieu à plus de M-centres que de F-centres. Par conséquent, parmi tous les défauts ponctuels de la barrière MgO, les centres M sont plus bénéfiques car ils ont une petite hauteur de barrière et améliorent relativement le TMR. Tout ceci rend intéressant l'étude locale de ces vacances d'oxygène en utilisant les rayons X synchrotron.

Les vacances d'oxygène créent des zones dans la barrière de MgO appelées points chauds qui canalisent le courant du dispositif. Une série de techniques sont utilisées pour explorer ces points chauds. L'AFM à pointe conductrice cartographie les points chauds, ce qui montre une conduction nanométrique. Une autre technique consiste à utiliser des rayons X de qualité synchrotron, où des rayons X d'une largeur de 80 à 800 microns inondent la totalité du MTJ à base de MgO d'une largeur de 20 microns pour étudier la propriété matérielle du point chaud, se référer à la figure 2. Dans une

expérience classique de rendement électronique total, on obtient des informations sur tous les atomes présents dans la jonction et même sur le matériau environnant. Un pas en avant de cette approche centrée sur le matériau est l'approche operando centrée sur le dispositif - qui lit les propriétés du matériau dans le courant du dispositif. En d'autres termes, nous concentrons les informations relatives à la XAS, à la sensibilité chimique et à la structure électronique sur les points chauds qui déterminent le fonctionnement du dispositif. Ici, l'énergie des photons des rayons X est accordée sur l'arête K de l'oxygène (545eV), c'est-à-dire le point chaud, se référer à la figure 2. La sélectivité du point chaud est possible parce que le courant circule à travers le point chaud qui forme le chemin de transport nanométrique pour les MTJ à base de MgO. Cette technique operando a été mise au point par notre groupe dans la ligne de faisceau deimos pour les MTJ de MgO. Dans la thèse actuelle, nous avons étendu cette technique à la ligne HERMES pour cartographier localement les vacances d'oxygène et les points chauds dans les jonctions tunnel de MgO en utilisant un nanofaisceau de rayons X.

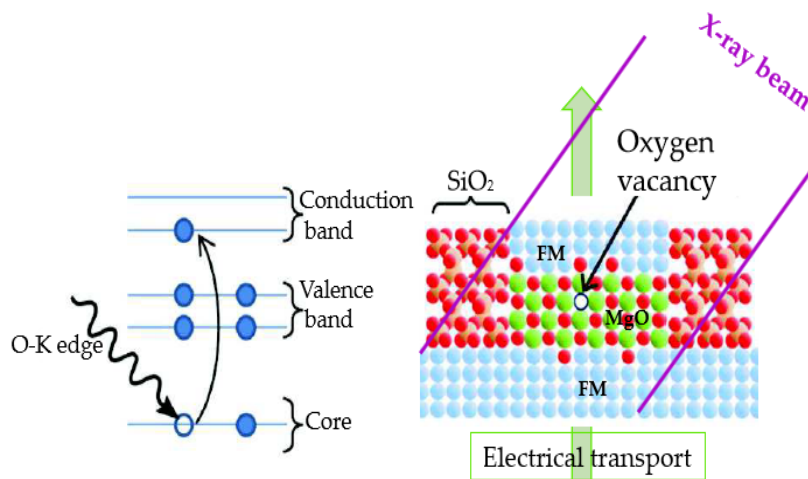


FIGURE 2: Schéma de l'impact des rayons X sur la MTJ à base de MgO de 20 microns. Image adaptée du [5]

À HERMES, nous avons utilisé la station finale de microscopie à rayons X à balayage transmisson (STXM). Le STXM est une technique de microscopie photon-photon utilisée pour sonder les propriétés volumiques des échantillons, offrant une analyse en profondeur jusqu'à quelques centaines de nm. Les rayons X synchrotron sont focalisés à l'aide d'une plaque de zone et un spot de rayons X d'une largeur

d'environ 30 nm est projeté sur l'échantillon. Cela excite les lacunes de O et le point chaud peut être résolu spatialement pour étudier leurs propriétés de magnéto-transport dans le dispositif.

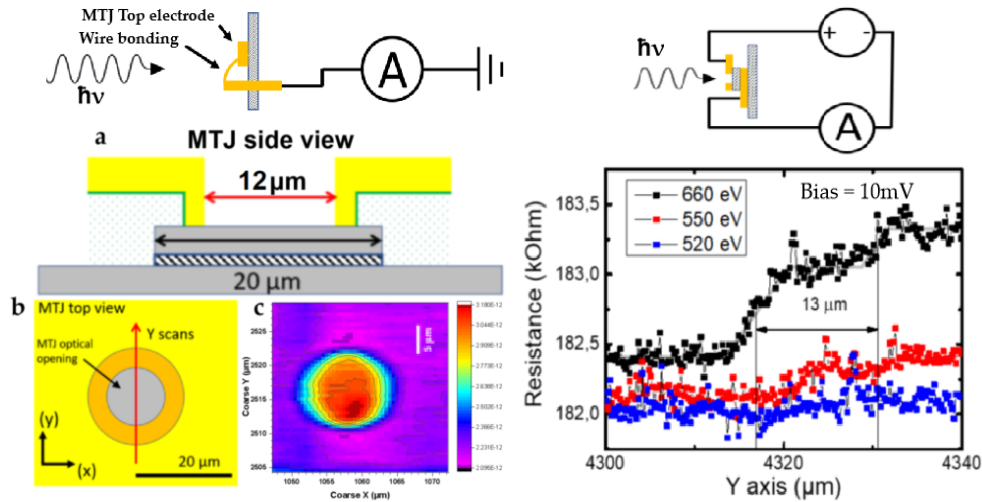


FIGURE 3: **Mesure du dispositif Operando à HERMES.** (a), (b) STEYM - Cartographie par microscopie à balayage du rendement électronique total d'un MTJ de 20 microns à l'aide d'un faisceau de nano-rayons X. (c) OSXM - Balayage linéaire par microscopie à rayons X à balayage opératoire à travers le MTJ localisé, montrant le changement de résistance pour trois énergies de rayons X. Les connexions électriques respectives sont indiquées en haut des images.

L'opération du dispositif se déroule en deux temps : Tout d'abord, la microscopie à balayage du rendement électronique total (STEYM) est réalisée pour localiser le dispositif à l'aide de rayons X, se référer à la figure 3(a,b). Le TEY est enregistré pendant le balayage avec des rayons X accordés à des énergies spécifiques de l'oxygène. La figure 3(b) représente la première carte STEYM de l'ouverture optique de 12 microns de la MTJ à base de MgO utilisant un nanofaisceau de rayons X. Une fois le dispositif localisé, nous passons au mode operando du dispositif en connectant la jonction respective et l'électrode inférieure. C'est ce qu'on appelle la microscopie à rayons X à balayage opératif (OSXM), se référer à la figure 3c. Des balayages linéaires sont effectués sur l'ouverture optique de la MTJ pour trois énergies de rayons X et, simultanément, la résistance du dispositif est enregistrée, voir Figure 3c. Au-dessus de l'arête O K, c'est-à-dire 660 eV, un plateau de résistance clair est observé. Ce

plateau est entouré de zones dans lesquelles la résistance augmente progressivement. Cela peut être dû à des effets de charge induits par le faisceau de rayons X. À 520eV (Figure 3(c) données bleues), c'est-à-dire sous le bord O K, l'augmentation de la résistance est fortement réduite. Ceci démontre clairement la sensibilité chimique. Ainsi, la technique OSXM révèle de manière factuelle l'implication des atomes de O dans le transport électrique à travers la MTJ MgO.

Nanocanal de transport dans les MTJ moléculaires : Centres paramagnétiques du cobalt dans les molécules de CoPc

Parallèlement aux MTJ MgO, il existe un fort intérêt pour l'étude de nouveaux matériaux, tels que les semi-conducteurs organiques (OSC), car ils présentent un faible couplage spin-orbital (SOC) et une interaction hyperfine (HFI). La faible force de couplage entre le spin de l'électron et les moments magnétiques nucléaires préserve l'orientation du spin de l'électron pendant une très longue période. Par conséquent, l'information sur le spin peut être préservée et transportée sur des échelles de longueur microscopique ($10^2 - 10^3 nm$), qui sont beaucoup plus longues que celles des semi-conducteurs classiques. Actuellement, des molécules nanocarbonées telles que le graphène, le nanotube de carbone et le fullerène, ainsi que des molécules organiques comme la phtalocyanine et la porphyrine de la famille des OSC sont largement utilisées dans les dispositifs spintroniques moléculaires.

Dans cette thèse, les molécules de phtalocyanine de cobalt sont utilisées comme espaceurs dans des jonctions spintroniques. La phtalocyanine de cobalt (CoPc) appartient à la famille des phtalocyanines métalliques, Figure 4. Le CoPc a une structure planaire et a comme ion métallique central le Co avec un spin 1/2, ce qui le rend paramagnétique. Alpha et beta sont les deux polymorphes les plus étudiés du CoPc et tous deux forment un empilement colonnaire qui se différencie par leurs angles d'empilement respectifs, Figure 4. Les études de microscopie à effet tunnel montrent que le CoPc est posé à plat sur le substrat et forme des chaînes de spin anti-ferromagnétiques unidimensionnelles, ce qui le rend avantageux à inclure

comme barrière dans les MTJ verticaux. L'ordre AFM est dû à l'interaction superexchange. L'étude par spectroscopie à effet tunnel des monocouches de CoPc montre que l'excitation d'une chaîne de spin peut conduire à une augmentation de la conductance, Figure 4. Les étapes d'excitation de spin correspondent aux transitions électroniques de l'état fondamental singulet à l'état excité triplet.

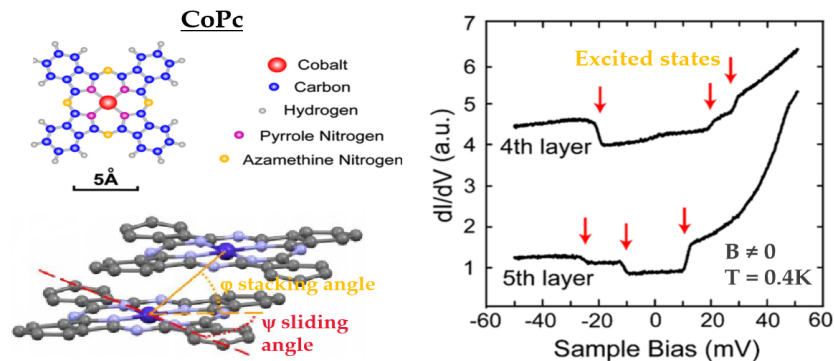


FIGURE 4: Illustration de la structure de la phtalocyanine de cobalt. Image de spectroscopie à effet tunnel montrant une augmentation de la conductance pour les monocouches de CoPc dans les films minces. Image adaptée de [6].

Les études de magnétométrie dépendantes de la température sur les poudres et les films minces de CoPc ont montré une forte interaction de couplage d'échange antiferromagnétique [6] (J/k_B) autour de 100K. La structure plane et le fort couplage antiferromagnétique (AFM) entre les chaînes moléculaires de CoPc sont intéressants pour explorer leur rôle dans l'interface métal/molécule ou spinterface [7]. Le couplage d'échange interfacial entre le FM et l'AFM donne lieu à une anisotropie unidirectionnelle ou biais d'échange qui se manifeste par un déplacement de la boucle d'hystérésis. Le biais d'échange de FM/MPc présente une forte dépendance à la température. Le biais d'échange diminue lorsque la température augmente. Cet effet est également observé dans d'autres complexes métalliques comme les porphyrines métalliques. La polarisation d'échange joue un rôle clé dans la spintronique car elle est responsable de la fixation de la direction de l'aimantation de la couche FM (couche de référence) avec sa couche AFM voisine.

Barraud et al ont également rapporté les premières expériences sur l'impact des chaînes de spin moléculaires portées par les molécules de phtalocyanine métallique

sur le transport polarisé en spin [8, 9]. Ce travail a introduit les notions de spectroscopie de spin-flip [6], normalement étudiées dans des jonctions modèles assemblées à l'aide d'un STM, aux dispositifs à l'état solide. En effet, ils ont lié les augmentations de conductance observées à l'ouverture d'un canal de courant dû aux excitations de spin. Pourtant, bien que ce canal de courant supplémentaire soit censé être entièrement polarisé en spin en raison des règles de transition [10], l'impact sur la MR n'a pas été discuté.

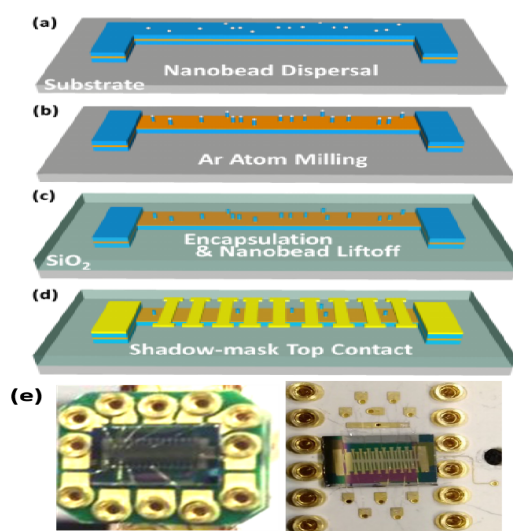


FIGURE 5: Diagramme des étapes de la fabrication de dispositifs nanomoléculaires sur puce par la technique de lithographie sèche. Image adaptée de [11].

Grâce à ces connaissances, nous avons fabriqué des nanodispositifs verticaux à base de CoPc en utilisant une nouvelle technique de lithographie développée dans le groupe. Le processus de fabrication commence par le dépôt de films minces dans des conditions UHV, puis la définition des jonctions de nanopiliers, le dépôt de nanosphères qui servent de masques, la gravure, la passivation et enfin le décollement des sphères, pour finir par la métallisation, Figure 5. L'échantillon est ensuite collé sur la puce correspondante, relié par fil et est prêt pour les mesures de caractérisation électrique et de magnéto-transport. Les dispositifs moléculaires ont été étudiés à la fois en laboratoire et sur la ligne de faisceau synchrotron DEIMOS, Figure 5.

Notre deuxième transport nanométrique implique des molécules de CoPc dans

la structure verticale du dispositif spintronique FM(50nm)/CoPc (20nm)/FM(10nm). Dans la Figure 6, nous examinons le transport polarisé en spin qui se déroule à partir de l'électrode inférieure de Fe à travers le CoPc MSC dans nos dispositifs. Dans l'encadré vert, le premier ensemble de flèches correspond aux canaux de transport de Fe avec une polarisation de spin positive et cette polarisation de spin positive est inversée et amplifiée à l'interface avec le CoPc. Cette polarisation de spin négative est inversée dans le transport lors de la génération de l'état excité de la chaîne de spin en raison des règles de sélection de spin, Figure 6.

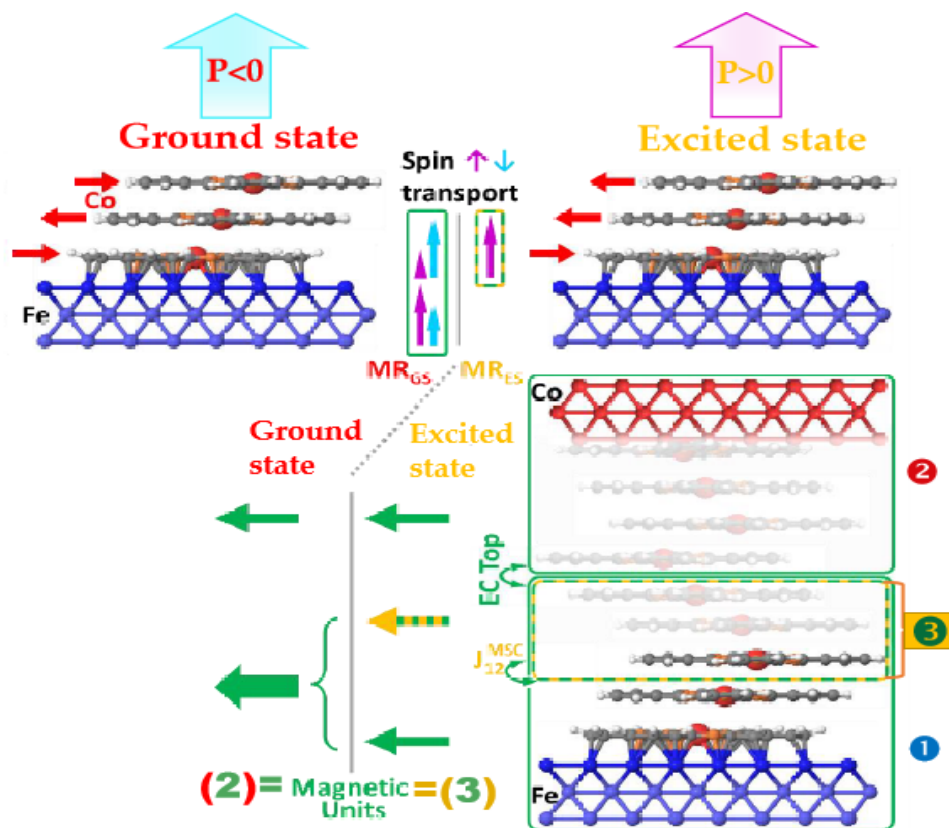


FIGURE 6: Schematic representation of three spin phenomenological mode for Fe/CoPc/Co system. Image adaptée de [11].

Le transport à travers l'état fondamental implique 2 unités magnétiques principales contenant les électrodes FM, le MR associé à cela est donné par MR_{GS} . Si nous changeons l'état de la chaîne de spin, l'anisotropie magnétique change et dans ces conditions, elle peut devenir une unité magnétique tant que l'énergie de formation de cet état n'est pas dépassée par l'énergie thermique des unités (expt+DFT 6.1meV). Par conséquent, dans l'état excité, l'unité magnétique inférieure comprend

une 3ème unité qui contribue uniquement à la MR_{ES} . $ECTop$ et J_{MSC}^{12} sont les termes de couplage entre les unités centrales et extérieures.

La mesure du dispositif se fait en appliquant une polarisation à travers les électrodes FM et un \mathbf{H} externe le long de la direction de magnétisation des électrodes. Voici la mesure de la résistance en fonction du champ magnétique pour une polarisation appliquée de 100mV à 17K. Le niveau de résistance près de $\mathbf{H} = 0\text{T}$ est dû à l'inversion de magnétisation de l'unité magnétique supérieure ; le changement de résistance autour de $\mathbf{H} = 1,5\text{T}$ est dû à la chaîne de spin excitée qui change son orientation magnétique en raison de la polarisation d'échange. L'inversion finale se produit à un champ beaucoup plus élevé $|\mathbf{H}| > 2\text{T}$. La DFT et la théorie phénoménologique confirment cette unité d'image. Les contributions MR des états fondamentaux et excités peuvent être déterminées expérimentalement et sont de signes opposés. Ce signe opposé des MR est une conséquence de l'inversion de la polarisation du spin de la contribution de la spinterface entre son état fondamental et son état excité. Cette MR est un moyen simple de montrer que nous étudions 2 mécanismes de transport différents de SP opposés.

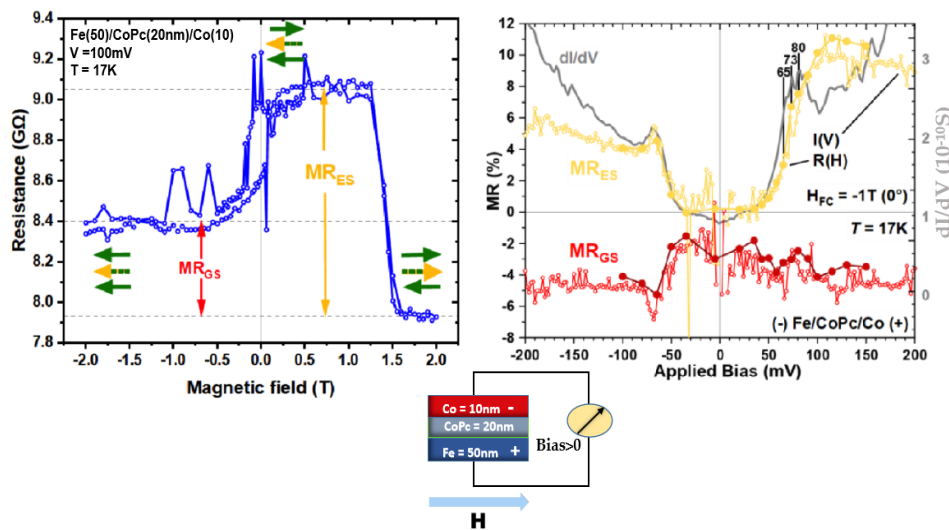


FIGURE 7: Diagramme des étapes de la fabrication de dispositifs nanomoléculaires sur puce par la technique de lithographie sèche. Image adaptée de [11].

La conductance différentielle en fonction de la polarisation appliquée montre des pics à $|V| \approx 70\text{mV}$. Ces caractéristiques et l'augmentation de la conductance sont la

signature de l'ouverture des canaux de spin-flip soutenue par les expériences STM. La MR des chaînes de spin excitées suit spectroscopiquement l'augmentation de la dI/dV . La caractéristique la plus frappante est les signes opposés des deux MRs de l'état fondamental et de l'état excité. Cette différence de signe des deux termes MR est une signature que nous étudions les MR des états fondamentaux et excités. Ce résultat est observé et rapporté pour la première fois.

La troisième voie de transport ressemble beaucoup à la précédente, mais elle a été légèrement modifiée. En fait, cette troisième voie ne concerne pas le codage de l'information mais se concentre sur la récolte de l'énergie. Par conséquent, pour comprendre ce contexte, nous devons nous éloigner un peu du magnéto-transport et considérer la récolte de l'énergie. Comme nous le verrons dans le thème général, les voies de nanotransport ne concernent pas seulement les molécules, comme dans la deuxième voie que j'ai décrite, mais aussi les voies de nanotransport dans lesquelles des lacunes en oxygène peuvent être impliquées.

La caloritronique de spin fusionne la spintronique et la thermoélectricité. Il s'agit d'un régime de thermodynamique classique, mais nous pourrions nous inspirer de cette page qui montre que le système a un taux de production d'entropie maximal à sa transition de phase [12]. Nous utilisons le meilleur des connaissances disponibles sur les moteurs quantiques existants, c'est-à-dire les moteurs mésoscopiques et atomiques, pour concevoir un moteur spintronique basé sur une molécule. La figure 8 représente le schéma théorique du moteur spintronique qui combine des sélecteurs spintroniques (SS) avec des états de spin discrets des centres paramagnétiques (PM) couplés par échange. Les interactions entre les deux sont modérées au moyen de fluctuations de transport de charge polarisées en spin. Δ = division de spin des centres PM, flèches circulaires = fluctuations thermiques sur les PM ; flèche verticale = occupation de spin du centre PM, épaisseur de la flèche = asymétries basées sur le spin dans les fluctuations de transport, Le moteur fonctionne en récoltant les fluctuations thermiques sur un centre PM et en appliquant stochastiquement une rétroaction sur l'occupation de spin de l'autre centre PM qui sont couplés par l'énergie d'échange magnétique J . Les fluctuations de transport vers/depuis les centres PM

se produisent à des énergies différentes à travers la jonction grâce aux électrodes de sélection de spin - générant une polarisation décalée V_{off} , c'est-à-dire une puissance de sortie électrique. Pour un moteur spintronique, il est naturel et très élégant de rompre l'équilibre détaillé.

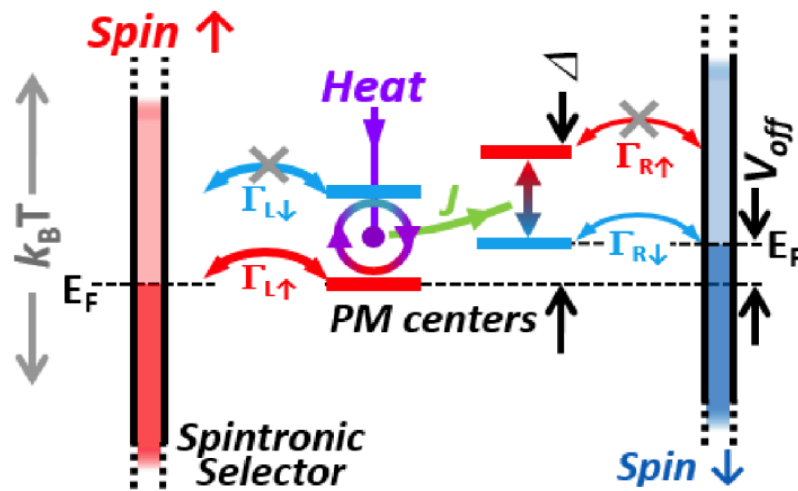


FIGURE 8: Représentation schématique du moteur moléculaire nano-spintronique.

L'une des observations intéressantes était le courant spontané persistant non nul $I_{sp} \approx -23 \mu A$ voir Figure 9. Son amplitude n'est pas fortement affectée par des balayages intermittents d'un champ magnétique externe jusqu'à 2T appliqué perpendiculairement aux magnétisations des électrodes. Cela confirme que le champ magnétique n'est pas la source principale du fonctionnement de nos moteurs à spin [13, 14].

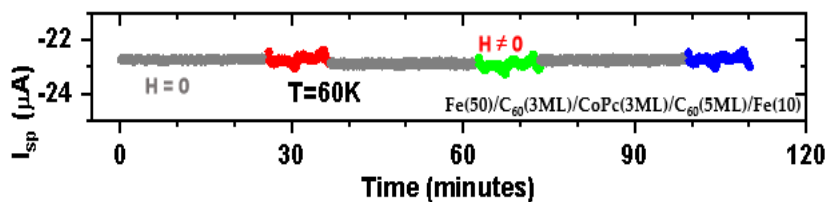


FIGURE 9: Courant spontané enregistré lorsque le champ magnétique appliqué est perpendiculaire à la magnétisation de l'électrode FM.

Dans la figure 10, nous voyons des balayages $I(V)$ répétés à 240K. La résistance de pente R_s calculée à partir du courant à $\pm 10 mV$, est de 157Ω . En comparant avec la dépendance temporelle de I_{sp} tracée dans l'encart supérieur, nous trouvons que

le courant de décalage $I_{Off} = -26 \mu A$ à $V = 0$ est le même que I_{Sp} . Nous en déduisons que l'application d'une tension de polarisation $V=0$ ne confère pas d'énergie au dispositif. I_{Off} et le décalage de polarisation complémentaire $V=4,05 mV$ à $I = 0$ (voir la dépendance temporelle dans l'encart supérieur), sont respectivement 230x et 100x plus grands que les erreurs de décalage expérimentales observées pour une résistance calibrée à 100 (point de croix magenta dans la Figure 10). La légère diminution de la conductance de la jonction avec l'augmentation de la température (voir Fig. 10) confirme la nature métallique de la nanojonction.

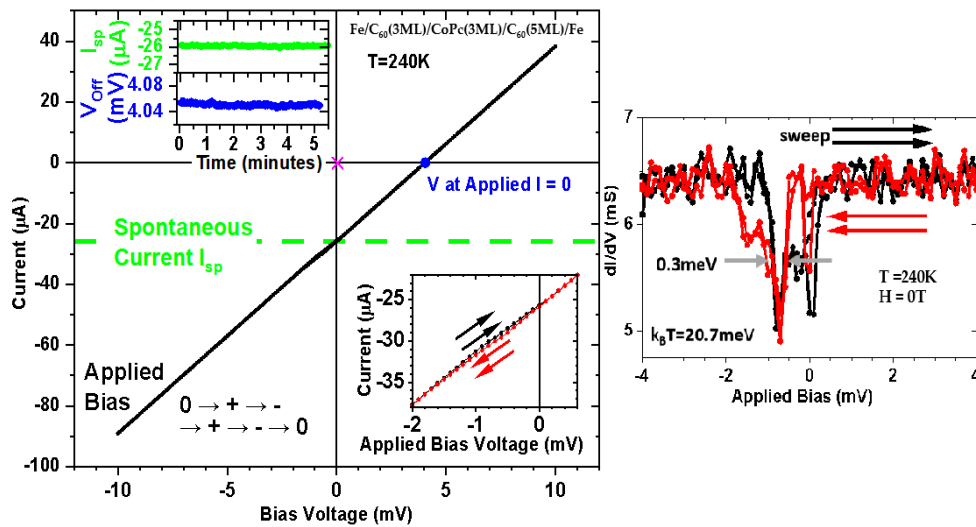


FIGURE 10: Les caractéristiques du courant en fonction de la polarisation appliquée montrent un comportement linéaire avec les décalages de courant et de tension. La croix magenta représente le décalage expérimental. L'encart supérieur montre la dépendance temporelle de l'offset et l'encart inférieur montre l'hystérésis de l'IV pour le balayage de la polarisation avant et arrière. A droite, la dI/dV avec FWHM inférieur à $k_B T$

L'encart inférieur de la figure 10 révèle une légère déviation hystérétique par rapport à une réponse linéaire qui dépend de la direction du balayage (flèches rouges et noires). Dans cette fenêtre de polarisation de 1,4 mV, la dérivée numérique (voir la figure 10) révèle des caractéristiques avec une FWHM aussi faible que 0,3 mV malgré un étalement thermique attendu de 2-3 $k_B T$ lors du transport, avec $k_B T = 20,7 mV$ ici. Cette résolution spectrale inférieure à $k_B T$ reste pratiquement inchangée lorsque les fluctuations thermiques sont réduites d'un facteur 6, tout comme les principales

caractéristiques spectrales (désignées par A, B et C sur la figure 11). Ces caractéristiques spectrales sub- $k_B T$, qui reflètent la réduction du bruit induit par la rétroaction [15], constituent une signature thermodynamique quantique des propriétés du bain non thermique de la spinterface. La fenêtre d'énergie de 1,4meV pour les déviations du comportement linéaire représente une limite pour l'étendue énergétique des états de spin du PM, voir Fig.11.

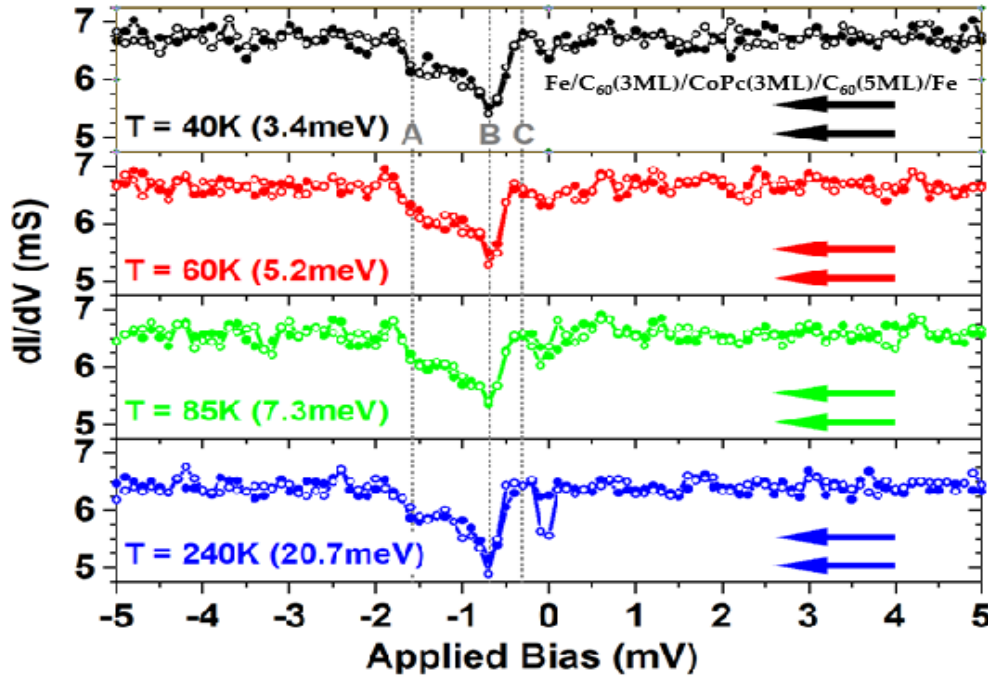


FIGURE 11: Traces de retour dI/dV pour 40K, 60K, 85K et 240K avec une résolution spectrale sub- $k_B T$ essentiellement identique.

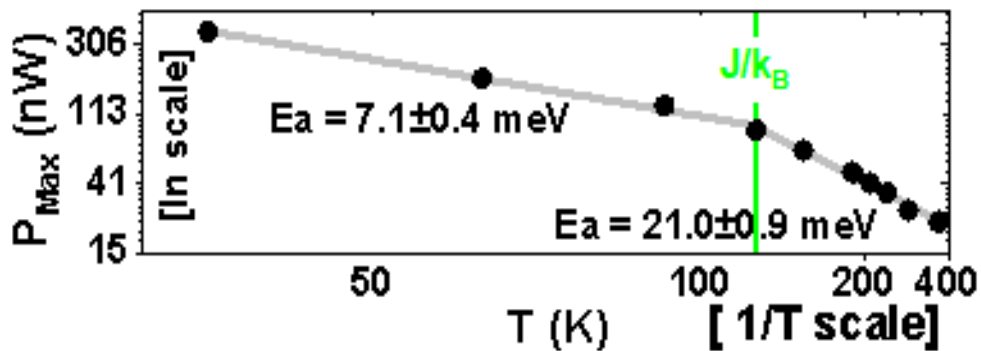


FIGURE 12: Caractéristiques de puissance du moteur nano spintronique avec une transition de phase magnétique à 120K.

Les courbes \ln vs. $1/T$ de la puissance de sortie suivent la loi d'activation thermique d'Arrhenius, voir figure 12. Le crossover à 120K, constitue une signature thermodynamique quantique de l'impact sur les performances du moteur. L'absence de

fluctuations de spin couplées pour $T > 120K$ est en accord avec la diminution plus rapide observée de la performance du moteur de spin. L'un des points forts de ce travail est la production d'une grande quantité de 450nWatt à 40K et 24nWatt à 360K (12). Notre moteur spintronique sur puce a une puissance de sortie qui peut être activée ou désactivée de manière spintronique, et persiste au-delà de la température ambiante, ce qui est prometteur pour les applications.

Thesis Outline

This Ph.D. thesis aims to bridge the knowledge gap in understanding the nano transport paths involved in MgO and organic-based magnetic tunnel junctions (MTJs) for information encoding and energy harvesting. In this regard, the focus is to scientifically understand the role of two quantum objects in the respective MTJs tunnel barrier, namely, 1) paramagnetic centers within cobalt phthalocyanine molecules of molecular MTJs and 2) oxygen defects in MgO based MTJs.

The manuscript is divided into three parts. The first part gives an overview of spintronics and its impact on the microelectronic industry, see Chap.1. It introduces the underlying physics governing spintronics and the transport behavior in oxide and molecule-based magnetic tunnel junctions. Unconventional techniques are employed to locally study the defect species' role in MgO Chap.2 and molecular Chap.3 transport devices. Additionally, we look into the significant breakthroughs, recent progress, and the knowledge gap in spintronics. One of the key highlights of this thesis is an experimental realization of the molecule-based quantum nano engine, which also behaves as a spintronically controlled switch of current flow and direction. To understand this a summary of the most critical literature on the quantum thermodynamic and spintronic based engines is discussed in Chap.4 to provide context for this thesis's experimental studies.

The second part is dedicated to discussing the essential experimental tools and sample preparation procedures employed throughout this research work. This includes a brief introduction to ultra-high vacuum (UHV) deposition systems used to make MgO & molecular heterostructures, characterization of thin films using superconducting quantum interference device (SQUID), x-ray reflectometry (XRR), and x-ray diffraction (XRD), TEM see Chapter 5. The processing steps involved to make

on-chip devices is walked through in Chapter 6. The experimental set-up used to study the MgO and molecular devices is discussed in Chapter 7, which includes the team's multifunctional magneto-transport bench and two SOLEIL synchrotron beamlines, namely DEIMOS and HERMES, which are involved in 'device operando' study of the respective nano-objects within the CoPc based and MgO based MTJs.

The third part discloses the results. The Chapter 8 experimentally shows the spin-flip spectroscopy concept, exchange bias phenomenon at the ferromagnetic metal/molecule interface (spinterface) and the spintronic anisotropy within the magneto-transport across solid-state nano-junction devices. This study constitutes an experimental benchmark for encoding information using an excited molecular spin chain. In Chapter 9 we experimentally investigate the conundrum of building a spintronic engine that harvests the thermal fluctuations on paramagnetic centers with the device at nominal thermal equilibrium. The first-hand result on spintronic energy harvesting at room temperature using molecular MTJs is a vital contribution of this thesis to the pool of existing knowledge of quantum engines. The Chap.10 is dedicated to discussion and perspectives.

Throughout this thesis, the engineering of molecular vertical nano devices was done using a solvent-free, resist-free process. This technique has enabled successful experimental implementation of studies that had not been realized due to technological difficulties. Appendix A provides a brief description of this novel solvent-free technique developed in the group to craft nano-pillar devices from the entire in-situ grown molecular thin-film heterostructures. Appendix B shows the TEM and SEM images of the silica spheres.

Chapter 1

Introduction

The booming pace of innovation in communications, computing, transportation, clean energy, and countless other applications is due to various semiconductors' contributions. Numerous industries boast semiconductors as the brains of modern electronics, producing exponentially advanced products at a lower cost. For instance, novel technologies such as neuromorphic computing, the Internet of Things (IoT), energy harvesting devices, automated devices, energy-efficient sensing, robotics, and artificial intelligence (AI) promise to alchemize society. Spintronics or electron spin-based electronics is one of the exciting fields that can support these technologies.

1.1 Spintronics and its role in the microelectronic industry

One quantum mechanical property associated with an electron is its spin; this is the key to quantum devices' functionality and underlines permanent magnetism. Spin can be traced back to the atoms' magnetic moment since the atomic magnetic moments are determined by electronic angular momentum. The connection between spin degrees of freedom and electron charge imposed by the Pauli exclusion principle has added a different level of practicality to quantum devices, creating a new branch of electronics called spin electronics or simply spintronics. Conventional electronics operate on the basis of electrons' motion and charge properties. Their integrated circuits are based on non-magnetic semiconductors, in which an electron's

spin property does not play a role in the operation.

Spintronics is closely related to magnetism, which studies the collective spin behavior of the bound electrons. It emphasizes on the moving electron whose spin coherence or collective transport is controlled to generate a measurable current variation. Thus, a spintronic device can be visualized as an apparatus to create a collection of spin-polarized electrons with an effective channel to transport these spin electrons to a separate apparatus, which then measures the spin in the form of change in resistance [16].

The recent development in the spintronics field exhibits the potential to influence key areas of information technology and microelectronics. The research can be dissected into four main regimes non-volatile memories, magnetic sensors, microwave devices, and beyond-CMOS logic. As the industrialization of solid-state devices based on GMR, TMR progress, the large scale manufacture of non-volatile magnetic random access memories (MRAM) marks the acceptance of the spintronics technology by the microelectronics industry. The faster integration of breakthrough technologies from the field, for example, ultra-low-power electronics, IoT, radio frequency (RF) communication, energy harvesting [17, 13, 18] artificial intelligence (AI), cryoelectronics, quantum engineering, and the list grows longer. With all the exciting opportunities and future challenges, advancement in spintronics has brought it to the limelight in mainstream technology. To sum this, electron spin property based spintronic devices promises to enhance the speed, the storage capacity of the device, and it has the potential to bring quantum physics to application.

1.2 Giant magneto-resistance (GMR)

The origin of spin-based electronics dates back to 1988 by discovering "giant magneto-resistance" - GMR independently by Albert Fert [2] and Peter Grünberg [19] (figure 1.1a). Giant magneto-resistance originates from a spin-dependent scattering of electrons due to different density of states at Fermi levels for a spin up and spin down electrons. The device based on the principle of GMR is termed as a spin valve, which

is a thin film composed of two ferromagnetic (FM) layers, which are separated by a non-magnetic spacer (figure 1.1b.) One of the broader commercial impacts of the GMR effect has been in spin valves used in magnetic recording for computer hard disk drives.

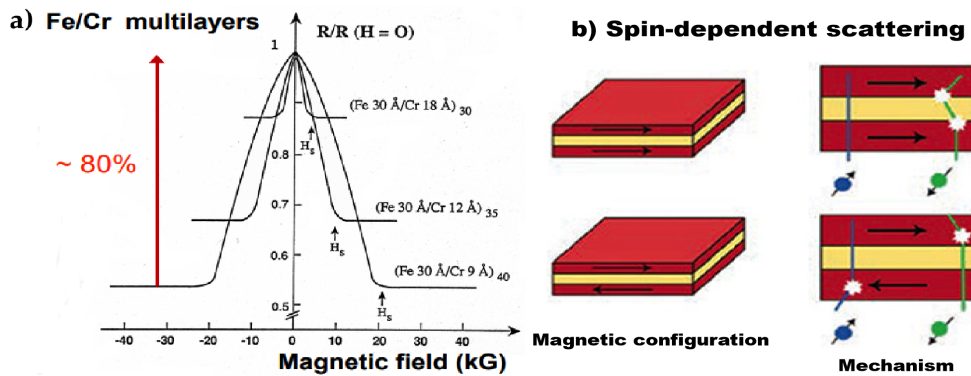


FIGURE 1.1: a) GMR effect observed in resistance vs magnetic field graph observed in Fe/Cr heterostructure. Image adapted from Ref [2] b) Spin-dependent scattering - basic principle of GMR .

A spin valve is a stack containing ferromagnetic and non-magnetic layers. This device controls the flow of current depending on the magnetization direction of the layers in the thin film. The spin valve is 'open' when the two FM layers' magnetizations are parallel or in a low resistance state. The valve is 'closed' when the two FM layers are anti-parallel or in a high resistance state see Figure 1.1b. The difference between the resistance in the parallel and anti-parallel configurations is termed magneto-resistance. GMR spin valves used as read head sensors in hard disk drives revolutionized the data storage industry. The first commercial use of this GMR - based sensor technology was by IBM, which released the hard disk drives, namely Deskstar 16GP Titan, in 1997, which had a storage capacity of 16.8 GB. Additionally, GMR technology found diverse applications as automobile sensors, solid-state compasses, and non-volatile magnetic memories. This vast technological impact of GMR in the industry gained a lot of attention, and in 2007 Albert Fert and Peter Grünberg were jointly awarded the Nobel Prize in Physics [1].

1.3 Tunneling Magnetoresistance (TMR)

Over the years, the field of spintronics has matured itself, and today the read heads in hard disks no longer use GMR but are based on tunneling magneto-resistance (TMR). In TMR based devices, the tunnel barrier is an extremely thin insulator (few nm's) sandwiched between ferromagnetic electrodes. Due to this thin insulating barrier, the electrons tunnel from one FM to the other, and hence tunnel magneto-resistance is a quantum mechanical effect. The origin of the TMR effect is spin-conserved tunneling, which is an interface sensitive phenomenon. TMR based devices are commonly known as magnetic tunnel junctions (MTJs).

Unlike the GMR-based spin valves, there is, in principle, no current propagation through an insulator of the MTJ but rather a tunnel current that flows directly between the FM electrodes. Achieving magneto-resistance using tunneling effect was modeled by Michel Julliere [3] in 1975, Figure 1.2a. The resistance of the TMR device depends on the relative magnetic orientations of the metallic electrodes. Since these electrodes are FM, their density of states (DOS) is spin-dependent due to exchange interaction J , as shown in figure 1.2b. The difference in the DOS at the Fermi energy level (E_F) for spin-up and spin-down electrons is the origin of tunneling magneto-resistance. Therefore according to this model, the tunneling current for each spin orientation is proportional to the product of the DOS at E_F in the electrodes on both sides of the tunnel barrier figure 1.2b.

The TMR effect is based on the assumption that electrons tunneling from a ferromagnet is spin-polarized, and their spin polarization P is given in terms of the spin-dependent density of states D^α of the ferromagnet by the equation below:

$$P = \frac{D^\uparrow(E_F) - D^\downarrow(E_F)}{D^\uparrow(E_F) + D^\downarrow(E_F)} \quad (1.1)$$

The classical theory of tunneling proposed by Merservey and Tedrow [20] states that the junction conductance is proportional to the product of the densities of states of the left and right electrodes. The TMR ratio can be written in terms of the effective

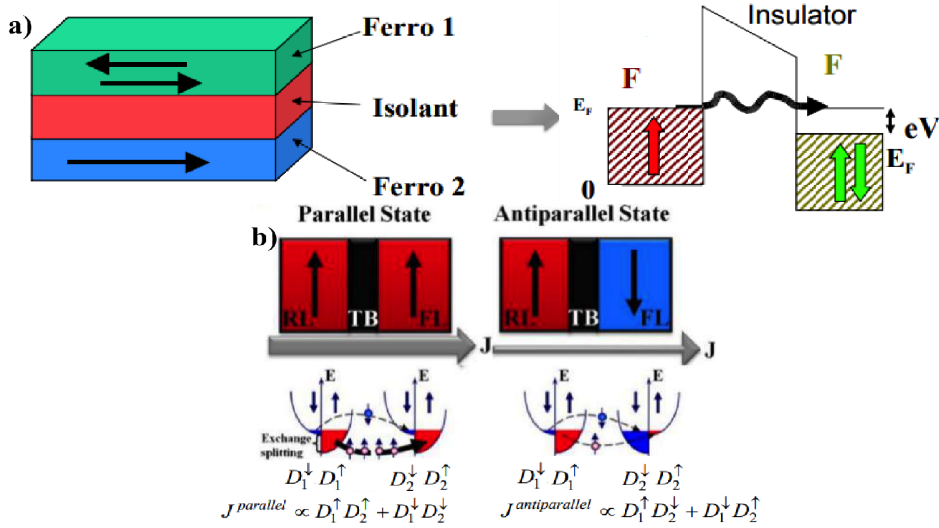


FIGURE 1.2: a) Illustration of Julliere's model of TMR in MTJ [3]. b) Spin filtering in TMR devices consisting of FM electrodes separated by thin tunnel barrier. An electron from spin-up (down) band can tunnel only through a thin barrier to the sub-band of the same spin configuration. In the P state the electrodes are strongly exchange coupled to each other with good band matching of the DOS which results in high current and low resistance amplitude. But in the AP state the band matching is poor due to weak exchange coupling between the electrodes.

spin polarizations P_1, P_2 of the electrodes, respectively:

$$TMR := \frac{R_{AP} - R_P}{R_P} = \frac{2P_1P_2}{1 - P_1P_2} \quad (1.2)$$

This model works fine to understand the tunneling magneto-resistance results in amorphous MTJs, where mainly s-like electrons, i.e., the free electrons, contribute to the tunneling phenomenon. However, this approximation predicted the TMR to be solely determined by the ferromagnetic electrodes' properties without considering the electronic character or changes in electronic structure induced at the FM/insulator interface. This called for further extensions to the model.

Stearns [21] work emphasized the importance of taking into consideration the character of the tunneling particles. Her work stressed that one must interpret the spin polarization values measured by spin-dependent tunneling (SDT) techniques as tunneling current on the DOS weighed by the tunneling matrix elements $|M|^2$ and not on the total DOS polarization at the Fermi level. These results were the first

pointer for understanding spin-dependent tunneling requires detailed knowledge of the entire heterostructure's electronic properties, including the tunnel barrier.

In 1989, Slonczewski [22] reported a calculation of a plane wave's propagation through a FM/tunnel barrier/FM sandwich. He showed the tunnel barrier's significance on the electrons' polarization and the resulting tunneling magneto-resistance amplitude.

1.4 Advancement in MTJs

The first MTJ devices were presented in 1995 by Moodera [23] in CoFe/ Al_2O_3 /Co MTJs and Miyazaki & Tezuka [24] in Fe/ Al_2O_3 /Fe MTJs (Figure 1.3a, b respectively). Independently this duo utilized amorphous alumina (Al_2O_3) barrier material, which exhibited quite a high intensity of 10% TMR amplitude at room temperature. Their work gained a lot of attention. Many efforts to increase the TMR magnitude were made by refining the quality of the device interfaces with Al_2O_3 films with a better homogeneity, roughness, and a significant decrease in the number of defects in the junction.

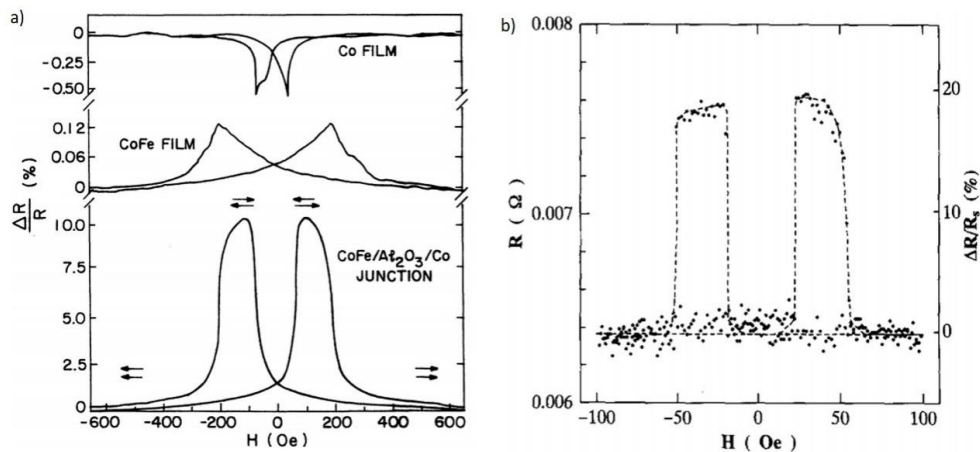


FIGURE 1.3: a) Room temperature TMR recorded using CoFe/ Al_2O_3 /Co junction. The arrows point the direction of magnetization in the CoFe and Co films. b) TMR recorded at room temperature using Fe/ Al_2O_3 /Fe MTJs. The images a) and b) are adapted from Ref [23] and [24].

A decade later, Wang's group [25] improved this result by optimizing the ferromagnetic electrodes using CoFeB/ Al_2O_3 /CoFeB MTJs. The TMR amplitude increased upto 70% at room temperature. However, this TMR value at RT is close to the Julliere limit for 3d FM-alloy electrodes if the decrease in polarization due to thermal spin fluctuations at finite temperatures' is taken into consideration. Therefore, an alternative to 3d FM metals is using higher spin polarization (SP) materials called half-metals. The common half-metals are $La_{0.7}Sr_{0.3}MnO_3$ (LSMO) [26], chromium dioxide (CrO_2) [27], and Fe_3O_4 with nearly 100% spin polarization. Bowen.M et al. [28] reported a transport spin polarization of 99.6% at 10K for LSMO/STO/LSMO magnetic tunnel junctions. At low temperatures very high TMR values ($> 100\%$) have been observed [29], but not at room temperature. At low temperatures, the SP and the MR amplitude of the half metals can be lower than their maximum values and rapidly decrease around temperatures where the half-metallicity disappears. The half-metals incorporated into the MTJs, have their half-metallicity vanishing above Curie temperature of the junction interface, which is often below the room temperature because of the interfacial alteration of the electronic structure [30].

A significant break-through in advancement of MTJs was the switch from amorphous tunnel barrier (AlO_x) to crystalline barrier layer (MgO). The crystalline structure of MgO served as an advantage to conserve the electrons' orbital character resulting in high TMR values [31, 32]. In the following chapter, a detailed discussion on structure and electronic properties of MgO crystal, interfacial effects at FM/MgO based MTJs and the tunneling phenomenon through a crystalline MgO (001) is presented.

Chapter 2

Nano transport path in MgO MTJs

The first-principle calculations predicted TMR values above 1000% for an epitaxial magnetic tunnel junction with crystalline MgO tunnel barrier sandwiched between ferromagnetic iron electrodes [31, 32]. Since then several groups have tested out this theory with Fe/MgO/Fe MTJs and also with other FM electrodes. In this chapter we will explore in detail the MgO structure and the interesting physics necessary to understand the role of oxygen nano-object in the transport across the MgO magnetic tunnel junction.

2.1 Crystalline structure of MgO

Magnesium oxide (MgO) is an ionic oxide with insulating properties and is composed of ion charges of magnesium $2+$ and oxygen $2-$. It has a cubic rock salt (fcc) crystalline structure, where each atom is six-fold coordinated in bulk, see Figure 2.1. The experimentally determined lattice constant of MgO is 4.207 \AA at $T = 0 \text{ K}$ [33]. When the effects of zero-point vibrations are removed, the lattice constant is 4.186 \AA [34].

The electronic system of MgO comprises a filled valence band (VB) that is mostly of oxygen character and an empty conduction band mainly from the magnesium states [35]. As a result of the electronic configuration, a charge transfer occurs from the Mg $3s^2$ orbital to the $2p^4$ orbital of O when the crystal is created, leading to insulating MgO [34]. The experimental band gap of bulk MgO is 7.8eV , as measured by

reflectance spectroscopy [36]. One of the shortcomings of all crystalline barrier material is the inseparable defects associated with them. Defects can be any dislocations and vacancies in the atomic framework of a crystal structure.

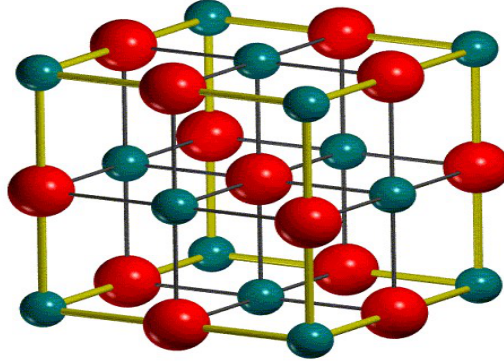


FIGURE 2.1: Face centered cubic Crystalline structure of MgO. Red spheres are Mg^{2+} atoms and greenish-blue colored spheres denote O_{2-} atoms covalently bonded.

2.1.1 Point defects within MgO

One of the common types of defects within the MgO crystal is point vacancies. The growing interest in studying the MgO vacancies has given rise to exciting optical [37], catalytic, and transport properties otherwise absent in an ideal crystalline material. In an ionic crystal-like MgO, several possibilities of lattice vacancies may occur, in which the ground states of cationic or anionic vacancies are either in neutral or charged form. In bulk MgO, the anion vacancy (O) is called an F center, and the cation vacancy (Mg) is called a V center. These vacancies can appear in neutral and charged (singly/doubly) state, represented as F^0 , F^+ , F^{2+} , V^0 , V^- , and V^{2-} . Interestingly, these vacancies can appear alone (F and V) centers or as a pair. For instance, a double oxygen vacancy is the combination of two oxygen vacancies M centers or F_2 and as oxygen-magnesium vacancies called P centers, as shown in Figure 2.2.

Table 2.1 provides information on the formation energies of all possible defect species within the MgO crystal structure. The formation energy for the oxygen vacancies is the lowest, and hence such defects are most likely to occur.

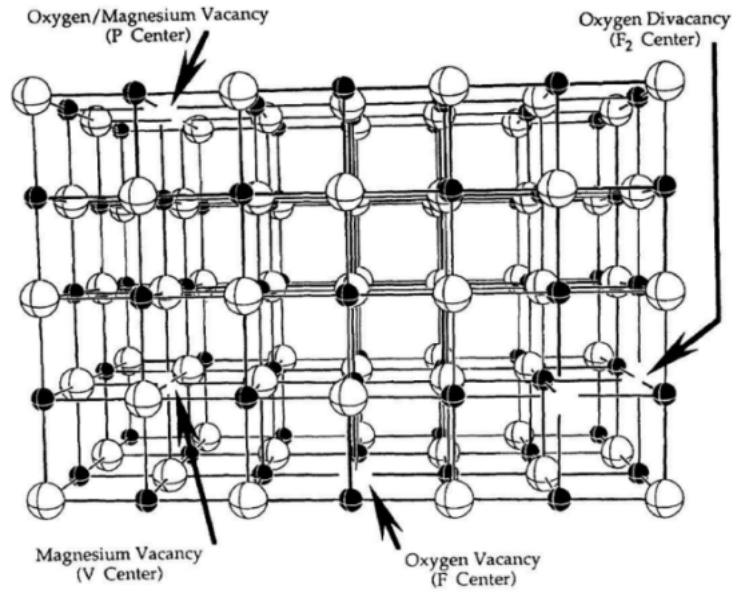


FIGURE 2.2: Schematic representation of crystalline MgO lattice defects or vacancies. Shaded spheres represent Mg [001] and white spheres are O atoms. Image taken from Ref [35]

Defect	F	F^+	F^{2+}	F_2/M	V	V^-	V^{2-}	P
Formation energy [eV]	1.82	3.67	5.47	3.23	13.82	14.83	16.35	3.48

TABLE 2.1: Calculated formation energies for defects in MgO. Values adapted from Ref [35].

2.1.2 Structure of Fe/MgO

Iron (Fe) is a ferromagnetic transition metal that typically crystallizes in a body-centered cubic (bcc) structure bearing a lattice constant of 2.867 \AA [38]. MgO has a face-centered cubic crystalline structure exhibiting a six-fold geometry. The lattice constants of the materials should match or be close to obtain structurally ordered magnetic hetero-junctions. This occurs for bcc(001) Fe electrodes and fcc(001) MgO barriers see Figure 2.3(a), (b) through a 45° in-plane rotation, with only a small lattice mismatch [39] of 3.8%, described in Figure 2.3 (c, d). It was experimentally shown that during the Fe/MgO growth process, the oxygen atoms are placed on top of iron atoms [39, 40].

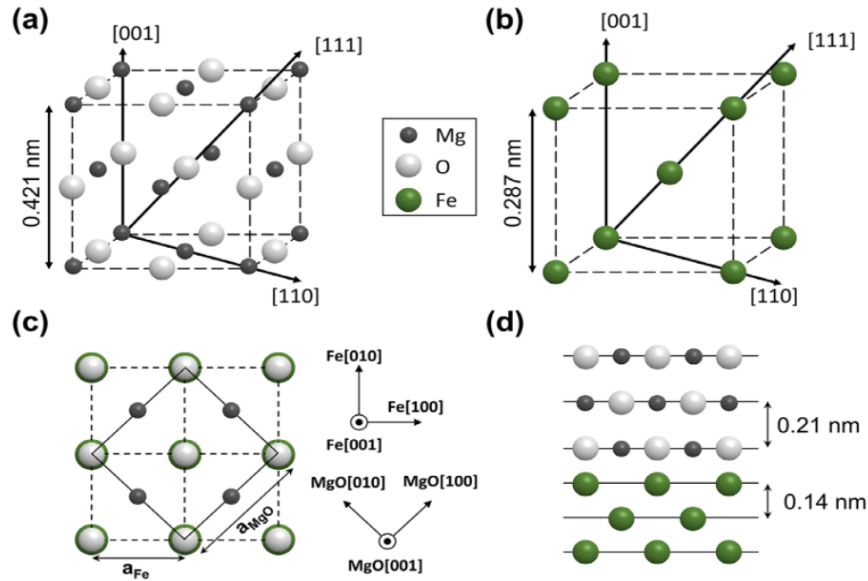


FIGURE 2.3: **Structure of Fe/MgO(001) interface.** Panel (a) and (b) depicts the crystal structure of MgO and Fe respectively. Epitaxial relation between the Fe and MgO is given in Panel (c) gives top view and (d) cross section of Fe/MgO interface. Image taken from Ref [41].

2.2 Symmetry filtering in crystalline barrier FM/MgO/FM MTJs

The magneto-resistive properties of inorganic based junctions containing amorphous tunnel barriers are aptly described using the Julliere model (see Chap.1 Sec. 1.3) and the free-electron models. But, in the case of crystalline tunnel junctions, the situation is complicated. The crystalline structure imposes particular properties for the electron's wave function because of the ions' periodic potential. This affects the tunneling process in the device. The electron wave functions can be grouped based on their symmetry properties, and each of these symmetries is coupled distinctly to the states in the crystalline barrier. As a result, the attenuation coefficient for each electron wave function is symmetry-dependent. Therefore, together with electron spin, the electron wave function's symmetry is also conserved during the transport. We will see, how a judiciously chosen combination of electrode and barrier can result in high TMR magnitudes for crystalline MTJs.

2.3 Bloch states and wave function symmetries:

An electron propagating through a crystalline junction experiences a periodic potential, and the wave function associated with it is described by Bloch wave function or Bloch states [42, 43]. Bloch's theorem gives insight into the formation of the valence band and conduction bands in a crystal system [43]. Generally, at each crystal interface, the wave functions have to be matched, and the matching depends on the incoming wave properties such as spin state and the symmetry of the Bloch wave function. As a result, the electrons can propagate only within the spin channel with a corresponding symmetry.

An amorphous tunnel barrier like AlO_x , sandwiched between two FM Fe(001) electrodes, is illustrated in Figure 2.4a. The FM electrode consists of Bloch states with different symmetries of wave functions. But the amorphous AlO_x tunnel barrier does not have a crystallographic symmetry. Hence, it leads to the coupling between Fe electrode's Bloch states of different symmetries with the amorphous tunnel barrier's evanescent states, which results in a finite tunneling probability. This type of tunneling process is known as incoherent tunneling.

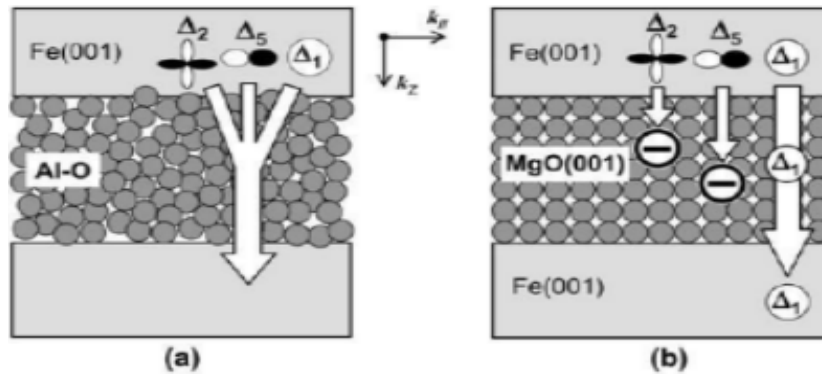


FIGURE 2.4: **Illustration of electron tunneling through AlO_3 and MgO barrier.** (a) Incoherent transport in amorphous AlO_3 tunnel barriers. (b) Coherent transport in crystalline MgO. Image taken from Ref [41].

For an epitaxially grown MgO(001) crystalline barrier on a bcc Fe(001), the tunneling process is coherent tunneling, see Figure 2.4b. In an ideal case, out of the three Bloch states $\Delta_1(s, p, d_{3z^2-r^2})$, $\Delta_2(d_{x^2-y^2})$ and $\Delta_5(p_x, p_y, d_{xz}, d_{yz})$, predominately

Δ_1 states are allowed to tunnel through the barrier. This novel mechanism of selective electron filtering was theoretically proposed by Butler et al. [31] and Mathon et al. [32] for Fe/MgO/Fe system. They also predicted high TMR amplitudes for these crystalline MTJs. According to this model, the amplitude of TMR is determined by the symmetry matching between the Bloch states for the majority (minority) spins of the FM electrodes and the tunnel barrier's evanescent wave functions.

The actual tunneling mechanism can be explained in the following way. Only those electrons that are in the vicinity of the Fermi level (E_F) can participate in the transport mechanism; hence it is crucial to distinguish the symmetry states of the electrons crossing the Fermi level. The preferential direction for the tunneling of electrons is perpendicular to the plane of Fe (001); that is, the lateral component of the wave vector, $k_{||} = 0$ direction, has a large tunneling probability. MgO (001) bandgap has three types of evanescent states, namely, Δ_1 , Δ_5 and $\Delta_{2'}$. When the tunneling wave functions are conserved, the corresponding Bloch states of Fe (Δ_1 (Δ_5 and $\Delta_{2'}$) couple with the evanescent states of the tunnel barrier MgO Δ_1 , Δ_5 , and $\Delta_{2'}$, respectively, see Figure 2.5a. The partial density of states (DOS) deduced from the first-principle calculations for the decaying evanescent states of MgO in parallel magnetic state, reported by Butler et al. [31], shows Δ_1 state has the longest decay length compared to Δ_5 and $\Delta_{2'}$ states, see Figure 2.5b. Hence, Δ_1 is the dominant tunneling symmetry state for parallel magnetic configuration.

Even though the Fe FM electrode's net spin-polarization is small due to different states at E_F , the Fe(Δ_1) band is fully spin-polarized, $P = 1$, at the Fermi level, see Figure 2.5c. The Δ_1 Bloch states are also highly spin-polarized at E_F in several bcc FM metals, including Co, based alloys like bcc Co-Fe, bcc CoFeB, and Heusler alloys. In the AP state, the absence of spin-matching Δ_1 electrons in the receiving electrode leads to a domination of the Δ_5 transport channel. Since the Δ_5 transport channel's decay rate across MgO is higher than that for the Δ_1 channel, a high TMR value is expected.

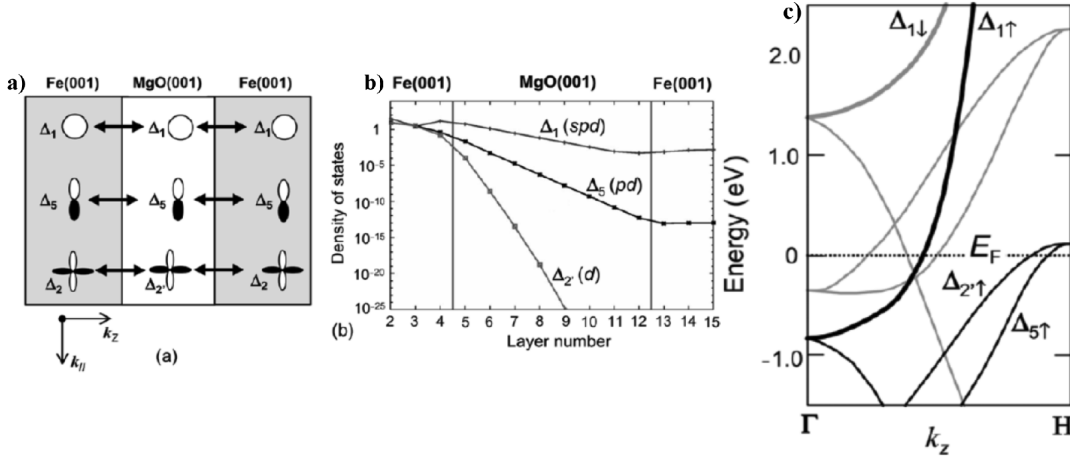


FIGURE 2.5: Schematic illustration of the coupling of electron wave functions between the Bloch states of FM iron and the evanescent states of the MgO tunnel barrier for the direction $k_{\parallel} = 0$. b) The image describes the partial tunneling density of states for the decaying evanescent states in MgO for Fe/MgO/Fe MTJ in the parallel magnetic state. c) The graph depicts the band dispersion of bcc Fe in the $[0\ 0\ 1]$ i.e., $k_{\parallel} = 0$ direction. The majority and minority spin bands; thick black and grey lines represent the majority and minority-spin of bcc Fe Δ_1 Bloch states. The Δ_1 states in bcc Fe is fully spin-polarized at Fermi energy level, (E_F). Images are adapted from Ref [41].

2.4 MgO magnetic tunnel junctions

In 2001, Bowen et al. [44] were the first to experimentally report a room temperature TMR of 60% at 30K in Fe(001)/MgO(001)/FeCo(001) MTJs, which implied symmetry filtering. Later, Faure-Vincent et al. [45] reported an observation of TMR=100% (at 80K), a value beyond that expected within a Julliere model [3] of free electron tunneling. Advancements in nano-fabrication techniques expanded the field, with experimental observations of high TMR values at RT reported by Yuasa et al. [46] (180%) and Parkin et al. [47] (220%) using Fe/MgO/Fe MTJs. TMR signal up to 600% has been reported at room temperature [48] in CoFeB/MgO/CoFeB MTJs pave the way for hard disk read heads.

All industrial applications of MTJs require high tunneling magneto-resistance ratios alongside with this is also the demand for miniaturization. A CoFeB/MgO based MTJs reported by Sato et al. [49] achieved TMR with junction diameter of 11nm. But the interfacial anisotropy prohibits further downscaling of the MTJs, thus imposing a physical size limit. To overcome this scaling problem, K. Watanabe et

al. [50] experimentally showed that using shape anisotropy property materials and switching magnetization using current, it is possible to achieve junctions smaller than 10nm. Several experiments report high TMR utilizing a combination of half-metallic Heusler alloys instead of traditional CoFeB/MgO/CoFeB MTJs. All these high TMR MTJs have helped to modernize the storage technology by their rapid commercialization. Mainly, the property of slow decay of the Δ_1 wave function of MgO results in a relatively low resistance, crucial for devices such as spin-torque switched MRAM and read sensors for HDD.

However, at room temperature, the TMR amplitude never reached the enormous values [31] ($> 1000\%$) predicted theoretically by changing the tunnel barrier from amorphous to crystalline MgO barrier. This inconsistency between the theory and experiment was loosely assigned to defects and structural imperfections in the tunnel junctions.

2.5 Magneto-crystalline anisotropy at FM/MgO interface

Meyerheim et al. [51] experimentally proved that a FeO layer could form at the interface between Fe and MgO when MgO is deposited onto a Fe (001) surface. The modification of the interface can drastically influence the spin-dependent tunneling when compared to an ideal interface. Zhang et al. [52] theoretically showed that a FeO intralayer has a negative impact on the spin-polarized tunneling process since it reduces the tunneling current of the majority spins. When the interface is oxidized, the FeO bonds are formed, and the Δ_1 Bloch states of Fe fail to couple effectively with the Δ_1 evanescent states of MgO. This restrains the coherent tunneling of Δ_1 state and results in a significant drop in the TMR amplitude. This proves that coherent tunneling is extremely sensitive to the interface's nature, and oxidation of a monolayer at the interface can drastically reduce the TMR ratio. Therefore, one of the challenges was to obtain an interface that is almost free from these defects. In this regard, Mathon et al. [53] performed calculations on epitaxial Fe/Au/MgO/Au/Fe(001) MTJ, suggesting that the insertion of two layers

of Au should prevent the oxidation of Fe electrodes and maintain a contamination-free interface. A theoretical study by Wang et al. [34] on Fe(001)/Mg/MgO/Fe and Fe(001)/Mg/MgO/Mg/Fe MTJs, reported that the Mg inter-layers could preserve the dominant Δ_1 symmetry state during the tunneling process.

Parallel to this, extensive studies were performed to investigate the origin of perpendicular magnetic anisotropy (PMA) in the Fe/MgO interfaces. The first principle calculations by Yang et al. [54] confirmed that the source of PMA at metal/oxide interface was due to the magnetic anisotropy arising from the coupling between the orbital and magnetic moment of the magnetic atoms spin-orbit coupling (SOC). Their calculations also predicted high PMA values for Fe/MgO interface and reduced PMA magnitude for over/under oxidized Fe/MgO interfaces. It was experimentally found that PMA energies were dependent on Fe/MgO's interfacial conditions, and it can be controlled by the post-annealing process [55]. Hallal, A et al. [56] conducted theoretical calculations to understand perpendicular magnetic anisotropy changes as a function of Fe and MgO thickness. They pointed out that large PMA values' origin is much complex than just the hybridization of iron (3d) and oxygen (2p) orbitals. This was backed by the results from their calculation that showed, PMA energy is not localized at the Fe/MgO interface; instead, it extends into the bulk of the structure, showing orbital dependent oscillatory damping character on moving away from the interface.

Furthermore, they concluded that the thickness of the barrier MgO did not affect the calculated PMA values. Instead, it is the Fe thickness that induces an oscillatory behavior on the PMA energies. This work successfully explained each monolayer's role of the Fe layers deposited on top of MgO, refer [56] for details. Okabayashi et al. [57] used an angular dependent x-ray magnetic circular dichroism (XMCD) technique to experimentally investigate the large PMA values at the Fe/MgO interface. They observed additional pre-peaks at the oxygen K-edge of the x-ray absorption spectra. This proved that the Fe-O bonding occurs at the Fe/MgO interface. Moreover, using XMCD measure Fe orbital moment results, they concluded that the anisotropic orbital magnetic moments contribute to the high PMA energies dependent on the annealing temperatures. An interesting experiment by Liang et al. [58]

using CoFeB/MgO proved the existence of both perpendicular magnetic anisotropy and Bloch state symmetry filtering across the FM/MgO interface. This is crucial towards producing massive electrical spin injection into GaAs at $\mathbf{H} = 0\text{T}$.

Numerous materials for buffer and capping were tested to find the best stack recipe for MgO-based MTJs, thereby having high TMR and large PMA values. The ab initio calculations indicated that a Fe/MgO interface has a higher PMA than a pure Co/MgO interface. Also, the density of thermal fluctuations is higher for the Fe/MgO interface than Co/MgO. In the first case, it seems promising to use Fe rich alloy of $Fe_{75}Co_{25}$ to get high TMR [39] but the latter case encourages to use of Co-rich alloy.

In summary, a balanced composition of CoFeB is an excellent trade-off to maximize the anisotropy and reduce the damping effect in MTJs. Moreover, this interfacial Fe layer also is proven to avoid oxidation of the lower electrode [59]. Moreover, the spin polarization of CoFeB measured by point-contact Andreev reflection method at room temperature is higher than its individual atoms [60]. The combination of CoFeB/MgO films therefore have high spin polarization allowing it to be a spintronic selector with industrial implication [17]. For the FeCoB/MgO interface to be an effective spintronic selector, it is crucial to control the defect species like oxygen vacancies and hence the transport path across spintronic devices.

2.6 Role of defects in MgO tunnel barrier

In oxides like MgO, oxygen vacancies are responsible for inducing electronic, structural modifications and sometimes enhanced reactivity [61]. Maio et al. [62] reported the impact of these oxygen vacancies in the MgO tunnel barrier MTJs. According to this work, the defect states within the MgO introduces a symmetry break that opens up non-coherent tunneling channels. The evanescent states within the MgO barrier will now have to undergo a two-step tunneling process, namely coherent \rightarrow non-coherent tunneling process, resulting in the drop of TMR amplitude.

Kim et al. [63] experimentally showed it is possible to control the nature and the

density of oxygen defects in the MgO barrier during its growth process by adding oxygen (0% to 10% O_2) to the Ar plasma during the rf sputtered MgO growth. They reported the spectral dependencies of optical absorption spectra of MgO(001) extracted from experimental transmission spectra, see Figure 2.6a. The three peaks observed in the spectra were associated with the different oxygen defect species of MgO. It is clear from the 2.6a that the increase in O_2 concentration, decreases the spectral weight of the three peaks. Additionally, they performed transport measurements across the MgO//MgO/Fe/MgO layers to study the role of oxygen defects. The local current-voltage characteristics was recorded using a conductive atomic force microscopy (CT-AFM). The I(V)s registered away and on the current hotspots, revealed that changing the O_2 concentration from 0% to 10%, locally increased the barrier heights, see graph 2.6b.

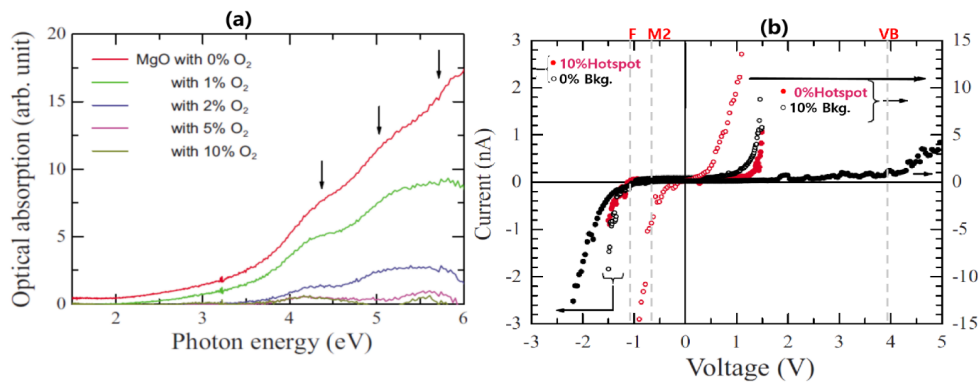


FIGURE 2.6: **a)** Schematic plot of optical absorption spectra of crystalline MgO(001)/MgO(50nm). The three peaks positions are indicated by arrows. The various peak at photon energy corresponds to the oxygen defects in MgO. The peak at : 4.2eV is of M centers; 5.0eV its' F/F^+ centers and 5.6eV corresponds to F^{2+} center. Colors indicate the plot for different oxygen proportion used during MgO deposition. As the O_2 concentration increases the peaks' spectral weights of the three peaks decrease respectively. **b)** I(V) curves for two oxygen proportion in MgO layer namely: 0% – O_2 and 10% – O_2 , measured on the hotspot and away from hotspot (Bkg.) using CT-AFM technique. For the I(V)s in the positive bias, increasing the oxygen concentration from 0% to 10% raises the barrier height from 0.9eV to 4.1eV for the Bkg. and from 0.4eV to 1.1eV for the hotspots. The gray dashed lines indicates the valance band (3.9eV), F center(-1.1eV) and M2 center (-0.71eV). Images reproduced from Kim et al. [63].

Interestingly, the I(V)s for 0% - O_2 /away-hotspot and 10% - O_2 /on-hotspot are identical, implying that increase of O_2 concentration from 0% to 10% eliminates the hotspots inducing defects such as 0.4eV barrier height in the 0% - O_2 sample, while the defects accountable for the 0.9eV background (Bkg.) in the 0% - O_2 sample

is now considered in the 10% - O_2 sample only for the hotspots relative to the improved background. In this experiment the authors assumed that, the Fermi level is fixed in the middle of the MgO band gap(7.8eV) and at 5eV above the valence band of F/F+ defects. Therefore, the F/F+ defects determines an effective barrier height of 1eV which corresponds to the observed I(V) data for 0% - O_2 /away-hotspot and 10% - O_2 /on-hotspot (Figure 2.6b) and is consistent with a complete disappearance of F/F+ absorption at 5eV with rise in O_2 concentration (Figure 2.6a). This is one of the initial experiments which attempted to describe a defect mediated potential landscape across MgO tunnel barriers.

A summary of several experimental groups' reports, which measured the barrier heights for MgO spacer-based MTJs, is listed in Table 2.2. These reported barrier heights are much lower than the nominal value of 3.9eV.

MTJ	TMR (%)	Barrier Height [eV]	t_{MgO} (nm)	Ref.
Fe/MgO/Fe	130 (190 _{1K})	0.38/0.82	2.5	[62]
Fe/MgO/Fe	180 (247 _{20K})	0.39	2.3	[46]
FeCo/MgO/FeCo	120-200	1.1-1.7	2-3	[47]
FeCoB/MgO/FeCoB	100	0.62/0.5	2.5	[64]
Fe/MgO/FeCo	23 _{4.2K} /20 _{70K}	0.9	2.6	[65]

TABLE 2.2: Experimentally reported values of barrier height of MgO MTJs

In 2014, Schleicher et al. [64] performed photoluminescence (PL) experiments on CoFeB/MgO MTJs and precisely pointed out the specific oxygen defect type responsible for altering the magneto-transport in a solid-state device. The key highlight of this work spectroscopic signatures of thermally activated F/F+ and F/F+* defect states that account for a defect-assisted magneto-transport. They reported a dominant F/F+ and F+* contribution in the parallel magnetic state of the MTJ, Figure 2.7a. On studying the thermal evolution of barrier height for F/F+ and F+, they concluded that both ground and excited states of F-centers decrease the tunneling magneto-resistance see Figure 2.7b. An increase in large TMR upon annealing CoFeB/MgO/CoFeB MTJ was attributed to the interface's structural modifications. In this experiment the dominant 1.1eV barrier height was assigned to the ground state of F center $30 < T(K) < 80K$, the dominant 0.8eV barrier height within $80 < T(K) < 250$ to the excited state of F center and finally the 0.4eV barrier height

for $T(K) > 250$ to the M centers anti-bonding ground state. However, we will see that in the following ab initio theory/experiments [66], that the PL based spectroscopic analysis of transport measurements on CoFeB/MgO MTJs is partly incorrect.

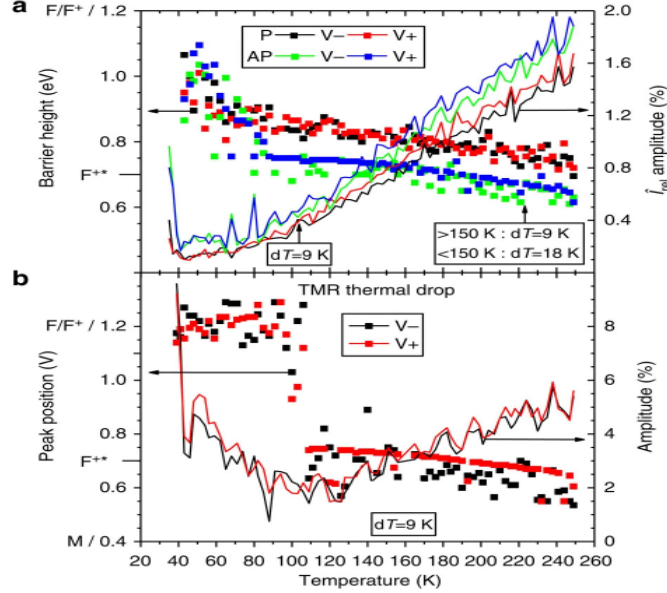


FIGURE 2.7: The plot displays the temperature dependence a) for the evolution of effective barrier height for the defect states and the maximum amplitude of \hat{I}_{rel} for parallel and anti-parallel magnetic states of the MTJ. b) the peak position and amplitude of TMR for $V > 0$ and $V < 0$. The \hat{I}_{rel} are associated with decrease in TMR at bias = 1.2V for $T > 30K$ in both P and AP state. Between $30K < T < 80K$ TMR amplitude decreases and stabilizes before increasing $> 100K$. Image reproduced from Ref [64].

Taudul et al. [65] performed theoretical calculations to study the complex band structure of MgO barrier with F and M centers using FeCo as ferromagnetic electrodes for the MTJ. They showed that the double oxygen M centers reduce the barrier height (0.4eV) and thus enhance the spintronic performance, which is in agreement with the experiment [64]. To study the thermal signature of the single (F) and double oxygen (M) vacancies, magneto-transport measurements were conducted on a CoFeB/MgO based MTJ. For this, the MgO was grown by sputtering Mg in a pure Ar partial pressure, subsequently oxidized in oxygen atmosphere, this type of growth ensures changes in the spintronic properties of the MTJ [67]. The samples were post annealed to a temperature (T_a). The effects of annealing the samples is shown in Figure 2.8. An increase in M centers' ratio to F centers was observed and a high TMR amplitude was recorded for low barrier heights.

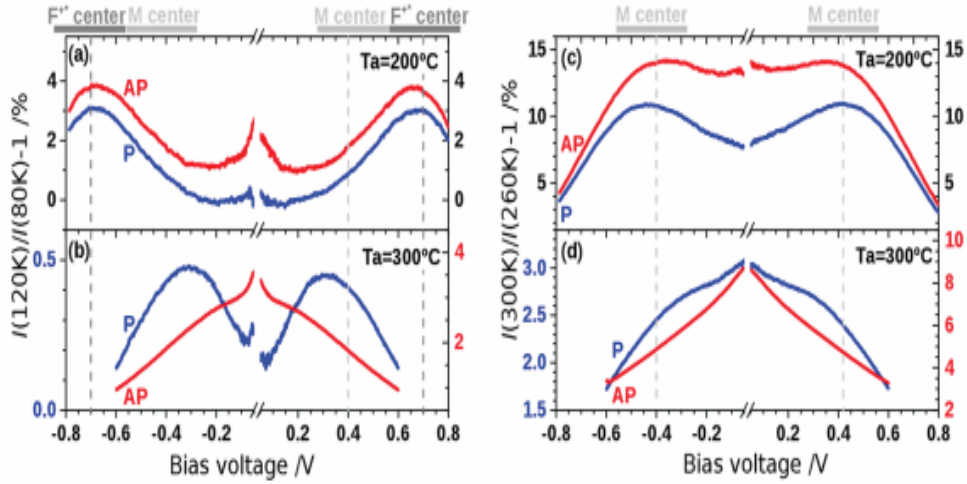


FIGURE 2.8: The graphs represents the effects of annealing over barrier heights and TMR for : (a), (b) $80K < T < 250K$ and (c), (d) for $T > 250K$ for MgO based MTJ in P and AP states. (a, c) : Annealing at $T_a = 200^\circ C$ gives expected T dependence for F and M centers driven barrier heights in P and AP states, as proposed by Schleicher et al. [64] (b, d): Annealing at $T_a = 300^\circ C$ shows reduced F to M center ratio and the F-center barrier vanishes, while the tunnel barrier for M-center is present only in P state. Thus the TMR indicated a symmetry-polarized transmission. Image taken from Ref [65].

In a combined experiment and ab initio theory by Schleicher et al. [66] a consolidated picture of the energy positions of the F and M centers, with respect to the Fermi level was obtained, which can be tuned by the appropriate choice of the electrodes. The report explores the evolution of experimental and theoretical evolution of defect barrier heights when the work function of the top ferromagnetic electrode is altered. For this FeCoB/MgO/FM MTJ with FM = FeCoB or FeB was adapted. They experimentally found that the effective barrier heights amplitude increased, when the FeCoB electrode was replaced with FeB as the top electrode. It is interesting to note that the energy shift can be equivalent to $0.4eV$ when the Co electrode is included instead of only Fe top FM electrode. The ab initio calculations ascribed this raise to enlarged energy separation between the localized states of F- and M-center and the Fermi level, E_F . Thus, all the localized states generated by single and double oxygen vacancies lie below the Fermi level. A consolidated visualization of the modification in the Fermi energy position based on the FM electrodes used in the MgO MTJ is represented in Figure 2.9. When Fe electrodes are used instead of FeCo, the energy position (E) of F-center shifts from $-0.9eV$ to $-1.15eV$ and for the M1/M2

defect states the shift is from (-1.42eV/-0.48eV) to (-1.63eV/-0.71eV). This theoretically confirmed the shift of MTJs Fermi level from the F and M centers ground states by 0.25eV. For a MTJ, with the MgO spacer sandwiched between Co electrodes the Fermi level moves closer by 0.15eV.

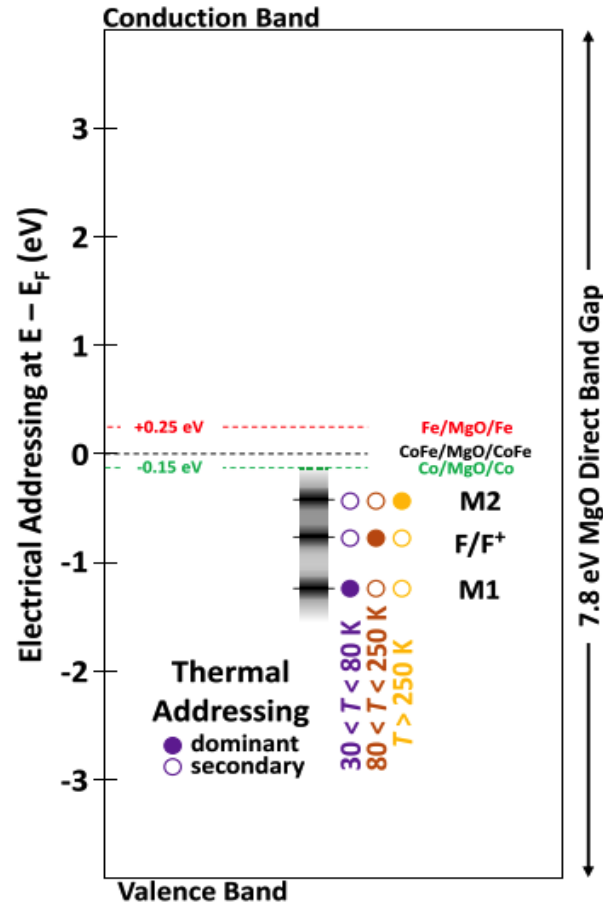


FIGURE 2.9: Illustration of an energy diagram that displays the energy positions of oxygen vacancies within a MgO optical band gap for different MTJ electrodes defined at Fermi energy level. The circles represent the temperature range at which the respective defect state experimentally dominates the potential tunneling magneto-transport landscape. The valance band is at -3.9eV. The shift in the energy for MgO MTJs based on FM = Fe, CoFe, Co is shown in red, black, green dotted lines, respectively. The dominant -0.71eV barrier height within $30 < T(K) < 80K$ is linked to M1 center (purple), the dominant -1.15eV height within $80 < T(K) < 250$ to the F centers' and the dominant 0.4eV barrier height for $T > 250K$ to the M center's anti-bonding ground state (M2). Image taken from Schleicher et al.(2019) [66].

Wang et al. [68] studied the structural, chemical properties and local defects in CoFeB-MgO based MTJs using high resolution TEM (HR-TEM), electron energy-loss spectroscopy (EELS) experimental techniques combined with density functional

theory (DFT) calculations. This work explored five types of boron defects and calculated the defect formation energies for four types of Fe and Co defects at the interface for both over oxidized and under oxidized CoFeB-MgO MTJs. The highlight of this work is that it proves that, due to annealing, the boron atoms from the CoFeB electrode diffuses into the adjacent Ta layer rather than into the MgO barrier of the MTJ structure. It is clearly demonstrated with the EELS mapping as shown in Figure 2.10a,b. Interestingly, EELS map shows no presence of Fe or Co in crystalline MgO layer. This helped to conclude that CoFe bonds directly with MgO via Fe(Co)-O bonds without diffusing Fe or Co into the MgO barrier. The TEM studies show that the Fe/Co atoms sit on top of oxygen atom rather than Mg atoms in a CoFeB-MgO based MTJ. Similar to the oxygen defect states that create extra energy states leading to new tunneling channels in MgO tunnel barrier and has a negative impact on the device performance. Over-oxidation of MgO barrier in CoFeB-MgO based MTJ can cause the B or Co/Fe to diffuse into the barrier and replace Mg, resulting in poor device performance. Therefore, this study provided crucial inputs into the fundamental understanding of the commercial CoFeB-MgO based magnetic tunnel junctions.

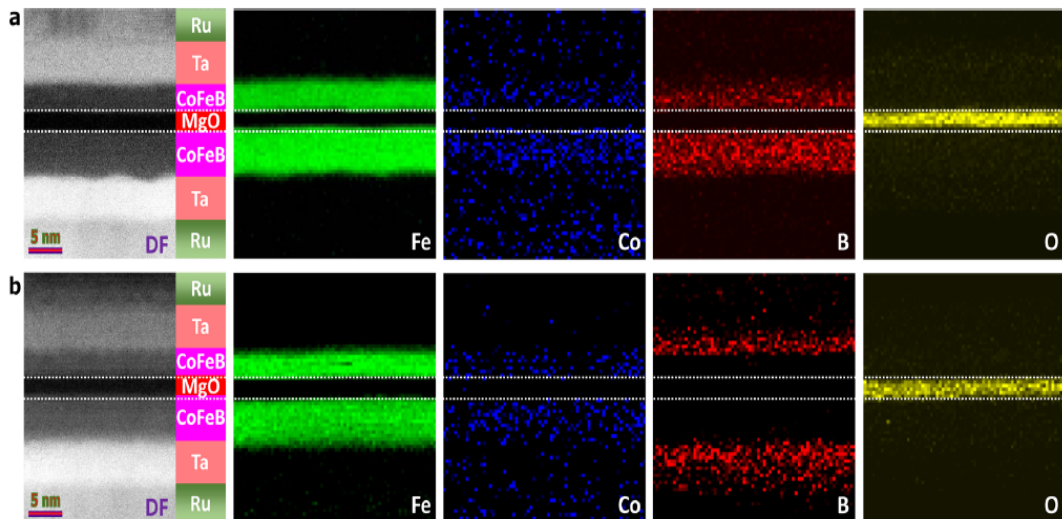


FIGURE 2.10: The figure describes a dark-field scanning TEM image and the corresponding EELS mapping of iron- $L_{2,3}$ edge, cobalt- $L_{2,3}$ edge, boron-K edge and oxygen-K edges of $Si/SiO_2/Ta(5)/Ru(10)/Ta(5)/Co_{20}Fe_{60}B_{20}(5)/MgO(2.1)/Co_{20}Fe_{60}B_{20}(3)/Ta(5)/Ru(5)$ magnetic tunnel junction for (a) as-deposited MTJ and (b) MTJ annealed at $500^\circ C$. The dotted guide lines represent the MgO tunnel barrier of the MTJ. Image reproduced from Ref [68].

All these studies reflect a strong correlation between the quality of the different layers, the nature of the interface, the role of defects, and the tunneling magnetoresistance of the MTJs. Hence, it is clear that a powerful local experimental probe is necessary to fully understand the spatial and chemical properties of defect species in MgO MTJs and therefore its impact on tunneling transport in the device.

2.7 "Device Operando" with X-rays

Studniarek et al. [5] reported two techniques to experimentally demonstrate the presence of defects (or hotspots) in MgO based spintronic device. In the first technique, they used a conducting tip atomic force microscopy (CT-AFM) to map the current fluctuations recorded during transport measurements Figure 2.11. One of the key results from this technique is to suggest a link between the TMR of the device with the transport via Fe-O interfacial bonds within the selected hotspot zones of the MTJ interface.

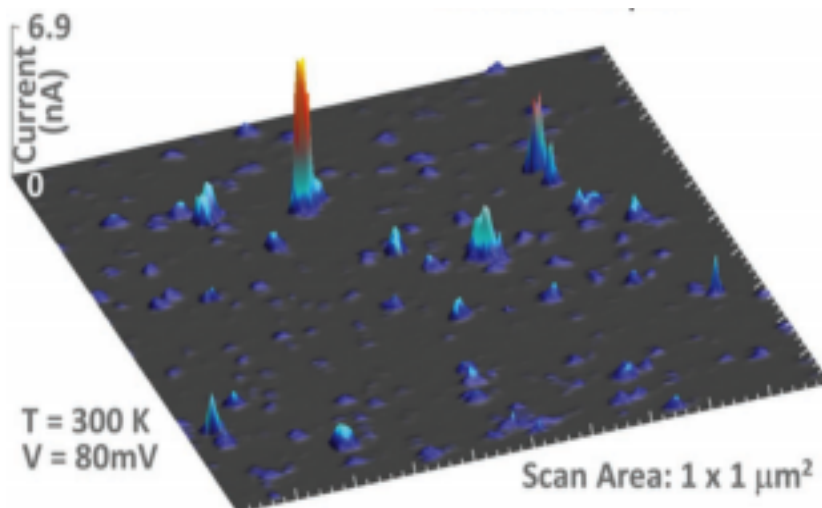


FIGURE 2.11: Schematic illustration of a current map for a MgO tunnel barrier exhibiting nano-scale regions with large current amplitudes or hotspots. Image adapted from Ref [5].

The second method is an indigenous technique, 'device-centric' operando. It utilized synchrotron brilliance x-ray photons, whose energy was tuned to match the oxygen atom's absorption on core electronic levels and simultaneously study the

change in the device response. They studied the direct impact on the MTJs magneto-transport when x-rays interact with Fe-O bonds parallel to the FeCoB/MgO interface. The studied samples included annealed, non-annealed MgO barrier, and SiO_2 encapsulated device, see Figure 2.12a. The XAS measurements at the pre-edge energy regime showed a decrease in the device's resistance at parallel (R_P) state when the Fe-O bonds' Δ_1^\downarrow absorption line was addressed (see Fig. 2.12b). There was no change in (R_P) at the K-edge energy absorption regime for oxygen atoms, but an increase in resistance at the anti-parallel state R_{AP} was observed, see Figure 2.12c. This accounted for a 0.5% TMR increase that evidenced the alteration to the device's operation induced by x-rays, is shown in Figure 2.12d.

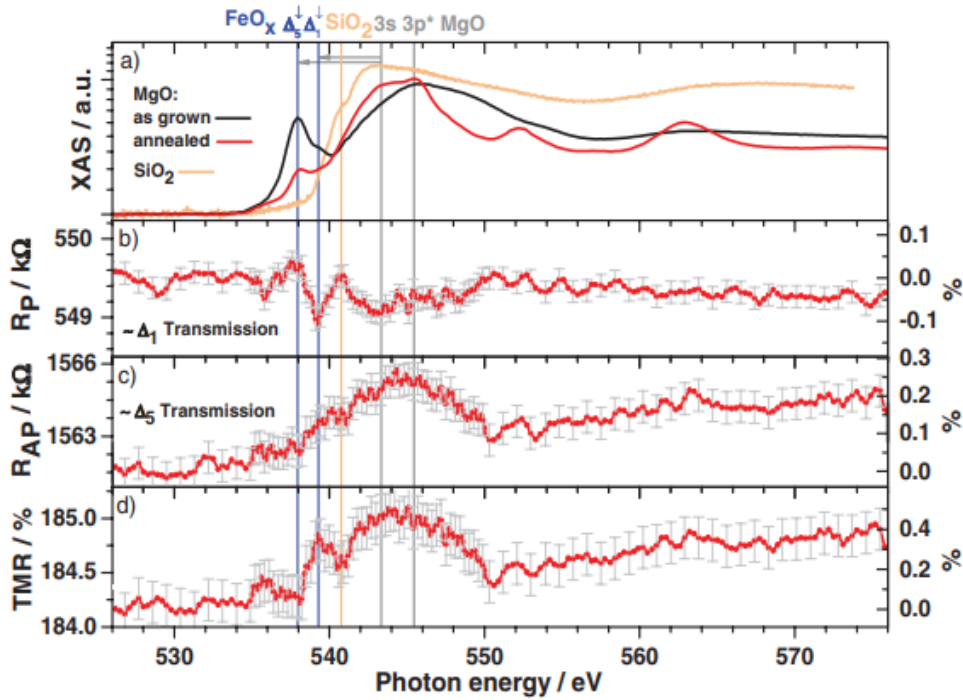


FIGURE 2.12: **a)** XAS reference for oxygen K-edge for two types of barrier growth annealed (red) and non-annealed (black) and SiO_2 encapsulated (salmon). Blue lines indicate the FeO and their energy positions (grey arrows) away from the 3s Mg XAS peak. The plots of photon energy dependence for the annealed MTJ at 10mV bias and $T = 20\text{K}$ in the **b)** parallel magnetization (R_P) state, **c)** anti-parallel (R_{AP}) state and **d)** TMR ratio. The scale on the right hand side gives the deviation from the pre-edge baseline. Δ_1 and Δ_5 are the electron symmetries. Image taken from Ref [5].

Results obtained using this 'device operando' technique distinctly link the high TMR spintronic performance of FeCoB/MgO/FeCoB MTJ to transport involving Fe-O interfacial bonds. This device operando approach provides insight into the

operation of a macro-scale MTJ on an atomic level, i.e. on the atoms that form the nanoscale conduction hotspot (see Figure 2.11). Therefore, this technique has promising advantages which can be used to exploit the device potential of materials involving complex oxides [5] and organic molecules [69].

Motivated by these results, the current thesis takes advantage of the device operando technique to study two nano-objects in two different type magnetic tunnel junctions:

1. **Oxygen vacancies:** the lateral dimensions of MgO based MTJs have shrunk to less than 20nm which is closer to the defects dimension, hence it is crucial to completely understand the role of oxygen vacancies within MgO in magnetotransport. So to expand our knowledge on the oxygen defect species, we studied an industrial class CoFeB/MgO based magnetic tunnel junction. The experiment made use of synchrotron grade x-ray beam of ~ 30 nm spatial resolution to map the nano-scale current hotspots created by the oxygen defects and attempted to drive a current in order to locally explore the MTJs spintronic performance. The measurements were performed in beamline HERMES of Synchrotron SOLEIL (Chap. 7).
2. **CoPc molecular spin chains:** the cobalt phthalocyanine molecules are structurally ordered and can form columnar chain like structure on deposition (details in Chapter 3). We attempted to locally probe the spintronic response and extract the information on the role of CoPc molecules in an organic MTJ. The experiment utilized the synchrotron's chemical, magnetic and spatial sensitivities to exploit the current-induced modifications to the magnetic properties of the CoPc molecular chains. The measurements were carried out in beamline DEIMOS of Synchrotron SOLEIL (Chap. 7).

2.8 Partial summary

From the discussion in the above sections one can conclude that the crystalline MgO tunnel barriers using the symmetry filtering mechanism along with prudently chosen electrodes can generate high tunneling magnetoresistance values. The high TMR amplitudes makes the MgO MTJs industrially attractive for information encoding. Moreover, the direct impact of oxygen defects species like the M-type (increase) and F- type (decrease) on the TMR of a MgO device can be locally investigated with the device operando technique using synchrotron x-rays.

Chapter 3

Nano transport path in molecular MTJs

Alongside oxide based MTJs, there is a strong interest in investigating new materials, such as organic semiconductors (OSC). These are a class of π -conjugated molecular systems which are mainly composed of light elements such as carbon and hydrogen, with few hetero-atoms such as sulfur, oxygen, and nitrogen included. Organic molecules furnish unique opportunities to exploit the electron's spin property, which opens up an attractive new direction of research in the field of spintronics, namely, molecular spintronics. The field was born in 1971 when B. Mann and H. Kuhn recorded a tunnel current across an insulating molecule to examine its electronic properties [70]. Historically, in 1974, A. Aviram and M. Ratner proposed utilizing a single organic molecule to make a rectifier [71]. The overall idea is that a single molecule can act as an efficient functional circuit component. The prospect of replacing an electrical component with a single molecule could serve as final miniaturization for devices.

Dediu et al. [72] reported the first experimental evidence of how incorporating an organic semiconductor (OSC) - sexithienyl (T6) into a spintronic device leads to spin injection and transport in the OSC. In this device, the T6 tunnel barrier was 100-500nm thick. The device exhibited strong MR amplitudes for barrier thickness up to 200nm, and above this thickness, MR vanished. Thus a spin diffusion length of 200nm was obtained for T6 molecules sandwiched between $La_{0.7}Sr_{0.3}MnO_3$ (LSMO)

electrodes. LSMO is a half-metallic colossal magneto-resistance material that is used to inject electrons with only one spin. A magneto-resistance of $\sim 30\%$ at room temperature was measured. This was associated with the spin injection from LSMO to T6. In 2004, Xiong et al. [73] reported a vertical organic spin valve using Co/tris-8-hydroxyquinoline aluminum(Alq_3)/LSMO heterostructure. They recorded an inverse magneto-resistance effect at 11K, meaning the device resistance decreased when the magnetization was switched from parallel to anti-parallel state. In the same year, Francis et al. [74] and later Mermer et al. [75] observed 10% of magneto-resistance, for $H < 100 \text{ mT}$, at room temperature, to a device consisting of organic material and non-magnetic elements electrodes. Up to 300%, TMR at low temperature was reported using very thin Alq_3 ($\sim 2 \text{ nm}$) molecular barrier [76]. The study was conducted using a nano-contact of the MTJ structure to probe the metal/molecule interface locally. This work laid the foundation to explore the interesting effects that occur at the metal/molecule interface.

3.1 Contrast between organic and inorganic materials used in MTJs

Organic molecules are nearly innumerable and can have a varied range of sizes. This creates unlimited opportunities to design organic semiconductors and is a massive advantage over inorganic semiconductors. Inorganic materials are structured by a continuum of energy states, and electrons are delocalized within the energy bands see Figure 3.1a. Organic materials are made up of discrete energy levels in (Fig. 3.1b). In organic semiconductors, the sp^2 hybrid configuration is applicable because the p_z electrons participate in a π -bond to increase the delocalization of electrons. These delocalized electrons give rise to molecular energy levels and the levels are filled with electrons up to a specific energy. This defines the highest occupied molecular orbital (HOMO) level and lowest unoccupied molecular orbital (LUMO) level straddling the material's bandgap. In this sense, the HOMO and LUMO energy levels are similar to the valence and the conduction band of inorganic solids.

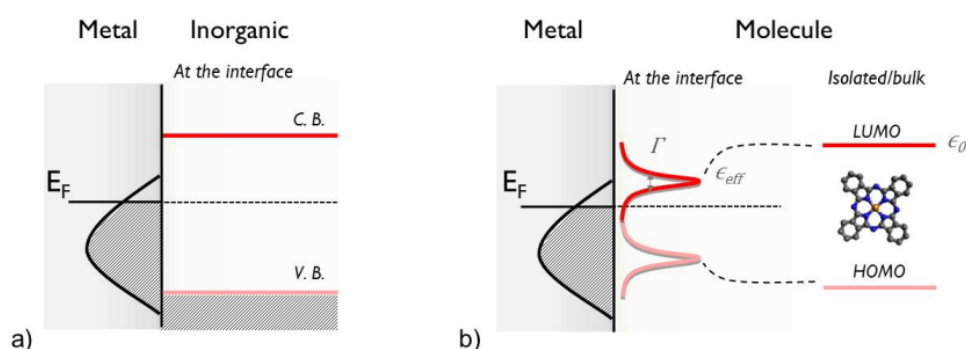


FIGURE 3.1: Schematics of (a) metal/inorganic interface where an inorganic interface has the regular conduction and valence band structure and (b) metal/molecule interface. Image taken from Ref [77].

When a π -conjugated molecular system is bound to a solid, their delocalized π -electrons overlap with each other. This results in conductivity [78, 79]. The inorganic semiconductors that form ionic, covalent or metallic bonds in the bulk and thin films, have an energy width from 1eV - 5eV. The organic molecular layers interact with each other due to the weak van der Waals interactions and has a wide energy width from 0.05eV - 5eV resulting in interesting properties. The molecular layer cohesion is due to the van der Waals interaction. These weak molecular interactions cause the electrons to have a free path that is nearly equivalent to the OSC's inter-molecular distance.

3.2 Salient features of organic semiconductors

The OSC has exhibited numerous unique advantages from a spintronics perspective. One of the primary reasons to focus on this path arises from the weak coupling between the electron's spin and orbital momentum. The spin-orbit coupling (SOC) scales with the atomic number (Z) as Z^4 and because the organic molecules are made up of light elements such as C, H, O, and N leads to weak interactions [80]. Another property of these materials that have invoked profound interest is the hyper-fine interaction (HFI). The low coupling strength between the electron spin and nuclear magnetic moments preserves the orientation of the electron spin for a very long time

[81, 82]. Therefore, the spin information can be preserved and transported over microscopic length scales ($10^2\text{nm} - 10^3\text{nm}$) [72, 83] which are much longer than conventional semiconductors.

In addition to these features, molecular spintronics include the possibility to explore molecular scale limit device dimensions; also have a comprehensive option to tune the chemical and physical properties of the molecules. Organic molecules can be deposited as molecular films by thermal evaporation, vapor phase deposition, or spin coating, and these types of films find application in LEDs. Polymer films use a variety of deposition techniques like inkjet coating or industrial roll-to-roll coating [84]. These economical processes adds to the advantage of using OSC and potentially fabricate competent devices that can replace inorganic metals and semiconductors.

As every coin has two sides, one of the disadvantages when using OSC is its low charge mobility. For example, rubrene, one of the highly conducting organic semiconductors, has a mobility value of only $100\text{cm}^2/\text{V} - \text{s}$ [85], whereas their inorganic counterparts have mobilities greater than several $100\text{cm}^2/\text{V} - \text{s}$. This results in resistance mismatch and integrability issues at inorganic/organic contact [86].

Irrespective of this, OSC are actively explored. Currently, nano-carbonaceous molecules such as graphene, carbon nanotube, and fullerene and organic molecules like phthalocyanine and porphyrin family of OSC are extensively employed in molecular devices [87]. Specially, metal phthalocyanine (MPc) molecules have attracted researchers, mainly for their planar structure, high thermal and chemical stability. Moreover, MPc molecules have a long spin relaxation time (milli-sec range) and spin coherence of $10\mu\text{sec}$ that makes them most suitable to include in a spintronic device. In this thesis work, cobalt phthalocyanine (CoPc) molecules were used as tunnel barriers in organic magnetic tunnel junctions.

3.3 Metal-Phthalocyanine

The metal phthalocyanine (MPc) is a macrocyclic planar aromatic molecule composed of four isoindole units connected via nitrogen atoms with a metal ion or two hydrogen atoms (H_2Pc) in the center Figure 3.2a. The phthalocyanine molecules have high chemical and thermal stability and low vapor pressure ($\approx 10^{-14} mbar$) that make these molecules attractive for applying in various heterostructures and working in ultra-high vacuum environments.

3.3.1 General properties of metal phthalocyanine molecules

The spatial geometry of MPc molecules is due to the van der Waals forces and $\pi - \pi$ interactions between them. Most of the metal phthalocyanines occur in polymorphic phases namely, α , β , γ and ϵ associated with their respective crystalline structure. The most common metastable forms are α - and β - phases. Both these phases form columns but the main difference between α - and β - phases is the stacking angle (ϕ) of the molecule within the columns and the arrangement of these columns in the crystalline structure. The stacking axis is defined by the direction of the molecular chains, the b-axis shown in Figure 3.2b. The stacking angle ϕ , between the b-axis and the normal to the molecule plane, along the intermolecular distance, gives rise to different polymorphs (Fig. 3.2b). The MPc molecules favor planar adsorption in the first monolayers and prefer to align themselves in either α - or β -phases in thicker films [87]. The phthalocyanine molecules maintain the same orientation in neighboring molecular columns for the crystal structure of α - polymorph [88]. This configuration is known as a brick-stack arrangement. The magnetic properties of metal phthalocyanines depend on the metal site's electronic ground states, determined by the nearest neighbor coordination and MPc polymorphism. This, in turn, depends sensitively on the molecular stacking geometry. All these factors play a crucial role in variation in the conductivity along the molecular chain. Therefore, using diverse substrates and deposition techniques unique heterogeneous polymorphic phase of metal phthalocyanines can be achieved.

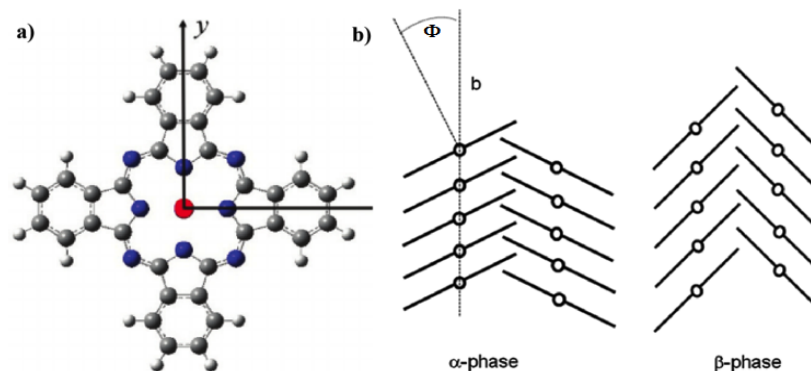


FIGURE 3.2: **Illustration of a metal-phthalocyanine molecule with four fold symmetry.** (a) MPc has a central metal atom (red) bonded to the nitrogen (navy) atoms (bonds not shown). (b) Schematics of the stacking of the herring-bone α and β -phases. ϕ , angle between the z axis of the molecule and the b axis of the structure. Note that α and β -phases exhibit clear difference in the stacking angle, ϕ .

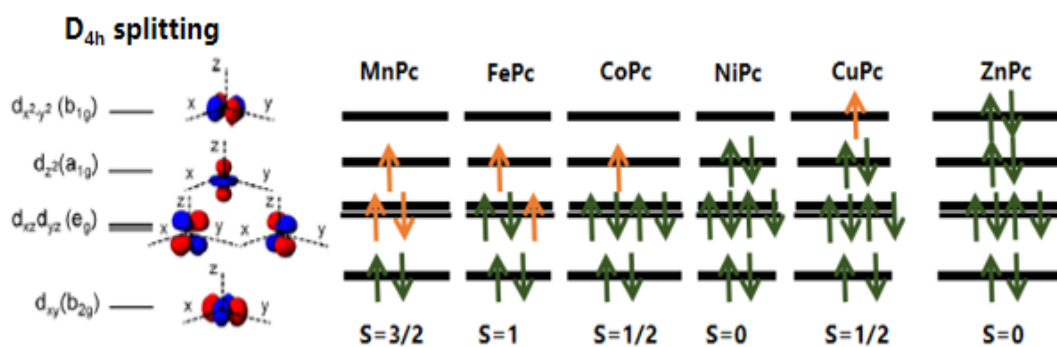


FIGURE 3.3: In the left is a schematic diagram of spatial electron probability density of metal-d orbital with respect to the phthalocyanine molecule axes. Colors blue and red represent the complex wave function phases. To the right is the electron occupation scheme for various metal phthalocyanines. The paired electrons are denoted in black and the brown denotes the unpaired electrons, below is S the total spin moment due to the unpaired electron for the respective MPc.

The MPc's central metal atom's electronic states are hybridized with the Pc molecular orbitals (MO) with dominant 3d electron character arising from the substituted metal. For example, the magnetic properties of the cobalt phthalocyanine (CoPc) molecules are due to an unpaired electron in the $3d_{z^2}$ orbital of the central cobalt atom, see Figure 3.3.

The selection rules govern the allowed transitions between the electronic energy states in quantum systems. Firstly, $\Delta S = 0$ is the spin conservation selection rule, according to which the allowed transitions should involve the promotion of electrons without a change in their respective spins. Second rule is known as the orbital or

Laporte selection rule $\Delta l = \pm 1$, meaning for centrosymmetric complexes the transitions s to s, p to p, or d to d are forbidden. Since every rule has an exception, the relaxation of these two rules can occur through :

1. Spin-orbit coupling - which gives rise to weak spin forbidden bands.
2. π -acceptor and π -donor ligands can mix with the d-orbitals therefore the transitions are no longer purely d-d.
3. Vibronic coupling - octahedral complexes may have allowed transitions where the molecule is asymmetric.

3.3.1.1 Cobalt phthalocyanine

Structurally, the CoPc molecule has a 4-fold rotational symmetry. The 3d configuration of the Co ($3d^7$) determines the CoPc molecular spin state as $S = 1/2$ and hence is a paramagnetic atom. CoPc has a complex multiplet structure, because the empty state is the higher d state (d_{z^2}) which is pointing out of molecular plane and is responsible for its magnetic state (Fig. 3.3). The a_{1g} singlet state of CoPc arising from the d_{z^2} orbital is weakly hybridized with the nitrogen s and $p_{x,y}$ states perpendicular to the molecular plane; the doublet e_g state molecular orbital results from the interaction between the Co(d_{xz}, d_{yz}) and the N- p_z states of the delocalized π -system [89].

The theoretical calculations and spectroscopy experiment suggests antiferromagnetic ordering of the CoPc molecular layers resulting from superexchange mechanism [6]. The superexchange path includes the e_g orbital of the CoPc molecule. According to this, when an electron from the Pc ring hops into the d_{z^2} orbital of the Co^{2+} metal ion, the leftover unpaired charge in the orbital is compensated by the d_{z^2} orbital of the neighboring Co^{2+} metal orbital. Thus magnetically linking the two adjacent Co^{2+} metal ions of the CoPc molecules.

The temperature dependent magnetometry studies on CoPc powders and thin films of CoPc showed strong antiferromagnetic exchange coupling interaction (J/k_B)

between 80K to 100K [7]. J/k_B is dependent on the Co-Co interaction and hence a stacking angle (ϕ) dependence can be explored, see Figure 3.4a,b.

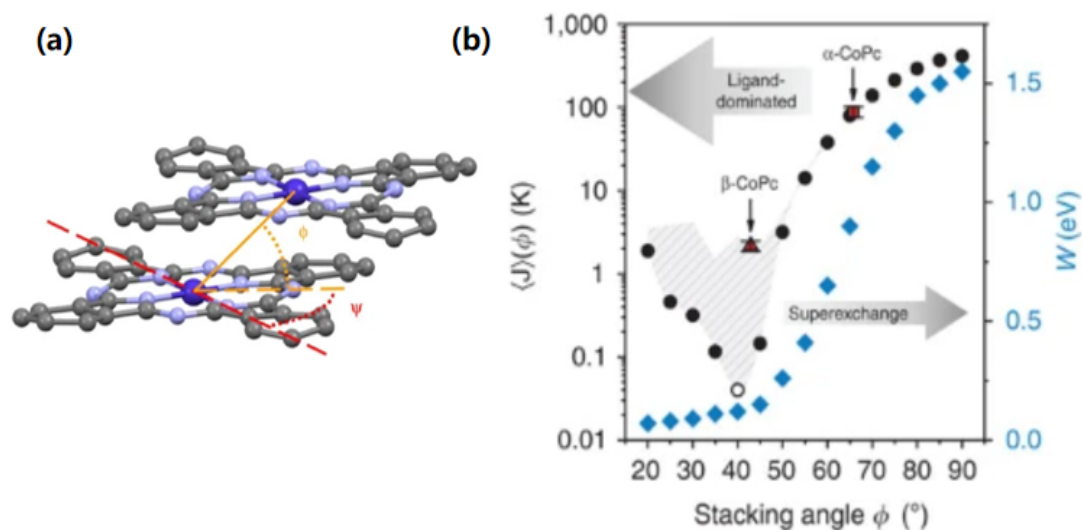


FIGURE 3.4: **Molecular stacking of CoPc molecules.** (a) with stacking angle ϕ and sliding angle ψ . The orange line corresponds to the Co-Co distance forming the stacking angle with the molecular plane. Its projection indicated by orange dashes and the Co-N axis, red dashed line is the sliding angle. (b) Stacking angle ϕ dependence on the theoretical band width (W) of the a_{1g} LUMO level of the Co atom of CoPc (blue) and the exchange energy $\langle J \rangle$ (black). The experimental values of J/k_B for the α -(100K) and β -(2K) polymorphs of CoPc are indicated along with the error bars. The maxima of $\langle J \rangle$ as a function of ϕ is at the top of the gray shaded region. For stacking angles greater than 50° , the height of this region is negligible and the superexchange mechanism is dominant for higher ϕ values, also observable in the bandwidth W . For $\phi < 50^\circ$ the ligand mediated exchange interactions are predominant. Image adapted from Ref [7].

The x-ray diffraction on CoPc thin films exhibited strong anti-ferromagnetic coupling between the molecular layers in α -phase and weak AFM coupling in β phase [7]. The experimental values of exchange energy, J , for α - and β -phase CoPc in thin films is found to be 100K and 2K respectively [7]. When $k_B T = J = 100K$, the CoPc molecules have strong AFM correlated fluctuations and above 100K the uncorrelated paramagnetic fluctuations dominate. Therefore, a magnetic phase transition is observed at 100K for CoPc molecules. Thanks to this phase transition the Co paramagnetic centers can be strongly coupled to each other in the molecular chain. For a perfect growth CoPc thin film, the even molecular spin chains have zero net spin moment ($S = 0$) and the odd spins have a non-zero spin moment of $S = 1/2$. Analogous to defects in inorganic crystals (Chap. 2, Sec. 2.6), imperfections within the spin chains like missing molecules, displacement of molecules can

weaken the exchange interactions producing broken-spin chain magnetic data [7]. To better understand the superexchange mechanism in individual molecules and complex molecular chains scanning tunneling spectroscopy (STS) techniques such as inelastic spin-flip spectroscopy and scanning tunneling microscope are widely used.

3.3.1.2 Spin flip spectroscopy and microscopy

The standard STM techniques used to study single atoms' electronic and magnetic properties is scanning tunneling spectroscopy (STS) and inelastic electron tunneling spectroscopy (IETS) [6, 90, 91, 92, 93]. The primary operation mode involves measuring the local sample density of electrons states (LDOS) by sweeping the electron energy. The electron energy is fixed by a bias voltage (V) between the sample and the tip.

The tunneling electrons transfer their energy to the spin degree of freedom of individual metal atoms or the atomic chains due to the spin-flip process [93, 94, 95]. When the tunneling electrons' energy is less than the spin excitation energy, the electron tunnels elastically, see Figure 3.5a. Suppose a tunneling electron's energy exceeds the spin excitation energy of atoms/molecules: electrons can tunnel further through the inelastic tunneling path by exchanging a spin, see Figure 3.5b. The additional tunneling channel induces steps in the differential conductance at a bias voltage that is proportional to the spin excitation energy or Zeeman splitting energy (ΔE). The inelastic excitations can cause a large increase in the current flowing across a set of coupled electron spins by inducing electronic transitions in a molecular spin chain system from its quantum ground state to an excited state. Due to the conservation of spin angular momentum and transition selection rules [96] (see Chap.3, Sec. 3.3.1), this spin-flip process causes minority spin states from the electrode to transport as majority states. The converse scenario is forbidden. The spin polarization of the spin excitation current is indirectly seen in scanning tunnelling spectroscopy experiments by comparing the amplitudes of the resulting conductance peaks upon reversing the bias voltage.

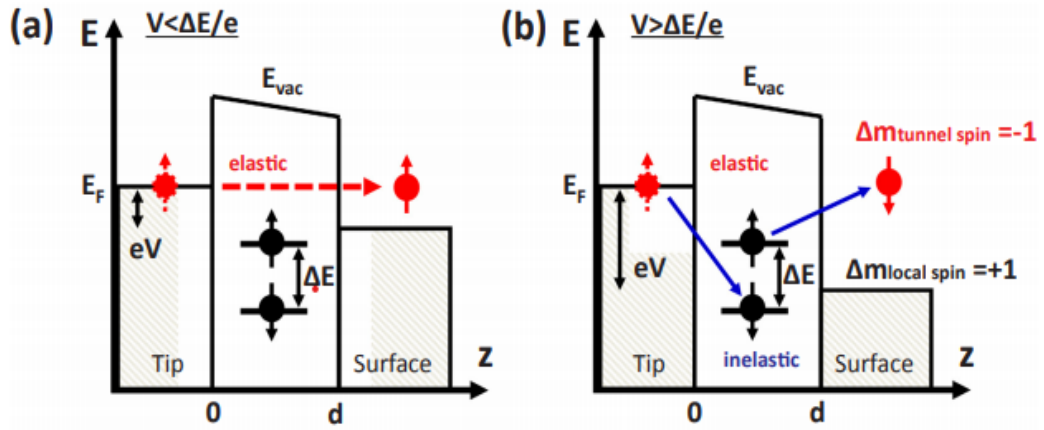


FIGURE 3.5: Schematic description of inelastic tunneling spectroscopy when the tunneling electrons energy **a)** is less than spin excitation energy (ΔE), electrons tunnel elastically; **b)** exceeds the spin excitation energy inelastic tunneling occurs by exchange of spin abiding to the spin selection rule. Figure adapted from Ref [97].

In 2008, Chen et al. [6] measured the collective spin excitations in individual molecular spin chains of cobalt phthalocyanine thin films by spin-flip IETS technique. In this work, they reported that the CoPc molecules formed one-dimensional anti-ferromagnetic (AFM) chains and lay flat on the surface of the film Figure 3.6 (a). The finite steps in differential conductance dI/dV plot are associated with inelastic tunneling indicated by arrows in Figure 3.6 (b and c). Interestingly, the single step in the differential conductance, dI/dV , split into three distinct steps under an external magnetic field application (see Fig. 3.6c). These features in the conductance curves suggest that the observed inelastic tunneling spectroscopy originates from the AFM coupling between the neighboring CoPc molecules in the molecular chain. The distinct steps correspond to the transitions from the singlet ground state to the excited triplet state due to the magnetic field's effect, which lifts the 3-fold degeneracy of the system. The unequal spacing of the spin split states reflects the magneto-crystalline anisotropy with a barrier height $> 1\text{meV}$. Intriguing information about the system is encoded in the line-shapes of the spectral features in the conductance curves.

Additionally, spin sensitive STM experiments using spin-polarized tips are used to detect individual spins from nano-structures. Such localized spin-polarized tunneling spectroscopy are crucial to understand the nature of bonding of the individual molecule with the ferromagnetic surface [6, 91, 92, 93].

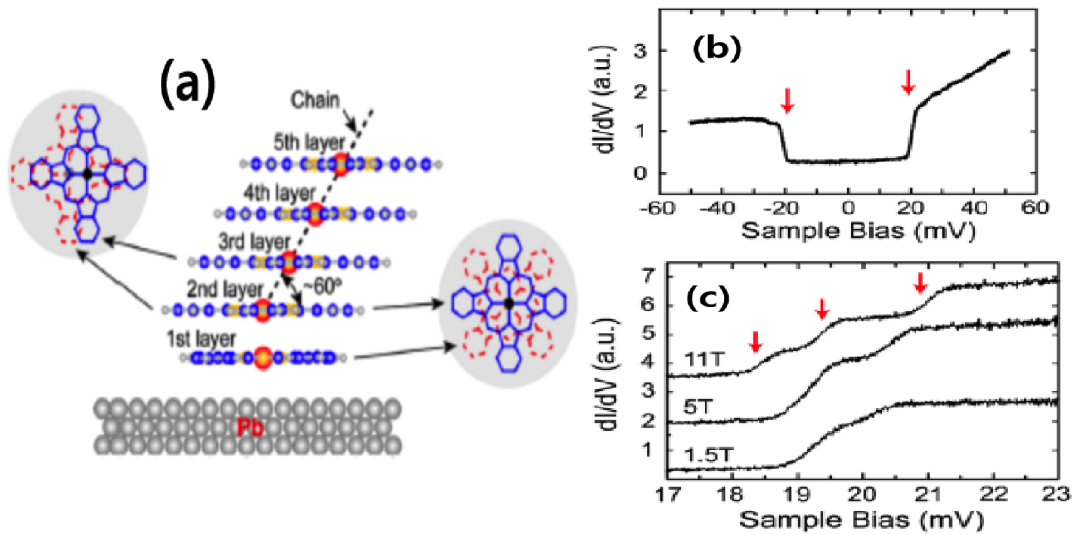


FIGURE 3.6: **Spin excitations** (a) of chain like stacks formed by CoPc molecules by spin tunneling spectroscopy measurements. Spin flip spectra of individual CoPc molecular chains for $T = 0.4\text{K}$ at : (b) $\mathbf{H} = 0\text{T}$ and (c) different magnetic fields for third molecular layer, the red arrows indicate the three steps induced by $\mathbf{H} = 11\text{T}$. Figures adapted from Ref [6].

To conclude, intricate knowledge of the structural and electronic properties of cobalt phthalocyanines using spin-flip spectroscopy has provided crucial information of the electron spin distribution and coupling between the spin chains. Hence, it is interesting to understand, how these structurally ordered molecules when incorporated as spacers in a spintronic device, can stimulate exotic phenomena at the metal-molecule interface.

3.4 Spin-dependent hybridization at FM/molecule interface

An isolated/ bulk or single-molecule has an infinite lifetime τ , with discrete energy levels ϵ_0 . But when it is brought to the vicinity of metal, the molecular orbitals undergo hybridization with the electronic energy levels of the ferromagnet leading to spin injection at the interface, see Figure 3.7a. Due to this FM/molecule hybridization, the molecular levels can experience the following phenomena:

1. In the proximity of metal, the lifetime of the molecular level becomes finite since the charge has a probability of escaping to the metal. As a result, there is energy broadening $\Gamma = \hbar/\tau$, (\hbar = reduced Planck constant) which is directly

proportional to the density of states (DOS) of the metal. Based on the strength of the interaction between the molecule and the metal, this broadening can range from a few meV up to eV [98].

2. Energy shift of the molecular level from ϵ_0 , the initial position of the isolated molecule to the final position ϵ_{eff} , see Figure 3.7a due to metal – molecule interaction. This shift is relative to the DOS of the metal and various other parameters, such as the combined effects of interfacial dipoles or image forces [99].

Barraud et al. [76] predicted the broadening of energy level and energy shift to be spin-dependent for a FM electrode. Therefore, the spin degenerated molecular levels become spin polarized (P) and spin-split. This results in two different broadening widths $\Gamma^\uparrow \neq \Gamma^\downarrow$ and two different energies $\epsilon_{eff}^{up} \neq \epsilon_{eff}^{down}$ for the spin up and down, which are dependent on the nature of coupling between the FM and the molecule (see Figure 3.7a).

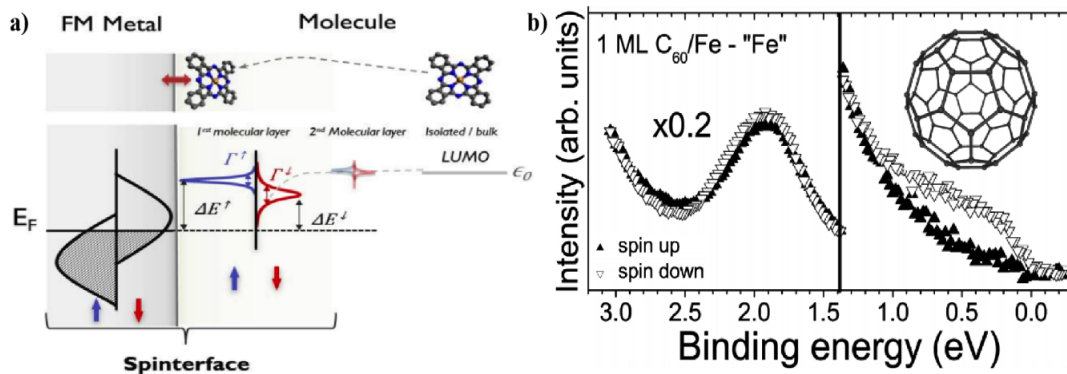


FIGURE 3.7: **Spin-dependent molecular hybridization.** (a) Theory inspired schematics of spin-dependent molecular hybridization at an interface with a FM metal. Top insert is an illustration of the molecule as it approaches the surface and eventually is coupled to the FM metal. The bottom is the DOS of the metal and molecular orbitals for the respective molecular positions. Due to difference in DOS for spin up and down electrons in FM metal, the broadening Γ and energy shift ΔE are spin dependent which induces a spin polarization on the first molecular layer and thus a new effective electrode namely spinterface. (b) Experimental observation of the theory using spin-resolved photoemission spectroscopy of 1ML $C_{60}/Fe(bcc)$ bi-layer at RT. Spin (\uparrow & \downarrow) states are given by shaded and open triangles respectively. Image a) taken from Ref [77] and image b) taken from Ref [100].

The coupling between the ferromagnet metal and first molecular layer of the organic molecule is called a “spinterface” [101, 102]. As a result of spin-dependent hybridization, two spinterface effects can be illustrated depending on the amplitude of broadening, Γ and energy shift, ΔE , from the metal Fermi level. When the $\Gamma \gg \Delta E$, it induces an inversion of spin polarization (ie., sign change of P) on the molecular orbital. This occurs for a strong coupling between the FM/molecule coupling at the interface. If the $\Gamma \ll \Delta E$, then an enhancement of spin polarization occurs. This corresponds to a weak interaction at the spinterface and amplitude of Γ is small enough to be ignored. Hence, a sharp FM/molecule interface can act as a spin filter that can boost the effective spin polarization to surpass the bulk spin polarization of the ferromagnetic materials [76].

Several experimental evidences for spin dependent hybridization have been reported for phthalocyanine molecules, C_{60} , and other molecules using spin-polarized scanning tunneling microscopy (SP-STM) [103, 104], spin-polarized photoemission spectroscopy (SP-PES) [105, 106], and magneto-resistance measurements in spintronic devices [107, 108, 109]. The Figure 3.7b is one of the experimental evidence for spin dependent hybridization at the interface of Fe/ C_{60} molecule. The spin-resolved photoemission spectroscopy of 1ML C_{60} /Fe(bcc) at room temperature reveal 89.1% spin polarization at Fermi energy. This highly spin polarized spinterface can serve as a potential candidate for spintronic selector (SS) for energy harvesting applications (Chap. 9).

Additionally, spin dependent hybridization alters the magnetic and electronic properties of the ferromagnetic surfaces. Often, any change in the electronic properties is linked to the magnetic moment of the material (Chap. 7, Sec. 7.2.2.4). The XMCD measurements Fe/ C_{60} showed a small change in the magnetic moment of bcc-iron after the deposition of C_{60} molecules [110]. The C_{60} molecules deposited on Co surface can switch the magnetic easy axis of cobalt layer from in-plane orientation to out-of-plane [111]. The most intriguing of the all is that deposited C_{60} molecules can induce permanent ferromagnetism in diamagnetic metals like copper [112].

3.5 Effects of hybridization at FM/AFM molecular interface

The ferromagnet/molecule hybridization gives rise to interesting phenomena at the interface, namely, interface polarization and exchange bias effect. This section provides an overview on how spin dependent hybridization can have an impact on spinterface properties.

3.5.1 Interface spin polarization

The spin-dependent hybridization allows the interfacial spin polarization and magnetism to be tuned, which helps control the spintronic response of the device. Experimental evidence for inverse spin polarization has been reported in metal - phthalocyanines deposited on a ferromagnetic surface. High spin polarization of nearly 80% was observed for MnPc deposited on cobalt surface [106]. The measurements were done at room temperature using the spin-resolved photoemission and inverse photoemission technique. The Pc molecule's external rings are antiferromagnetically coupled to the Co surface, whereas the Mn central atom is ferromagnetically coupled. This induced spin polarization is also observed for other MPc's and molecules such as phenanthroline, pentacontane and amorphous carbon [100]. XAS and XMCD synchrotron-based studies of the bcc Fe/C₆₀ interface revealed spin-dependent hybridization between the two layers resulting in strong polarization [110]. Djeghoul et al. [100] performed spin-resolved photoemission spectroscopy measurements at room temperature on various metal/molecule stacks and concluded that high spin polarization at spinterface is a generic phenomenon that it is independent of the molecule. An experiment with zinc methyl phenalenyl (ZMP) molecules deposited on cobalt surface Co(8)/ZMP(40)/Cu(12) - nm scale, evidenced for different spin polarization at each molecular layer [108]. It showed that the first ZMP molecular layer is strongly hybridized with Co and the second spin-polarized molecular layer operates as a 'spin filter'. This experiment emphasizes that magnetic hardening effect is purely interfacial and the adsorbed magnetic molecule can act as a magnetic bit that can be controlled independently. The LSMO/Alq₃(2nm)/Co MTJ was the first spintronic device to point out the spin dependent hybridization at the FM/molecule

interface. A spin polarization of $\sim 60\%$ was calculated for Alq_3/Co interface. A negative magnetoresistance was recorded for this MTJ. The change in MR sign was associated to the interfacial effects thus inverting the spin polarization [76]. Therefore, interface polarization has a vital role in the magneto-transport properties of the molecular magnetic tunnel junctions.

3.5.2 Exchange Bias

It is often referred to as unidirectional or exchange anisotropy, which describes magnetic coupling phenomena that occur due to the interface exchange coupling between ferromagnetic and anti-ferromagnetic (AFM) layers [113, 114]. The spin orientation of the AFM layers is unaffected by small applied magnetic fields; hence the exchange coupling shifts the hysteresis loop of FM in one field direction, leading to a unidirectional anisotropy [115]. This property of exchange bias plays a key role in spintronics, like in spin valves [116]. It is responsible for pinning the magnetization direction of one of the FM layer (reference layer) with its neighboring AFM layer. In contrast, the other layer (free layer) can rotate independently in the presence of an applied magnetic field \mathbf{H} .

Some of the essential pointers for the presence of exchange bias effect in a system are: a horizontal shift of the field cooled (FC) hysteresis loop along the magnetic field axis; an increase in coercivity in a FC hysteresis compared to a zero-field cooled (ZFC) hysteresis study; the training effect - a gradual decrease in the exchange bias field with the increase in the number of loop cycles in a magnetic hysteresis study; the presence of unidirectional anisotropies [115], an asymmetric reversal of hysteresis loop [117], and finally, the difference between MR vs. magnetic field curves in ZFC and FC studies [118, 119] are all signatures of the exchange bias effect in action. It is fascinating to realize that all these effects originate at the interface shared between the FM and AFM layers.

To establish an exchange bias effect, a field cooling (FC) procedure is done on the FM/AFM system. The FC steps proceed from a temperature T such that $T_N < T < T_C$ is the state 0 of Figure 3.8, where an external magnetic field (\mathbf{H}) is applied to

the system, and FM spins align along \mathbf{H} while AFM remains random. A hysteresis curve measured at this temperature will be symmetrical at the origin. The FM/AFM system is cooled down to a temperature below T_N of AFM while retaining the same field direction. This completes the field cooling procedure that enables us to observe the exchange bias effect.

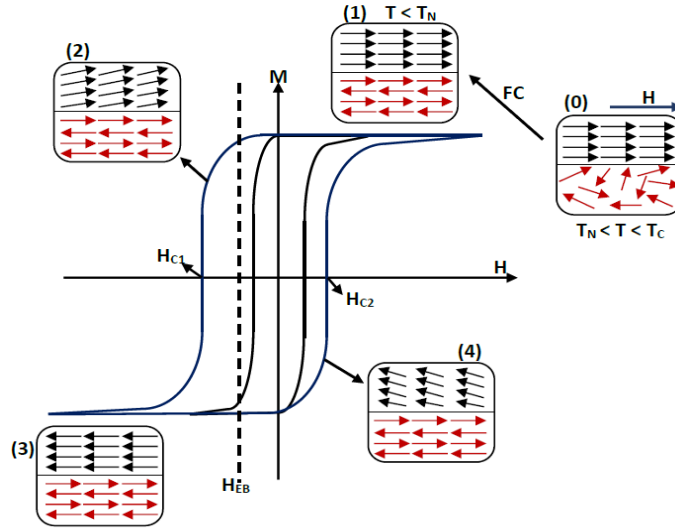


FIGURE 3.8: Graphical representation of the hysteresis loop along with the spin configurations of a coupled FM/AFM system at different stages of field cooling (magnetization vs magnetic field measurements). Black loop indicates the hysteresis loop of FM showing symmetrical magnetization loop before FC. Blue loop hysteresis loop after field cooling with different states corresponding to the spin orientations in the exchange biased FM/AFM system. H_{C1} and H_{C2} are the coercivities while H_{EB} represents the exchange bias field. Image taken from Ref [120].

After the field cooling, due to exchange interaction at the FM/AFM interface, the first monolayer (ML) of the AFM will align parallel (i.e., ferromagnetically; see Figure 3.8: state 1) or anti-parallel (antiferromagnetically) to the spins of the FM layer. Subsequently, the neighboring spins in the AFM layer follow the interfacial spin orientation, such that the net bulk magnetization of the AFM is zero. Now, if the applied magnetic field is swept from positive to negative, the FM spins will try to follow the field, but the AFM spins will remain rigid due to high anisotropy (state 2 of Fig. 3.8). However, more Zeeman energy would be required to rotate the FM spins, which would increase in the left coercive field. Eventually, when the negative applied field (H_{C1}) is greater than the exchange interaction, all the FM spins get reversed (state 3 Fig. 3.8) with a negative saturation leaving the AFM

spin configuration unaltered. On the return from negative to the positive field, the FM spins require less Zeeman energy, and the second reversal (\mathbf{H}_{C2}) occurs for a smaller positive field denoted by state 4 in Figure 3.8. The overall consequence is a shift of the FC-hysteresis loop along the magnetic field axis. The amount by which the center of the FC-hysteresis loop shifts from the \mathbf{H} axis origin is defined as the value of the exchange bias field EB. Mathematically, the exchange bias field EB and coercivity (H_C) are calculated from the coercive fields (\mathbf{H}_{C1}) and (\mathbf{H}_{C2}) obtained from the hysteresis loop as:

$$H_{EB} = \frac{\mathbf{H}_{C2} + \mathbf{H}_{C1}}{2} \quad (3.1)$$

$$H_C = \frac{\mathbf{H}_{C2} - \mathbf{H}_{C1}}{2} \quad (3.2)$$

In general, the temperature threshold where the exchange bias sets in are lower than the T_N of the anti-ferromagnetic layer. This temperature is known as the blocking temperature (T_B). This is one of the simple models to understand the various features of the exchange bias effect, but various other models have been put forward, often driven by an attempt to satisfy the experimental results qualitatively. In fact, there is no single model yet which could account for all the observed results of exchange bias effects for diverse systems. Nevertheless, these models [114, 121] are individually quite successfully and can explain various systems that serve as a cornerstone for future work.

The magneto-transport measurements on Co/CoPc/Co MTJs showed inverse tunneling magnetoresistance, (see figure 3.9a), meaning the two FM/molecule interfaces have different spin polarization sign [9]. The inverse polarization at the bottom spinterface is in agreement with the spin polarized STM experiment performed on single CoPc deposited on Co electrode [103, 122]. It was assumed that top and the bottom spinterfaces have different coupling strengths. This difference was attributed to the heterogeneous Co/CoPc contact geometry caused by the evolution of the stacking order of the molecular spin chains of CoPc films with thickness. The

thin films with CoPc molecular layers may exhibit a lower coercive field amplitude for higher bias values as observed in figure 3.9b. This can be explained using the electron spin pairing effect that alters the AFM ordering of the spin chains of CoPc during transport [9].

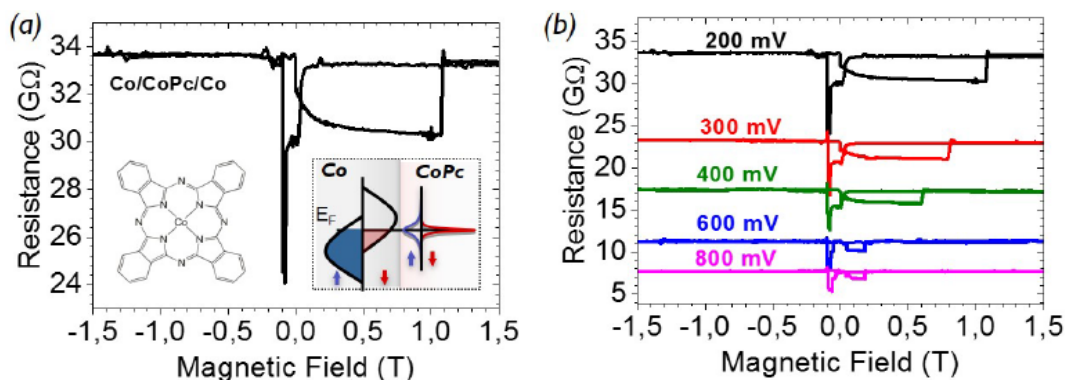


FIGURE 3.9: **Magnetoresistance curves for Co/CoPc/Co MTJ** recorded at 2K, 90° (a) at -200mV and (b) a range of positive bias values. The inverse TMR observed in the MTJ indicates that the spin polarizations at both top and bottom Co/CoPc interfaces have opposite sign. Image adapted from Ref [9].

Gruber. M et al. [123] experimentally showed that exchange bias can be achieved on cobalt layers by depositing manganese phthalocyanine (MnPc) molecules, which has an AFM ordering. The Co/MnPc spinterface exerts an exchange bias field on the FM layer, and it has a magnitude of 60mT at 14K, see Figure 3.10a. The Co/MnPc system has a blocking temperature (T_B) of 100K as plotted in Figure 3.10b. These studies were extended to other Pc family members such as CoPc, FePc, and ZnPc by depositing on Co film [124]. It was found that these molecules also exhibit the effects of exchange bias with blocking temperatures (T_B) \approx 100K. The experiment on CoPc and $H_2Pc/MnPc$ molecules spacers in MTJs also confirmed spin dependent tunneling effects. CoPc based MTJs recorded both spin-dependent tunneling magneto-resistance (TMR) and tunneling anisotropic magneto-resistance (TAMR). TAMR effects are due to anisotropy of the density of states as a function of the FM electrode magnetization direction. Both CoPc and $H_2Pc/MnPc$ based MTJs, showed unidirectional TAMR effect [8].

Besides these, molecular exchange bias has been observed in bi-layer studies of cobalt and metal-octaethylporphyrin (MOEP, M=Ni, Cu, Zn) planar molecules [125,

126]. The field cooled bi-layer sample showed a shift in the hysteresis loop, suggesting the presence of molecular exchange bias due to the Co/MOEP interface interactions [125]. The exchange bias was absent for the reference sample without the MOEP layers. Thus, the exchange bias originated from Co/MOEP interface and not from surface oxidation of the metal Co layer (Co/CoO). In addition to this, organic molecules such as π -conjugated molecules' like α -sexithiophene (or paraseixiphenyl) [127]; cobalt (II) and nickel (II) containing complexes like $[\text{Co}(\text{Pyipa})_2]$ and $[\text{Ni}(\text{Pyipa})_2]$ [128] when deposited on metal electrodes also exhibit exchange interaction. The XMCD measurements and DFT calculations showed that $[\text{Co}(\text{Pyipa})_2]$ molecules are FM coupled to epitaxial Fe_3O_4 surface and, $[\text{Ni}(\text{Pyipa})_2]$ molecules are either not coupled or couple AFM to Fe_3O_4 surface [128]. Therefore, it is clear that understanding and controlling the magnetic exchange interaction at the FM metal/molecule interface is crucial to achieving multi-functional spintronic devices.

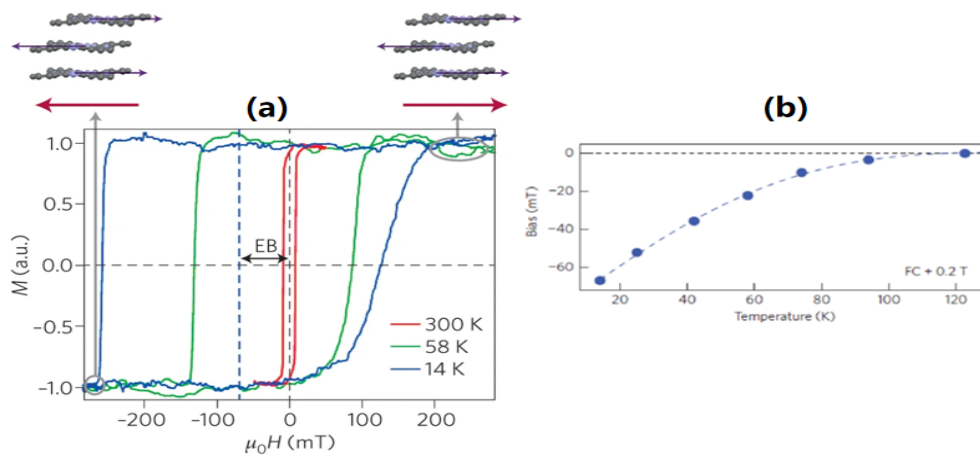


FIGURE 3.10: (a) Magneto-optic Kerr effect (MOKE) experiment measurement of the field dependent magnetization of Co(20ML)/MnPc(25ML) bi-layer capped with 20ML Au at RT (red), post FC at 14K (blue) and at 58K (green) for an in-plane $\mathbf{H} = +0.2T$. The red arrows represent the magnetization, M , of the cobalt substrate and the purple arrows indicate the MnPc molecular spin orientation. The dashed vertical blue line corresponds to the centre of the hysteresis curve at 14K, and the exchange bias (EB) is the shift of the magnetic field with respect to the zero shift hysteresis curve (indicated in black double arrow). The EB exists at 58K but disappears at 300K. (b) Temperature dependence curve of exchange bias obtained for a HFC of $+0.2T$ exhibiting a blocking temperature of about 100K.

Image adapted from Ref [123].

3.6 Partial summary

Organic semi-conductors have weak spin-orbital coupling (SOC) and hyperfine interaction (HFI) which makes them strong candidates for spacers in MTJs. The CoPc molecules are popular thanks to its anti-ferromagnetic exchange interaction (J/k_B) around 100K in thin films and powder form. Together with the metal/organic interface, this gives rise to several interesting magnetic phenomena such as exchange bias and interface polarization that directly impact the metal-organic hybrid system's properties. It is clear that spin-dependent hybridization plays a crucial role in molecular spintronic devices. The high spin-polarized metal/molecule interface constitutes a spintronic selector crucial to multifunctional MTJs as spintronic engines [17, 13, 18]. Hence, controlling the degree of spin hybridization and manipulating the spin dependent effect occurring at the spinterface will influence the efficiency of spin polarization and spin injection at the metal/molecule interface.

Chapter 4

Thermoelectric energy generators

Energy technologies can explore efficient, eco-friendly, and economic processes to transform input energy (e.g., heat) into a desirable form of energy (e.g., electricity). The phenomenon of thermoelectricity, where the heat and electric currents are coupled, has been around for nearly two centuries. The important mechanisms associated with thermoelectricity are the Seebeck and Peltier effects. In the Seebeck effect the heat is directly converted into electricity (eg., power generators, thermocouple). The Peltier effect is the inverse mechanism of the Seebeck effect and finds application in thermoelectric cooling devices (eg. refrigerators).

4.1 Classical thermal devices

Conventional thermal devices operate on classical effects such as Seebeck and Peltier effects. The device has a two-terminal geometry such that the two electrode reservoirs have a thermal difference which drives the heat flow. The heat flow is accompanied with a charge current. The classical thermal devices are based on energy-dependent transport which occurs due to the charge-hole asymmetry and are termed as particle exchange (PE) heat engines. In general, thermoelectric, thermionic devices are all PE heat engines (or meso-engines) [129]. The Seebeck and Peltier processes are explained using Boltzmann transport theory which considers only the particle nature of the electrons and energy states in continuum.

The concepts of thermoelectricity was revised by incorporating the electron spin

properties and a new branch of physics emerged - spin caloritronics (or thermal spintronics). It combines two distinct fields: spintronics (spin-dependent transport) and thermoelectricity (heat transport), to study the interaction between spin and heat currents in magnetic tunnel junction devices. Spin caloritronics is one area of research that has attracted immense research interests. It explores the various effects that occur in the bulk materials and at the interfaces between materials. Several spin-dependent spin caloritronic effects have been discovered for the classical Seebeck and Peltier effects in the bulk materials.

The Seebeck effect that is observed in bulk of the ferromagnets, due to spin split states in the electronic band structure of the ferromagnet (FM), is termed as spin-dependent Seebeck effect (SDSE). The spin splitting is responsible for the unequal spin up and spin down charge currents. Ideally, SDSE can be realized by creating a closed electrical circuit of any FM metal and applying a temperature gradient to the circuit [130]. In 2008, Uchida et al. [131] reported the discovery of spin Seebeck effect (SSE), a new kind of thermo-magnetic effect that differed from the original idea of thermal transport due to spin-dependent electron. The spin-Seebeck effect occurs at the interface between a highly spin-polarized FM and a normal metal (NM). It is a two-step process. In step one, a pure spin current is generated due to the temperature gradient applied across the spin-polarized FM, which drives the spin carriers out of equilibrium and produces a heat flux. The spin current is injected into the normal metal via the interface because of the spins non-equilibrium between the spin-polarized FM/NM interface. Thus, a spin or magnetization flux is recorded. Unlike SSE, the spin-dependent Seebeck effect can be realized in the absence of interface and does not require a thermal spin injection.

Experiments [131] and theoretical calculations [132] evidenced that spin injection using a spin Seebeck effect can generate massive spin current densities. The thermoelectric performance of a device is evaluated by the Seebeck coefficient (S) or

thermopower amplitude at room temperature. On searching for high Seebeck coefficient materials, anti-ferromagnets are fairly attractive due to their localized magnetic behavior at their critical temperatures (T_N). A recent report on temperature-dependent measurements of IrMn/CoFeB based MTJs show high thermopower values around the critical temperature of the IrMn layer ($T_C = 285\text{K}$), which varies with the thickness of AFM IrMn layer [12]. This strong temperature dependence of the S around was explained by invoking the coupling of transport with spin fluctuations, which are maximum near the anti-ferromagnets critical point. This work hints that the IrMn anti-ferromagnets phase transition is responsible for the enhanced thermopower.

Several other materials like metallic Cr [133] and iron pnictide superconductor - EuFe_2As_2 [134] also exhibited increased thermopower around their critical temperature, allowing them to generalize it for anti-ferromagnets [12]. The high Seebeck coefficient of $390\mu\text{V/K}$ at room temperature recorded for IrMn/CoFeB MTJ proves that FM/AFM interface plays a key role in the spin Seebeck effect [12]. These IrMn/CoFeB MTJs can harvest the waste heat for useful work for ultra low power devices. The replacement of charge based Seebeck devices with spin Seebeck devices is a stepping stone to investigate thermal effects in spintronics and solve the heating issues in modern solid state devices.

4.1.1 Classical vs quantum thermal devices

The length-scale of a classical thermal device is longer than the length-scale on which the electrons relax to a local thermal equilibrium, see Figure 4.1a. Therefore, all the electrons at every point in the device length-scale can assumed to be in local thermal equilibrium and the thermalization occurs within the device. The physics of such a system is described using Boltzmann transport theory. The energy selection is stimulated by bulk semiconductors band-structure. The charge carriers flow at energies in continuous bands and not in the band gaps.

On the contrary, nano-scale thermal devices have similar or smaller length-scales' than the length-scale whereon the electrons relax to a local thermal equilibrium, see

Figure 4.1b. Such systems differ from the classical system because there is no local thermalization and the quantum devices exhibit strong non-equilibrium distribution of electrons, which is explained using quantum transport theory by considering entropy and solving Schrodinger's equation. The nanostructures have quantized energy states due to their size compatibility with electrons' wavelength and hence, can be assumed as *artificial atoms*. The patterned semiconductor heterostructures, quantum dots and molecules like carbon nanotubes sandwiched between metal electrodes can act as nanostructures. The electrons conserve the quantum wavefunctions' phase while traversing the nanostructure. Therefore, nanostructured devices serve as a playground to explore the quantum physical phenomenon like quantum interference effects. Additionally, the electrons' long coherence time allows the entanglement between the electrons to survive for a long duration, so as to observe an impact on the device operation. An ambitious prospect for nanoscale thermal devices is to develop on-chip refrigeration and waste heat recovery systems for practical applications in nano-electronics.

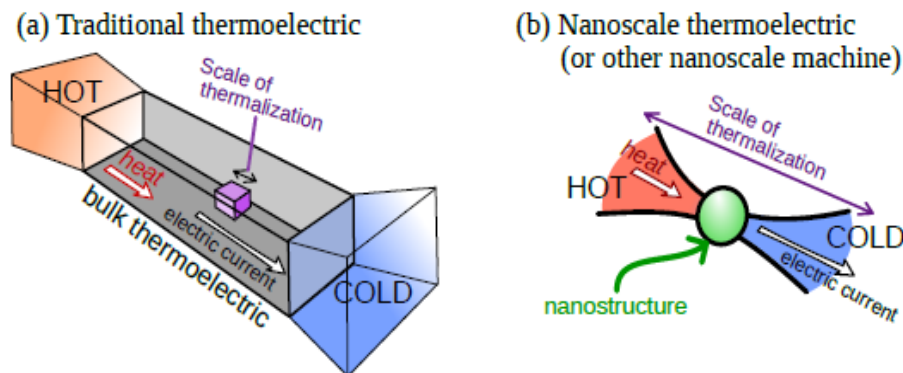


FIGURE 4.1: Illustrative drawing of: a) traditional thermoelectric device and b) nanoscale thermal device depicting the key difference in the scale of thermalization in both types of thermal devices. The Image is taken from Ref [135].

4.2 Quantum thermal devices

The thermodynamics in the quantum regime deals with the subtle relationship between the classical and non-equilibrium thermodynamics with quantum mechanics.

The quantum thermal devices operates by manipulating the heat currents of macroscopic thermal reservoirs in a microscopic scale.

4.2.1 Quantum heat engine

A thermal device that uses quantum materials as a working substance (WS) to generate power is known as a quantum heat engine (QHE) [136, 137]. The working substance in QHE can be a single atom [138] or multi-level [139] quantum system, spin systems [17, 13, 18] quantum dots [140, 141, 142, 143, 144] exhibiting exotic properties governed by the laws of quantum statistical mechanics. For instance, a quantum heat engine's efficiency is higher than that of a classical Carnot (or meso) engine [145]. The quantum heat engines generate work due to the thermal difference between the two electrode reservoirs (or baths) by utilizing quantum physics based phenomenon such as discrete energy levels [136, 137, 145, 146, 147], quantum coherence [145, 148], or quantum confinement [146]. Like classical thermal devices, the direction of heat flow defines a quantum heat engine or a quantum refrigerator. Both quantum heat engine and quantum refrigerators have the same design structure, but the latter extracts heat from cold reservoir and deposits on a hot reservoir by consuming energy [149]. Quantum heat engines are incredibly appealing because, unlike regular heat engines, their design does not include any moving components and performs noiseless operations. Interestingly, these QHEs can be realized by common solid-state materials. Especially, thermoelectric power generation using organic materials is a potential candidate for realizing low power devices that are cost-effective and eco-friendly.

4.2.1.1 Quantum Particle exchange heat engines

Similar to classical heat engines, the quantum version of the particle exchange heat engine operates based on energy filtering mechanism. The exchange of particles is allowed only when the energy levels of the particles' occupation state are the same in both hot and cold baths of the device. The temperature difference across the thermal baths can drive the electrons flow against the electrochemical potential gradient and

produce thermoelectric heat engines. In particle exchange heat engines, the general norm is that the efficiency at maximum power (EMP) is the upper bound for optimal operation conditions of quantum heat engines.

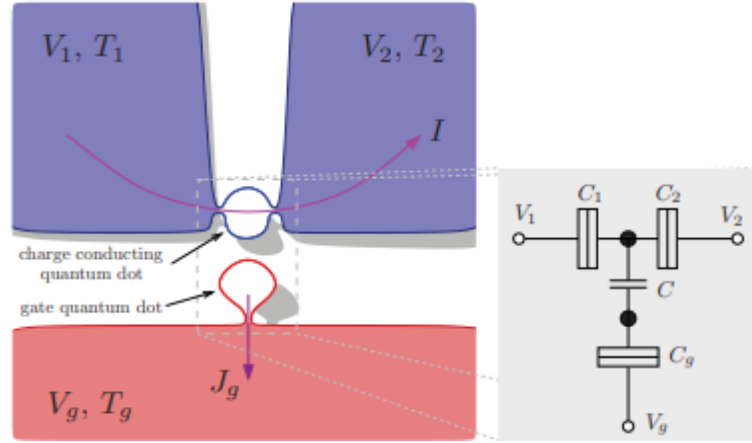


FIGURE 4.2: **Nano-sized structure of a energy to electric current converter** displaying two islands (dot) namely, conductor dot (blue) open to transport for two thermal baths at voltages V_1 and V_2 with temperature T_1 and T_2 respectively. The conductor dot is capacitively coupled to second dot which behaves as fluctuating gate (red) coupled to bath at voltage V_g and temperature T_g . Image taken from Ref [143].

In small-scale systems, it is common to observe fluctuations that are important compared to the average behavior. Guiding these fluctuations in a controlled way allows producing electric current by transforming environmental energy into directed motion. Sanchez and Buttiker [143] proposed a theoretical model to explain this mechanism to generate directed charge motion in a quantum dot system by electrostatic coupling to a fluctuating gate nano-sized structure different temperature, see Figure 4.2. One of the crucial aspects of this model is to decouple the direction of energy flow and the direction of charge/electron motion. This allows for multiple pairs of QDs to transfer heat in parallel, thereby increasing the total available power. Also, the exchanged energies are quantized and depend solely on the geometric capacitance of the quantum dots.

In the model, the quantum dot connected to one of the thermal baths (hot/cold) acts as a gate, and the dot connected to two leads of the bath is the conductor. The operation of this energy selective configuration proceeds as follows. There can be two possibilities when an electron tunnels into the quantum dot from lead L of a conductor. The electron can either be transmitted to lead R by absorbing energy from

the gate or the electron tunnels back to lead L without any energy exchange with the gate. The latter process does not contribute to charge or heat currents; hence the efficiency is unaltered. Thus each time energy E_C is absorbed, an electron will be transferred from one lead to another in the conductor. When the electron is transferred in the opposite direction, an equal energy E_C is returned to the gate. In that case, the probability of transferring a particle from left to right leads of a conductor by absorbing energy is directly proportional to the tunneling rates (Γ). Finally, the energy diagram of the energy converter shows the tunneling sequences that contribute to electron transport, see Figure 4.3. The arrows depicted in the Figure 4.3a,b indicate the allowed processes where the electron increases its energy when traversing the QD and thus contributes to an electric current; the processes in the opposite direction are exponentially suppressed as they reduce entropy. Therefore, this model gives a direct link between an increase in the asymmetries during transport and an increase in the system's efficiency.

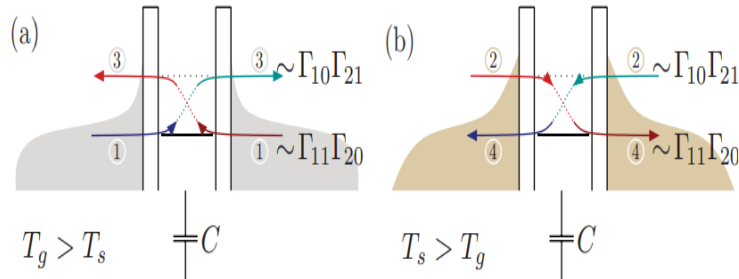


FIGURE 4.3: **Tunneling sequences of energy converter** that contribute to electron transport in an unbiased conductor. For temperature gradient: (a) $V_1 = V_2$ & $T_g > T_s$ and (b) reversed $T_s > T_g$ then the fluctuation generated current flows in the opposite direction. Colored regions indicate Fermi-Dirac distribution of each reservoir. Image reproduced from Ref [143].

Several other particle exchange engines include the following. Thierschmann et al. [140] utilized the energy filtering mechanism to experimentally achieve a three-terminal thermoelectric energy harvesting device using GaAs/AlGaAs two coupled quantum dots. Josefsson et al. [144] experimentally proved that PE engines can reach Carnot efficiency limits by using the concept of energy filtering using quantum dots. The QDs were formed by thin InP segments embedded onto InAs semiconductor nanowire, see Figure 4.4a. These quantum dots are tunnel coupled to both the reservoirs, as shown in Figure 4.4b. The experiment was performed at low temperatures

(< 1K), and an electric power output of $\approx 10^{-15}$ watt was reported. The power output combined with electronic heat flow determined the electronic efficiency η , which is more than 70% of the Carnot limit and is comparable to the conventional cyclical heat engines.

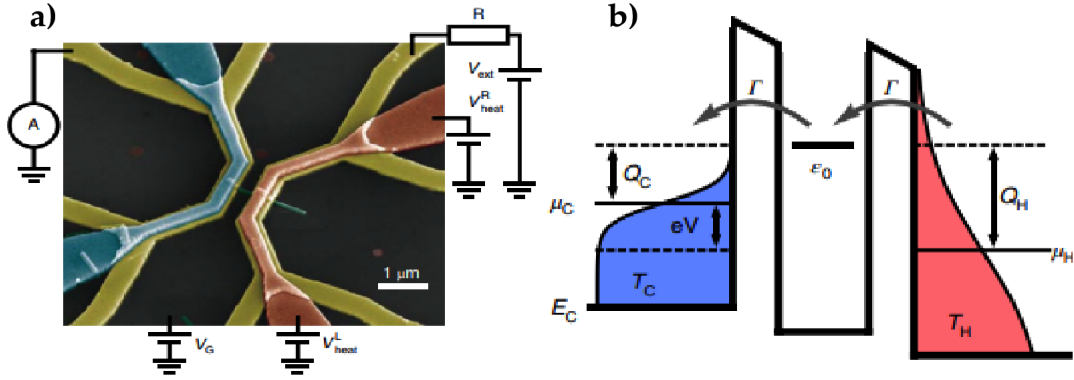


FIGURE 4.4: **Particle Exchange Heat Engine.** (a) Pseudo-colored SEM image of InAs/InP/InAs/InP/InAs heterostructured nanowire device studied in the experiment. Yellow colored are the metallic leads that contact the nanowire in green. Red and blue colored are heaters, the former is used for thermal biasing the latter is unused. (b) Quantum dot based PE heat engine corresponding to a resonance energy ϵ_0 . T_H (hot reservoir) is higher than T_C (cold reservoir) which is distinguished by different shapes for Fermi-Dirac distributions characterized by μ_H and μ_C and colored in red and blue respectively. The electron traversing the QD at energy ϵ_0 removes Q_H amount of heat from T_H and a part is converted into useful work eV and the remaining part is deposited as heat, Q_C on T_C . Image taken from Ref [144].

The majority of the demonstrated experiments on particle exchange engines are based on spatially confining a two-dimensional electron gas at III-V heterostructures using electrical gating techniques [140, 143]. Hence, the resulting quantum dots will always contain many electrons such that altering the electronic population by one electron amounts to $\sim 100\mu\text{eV}$ energies, which ultimately push these engines to operate at sub-Kelvin temperatures. Another drawback is breaking a careful balance of charge transport, which requires tuning the transmission properties on either side of the transport quantum dots, such as barrier height, thickness, energy level positions, transmission rates, and many others.

4.2.2 Spin Engines

A quantum heat engine that uses electron spin systems as the working substance is known as a quantum spin heat engine (QSHE). A notable difference in the reported quantum spin engines [17, 13, 18, 150, 151, 152, 153, 154], is that the operation of some engines [150, 151, 152, 153, 154] are explained using quantum thermodynamics (ΔT necessary) and the remaining quantum engines [17, 13, 18] are based on spintronics (ΔT not necessary).

4.2.2.1 Quantum Spin Heat Engines

Wang. W. et al. [151] experimentally realized the gedanken experiment, Maxwell's demon, by using the spins in diamond NV centers. This report experimentally confirmed that quantum entanglement could act as the source of negative entropy. J. Klatzow et al. [152] experimentally reported the observations of quantum coherent superposition effects in quantum spin heat engines. This was demonstrated by using microwaves to steer the operation of the quantum heat engine. The negatively charged nitrogen vacancies/defects (NV center) inside the diamond were used as the working substance. The ground state of the NV center consists of three spin states $|0\rangle$, $|+1\rangle$, $| - 1\rangle$, and thus can preserve the quantum coherence for an extended period at room temperature.

In an interesting report by Peterson et al. [150] the QSHE was realized using the nuclear spin 1/2 of a ^{13}C -labeled chloroform (CHCl_3) molecule diluted in acetone-D6 liquid. The study was carried out using a nuclear magnetic resonance (NMR) technique with radio frequencies (rf) to explicitly manipulate the nuclear spin of carbon-13 isotope and thus generate four-strokes of the Otto cycle at the quantum scale, see Figure 4.5a. It is important to note that this particular quantum thermodynamics based spin engine operates in the $\Delta < k_B T$ regime, where Δ ($=8.27\text{peV}$) is the separation of the quantum energy levels and $k_B T$ ($=15\text{peV}$) is the thermal energy scale [150]. The cycles of the proof-of-concept experiment is illustrated in Figure 4.5b. The nuclear spins of ^{13}C and ^1H are thermally prepared to act as hot and cold

baths. The high radio frequency modes near the Larmor frequency of hydrogen corresponds to the hot condition and the low rf modes near resonant frequency of carbon acts as cold condition. The four strokes of the Otto cycle is driven by the finite-time expansion and compression of the energy gap. An interferometry technique is utilized to measure the quantum energy fluctuations to explain the working of the spin engine.

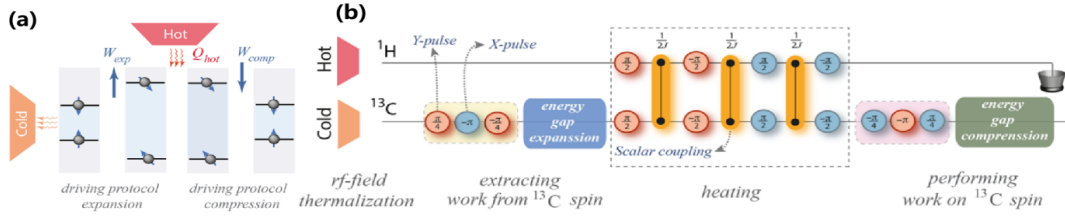


FIGURE 4.5: **Quantum Spin Engine.** (a) Schematics of a thermodynamic cycle employing spin 1/2 as WS [148]. (b) Experimental procedure to explain the operation of a spin engine using radio pulse sequences. The ^{13}C and 1H nuclei play the role of cold source (T_1) and hot source (T_1) thermal reservoirs respectively. The blue (red) circles correspond to the rotational angles x (y) produced by the transversal rf pulses. A unitary process for the energy gap expansion and compression procedure is driven by the time-modulated rf field resonant with the ^{13}C nuclear resonance frequency. Image reproduced from Ref [150].

In simple terms, the energy difference between the spin-up and spin-down nuclear states is increased and decreased using radio-frequency signals. This can be naively compared to the macroscopic engines' piston expansion and compression. The QSHE, while performing a quantum Otto cycle at maximum power, recorded an efficiency of $\eta \approx 42\%$ that is close to its thermodynamic limit of $\eta \approx 44\%$. Thus it proved that a quantum spin heat engine at maximum power approaches an efficiency near its thermodynamic limit. One of the key highlights of this work is the successful measurement and characterization of the quantum fluctuations and heat fluctuations in a thermodynamic cycle. They also introduced quantum friction to account for the reduction in the device's performance and associated this friction with a rise in entropy [150].

Altogether, these experiments successfully demonstrated some of the elusive quantum phenomena such as quantum entanglement [151], quantum superposition effects [152] using spin engines. Recent experiments employ mono-layer of doped

graphene [153], single-electron spin [154] as a working substance for QSHE, which prompts the diversity and flexibility of spin quantum heat engines. However, the architecture and realization of the quantum thermodynamic based spin engines are complex compared to the magnetic tunnel junctions' of the spintronic engines [17]. Therefore, this makes it challenging for these engines to compete with MgO based spintronic engines to penetrate industries.

4.2.3 Spintronic engines

Several experimental quantum engines are studied using the quantum spin systems [17, 13, 18, 155, 156, 157, 158], amongst these a striking difference is that some of the quantum spin based engines [17, 13, 18], are operating nominally at thermal equilibrium to produce net power output, without violating the second law of thermodynamics [159, 160, 161, 162, 163]. Also, unlike quantum engines [140, 144, 164], the operation regime of spintronic engine is $\Delta < k_B T$, where $k_B T$ is the thermal energy and Δ is the spin-splitting energy between the paramagnetic (PM) centers spin states.

In order to explain this conundrum we take help of advancement in spintronics research. Wherein, a current flowing between non-magnetic leads across a PM center can locally increase its temperature [165] by lifting its spin degeneracy and by modifying the exchange coupling between a pair of PM center [166, 167]. The current-induced entropy production on PM centers is possible at a magnetic phase transition even without a temperature difference between the leads [168]. Moreover, non-linear transport can promote local diversions from thermal equilibrium, one good example is the quantum magnetic fluctuations due to spin-shot noise [169, 170]. This hints for the different temperatures in the spintronic engine for the conduction electrons, for the FM magnetization and the FM's atomic lattice [171].

In an experiment by Hai et al. [13], it was shown that a magnetic tunnel junction (MTJ) made up of superparamagnetic MnAs nano-particles (Figure 4.6a) acts as the working substance that can generate a spin-based electro-motive force, namely, spin-motive force (SMF) [159], when subjected to an external applied magnetic field

H. The source of this SMF is the transformation of MnAs nano-magnets magnetic energy into electrical energy due to the quantum tunneling process. Since the huge voltage offset (Voffset) appears only in the presence of a magnetic field, it can be inferred that the external applied magnetic field is injecting energy into the system, see Figure 4.6b. The spin-based electro-motive force reported in this experiment can be an attractive option to replace the traditional chemical-based batteries with a *spin battery*.

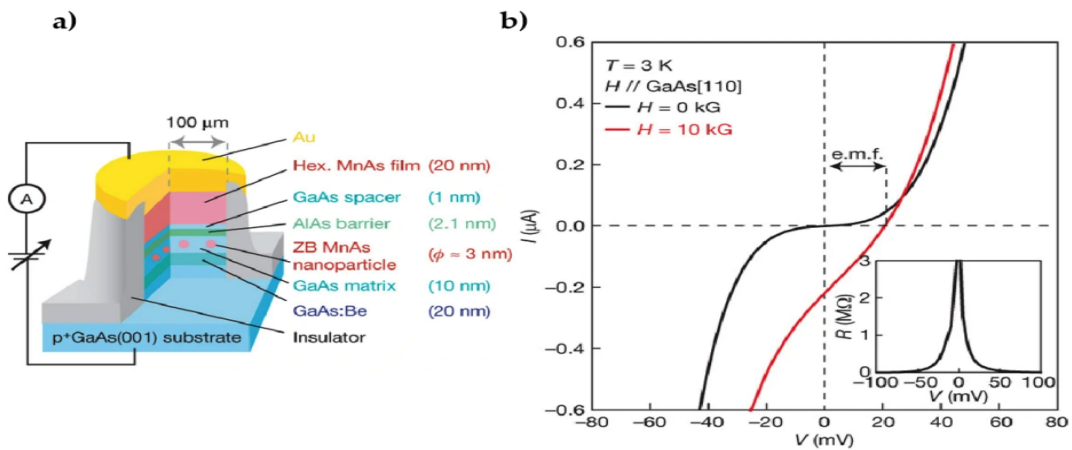


FIGURE 4.6: **Spin Battery**. (a) MTJ structure. (b) Current vs voltage plot measured at $T = 3\text{ K}$ without (black) and with (red) $\mathbf{H} = 1\text{ T}$ applied in-plane to GaAs[110]. In the presence of a magnetic field a positive current is induced for a negative voltage bias. Inset gives the MTJs resistance sweep for $V = \pm 100\text{ mV}$ at $\mathbf{H} = 0\text{ T}$ and 50 meV of Coulomb blockade was observed. Image taken from Ref [13].

Miao et al. [18] demonstrated a technique called spin filtering [160] to directly probe the energy levels on the spin channels of a $\text{EuS}/\text{Al}_2\text{O}_3/\text{Al}/\text{EuS}$ MTJ. In this MTJ heterostructure, the europium sulfide (EuS) layer acts as a spintronic selector (non-thermal bath) and the Al quantum dots are the working substance. The spin-based charge transfer across the device generates a spontaneous spin current and spontaneous bias voltage that can be of practical importance for controlling the spin flow in devices and thus harvest these spin excitations to do useful work. A spin filter, here EuS layer preferentially allows electrons of one spin-type to communicate across it. Thus the detector electrode is continuously probing the energy level of this spin-type. The reversal of the magnetization orientation of the EuS electrode bath layer allows probing the opposite spin type.

When measured as a function of the applied magnetic field \mathbf{H} , the spontaneously

generated bias voltage reveals two distinct voltage levels associated with the spin-up and spin-down channels, see Figure 4.7a. Intuitively, it is appealing to generate spontaneous spin current using this MTJ system. Therefore, the device is electrically connected to a pico-ammeter and a resistance box in series, as shown in the drawing insert of Figure 4.7b. The current output as a function of the applied magnetic field is recorded for parallel and anti-parallel spin orientations, see insert of Figure 4.7b. Interestingly, the device does not require any bias voltage to observe the spontaneous spin current effects. The measured difference in spontaneous current (ΔI) between P and AP magnetic states, as a function of load resistance for different thicknesses of Al layer, displays a maximum power of 27 fW at 1K for 0.6nm Al thickness. The device is highly resistive for the thinnest Al layers, and hence the power output drops to almost zero, see Figure 4.7b. This is because the tunneling electrons have a high probability of scattering within the Al insertion layer. Therefore, it is clear that spin filter electrode thickness plays a vital role in the spintronic engine's efficiency. These factors can help control the flow of spin current in solid-state devices and harvest spin fluctuations to do useful work.

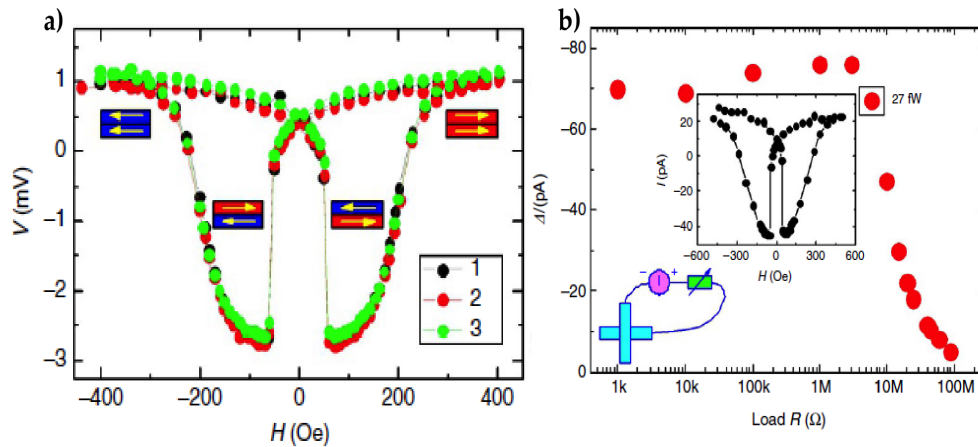


FIGURE 4.7: **Low T spintronic energy harvester.** (a) Experimental measurement of spin-dependent spontaneous bias voltage with respect to the applied magnetic field for parallel and anti-parallel magnetizations. The results are a comparison between three different MTJs plotted in black, red and green for 0.5nm thickness of Al insertion layer, at $T = 1K$. (b) Spin dependent spontaneous current measured in the presence of load resistance R , exhibits \sim femto watt output power. Inset shows the setup with all components in series and the graph is a current vs field (I vs H) curve at $T = 1K$, exhibits two well defined I states corresponding to spin-parallel and anti-parallel alignment on switching magnetic field and I changes sign for the applied field. Plots taken from Ref [18].

The spintronic engines investigated by Hai et al. [13], Miao et al. [18] operate at low temperatures ($T < 3K$) and harvest the thermal fluctuations on paramagnetic (PM) centers using spintronics. The experiment by Katcko et al. [17] generalizes this concept of generating work by harvesting thermal spin fluctuations on PM centers using spintronic selectors (SS) and thus places the two previous work within the context. In this experiment, the FM metal/molecule interface serves as a spintronic selector, and the C atoms in the MgO are the PM centers. The model of a simplified spintronic engine, Figure 4.8a, describes a single PM center which has spin-split energy levels, and the thermal spin state mixing on the PM center allows the current to flow from one spinterface [101, 102] to the other, even against the built-in ΔV in the MTJ's anti-parallel magnetic state. Here, unlike most quantum engine operations, the energy splitting between the PM center's spin levels is lower than the thermal energy $k_B T$ i.e., $\Delta < k_B T$, see Figure 4.8a.

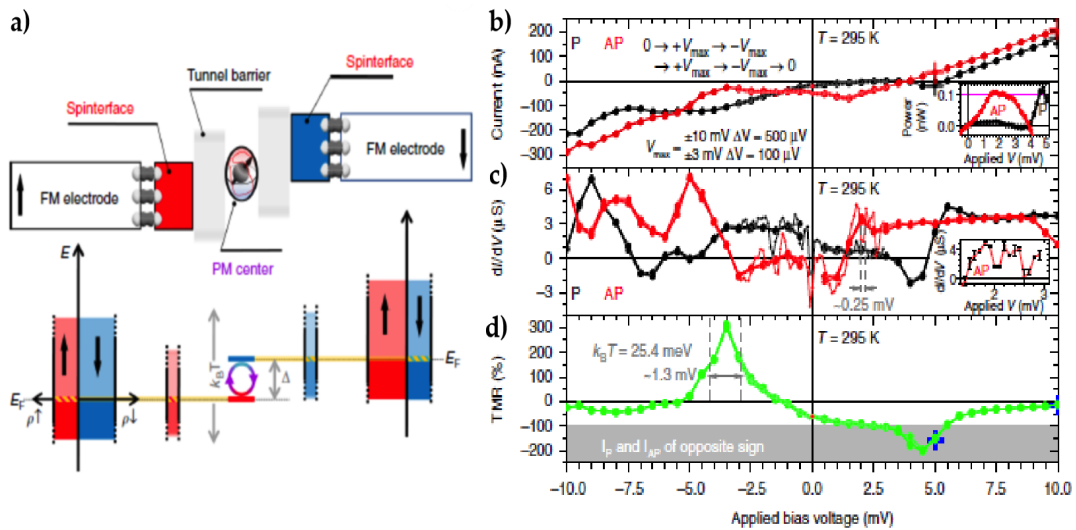


FIGURE 4.8: **MgO based room temperature spintronic engine.** (a) Schematic representation of a spintronic landscape across a MTJ. In all the panels the red (blue) correspond to spin up (down). The spintronic engine generates work by harvesting thermal spin fluctuations ($k_B T$) on the PM center. (b) $I(V)$ plot at $T = 295\text{ K}$ for parallel (black) and anti-parallel (red) magnetic states. The inset is the power output at P and AP states at 295K is 0.1 nWatt. (c) Sub- $k_B T$ spectral resolution of conductance curve for P and AP states of MTJ. (d) Tunneling magneto-resistance (TMR) $\sim 300\%$ at 295K. Images reproduced from Ref [17].

One of the exciting results from this experimental work is the power output of 0.1nWatt recorded at room temperature Figure 4.8b. This MgO based spintronic engine is an industrial-grade microelectronic device, and this experiment proves that

spintronics is a way for quantum engines to enjoy practical applications. This report [17] was based on one device. The low success rate was attributed to the difficulty in positioning the C atoms onto the oxygen vacancies in the MgO sub-lattice, which serve as PM centers of the spintronic engine. Therefore it became crucial to integrate the paramagnetic centers and spin selectors to achieve high power output at room temperature. Although single spin experiments using scanning tunneling microscope [93, 152, 153] allows controlling the discrete PM centers, it has been only emerging for solid-state devices [6, 161, 162]. In this thesis we overcome this bottleneck by using Co PM centers of cobalt phthalocyanine molecules and propose a molecular nano engine Chapter 9.

4.2.4 Partial summary

Nearly half a century ago, Scovil and Schulz-DuBois [136] had proposed the idea of quantum scale thermal devices like quantum heat engines using three-level masers with distinct energy levels. It was only recently the thermodynamic cycles were realized at a laboratory setup testing out various working media. One of the growing interest is to explore exotic quantum properties like the quantum coherence superposition effect [152], quantum entanglement [151] etc. As quantum systems have the property of superposition of states, it was interesting to verify if coherence amongst the energy states can increase the efficiency of the quantum heat engine.

The basic idea of a quantum heat engines is to exploit the energy fluctuations present in the system in a controlled manner to produce useful work. The efficiency of these quantum engines can exceed Carnot efficiency [152]. The quantum spin engines can be classified broadly as thermodynamic engines : $\Delta > k_B T$ and spintronic engines : $\Delta < k_B T$, where $k_B T$ is the thermal energy and Δ is the splitting of the quantum energy levels. Another key difference is spintronic engines [17, 13, 18] operate with non-thermal baths i.e., without any T gradient by harvesting thermal fluctuations on spin-split paramagnetic centers. As evidenced in the work by Miao et al.[18] it is not necessary to have an initial current flow across the device for the generation of output power. So, one can have a thermodynamical imbalance because

of thermodynamical induction [172, 173], which is quite feasible in a hopping transport regime. Here, at a stable temperature, fast spin dynamics on the paramagnetic center can produce slow changes to the charge current and the FM electrode magnetization. Moreover, these spintronic engines' [13, 18, 17] operation contrasts with the classical physics of spin caloritronics that deals with the heat gradients promoting spin-based thermoelectric phenomena.

Spintronic engines' find applications as spin batteries [13], spintronic energy harvesters [17, 18], low power magnetic sensors etc. Overall, in comparison to charge transport based quantum engines [140, 144, 164], the spintronic engines [17, 13, 18] have elegant approach to break the detailed transport balance on a designed ensemble of spins and is industrially attractive than known quantum engines [150, 151, 152]

Note to the reader, the idea of quantum resources and ergotropy emerged at a latter stage of this thesis (Dec. 2020), hence these concepts will be directly discussed in the results Chapter 9.

4.3 Conclusion

Over the years, research in spintronics has matured by efficiently employing the electron's spin property to control the flow of charges in solid-state devices. The pioneering discovery of giant magneto-resistance revolutionized the storage industry when IBM, in 1977, used spin-valve sensors in commercial hard disk drive read heads. The Deskstar 16GP Titan hard disk provided a storage capacity of 16.8GB. In recent times the read heads based on the effect of giant tunneling magneto-resistance are in usage, details in Chapter 1. Further optimization of the tunneling magneto-resistance and perpendicular magnetic anisotropy led to a better understanding of various phenomena scaled down to quantum level and helped realize nonvolatile magnetic random access memories (MRAM) that currently have been the hot topic for research and industry.

The magnetic tunnel junctions based on FeCoB/MgO have already found their entry in industries due to the high spin polarization of tunneling current by symmetry filtering at room temperature. However, theoretically expected high MR values for MgO based MTJs are not yet achieved. One of the main reasons is the oxygen defect species within the MgO barrier. Therefore, a complete understanding of their direct impact on the magneto-resistance of a tunneling spintronic device is crucial to gain control over the oxygen defect species, details in Chapter 2.

Alongside MgO MTJs, there is a strong interest in investigating new materials, such as organic semiconductors with tunable magnetic properties - molecular ferromagnets [163] and the integration of organic molecules in bio-inspired computing [174]. The metal/molecule interface envelops rich physics and is dubbed as a spinterface [101, 102]. This interfacial hybridization enormously impacts the spin injection [175, 176], enhances the magnetic ordering due to exchange interactions, and induces interface polarization that can act as a spintronic selector, details in Chap. 3. Therefore, controlling the extent of hybridization and engineering, the spin-dependent effects occurring at the metal/molecule interface may produce a multi-functional molecular spintronic device for information encoding and energy harvesting, proofs in Chap. 8 and Chap. 9.

The field of spin caloritronics has brought together spintronics (spin-dependent transport) and thermoelectricity (heat transport) to study the interaction between spin and heat currents in MTJ devices. Several theoretical reports [177, 178, 179] elucidate a quantum spin-based engine that combines the spintronic selectors (SS) with the discrete spin states of the paramagnetic centers (PM). These models apply thermodynamics' second law to generate work due to the temperature difference between the device components. Such heat engines' are experimentally realized using quantum dots to generate discrete electronic states, and heterostructure design creates the imbalance needed to operate the engine [140, 144, 96]. An elegant way to realize transport asymmetries is to use spintronics [17, 13, 18, 164] which does not require complex device design or exotic experimental setup to realize the operation of the quantum engine. Additionally, spintronics enjoys industrial superiority hence, amalgamation of spintronics and thermodynamics can pave way for multifunctional engines, see Chapter 4.

With numerous interesting phenomena being explored using MgO (Chap. 2) and CoPc (Chap. 3) based spintronic devices it is crucial to explore the spintronic nano transport path exhibited by two nano-objects, oxygen vacancies in MgO and the Co paramagnetic centers, with a focus on developing operando techniques based on synchrotron radiation. A novel technique called device-centric operando approach reveals the material properties within the device parameters (see Chap. 7, Sec. 7.4.2). It emphasizes material characters of only those atoms that drive device's operation and hence exclusive information on the nano transport path can be obtained.

Altogether, the developments in the field of spintronics guarantees for better prospects to perform frontier research. Over the years the field has discovered interesting phenomena, some of which have already been adopted in the industries for applications. Spintronics has proven to be the future for the next-generation nano-electronic devices with their capability to decrease power consumption and to increase their storage and processing ability.

State of the Art

The Chapter 5, of the thesis describes the experimental techniques used to fabricate and study thin films. It provides highlights on some of the ultra high vacuum (UHV) deposition technologies for fabricating thin and ultra-thin films. In this thesis's framework, two types of thin films are studied, namely, metal/organic-based stacks and MgO-based stacks. The CoPc stacks were fabricated in the Institut de Chimie et de Physique des Matériaux de Strasbourg (IPCMS) using the home-built hybrid deposition chamber. The MgO stacks were fabricated in Institut Jean Lamour of Nancy (IJL), thanks to the close collaborations between my home institute, IPCMS, and IJL. Our collaborators are specialists in the growth of thin-film heterostructures using sputtering. Conventional methods like x-ray reflectometry, x-ray diffraction etc were used to characterize the stacks.

The Chapter 6, emphasizes the key difference in processing steps of MgO and molecular stacks. A standard UV lithography technique was employed to process the MgO stacks into 20 micron-sized magnetic tunnel junctions. A novel technique using a solvent-free, chemical-free nano-silica lithography (see Appendix A) developed in the group was used to process the metal/molecule junctions. The technological steps from stacks to on-chip devices is discussed in detail here 6.

Finally, the Chapter 7 explains the measurement set-ups used in thesis. The devices were electrically characterized in the group's Fert bench set-up before studying them in Synchrotron SOLEIL. With a detailed overview on the two technologically advanced beamlines of the Synchrotron SOLEIL, namely, DEIMOS and HERMES beamlines we will explore the progress made in the x-ray studies to explore the nano-transport path in MgO (oxygen vacancies) MTJs and molecular MTJs (Co PM centers), respectively.

Chapter 5

Thin film engineering

Thin film engineering is a leading industrial technology to deposit layers of materials, as thin as an atomic layer, on to a wide range of surfaces. Thin films offer countless advantages to manufacturers in terms of cost efficiency, production time, increased flexibility of materials. Thin film technology is prevalent across materials science for industrial applications such as memory devices, energy storage, micro-mechanics, photovoltaics, sensors (chemical/optical/magnetic) and many other solid state devices. The surface modification through thin film deposition is the basis for thin film technology. The properties of thin films are highly dependent on the morphology, surface roughness, conductivity of the materials. Hence, a comprehensive knowledge about the atomic details of the thin film growth process helps for the development of complex devices.

5.1 Physics of thin film growth

This section illustrates the basic parameters that influence the morphology of depositing materials on a surface. Thin film deposition and film growth are highly dependent on materials involved in the process, on the energy of the impinging atoms, their arrival rate, and on the substrate temperature. The formation of thin films proceeds through a series of growth stages, starting with, (a) adsorption (physisorption), (b) surface diffusion, (c) chemical binding (chemisorption), (d) nucleation, (e)

microstructure formation and bulk changes at the surface [180]. Since thin films experience distinct growth stages, each step affects the final microstructure and thus its physical properties.

The adsorbed atoms on the substrate can have any one of the following three growth modes for the formation of thin films [180], namely :

a) **Volmer-Weber mode** : In this mode, stable clusters develop into 3D islands which fuse to form a continuous film. This growth mode is common in metal films on insulators, where the adsorbed atoms (adatom) are strongly bound to each other than to the substrate (Figure 5.1-row 1). Ex: metals on SiO_2 .

b) **Frank-van der Merwe mode** : This mode corresponds to a 2D layer-by-layer growth and exhibits opposite characteristics to the previous mode, (Figure 5.1-row 2). Here, the adatoms are strongly bound to the substrate than to each other. Therefore, the first adatoms condense to form a complete monolayer on the substrate surface. Ex : Cu/Cu, Si/Si, GaAs/GaAs.

c) **Stranski-Krastanov (S-K) mode** : This growth mode is the combination of the first two modes. Here, once the 2D monolayers are formed the further layer growth becomes energetically unfavorable and 3D island growth is favored [181], (Figure 5.1-row 3). Ex : In/Si, Ge/Si, InGaAs/InGaAs.






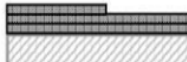


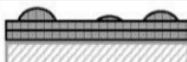
Coverage Mechanism	$\theta < 1$ ML	$1 < \theta < 2$ ML	$\theta > 2$ ML	Examples
3D island growth				Metals on SiO_2
2D layer growth				Cu/Cu, Si/Si, GaAs/GaAs
S-K growth				In/Si, Ge/Si, InGaAs/InGaAs

FIGURE 5.1: Representation of three types of thin film growth modes on substrates. θ indicates the coverage in monolayers (ML). Image adapted from Ref [182].

5.1.1 Atomistic mechanisms on surfaces

The Figure 5.2a describes the individual atomic processes which are accountable for the adsorption and crystal growth on substrate surfaces. An atom approaching the substrate can either be reflected or absorbed on to the surface. This process is dependent on the incoming flux of the atoms, trapping probability and the sticking probability [180, 181].

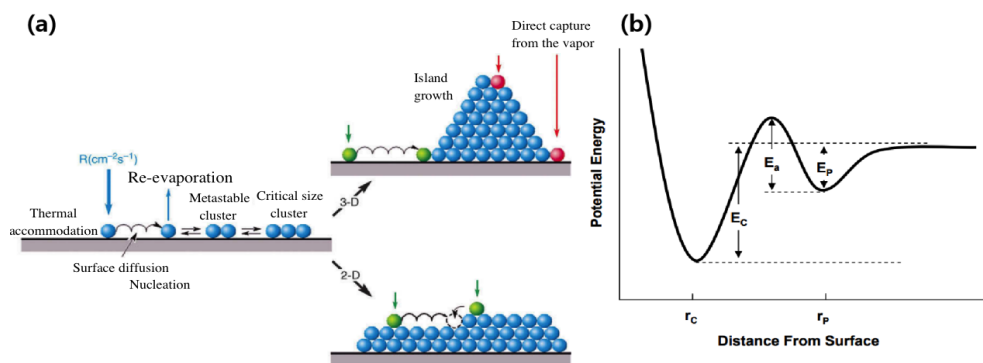


FIGURE 5.2: **Individual atomic processes responsible for adsorption and crystal growth on surfaces.** (a) R is the rate of arrival of atoms at the substrate surface. (b) The rate R is thermally activated and follows Arrhenius exponential equation with activation energy E_a , the potential energy for physisorbed atom is E_P and chemisorbed atom is E_C . Image a taken from Ref [182].

Physisorption occurs when no chemical bonds are formed at the interface, leaving the adatom's chemical species and the substrate intact. Physisorption describes weak electrostatic interactions such as the van der Waals forces, dipole-dipole interactions, and London forces. The formation energy of these weak physisorbed interactions ranges between 10-40kJ/mol [183]. The physisorbed atom can either be chemisorbed or desorbed (ejected) by overcoming the local energy barrier, see Figure 5.2b. Chemisorption occurs when the adatom is covalently bonded to the substrate due to sharing/complete transfer of electrons. These interactions are almost two orders of magnitude stronger than that of the physisorbed atoms (≈ 200 to 400 kJ/mol) [183].

The weak bonding between the adsorbed atoms and the substrate results in the diffusion of physisorbed atoms on the substrate. The diffusion of the physisorbed atom increases with the available energy, but is inversely proportional to the atoms'

arrival rate, R . If the arrival rate of atoms is high, then the surface atoms will rapidly collide with new arriving atoms. This limits the diffusion and strongly influences the growth mode. In addition to diffusion, the physisorbed atoms may bind to defects in the substrate or kinks, exhibit nucleation with other atoms, and form clusters. The nucleation energy increases with the available surface energy. An atom or molecule with sufficiently high energy can desorb from the substrate surface. The probability of desorption is smaller for clustered atoms compared to single atoms. Once there are sufficient atoms on the substrate, the film starts to grow, and at this stage, the role of interface stability becomes crucial. Thermodynamics can be used to determine if the atoms will be chemisorbed or not [184]. Interested readers can check the reference Venables et al. [180] for a brief introduction to thermodynamics of thin films' adsorption.

5.2 Instrumentation and thin film metrology techniques

The hybrid growth cluster in IPCMS comprises five different chambers maintained under ultra-high vacuum (UHV) conditions, namely the load-lock, robot, magnetron sputtering, thermal evaporation, and organic molecular beam epitaxy (OMBE), see Figure 5.3. All these five units are accessible using a robotic arm, enabling the transfer of samples between the chambers in UHV conditions. Therefore, the thin films fabricated in this set-up avoids oxidation and any contamination of interfaces before final capping. An impurity-free interface is crucial for the spin-dependent properties (see Chap. 2, 3) of the deposited materials that form the thin film.

The hybrid systems' physical vapor deposition (PVD) techniques have been rigorously used in this thesis to fabricate in-situ metal/organic-based thin films. Specifically, the magnetron sputtering and organic molecular beam epitaxy (OMBE) deposition chambers are significantly used for the optimization of the growth conditions of metal buffers, capping (Cr, Ta); FM electrodes (Fe, Co); and organic spacers (CoPc, C₆₀), respectively.

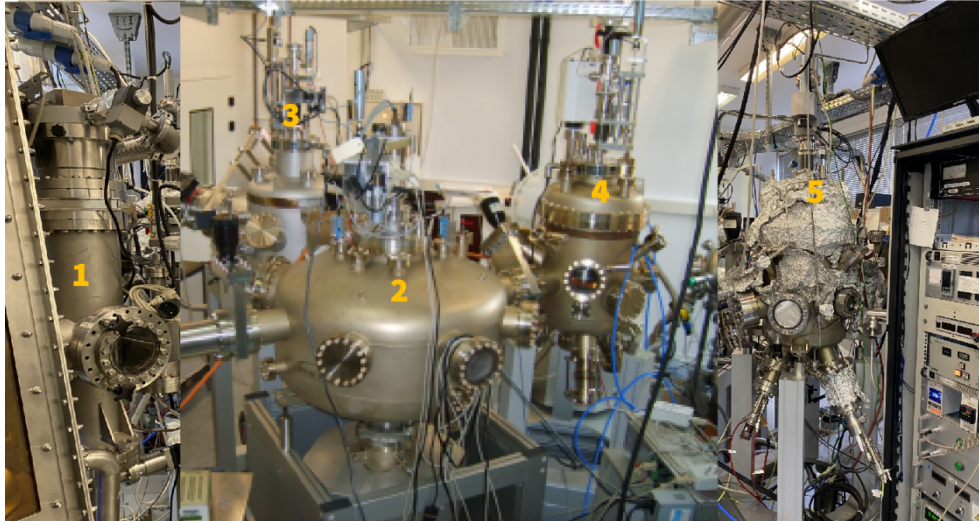


FIGURE 5.3: **UHV chambers of the IPCMS Hybrid growth cluster.**
1) load-lock, 2) robot, 3) sputtering, 4) evaporation and 5) molecular beam epitaxy for organics.

5.2.1 Physical vapor deposition (PVD)

Physical vapor deposition (PVD) is a process of vacuum coating a material, usually done by deposition of the target material atom by atom onto a substrate by condensation from the vapor phase to the solid phase. Numerous physical vapor deposition techniques have been developed for fabricating thin-film coatings under vacuum conditions. PVD techniques for coating was popularized in the 1970s and has ever since been on demand in various industries. The most common used PVD processes are:

1. **Thermal evaporation** techniques where the material to be deposited is heated under vacuum until its vapor pressure is higher than the ambient pressure. There are two types of thermal evaporation process pulsed laser deposition (PLD) and electron beam deposition. PVD techniques are extensively used in microfabrication industries.
2. **Sputtering** involves the bombardment of high-energy particles that knock off the atoms or molecules from the target surface. In sputtering PVD, the deposited layers are either amorphous or, at times polycrystalline, but never monocrystalline. Two main types of sputter deposition are currently being

used in manufacturing applications: ion beam sputtering and magnetron sputtering.

In this thesis work, electron-beam deposition, magnetron sputtering, RF sputtering and OMBE techniques are used. Hence, in the following sections, the focus will be mainly on these individual processes.

5.2.1.1 Magnetron sputtering

Sputtering is one of the extensively used physical vapor deposition techniques for thin film deposition. In the mid-1970s, the diode sputtering was replaced by magnetron sputtering. Since then, it is a widely used vacuum coating technique for depositing metals (Fe, Co, Cr, etc.), alloys, compounds, and refractory materials like oxides of aluminum, silicon, and more [185, 186]. Magnetron sputtering has several advantages over other vacuum coating techniques, for instance :

1. The versatility of materials that can be used range from metals to semi-conductors.
2. The deposition of materials can go up to a thickness of millimeters and hence high deposition rates.
3. The magnetron sputtered atoms form denser films with smaller grain sizes, which leads to high-quality films.
4. Sputtered atoms contribute to the strong adhesion of the films to the substrate.
5. Uniform rate, therefore, maintaining the stoichiometry of the film.

Thanks to all these vital advantages of magnetron sputtering has paved the way for developing countless commercial applications ranging from complex microelectronics fabrication to simple decorative coatings.

5.2.1.1.1 Working of magnetron sputtering Magnetron sputtering process takes place within a vacuum chamber, where the material to be sputtered forms the target

(cathode). A magnetron composed of powerful permanent magnets is in close contact with the target. The magnetron sputtering proceeds by introducing inert gas like argon in to the vacuum chamber, which is accelerated by a high voltage being applied between the target and the substrate in the direction of the magnetic field. The high voltage across the electrodes ionizes the incoming Ar gas atoms into electrons (e^-) and Ar^+ ions. These energetic Ar^+ ions are accelerated towards the negatively charged cathode, where they bombard with the target to eject atoms, and secondary electrons from the target surface, see Figure 5.4. The ejected atoms as a result of kinetic energy transfer by the Ar^+ ions move towards the substrate creating a solid thin film.

The ejected secondary electrons which usually in a diode sputtering would bombard with the substrate and damage it by overheating, is prevented in magnetron sputtering. The magnets behind the cathode traps the secondary electrons confining them closer to the target surface. Hence, it is feasible to use low voltage values and low-pressure amplitudes in magnetron sputtering, which allows for the deposition of high- purity thin films. Additionally, the ejected secondary electrons are responsible for maintaining a stable plasma. Without these secondary electrons, the plasma vanishes. In the plasma state, the electron energy is sufficient to excite atoms to higher energy levels where they emit light upon relaxing to a lower energy level. Hence the plasma is luminous, and this regime is called the glow regime. In the glow regime, the plasma formed is stable and energetic enough to be used in micro-fabrication technologies like sputtering and dry etching (cathodic cleaning). The localized plasma in magnetron sputtering, accounts for increased deposition rates and prevents the damage of substrate or growing film as fewer electrons collide.

In the IPCMS hybrid sputter deposition system, we mainly used Ar as sputter gas. The sputtering chamber has a design that allows for three sputtering magnetron sources which is sufficient for the device structure studied in this thesis, see Figure 5.5. The set-up consists of a UHV sample heater used to anneal the substrate before deposition of the entire thin film stack. The sputtering deposition rates were closely calibrated using the Sigma SQM-160 quartz monitor. The chamber is also equipped with a residual gas analyzer (RGA), which allows for optimal control over the gases'

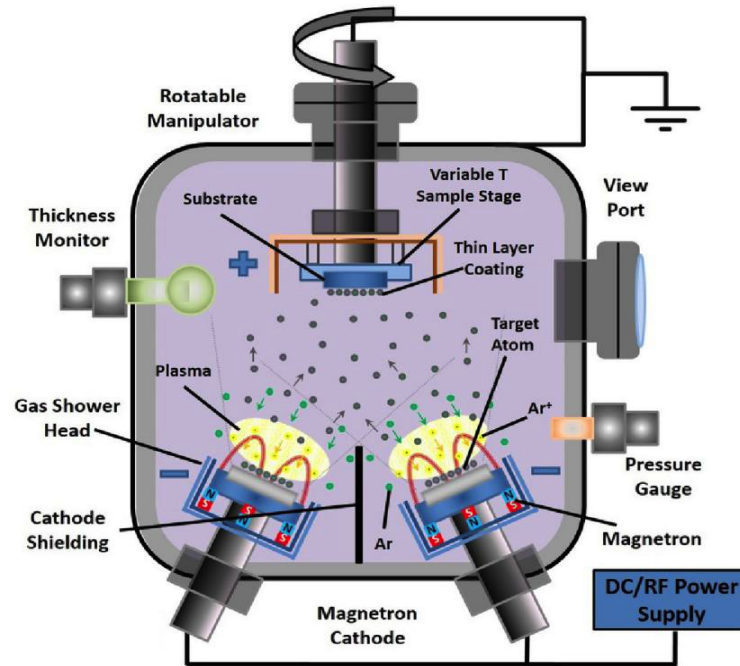


FIGURE 5.4: Diagrammatic sketch of magnetron sputtering in a UHV chamber. Image taken from Ref [187].

partial pressures inside the chamber. The sputtering chamber usually has a base pressure of $2e^{-9} mbar$, therefore better growth of the metallic layers. In this thesis, the DC magnetron sputtering was extensively used to deposit Fe, Co, Cr, Ta metallic layers for the CoPc based molecular devices.

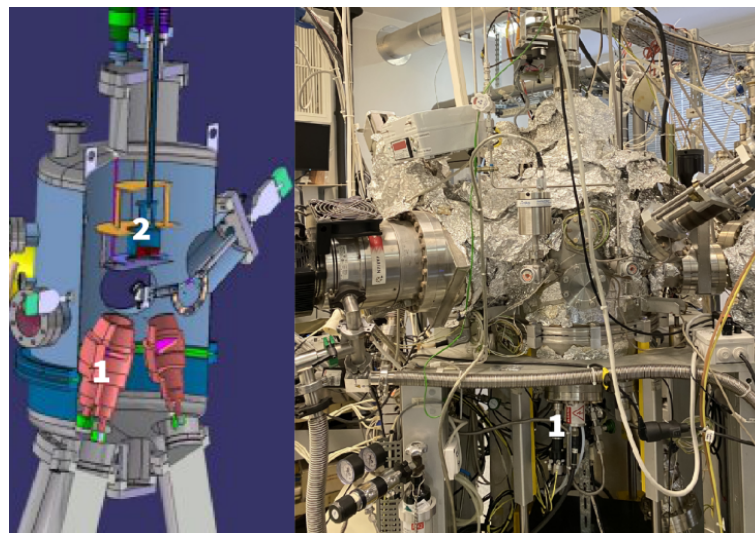


FIGURE 5.5: **Sputtering chamber of the hybrid cluster**, left image is artist illustration of the real set up in the right. 1) three reclining magnetrons 2) sample holder manipulated by with the vertical tower.

5.2.1.2 Organic molecular beam epitaxy (OMBE)

Crystalline material films are fabricated using molecular beam epitaxy (MBE), which is not possible using e-beam evaporation and sputtering PVD techniques. In the mid-1980s, the organic molecular beam epitaxy (OMBE) growth of organic thin films under ultrahigh vacuum emerged. It is quite similar to conventional MBE growth systems [188, 189]. Typically, the purified organic source material, mostly in powder form, is loaded into a crucible (ex. quartz crucible), which is mounted inside an effusion cell (also called Knudsen cell) [190] for sublimation, see Figure 5.6a. The background pressure inside the chamber is usually ranging from 10^{-7} mbar to 10^{-11} mbar. The basic principle of working involves the heating of the crucible when the cell's temperature exceeds the molecule's respective sublimation temperature but is lesser than the decomposition temperature of the organic molecules to be sublimed. This organic evaporant migrates through the UHV environment within the chamber, where it is collimated by passing through a series of orifices and then reaches the substrate to form a film.

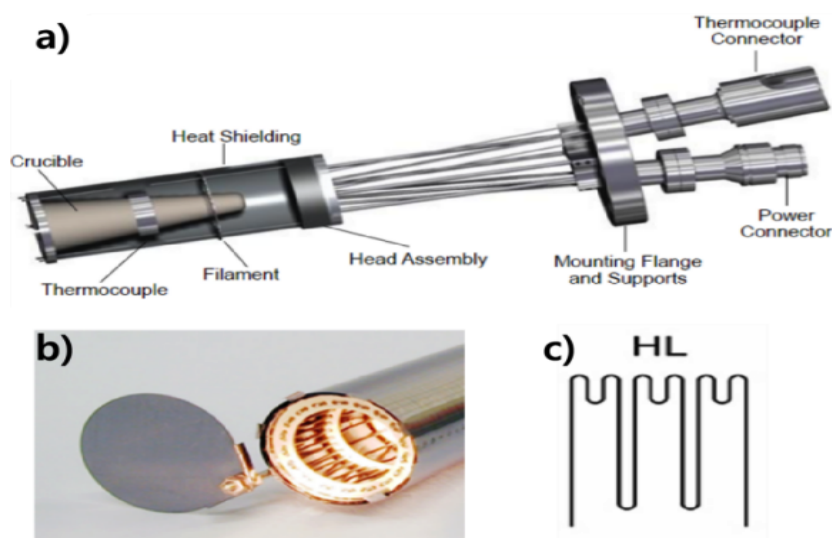


FIGURE 5.6: **Knudsen cell.** a) overall cell view. (b) close up top view of the hot lip filaments of the Knudsen cell. The filaments are closely wired near the tip of the crucible, (c) schematic of series of three hot lip (HL) filaments which are responsible for the uniform temperature gradient over the entire crucible length. Image adapted from Ref [191].

At IPCMS, our hybrid growth system has a thermal evaporation chamber exclusively used to deposit organic molecules. The system has a provision for four

different Knudsen cells. These cells are equipped with hot lip filament, HL (Figure 5.6b,c), which is crucial for the deposition of organic molecules. A hot lip filament is wired more densely at the top portion than a standard heating system, resulting in a slightly higher temperature near the crucible lip, see Figure 5.6b. It helps maintain a uniform distribution of heat over the crucible length carrying the organic molecule. Therefore, this HL filament prevents the condensation of the molecules on the lip of the crucible during the molecular depositions. These effusion cells also have a mechanical shutter that can be used to control the molecular beam flux from on to off. In our set-up the sample stage is continuously in rotation mode at a fixed speed to maintain a uniform molecular deposition. The thin film's growth rate is measured using a quartz thickness monitor within the OMBE chamber, and also, there are temperature regulators for the respective cells. The main advantage of the OMBE technique is that it provides close control over the deposited layer thickness and an atomically clean surrounding. In this thesis, the growth of the multilayer structure of organic molecules specifically targeted cobalt phthalocyanine (CoPc) and fullerenes (C_{60}) thin/ultra-thin films utilizing the sequential shuttering from one Knudsen cell to another.

5.3 Molecular stacks

In order to obtain a uniform growth, in our study, we have used Si substrates with 500nm-thick RF-sputtered SiO_2 . These substrates were cleaned with acetone, isopropanol, and ethanol sequence in two batches for five and ten minutes each respectively, in an ultrasonic bath. The cleaned $Si/SiO_2//$ substrates were mounted on a molybdenum sample holder, and a high precision laser-cut stainless steel mask is used to define the growth of the thin film on the substrate Figure 5.7.

The stainless steel shadow mask was designed and developed within the time frame of this thesis as a collaboration with IREPA laser company. The masks have been extensively used in defining the growth layout of the thin film. The solvent cleaned shadow masks are laid on top of the $Si/SiO_x//$ substrates. Thanks to the robust laser cut steel mask when fixed with care lays flat on the substrate. This is

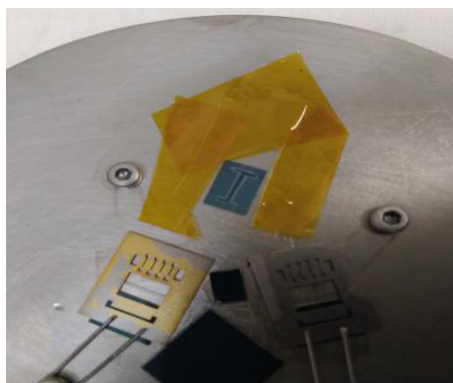


FIGURE 5.7: Stainless steel masks fixed on Si/SiO_x / substrates using tantalum pins.

important to eliminate any shadow effects during deposition of successive layers of the thin film.

In the framework of this Ph.D., a variety of molecular stacks were fabricated and studied under UHV conditions. The substrates were annealed up to 120°C and cooled to room temperature before the deposition of the thin film. Predominantly for molecular MTJs, Cr was used as buffer and capping, Fe and Co as ferromagnetic (FM) electrodes. All of them were deposited at room temperature within a $3e^{-4}$ mbar Ar pressure in the sputtering chamber. The chamber's base pressure was $1e^{-9}$ mbar. Once the buffer and FM electrode is grown, the sample was transferred using a robotic arm to the OMBE chamber for molecular deposition. The robot chamber has a base pressure of $5e^{-10}$ mbar. The time spent between the sample transfer from the sputtering chamber to the OMBE chamber is less than 10 minutes. The organic molecules CoPc and C_{60} , which serve as the spintronic spacer layers in the stack, were epitaxially grown at room temperature in the OMBE chamber. The OMBE has a base pressure of $7e^{-10}$ mbar. The organic molecules were sublimed at their respective sublimation temperature using Knudsen cells under the pressure of $2e^{-9}$ mbar. Finally, the samples are transferred back to the sputtering chamber via the robot chamber. The upper ferromagnetic electrode Fe or Co is sputtered on top of the deposited molecular layer. Then the entire stack is protected by a thick sputtered capping layer of Cr. Table 5.1 gives a detailed description of the respective layers deposited and the parameters used.

Material	Function in stack	Method of deposition	Deposition pressure (mbar)	Rate of deposition
Cr	Buffer and Capping	Magnetron Sputtering	4.8e-4	0.3 $\text{Å}^\circ/\text{s}$
Ta	Buffer and Capping	Magnetron Sputtering	4.8e-4	0.6 $\text{Å}^\circ/\text{s}$
Fe	FM electrode	Magnetron Sputtering	4.4e-4	0.25 $\text{Å}^\circ/\text{s}$
Co	FM electrode	Magnetron Sputtering	4.4e-4	0.2 $\text{Å}^\circ/\text{s}$
CoPc	Insulating molecular barrier and source of PM center	Molecular epitaxy	1.0e-9	0.005 ML/s
C ₆₀	Insulating amorphous molecular barrier	Molecular epitaxy	2.6e-9	0.0036 ML/s

TABLE 5.1: Deposition techniques and the different deposition parameters for the different materials used in preparing the organic hybrid heterostructures. All depositions were done in-situ at room temperature.

5.4 MgO stacks

The inorganic magnetic tunnel junctions with MgO spacer sandwiched between CoFeB electrodes studied in this thesis were also fabricated by using a sputtering system. The MgO stacks were fabricated by our close collaborator Dr. Michel Hehn, IJL, Nancy. Only a general growth procedure for MgO stacks is described in this thesis; for more details, consider reading the reference J. Bernos and M. Hehn et al. [192].

5.4.1 Fabrication of MgO stacks using Nancy Sputtering

The MgO spacer based thin film stacks were grown on a clean amorphous corning 1737 glass substrate. The stack is composed of Glass//Ta(5)/Co(10)/IrMn(7.5)/CoFeB(4)/MgO(2.6)/CoFeB(3)/Ta(2)/Pt(1). The thickness of the layers are in nm's. Ta is used as a buffer followed by the sputtering of ferromagnetic Co layer to improve further texturization, as cobalt has shown good adhesion with tantalum. The next layer is an antiferromagnet IrMn which acts as a pinning layer. This is followed by the sputtering of CoFeB/MgO/CoFeB tunneling structure with CoFeB. The CoFeB was rf sputtered using a $\text{Co}_{40}\text{Fe}_{40}\text{B}_{20}$ alloy target. Finally, the stack was protected with a capping of Ta/Pt bi-layer.

5.4.1.1 Annealing of MgO stacks

Since CoFeB is an amorphous material the first few monolayers of MgO grows amor- phously on top of it. Gradual growth into several layers of amorphous MgO results in the appearance of crystalline MgO structure [193]. Therefore, this type of MgO is not perfectly epitaxial rather it is a textured crystal made up of (001) crystalline do- mains separated by grain boundaries and amorphous regions. The top CoFeB elec- trode grows amorphously on the underlying textured MgO. In order to achieve com- plete crystallinity of the barrier and interfaces, the entire stack is annealed ($> 300^\circ\text{C}$). This results in the distribution of the crystalline structure arising from the textured areas of the MgO spacer [193, 194]. Once the crystallization stretches into the in- sulator/FM interface, the latter begins to shape into bcc crystal structure instead of fcc (111), thus adapting to the underlying MgO cubic arrangement. The crystalline order of the CoFeB/MgO/CoFeB MTJ is presented in the TEM image of Figure 5.8a. In spite of the polycrystalline character of the MgO barrier, it has little or no influ- ence on the electron transport by the grain boundaries [195]. Hence, non-annealed MgO samples have very small TMR vales as compared to the annealed because the former is a amorphous system that promotes incoherent transport due to symmetry mixing [194]. The Figure 5.8b shows the TMR variation in the annealed MgO sam- ples measured at room temperature. In addition to achieving crystallinity annealing also plays another crucial role in pinning the lower CoFeB electrode by exchange bias (EB concept explained in Chap. 3).

In our experiment the fully grown MgO stacks were post-annealed for 1hour in a high vacuum chamber varying the annealing temperature between 200°C - 300°C in the presence of an external magnetic field of 200Oe applied in plane to the sam- ple. The annealing temperature is above the T_N of IrMn and below the T_C of CoFeB electrodes. The procedure enables the alignment of antiferromagnetic IrMn and fer- romagnetic CoFeB electrode domains on subsequent cool-down, thus achieving the exchange bias of the lower electrode. The Figure 5.8b describes the TMR depen- dence at different annealing temperatures (T_{ann}) for a MgO barrier thickness varied between 2nm-3nm.

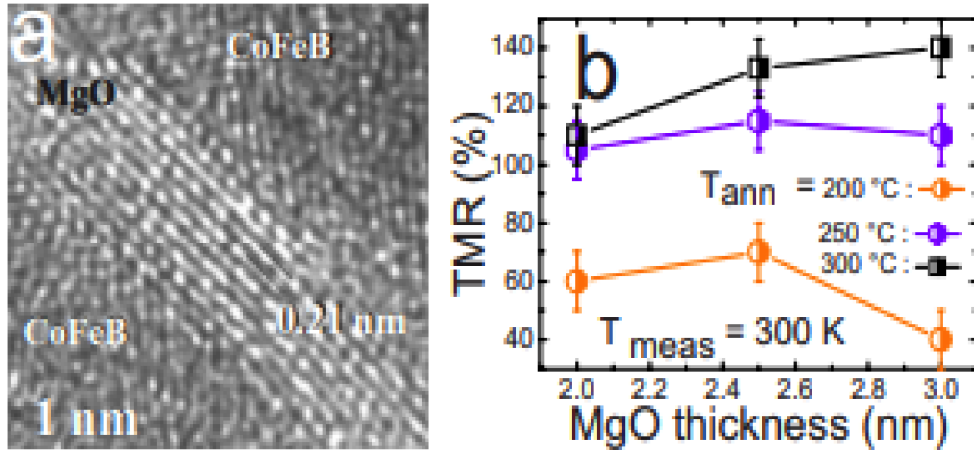


FIGURE 5.8: a) The TEM image of a CoFeB/MgO/CoFeB magnetic tunnel junction for MgO thickness of 2nm after a post thermal annealing at 300°C. b) The TMR vs. MgO thickness plot of a MgO MTJ measured at room temperature for three different annealing temperatures (T_{ann}). Figure reproduced from Ref [192].

This growth approach has few shortcomings when compared to the one discussed in the Yuasa et al. [193] work, particularly the Mn diffusion from the IrMn, during annealing. This affects the pinning strength which is decreased due to the Mn deficiency in the AFM IrMn. The effect is paramount when the annealing temperature or time is increased [196].

The fabricated MgO stacks were processed into MTJs (see Chap. 6) and electrical characterization was performed in IPCMS, Strasbourg, prior to synchrotron measurements at HERMES beamline (see Chap. 7 Sec. 7.4).

5.5 Characterization techniques

This section describes some of the standard characterization techniques used in this thesis to investigate the physical and structural properties of the in-situ fabricated molecular thin films.

5.5.1 Super conducting quantum interference device (SQUID)

SQUID is a highly sensitive magnetometer is designed to detect and measure the minute perturbations in a magnetic field which is induced by structural anomalies

located at the surface or within the material volume. It is the only technique which directly detects and determines the overall magnetic flux of a sample, using which the magnetization and the magnetic susceptibility can be derived.

The operation of SQUID magnetometer is based on superconducting loops containing Josephson junctions (see Fig. 5.9). The magnetic signal from a given sample placed in a liquid helium bath, is acquired by a superconducting pick-up coil by vibrating the sample through them. The SQUID sensor detects the current in the rings of the coils and converts the magnetic flux signal into voltage signal. This voltage signal is then amplified and read out by the magnetometer's electronics and this output voltage is proportional to the magnetic moments of the sample under study.

In this thesis a commercial SQUID magnetometer system from Quantum Design (MPMS3) was used to investigate the magnetic properties of the organic heterostructures. A plastic straw is used as a sample holder as it does not contribute any additional magnetic signal to the sample. A $(3 \times 3) \text{ mm}^2$ dimension sample is used which fits quite well within the straw holder. Then the sample in straw holder is introduced in SQUID apparatus, see Figure 5.9. The sample is carefully fine tuned such that the position of the vibrating sample does not overshoot the distance of the pick-up coils. This ensures maximum capture of the output voltage and hence the total magnetic moments of the sample.

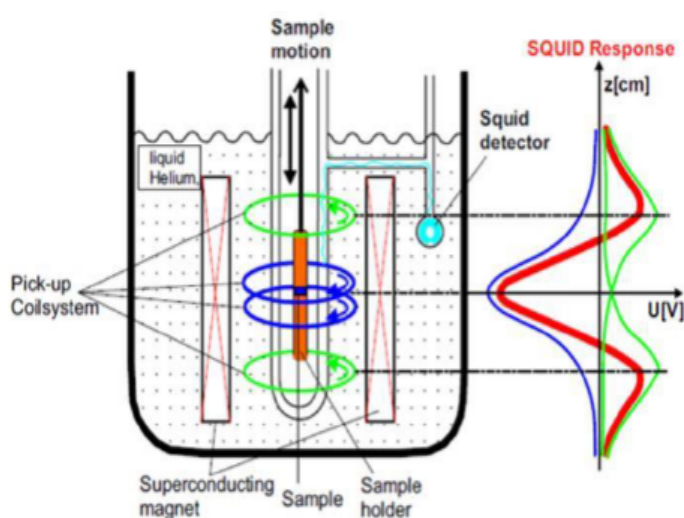


FIGURE 5.9: **SQUID set-up.** The best position for optimum SQUID output voltage is recorded for the sample is when it is in between the blue colored pick up coils. The figure is adopted from Ref [120].

In this work, the SQUID was operated in dc mode where static magnetic field is applied to study the macroscopic magnetic properties of the tri-layer heterostructures. To study the effects of exchange bias in organic tri-layers a magnetic field of 7T was applied while cooling down the sample from 300K to 4K. This field cooling procedure is crucial to study the effects of magnetization in magnetic thin films (details in Chap. 3). The SQUID magnetometry results for CoPc based molecular stacks are discussed in Chapter 9.

5.5.2 Electron microscope:

An electron microscope is a powerful tool that uses a beam of accelerated electrons to produce an image of the object under study. Unlike optical microscopes in which magnification of the sample image is obtained by a system of optical lenses, an electron microscope uses electromagnetic fields for image magnification. An electron microscope has a high resolution and can resolve objects as small as 10\AA as compared to 0.2 micron by an optical microscope. In the field of material science, electron microscopes are extensively used to study the interaction of an electron beam with the sample and thus obtain information on its structure, morphology and composition. In the framework of this thesis two main types of electron microscopes were used namely, transmission electron microscope and secondary electron microscope. The former was used to understand the interfacial features at the metal and molecule and the latter was used to image the silica nano spheres used for patterning nano organic junctions.

5.5.3 Transmission Electron Microscopy (TEM)

A transmission electron microscope can be used to study the features of a crystal structure such as dislocations and grain boundaries of a very thin sample. Specifically, in this thesis TEM was used to study the growth of the organic thin film layers and their composition. TEMs can reveal finest details of an internal structure which helps to visualize the growth preference in thin films. The TEM measurements were

performed with a collaboration with Karlsruhe Institute of Technology (KIT), Germany.

5.5.3.1 TEM specimen preparation

Sample preparation is one of the crucial aspects of TEM analysis as it demands that the specimen be thin enough so it can transmit sufficient electrons to produce an image with minimum energy loss. Numerous techniques have been developed to prepare TEM samples and depending on material properties, analysis type the appropriate technique is selected. The techniques can be broadly classified as mechanical, ionic, chemical, electro-chemical and mechanical-physical techniques. The TEM sample under focus in this thesis is an organic based thin film, which can be completely contaminated and destroyed by TEM sample preparation techniques which involves gluing, polishing with chemicals and heat treatments. In order to safeguard the organic layers, here, focused ion beam (FIB) thinning is used to produce electron transparent cross section sample lamella of constant thickness [197]. FIB uses a focused beam of ions and these ions are accelerated to an energy close to 5 - 30 keV and then focused on to the sample surface. This method has a resolution in the nano-scale and thus allows for the extraction of thin layer of the chosen region of the sample. The TEM results for FM/CoPc/FM molecular heterostructure can be found in Chapter 8. TEM was also used to image the nano-silica spheres used for defining the molecular junctions, see Appendix B.

5.5.4 Scanning electron microscope (SEM)

One of the standard techniques for imaging the microstructure and morphology of various materials is scanning electron microscope (SEM) (Fig.5.10a). It uses a focused beam of high energy electrons to radiate the material and thus scan the surface of the sample. This electron-sample interaction reveals a lot of information about the external morphology, crystalline structure and many more. Moreover, SEM provides a resolution of 10nm, which is highly attractive and some of the advanced versions of these set-ups can go to a 2.5nm resolution.

In the operation of scanning electron microscope, the sample surface is exposed to a narrow beam of electrons produced from an electron gun. This electron beam sweeps or scans the sample surface, which releases a variety of signals. The signals include secondary electrons, back-scattered electrons (BSE), diffracted electrons (EBSD), photons (characteristic x-rays and continuum x-rays), visible light and heat, see Figure 5.10b. Secondary electrons and back-scattered electrons are mostly used to image the sample. Specifically the secondary electrons provides explicit information on the morphology and topography of the samples and the back-scattered electrons are crucial for illustrating contrasts in the composition of multi-phase samples. Diffracted back-scattered electrons are used to determine the crystal structures and orientations of minerals, characteristic x-rays are most commonly used for elemental analysis [198].

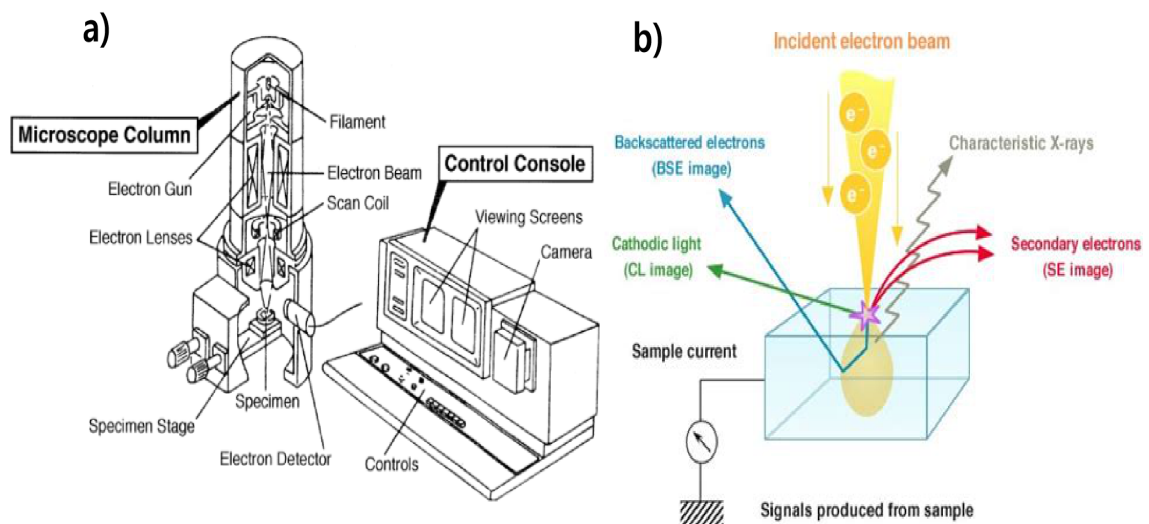


FIGURE 5.10: **SEM set-up and signal types.** (a) The path of focused high energy electron beam collimated by sophisticated magnetic lens to irradiate the sample and collect the BSE and SE image. (b) The result of electron beam interaction with the sample leads to emission of variety of signals. Image taken from Ref [198].

Although SEM is considered to be a non-destructive method, meaning there is no loss in the volume of the sample, conductive samples often get damaged and cannot be analyzed for a long time or repeatedly. Conventional SEM can offer to image only solid samples and the liquid or wet samples often out-gas hence are incompatible to be used in vacuum conditions of a SEM set-up.

In this thesis, the SEM setup of IPCMS was mainly used to image the silica nano

spheres which act as the mask to define the vertical molecular junctions. The SEM images of the nano spheres can be found in Appendix B.

5.5.5 X-ray reflectometry and X-ray diffraction

X-ray reflectometry (XRR) is a fast and non-destructive analytic tool used to study the surfaces, interfaces of thin layered structures. It works on the principle of total external reflection of x-rays; where at every interface a portion of the x-rays is reflected and the interference of these partially reflected x-rays produces a reflectometry pattern. The structural characterization of thin films can be done using XRR as it can be used to determine the thickness, density and surface roughness for a single/multi-layer stacks of crystalline and amorphous materials.

When x-rays are incident on to the material surface at grazing angle of incidence, total reflection occurs at/below a critical angle, θ_C , and the reflected x-rays create an interference pattern because at the interface, different materials have different refractive indices. The critical angle varies depending on the material's electronic density. The higher the incident x-ray angle relative to the critical angle, the deeper the x-rays transmit into the material. Suppose a material has a rough surface it results in a dramatic decrease in the reflectivity. If such a material acts as a substrate and a layer of another material with a different electronic density is deposited, then the reflected x-rays from the interface between the substrate and the thin film along with the top free surface of the film will either constructively or destructively interfere with one another. This results in an interference oscillatory pattern, see Figure 5.11.

To first approximation, the intensity scattered by the sample is proportional to the square of modulus of the Fourier transform of the electron density. Thin film stacks with more electronic density contrast between its layers will give a larger amplitude signals in the fringes. Hence, the electron density profile can be deduced from the measured intensity pattern. In addition to this, the film thickness can be determined from the periodicity of the oscillation and the surface, and the interface root-mean-square (rms) roughness can also be derived from the rate of signal decay

(see Fig. 5.11). The density of the material is determined from the critical angle i.e., the initial drop in signal.

X-ray diffraction (XRD) is a non-destructive technique based on Bragg's law ($n\lambda = 2d\sin\theta$) used to characterize the crystallinity of the thin films. A monochromatic x-ray beam is incident on the sample and the reflected x-rays are collected by a detector. The x-ray diffraction pattern exhibits sharp peak intensities for crystalline materials and broad peaks for amorphous. The peak intensities are determined by the atomic positions within the lattice planes of the sample. Therefore, the XRD pattern acts as a fingerprint to distinguish the periodic atomic arrangements in the sample.

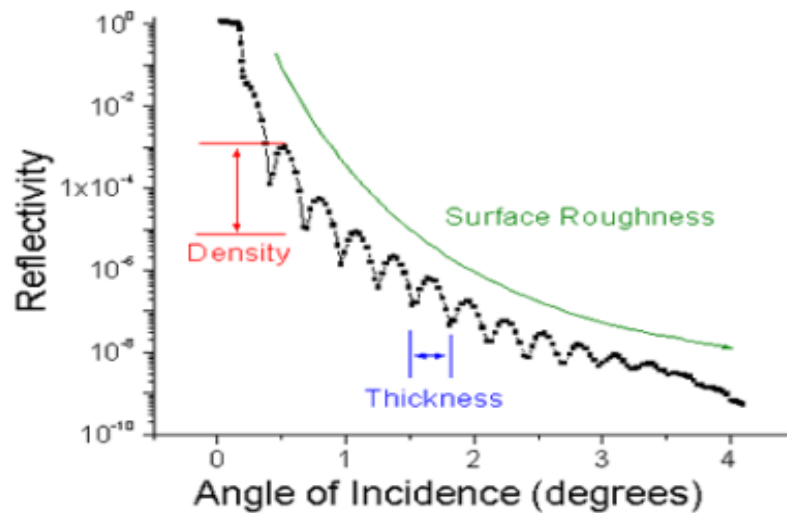


FIGURE 5.11: X-ray reflectometry of a thin-film. From the graph, slope gives the surface roughness ; drop in signal determines the density of the material and the distance between the fringes gives the thickness of the thin film. Figure adapted from Ref [199].

In this thesis, the thickness calibration of metallic and organic layers of the thin film was done using Rigaku set-up by working closely with Mr. Guy Schmerber. The deposition rates of the materials were closely monitored using the quartz crystal thickness monitor. In order to know the thickness of the material being deposited onto the substrates, a physical measurement of each layer and a multi-layer stack was done using XRR. The XRR values were carefully compared with the number of units read by the quartz monitor. Since, the quartz crystal cannot be placed exactly in the same position as the substrate being coated, a correction term called 'tooling factor' is programmed into the quartz monitor data for each material. This factor is

dependent on the distance of the quartz from the sample. The tooling factor of the crystal monitor is given by the formula $F_m = F_i(T_m/T_i)$, where, F_m =calculated tooling factor, F_i = initial tooling factor, T_i = thickness in units read by the quartz monitor and T_m is the XRR measured thickness (in nm) of the deposited film material. Suppose there was no initial value assigned to tooling factor one can begin with $F_i=1$. The tooling factor is tuned at least three times on the same nominal thickness of the material before fixing its value. So its important to evaluate the tooling factor value by measuring the thickness of the materials from XRR and comparing it with the thickness reading in the quartz monitor. With the tooling factor and the density of material programmed into the quartz monitor the rate can be easily controlled as per requirement of the user. The calibration was performed each time before fabricating new organic stacks, especially when the sputtering or OMBE chambers were vented to atmosphere or changed targets/molecules. The XRR and XRD characterization results for molecular hetero-stacks can be found in Chap. 8 and Chap. 9.

Chapter 6

From thin film stacks to magnetic tunnel junction devices

The thin film stacks were processed carefully involving various technological steps which are detailed in this current chapter.

6.1 Front-end process

Solid state devices are fabricated by the front-end process which includes various steps of wafer/thin film process operations like thin film deposition (Chapter 5), mask fabrication, patterning, etching, passivation, metallization.

6.1.1 MgO thin films patterning

Photolithography technique is widely used in semiconductor patterning. The technique utilizes a radiation source like UV rays or x-rays to transfer the pattern from a photomask to the substrate surface, then etching away the unprotected mask surface. The photomask is a transparent plate with patterned chromium areas printed on it. A radiation sensitive resist/polymer is used as a primary mask layer, which undergoes chemical changes when exposed to specific wavelengths through a photomask. The photoresist after exposition to radiation is more susceptible to dissolve

in photoresist developer. There are two types of photoresists namely, positive photoresist and negative photoresist, see Figure 6.1(a,b).

In **positive photoresist** the photochemical reaction during exposure weakens the polymer making it increasingly soluble in the developer and a positive pattern is achieved. The developed pattern on the substrate is an exact copy of the design chosen from the photomask. Therefore, the pattern on the sample acts as a stencil for the following processing steps. Positive resists are popular in semiconductor industries as they offer better resolution and good thermal stability.

In **negative photoresist**, the exposure to radiation results in polymerization of the photoresist. On developing, the negative resist remains on the surface of the substrate where it is exposed and is removed from the unexposed areas. Hence, the negative photoresists leave the sample with the opposite pattern of the original photomask. The advantages of negative resists are good adhesion to silicon, low cost, and offer a shorter processing time.

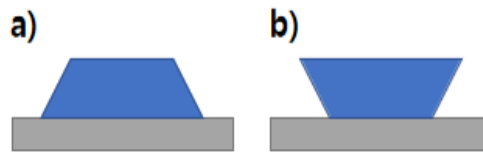


FIGURE 6.1: Illustration of cross-section of (a) positive resist and (b) negative resist after UV insulation and development. The negative resist displays an overhang.

The following are the key steps in photolithography :

1. Choice of appropriate photoresist (+/-ve) based on the desired pattern of the photomask.
2. Deposition of the photoresist over the sample using spin-coating technique which forms a thin and uniform film.
3. The development of the pattern.

Once the development of pattern is complete the sample is ready for processing. In this thesis, for the photolithography of MgO stacks a 365nm UV lamp source, and

AZ505 (+ve resist), AZ515 (-ve resist) were utilized. The photomask used for the process was initially designed by A. Anane of UMPy CNRS/Thales in 2002, after several iterations of refinement by Dr. Filip Schleicher and Dr. Martin Bowen within the group, the present design can be seen in Figure 6.2.

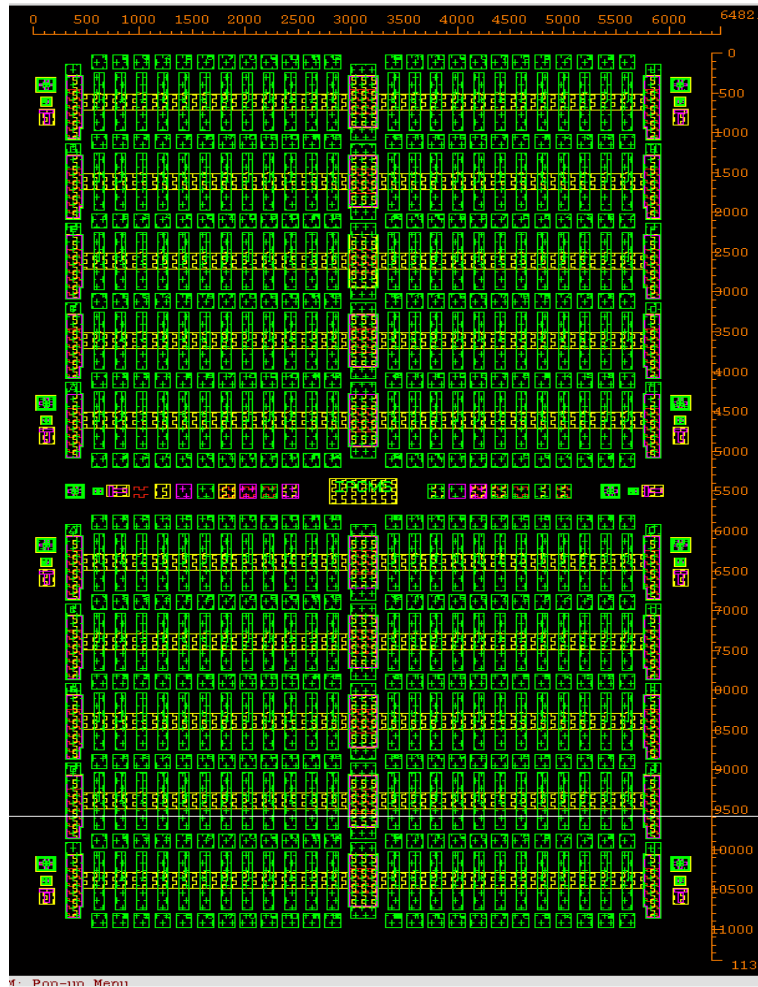


FIGURE 6.2: **Optical mask** used for MgO patterning includes all the four steps needed to create 20micron sized inorganic MTJs

6.1.2 Processing of MgO stacks

The MgO based thin film stacks are processed in four steps using photolithography. The first step is to define the micro junction pillars, followed by electrode patterning, passivation and metallization. The following sub-sections details all the steps involved to make MgO MTJs.

6.1.2.1 Step I : Defining micro pillars

The sample is spin coated with a positive resist AZ5105 which provides a uniform surface (Figure 6.3a) so the photomask could be aligned to define the junction pillar pattern and the large common contact pads. One crucial point to remember is to determine the micro-pillars along the direction of the exchange bias, which is defined during the annealing of the MgO growth process. The photomask is placed in contact with the resist coated sample and flooded (Figure 6.3b). On development with AZ726 developer the photoresist is removed from all areas except on the pads and the to be defined micro pillars circular region, see Figure 6.3c.

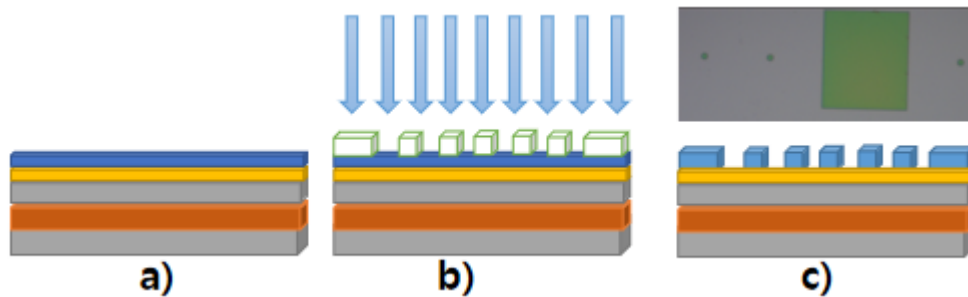


FIGURE 6.3: **Sub-steps involved in patterning of micro-pillars.** The colors : gray - electrodes, brown - MgO barrier, orange - metallic capping, blue - photoresist, and white - shadow mask opaque regions. (a) Photoresist spin coated on the sample, (b) selective UV exposure by the chromium on the glass photomask, (c) patterned photoresist remaining on the sample surface. The top insert is the real sample post developed image in which the circle is the micro pillar and square is the contact pad protected by the photoresist and the remaining is the naked sample surface. Note the drawings are not scaled to real sample dimensions.

To define the micro pillars MgO heterostructure stacks are etched up to the MgO tunnel barrier using neutral beam etching and analyzing with Auger spectroscopy.

Neutral beam (NB) etching : The nano-pillars are defined by etching using a neutral beam removing the uncovered materials. The main advantage of NB etching technique is it can etch large area of the sample without causing electrical and physical damages which is crucial to protect the MTJ. The damage-free instrument comprises of an ion source for extracting and accelerating an ion beam with a specified polarity; a grid positioned at the rear of the ion source with multiple grid apertures through which the ion beam travel and a reflector with same plurality of holes

as grid holes is closely connected to the grid. In our set up Ar gas introduced into the chamber and split into ions to create a plasma. The Ar^+ ions existing the gun was neutralized by electron emitting filament and was accelerated towards the sample. Charge evacuation from the sample was done by covering the side pads of the thin film structure with Al foil strips using UHV compatible high temperature kapton tape. This is crucial to read sample current and detect Auger signals. For uniform etching the sample was at an angle of 45degree to the beam and was continuously rotated during the entire etching process.

The etching was performed by close monitoring and controlling the sample current. The etching dose was calculated by evaluating the sample current for unit time (mA.min). The crucial point in the etching step is to create the junction pillar with all top layers up to the mid of the tunnel barrier. Etching beyond the tunnel barrier can cause the underlying FM layer of the stack to be over-etched. The decrease in effective thickness of the FM affects its electrical conductivity and magnetic coercive field. The excess etched material can be redeposited on the tunnel barrier resulting in short circuit devices. In order to have full control of the etching depth, in situ Auger electron spectroscopy was employed to study the thin film layers before and after etching.

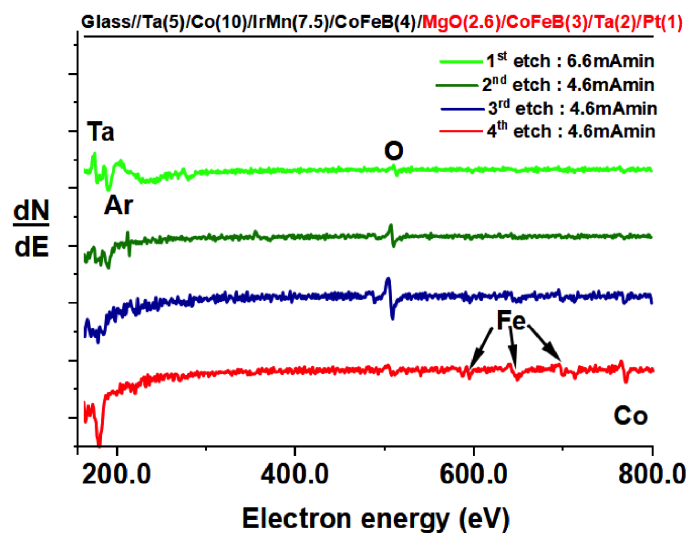


FIGURE 6.4: Auger energy spectra for each etching step of CoFeB/MgO/CoFeB stack. Each color of the graph indicates AES for consecutive steps of etching in mAmin. The Auger signals of the materials in the stack at different etching stages, starting from the lower energy of the Auger spectra Ta : 165eV, 170eV; Ar : 180eV; O : 503eV; Fe : 598eV, 648eV, 701eV, 715eV, and Co : 771eV.

Auger electron spectroscopy (AES): The technique utilizes high energy of finely concentrated electron beam as an excitation source. AES is based on the Auger Effect. The Auger electrons are generated when the excited atoms release the additional energy to an electron which is emitted as an Auger electron. AES operates by collecting and measuring the kinetic energies of the emitted Auger electrons, which corresponds to the respective elements present at the surface of a sample. This allows for the surface chemical analysis of the thin films samples. The typical sampling depth of AES is between 2nm to 5nm, makes it a powerful surface sensitive analytical tool.

An AES system comprises of an electron gun for sample examination and an energy analyzer for detection of Auger electron peaks in the total secondary electron energy distribution. The set up used in this thesis has AES equipped in the etching chamber and utilizes a 3keV energy of electron beam. The detected Auger peaks are usually superimposed on a continuous background, for easy detection the energy distribution function $N(E)$ is differentiated and the Auger spectrum is the function of $dN(E)/dE$. The peak-to-peak magnitude of an Auger peak in a differentiated spectrum can be directly associated with the surface concentration of the element which produces the Auger electrons.

Here, the Auger electrons emitted from the first few nm's of the thin film surface were studied in their kinetic energies up to 1000eV. In the experimental set up the Auger gun and the detector are mounted in different position from the etching gun. In order to perform the AES measurements the sample is transferred to Auger position within UHV conditions. To begin a pre AES spectra is recorded and thereafter, for each etching the spectra is analyzed to determine the successive etching dose.

The Figure 6.4 is an example of CoFeB/MgO/CoFeB stack etched up to the mid of the MgO tunnel barrier. For the first etching of 6.6mAmin strong Ta peaks at (165eV, 170eV) are clearly visible at the lower end of the energy spectrum (Fig.6.4, green). Faint peaks of Co (771eV) and Fe (598eV, 648eV, 701eV, 715eV) appear with traces of Ta, indicating the top Ta/CoFeB interface (Fig.6.4, olive). A strong O signal from MgO is observed at the end of third etching (Fig.6.4, navy). The etching is

stopped when the strong O signal from the MgO decreases and Co and Fe signal increases, confirming the lower CoFeB/MgO interface (Fig.6.4, red). For this sample, a total of 20.48mAmin was required to reach the mid of the barrier. The resist covered regions are not etched and hence 20 micron sized pillars are defined on completion of etching process (Figure 6.5).

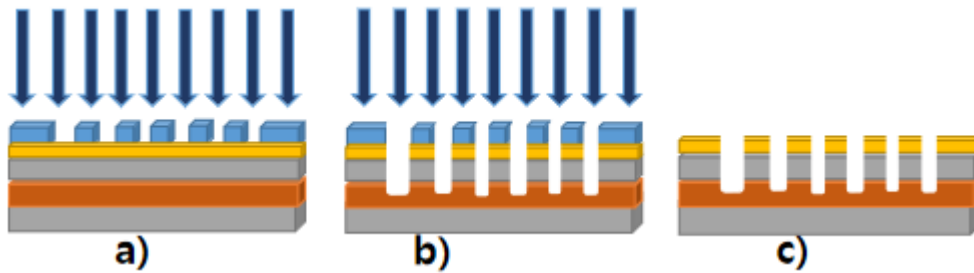


FIGURE 6.5: **Step I etching procedure.** (a) before and (b) after neutral beam etching up to the mid of the MgO barrier, (c) Post solvent cleaned sample with 20micron pillars.

6.1.2.2 Step II : Bottom electrode

Once the pillars are defined, the photoresist from the step I is removed by ultra sonication process using acetone and ethanol solvents for ten minutes each. The bottom electrode is defined using positive resist AZ501 following the same procedure as step I, see Figure 6.6a; except for the photomask pattern is of second step.

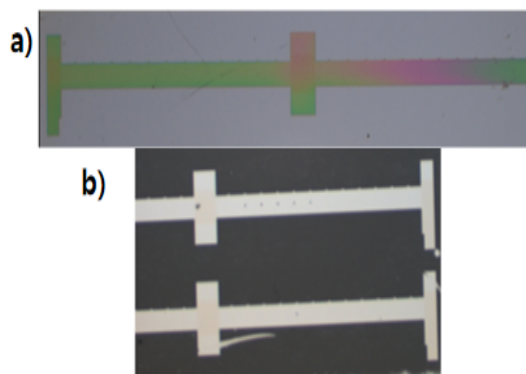


FIGURE 6.6: **MgO bottom electrode.**(a) One of the ten bottom electrode's image defined in the step II. On development, the resist is retained only on the bottom electrode pattern. (b) Post etching and solvent cleaned sample has material only within the bottom electrode pattern (light region); the dark remaining area is glass substrate.

Post development, the sample is etched down to the substrate, and over-etching is avoided for any unnecessary re-deposition giving rise to short circuit devices. The

contact pads allow the current to flow towards the lower electrode which is defined in the current step. Once etching is completed the sample is solvent-cleaned which exposes the bottom electrode with pillars (Figure 6.6b) and is prepped for passivation.

6.1.2.3 Step III : Passivation

Before depositing the dielectric SiO_2 layer, a negative photoresist AZ5214 was coated and exposed with third step photomask pattern. The negative resist deposited sits on top of the areas where the SiO_2 presence was to be avoided i.e., the areas above the pillars which provides the electrical access to the MTJ and the metallic contact pads, see Figure 6.7a. The negative resist forms an overhang after development. The 135nm thick SiO_2 was sputtered to form the dielectric layer similar to the passivation in organic processing.

Lift off: Since the deposited SiO_2 layer has limited adhesion to different materials ultra-sounds cannot be controlled to selectively remove the resist and SiO_2 only from the pillar. So the sample is left in the acetone bath for minimum 2 hours. Thanks to the presence of the resist overhang, the acetone strikes the naked sides (ie.,without SiO_2) of the negative resist layer and dissolves it. The dissolved resist layer carries with it the SiO_2 layer leaving behind an electrical opening in the passivation layer giving direct access to the MTJ, see Figure 6.7b.

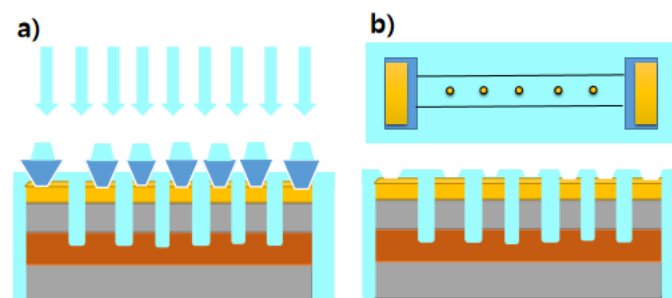


FIGURE 6.7: **Step III - dielectric deposition.** (a) The negative resist on selective development and sputtering deposition of SiO_2 layer. (b) Sample view after lift off process, with the insulating layer (cyan) on top of pillars and contact pads to avoid electrical short circuits. Note in the top inset the color blue is only for a visual contrast to distinguish the beneath layers.

6.1.2.4 Step IV : Metallization

The SiO_2 insulating layer covers the entire sample except for the junction pillar and the contact pads. A negative resist AZ5214 is coated on the sample, on exposure and development the photoresist is preserved all over the sample except the areas where the conductive contact pads are to be deposited, see Figure 6.8a. A metallization is performed on the sample by depositing a bi-layer of Al(110nm)/Au(35nm) in UHV environment (Figure 6.8b). In this step the lift off is easy, as the resist covers large surface area. Short ultrasonic pulses is enough to dissolve the resist leaving behind only the metallic contacts with 12 micron optical opening to the 20 micron sized MgO MTJs, see Figure 6.8c. This completes the processing of MgO MTJs. The samples are ready to be probed and bonded to perform further measurements.

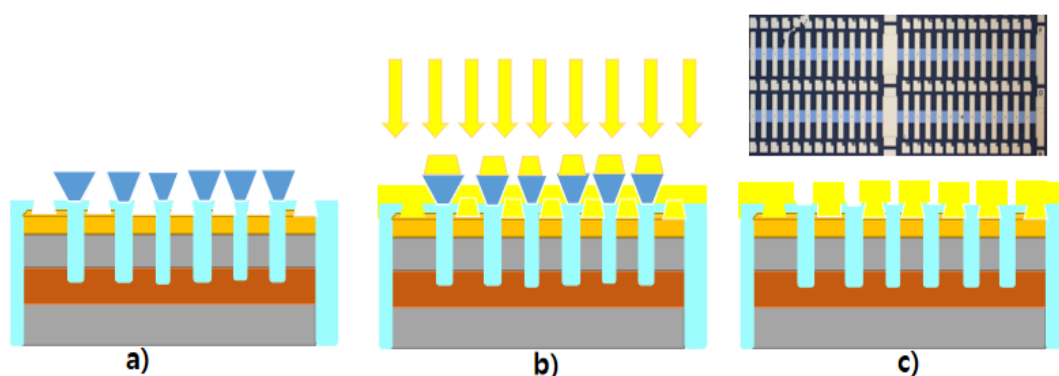


FIGURE 6.8: **Step IV : Metallization.** The final step of the lithography process. (a) The negative photoresist after selective development, (b) metal deposition of Al, Au layers as electrical electrodes, (c) Final sample structure after lift off. The top insert is the real sample image showing top contacts & contact pads (pale color) and little depressions of $12\mu\text{m}$ optical openings to the MTJs. The horizontal bar is the bottom electrode (blue).

The discussed photolithography technique used to fabricate 20 micron sized MgO MTJs is not suitable for molecular stacks because of the solvents and photoresists involved in the processing degrades the organic layers. Therefore, a novel solvent-free, resist-free lithography technique was developed in our group by Dr. Urbain, and refined by L. Kandpal, using silica spheres to produce organic nano junctions, for details see Appendix A. Therefore, the processing will for organic thin films will be discussed separately in the next section 6.1.3.

6.1.3 Processing of organic thin films

Unlike MgO, the bottom electrode patterning is done in situ using shadow masks for molecular stacks as discussed in Chap. 5, Sec. 5.3. The UHV deposited CoPc based thin film stack undergoes a five step processing to create a vertical organic nano MTJ. Since, alignment of masks are done manually good attention to detail is prioritized to achieve high throughput.

6.1.3.1 Step I : Nano-sphere lithography

Using the group's solvent-, resist-free nano junction process 300nm - 500nm silica spheres were deposited on the organic stacks (ex situ). The silica spheres served as masks when deposited on top of the thin films, see Figure 6.9. The area occupied by the silica sphere serves as the effective junction size which is ($\sim 300\text{nm} - 500\text{nm}$), for details of the silica lithography procedure consider reading Appendix A.

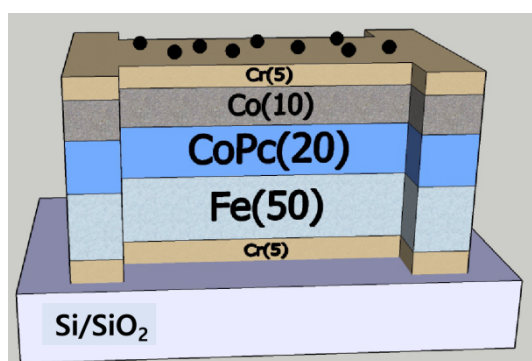


FIGURE 6.9: Illustration of nano sphere (black) deposition on a molecular thin film stack with CoPc spacer.

6.1.3.2 Step II: Patterning nano-pillar MTJs

Similar to the MgO etching procedure, the organic stacks are mounted on the sample holder and the charge evacuation from the sample was done by covering the side pads of the thin film structure with Al foil strips using kapton tape as shown in Figure 6.10a. To begin a pre AES spectra is recorded and thereafter, for each etching the spectra is analyzed to determine the successive etching dose. The graph 6.10b, is an example of the etching sequence followed for a $Fe/C_{60}/CoPc/C_{60}/Fe$ thin film

system. The pre-etch data (blue) displays strong CrO and C peaks at their respective energies. The Cr peaks at 489eV, 527eV, 571eV are from the capping layer, a thin CrO layer is formed due to surface oxidation, oxygen peak at 511eV and a contaminant C peak appears around 266eV. After etching for 103mAmin, all contaminants are removed leaving behind only Cr capping (Fig.6.10b: black). End of fourth etch, the top Fe/Cr interface appears (Fig.6.10b: green). From here onwards small doses are sufficient to reach the mid of barrier. Care is taken not to over/under etch the sample. The etching is complete when the peak ratio of carbon (276eV) from C₆₀ decreases with respect to Fe peak ratio, which is an indication for exceeding the mid of the tunnel barrier (Fig.6.10b: orange, pink, red). Roughly, 22mAmin is sufficient to reach the mid of barrier from top Fe/Cr interface. This completes the etching process. The silica spheres play the role of resist protecting the layer underneath and resulting in the creation of nano pillars, see Figure 6.11. This completes the step II of the organic sample process.

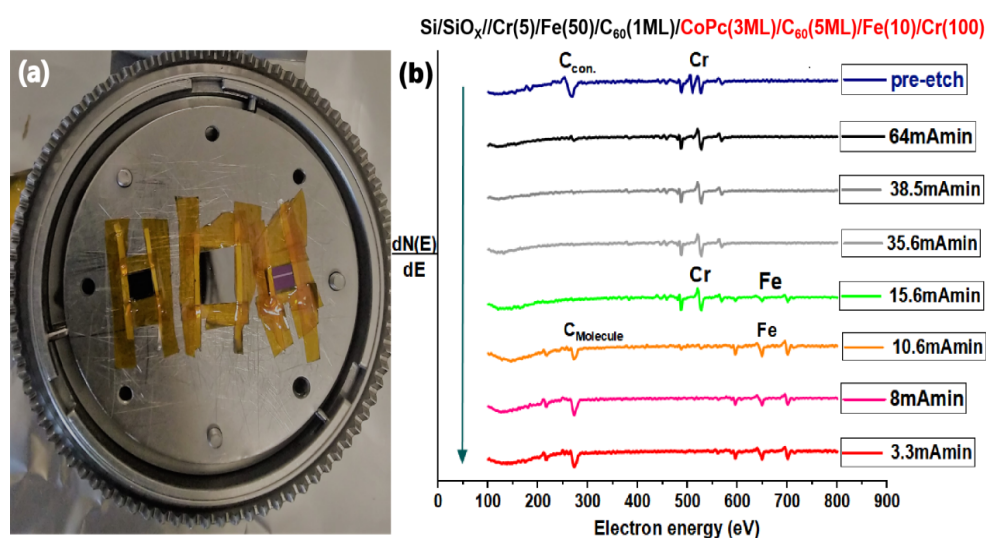


FIGURE 6.10: **Auger spectroscopy on CoPc molecular stacks.** (a) Organic stacks and the reference sample (center) fixed on the sample holder using UHV compatible Kapton tape, ready to be etched. (b) Auger peaks for the sample $Si/SiO_x//Cr(5)/Fe(50)/C_{60}(1ML)/CoPc(3ML)/C_{60}(5ML)/Fe(10)/Cr(100)$. The pre - etching curve has CrO layer peaks and carbon contaminants (266eV). Consecutive etching steps are color coded. After the first etching CrO is removed and only signal is from Cr capping (shades of black). Only after four etchings the top Fe/Cr interface appears (green). The etching is terminated when the C₆₀ signal (276eV) decreases and Fe signal increases indicating lower Fe/C₆₀ interface (red).

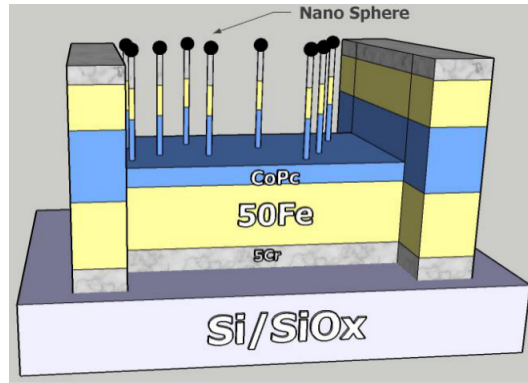


FIGURE 6.11: **Nano-pillars.** Etching process up to mid of CoPc barrier. Al foil protects the side pads during etching (not shown).

6.1.3.3 Step III : Passivation

Once the nano pillars are defined the samples are carefully transported to cleanroom for dielectric deposition. The dielectric SiO_2 is rf sputtered using Alliance concept EVA300+ system. The chamber has a base pressure of $\approx 5e^{-8}$ mbar. SiO_2 thickness greater than 110nm is best to prevent any leakage current (separately tested at 80V) in the devices. The maximum thickness of the dielectric depends on the size of the silica spheres used in patterning. As seen in Figure 6.12a, the spheres have to be half way above so it is easy to lift them off. For instance, a thickness of 135nm of SiO_2 was used with 300nm silica spheres. It is vital to cover the side pads of the thin film during passivation in order have a region available for electrical characterization. For this, thin Al strips were held using kapton tape without disturbing the etched regions and the nano-pillars.

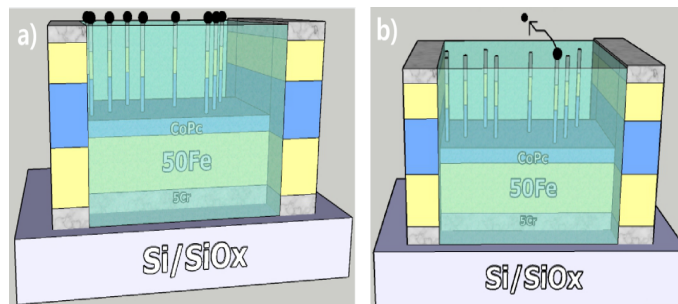


FIGURE 6.12: **Passivation and Lift-off.** (a) The dielectric SiO_2 is deposited every where except the side pads. (b) The nano-sphere are lifted off leaving the naked vertical MTJs.

Lift off : Following the dielectric deposition, the nano sphere lift off procedure was done by supplying ultra sonic shocks to the substrate using hybond wire

bonding machine. Subsequently using a strong jet of nitrogen to blow off the nano spheres, see Figure 6.12b.

6.1.3.4 Step IV: Metallization

The post lift off sample has SiO_2 covering the entire thin film except the side pads and the nano-pillars. The sample is moved to PlassysMEB550S metal evaporation system. The top electrical electrodes are templated on the sample using steel masks designed and manufactured with IREPA laser company. The top contact masks are fixed flat on the sample to define the electrical contacts and care is taken to align the bottom template with the current mask template. A bi-layer of Al(110nm)/Au(35nm) is deposited using e-beam evaporation method. The chamber has a base pressure of $2e^{-9}$ mbar and the deposition pressure of $5e^{-9}$ mbar. The rate of deposition for Al is 0.5nm/s and for Au is 0.2nm/s. Al has a good adhesion to the underlying dielectric layer and is robust to ultra sonic power while wire bonding. Au capping provides best protection against oxidation. This completes the 5-step processing of organic nano devices and are now ready for electrical characterization (Figure 6.13).

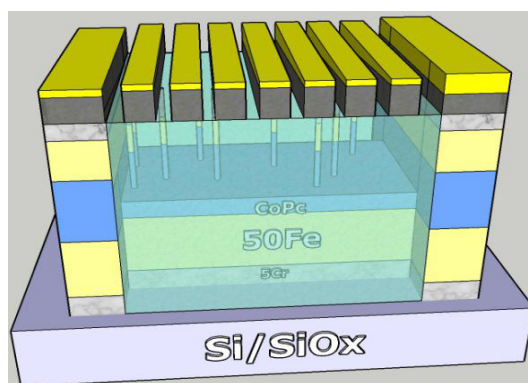


FIGURE 6.13: **Metallization.** E-beam deposition of Al/Au electrical electrodes using shadow mask. The region that includes the pillar and the top contact electrodes form the organic nano device ready to be probed.

6.2 Back-end process

In general, the back end process is the assembly and testing stage. Here, the defective devices are sorted from the non-defective ones. In general, the processing steps could create some defects like metal shorts, or failure in lift-off process, for example, in organic MTJs if the nano spheres are not lifted off, the device would be open circuit. All these defects are screened before wire bonding the devices for the final test stage.

6.2.1 Electrical characterization of magnetic tunnel junctions

The organic shadow mask allows for 23 junctions and the photolithography based MgO has 160 junctions on a single sample. In order to distinguish between the defective and non-defective junctions a probe instrument was used to study their resistances and IV behaviors.

6.2.1.1 Point probe (2-pp/ 4-pp):

One of the most common techniques to measure electrical resistance is two-point (2-pp) or four point (4-pp) probe methods. In a 2-pp mode the two tungsten carbide needles serve as both current and voltage sensing probes. Here, the bottom electrode resistance contribution is always included in the measurement loops and might vary the overall resistance from the individual junction electrodes. In order to have precise measurements 4-pp mode is useful. In a 4-pp, a known value of bias voltage is applied between two probes and the resulting current is measured using the other two probes. The Karl Suss PM8 prober was used to perform 2-pp and 4-pp measurements on organic and MgO devices.

The resistance of bottom electrode and contact resistances were qualified using 2-pp configuration. The resistance of the bottom electrode for both MgO and organic devices depends on the thin film structure and the etching depth during pillar formation. Usually the bottom electrode yields a resistance range of 100Ω to 500Ω . The

4-pp allows to probe the junction resistance (Figure 6.14a). This is advantageous as the current flowing through the cross-section (junction) can be exclusively investigated by exempting the contact resistances. Normally, the top contacts resistance is in the range of $\approx 10\Omega - 15\Omega$ which reasonable for Al/Au combination. It is important to qualify the top contact resistances before bonding the sample, to ensure the continuity of the top Al/Au electrode, especially for organic devices which uses shadow masks. Suppose one of the contacts is somehow open-circuit (cut across electrode, poor bond, etc). In that case, a fake 4-pp method can be used to study the junction see Figure 6.14b. Special care is taken while probing the potential organic energy generating junctions. The Keithley (current, voltage) range is adjusted (eg. 200mV, 10 μ A) to drive least current through the junction. The junction is measured by applying very low bias (forced $V < 0$) and IV is recorded for small voltage range depending on the offset current value. If the IV has a current and voltage offset greater than the experimental set-up then such junctions are noted for further studies. For MgO junctions, the resistance-area (RA) product method is used to statistically analyze the quality of the junctions. The magnitude of the RA products allows to distinguish if the devices are short circuited (-small RA product) or open circuited (-large RA). Nominally, the RA product is in the range $e^7 - e^8 \Omega \mu m^2$ for MgO target sputtered barriers that are 2.5nm thick.

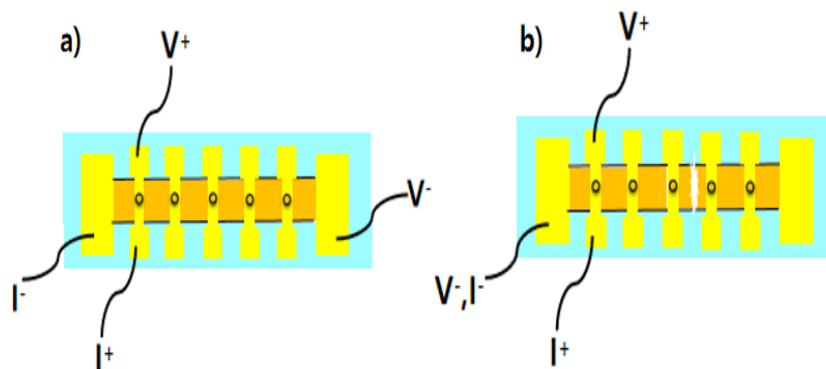


FIGURE 6.14: **Electrical 4-point contact measurement.** (a) Voltage is applied between the top and bottom electrode contacts and the current flow between the separate electrodes are measured. The current recorded is the current flowing through the point of intersection only ie., the MTJ. (b) A fake 4-point contact measurement is useful when there is an electrode which has excessive resistance or has a discontinuity/damage to the bottom electrode (cracks -white color).

6.2.2 Cutting and wire bonding

In contrast to organic MTJs which are fabricated on $(5 \times 7) \text{mm}^2$ cut Si/SiO_x// substrates, the MgO samples are cut after the entire lithography process. To protect the MgO devices the entire sample is coated with photoresist. Then, using a diamond wire saw cutter or Accretech SS10 dicing machine $(5 \times 7) \text{mm}^2$ sized samples are cut and finally solvent cleaned.

The MgO and organic samples are then glued on to Fert (or respective beam-line) chips and wire bonded using Hybond 527A machine available in the STNano platform. While bonding, the sample is electrically grounded to avoid any electrostatic currents that can possibly damage the device. The on chip bonded samples are probed to confirm that the device state has not been disturbed due to wire bonding. Finally, the devices are ready to perform magnetotransport measurements in the group's magnetotransport benches, and device operando studies at Synchrotron SOLEIL.

Chapter 7

Magnetotransport and Operando measurement set-ups

In this chapter we will explore the experimental set-up used to perform magnetotransport measurements at the laboratory and synchrotron beamlines. The chapter discusses the group's Fert set-up and significant sections describe the set-up utilized for device operando measurements in SOLEIL synchrotron's two beamlines HERMES and DEIMOS respectively.

7.1 Introduction to magneto-transport Fert bench

The components of the setup includes a cryostat, two magnets, a sourcemeter (Keithley), a proportional-integral-derivative (PID) temperature regulator, pumping and cooling systems. Thanks to the group's efforts, the setup includes unique enhancements such as: the cryostat equipped with optical windows mounted on a rotation plate, an optical table coupled to the cryostat's ledge, four precision motors for XYZ motion of the cryostat and magnets, and an electrical multiplexor.

The Fert set-up offers several fully and semi-automated operation options for measurement of devices. The wire bonded sample can be mounted in a vacuum environment within the cryostat located between a powerful 2T electromagnet. Low temperature measurements upto 2K can be performed by filling the cryostat with

helium gas. Based on the sample placement within the cryostat in-plane (horizontal) and out-of-plane (vertical) magnetic field measurements can be conducted. A LabView software interface allows to operate the system for automated temperature-dependent studies using multiplexor to switch between samples, control the applied bias, and magnetic fields. Additionally, it is possible to perform magnetotransport measurements for multiple sample-to-field angles. Finally, a precise temperature-dependent current-voltage characteristics and resistance-field plots can be performed which can provide information about the samples quantum nano-objects in the device and also the magnetic orientation of the ferromagnetic electrodes.

7.1.1 Operation cycles of the cryostat

The operating cycle of the cryostat is based on the Grifford-McMahon (GM) cycle [200] which has the following components cold head (or expander), also a chamber where the gas can be compressed/expanded, a regenerator - its porous system through which the gas can flow back and forth, a displacer (piston), low and high pressure valves, a rotating valve and lastly a motor to drive the displacer. In our cryostat the regenerator and displacer are merged. A compressor usually supplies the cold head with a high pressure and the rotating valve allows for pressure variation by open and close movement of the high pressure inlet and low pressure exhaust. This is carefully in sync with the motion of the displacer. Generally, the GM cooling cycle is divided into four stages, they are :

1. **First stage** : In this stage the GM cycle begins with the displacer-regenerator down so the high pressure inlet is opened allowing the high pressure He to fill the upper section of the chamber. The entire system is at room temperature (Figure 7.1a).
2. **Second stage** : When the high pressure line opens, the displacer-regenerator starts to move upwards forcing the gas through the regenerator, see Figure 7.1b.

3. **Third stage** : When the displacer is up, the high pressure valve is closed and the low pressure valve is opened. The high pressure gas in the lower part of the chamber is able to expand and cool due to Joule-Thomson process. Certain amount of gas is forced to exhaust through the regenerator and thus generating work. This is main cooling step, see Figure 7.1c. The direct thermal contact with the gas drives the heat out of the cold finger.
4. **Fourth stage** : In the final stage, the displacer moves down forcing the gas to discharge through the regenerator. This process cools the regenerator and in return the regenerator cools the gas in stage two (Figure 7.1d).

The system is cooled by the systematic repeating of this cycle. In a multiple stage GM cooler, every stage is fed with low pressure gas from the earlier stage, and all the displacer-regenerators move in sync. Our groups cryostat has two stages. The first stage allows to reach a temperature of 80K which cools the radiation shield and in the second stage the temperature reaches $\sim 2\text{K}$ cooling the cold finger.

The GM cryocoolers are advantageous as they can operate in a closed loops and can be used for long term without additional maintenance or He refill. They are cost efficient and user friendly. A few drawbacks of GM coolers is these are mechanical refrigerators so one can always expect vibrations induced due to the motion of the rotating valves and the displacers. Usually, the vibrations are in the range $20\mu\text{m}$ (parallel) - $5\mu\text{m}$ (perpendicular) to the axis of the cold finger. For sensitive experiments this could be troublesome. In our case the cryostat uses internal pressure differential to move the displacer, which reduced the general vibrations of the whole structure. The system also has pneumatic anti-vibration columns installed to further decrease the vibrations transmitted through the mounting flange to the optical table.

7.1.2 The group's magneto-transport bench

Our group's cryostat operates by a pneumatically driven two stage Grifford-McMahon refrigerator [200] (Figure 7.2). The set-ups major component is the expander (/cold head) because this is zone where the cooling occurs. A cold finger is in direct contact

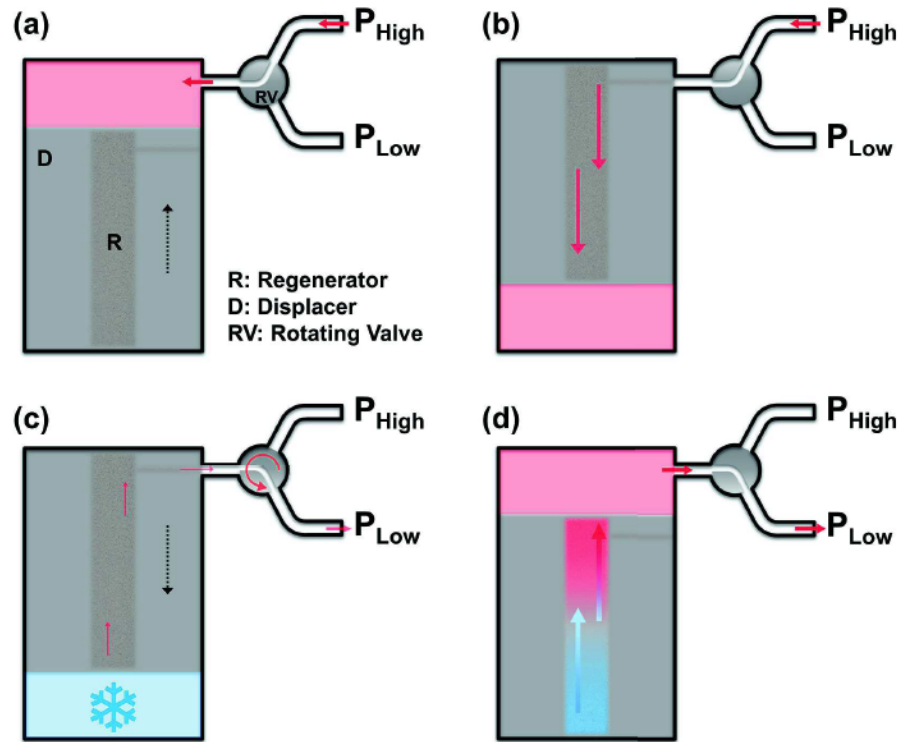


FIGURE 7.1: **Visual representation of the Gifford-McMahon cycle:** (a) High pressure gas line is opened (b) the displacer D shifts to the upper position, forcing the high pressure He gas to the lower part of the chamber via regenerator R. (c) the rotary valve RV, opens the low pressure gas line and the gas extends and cools down due to Joule-Thomson process. (d) the displacer now reverts to its initial position and the cold gas is forced out of the regenerator. This cools the regenerator and leaves the cold head at near room temperature.

Image borrowed from Ref [201].

with the stage two of the expander and is cooled upto 4.2K. A protective radiation shield which safeguards the cold finger from room temperature thermal radiations is fastened to the expander's stage one. This is cooled to 77K thanks to the 77K shield. Lastly, a vacuum shroud is fixed vertically which enclose everything in place. Both radiation shield and vacuum shroud are designed to accommodate optical access to the vertical sample. Almost 34 fragile copper wires are electrically connecting the sample holders, with two temperature sensors and the heater.

To perform temperature dependent magnetotransport measurements with accurate quantitative values it is necessary to have a robust control system. A resistive heater located near the second stage of the expander enables the temperature control. The heater is coupled to a Lake Shore cryotronics 332 PID controller. The two sensors allow for temperature reading at two spots of the cryostat. First one is on the

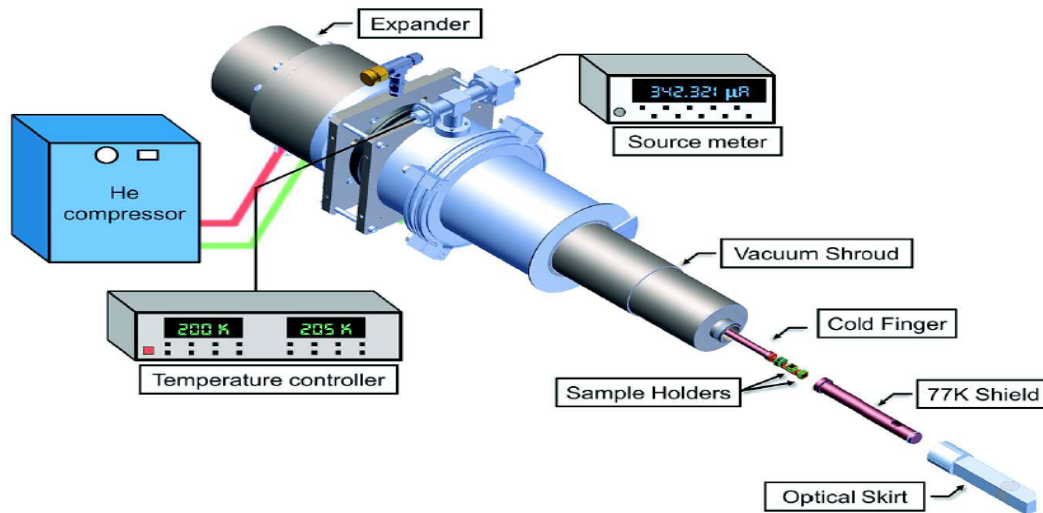


FIGURE 7.2: **Experimental Fert magnetotransport bench based on Grifford-McMahon cryostat.** The set-up is made up of a cryostat, temperature controller, Keithley sourcemeter, sample holders - vertical (top chip) and horizontal (bottom chip), gold coated 77K shield, optical shroud. Other components like PC with LabView control program, electrical multiplexor, magnets, motors, optical bench and its elements are not illustrated here. Image is adapted from Ref [201].

heat station of the second cooling stage top of the cold finger. Second one is present in the end of the cold finger, next to the sample holders. It is the latter that gives the closest value of the real sample temperature.

To get a feel for how readings are recorded from the sample its good to quickly understand the electrical part of the system. There are 24 wires which are connected to the sample holder that enable the electrical contact to the sample. This essentially allows to connect 10(5) devices in two (four) points mode. The connector of the wires is plugged to an electrical multiplexor [202]. So one can imagine multiplexor as a relay between the Keithley and the sample which allows to switch routinely between the devices connected on the sample. This helps to perform automatic measurements on multiple samples. Thanks to the systematic automation of the system using advance LabView programs it is convenient to perform $I(V)$, $R(H)s$, $R(T)s$. For detailed information on set up calibration readers can refer U.Halisdemir thesis [201]. The results presented in the Chapter 8 was performed using this Fert bench set-up.

7.2 Synchrotron based experiments

In this section a brief introduction to synchrotron based experiments performed during the course of this thesis is provided. The study utilizes various x-ray based physical fundamentals such as x-ray absorption spectroscopy (XAS), x-ray magnetic circular dichroism (XMCD), scanning total electron yield microscopy (STEYM) and operando scanning x-ray microscopy (OSXM). A good amount of the section covers all the necessary tools required to understand how the experiment is performed. Ending with a quick overview of the SOLEIL French synchrotron beamlines namely DEIMOS and HERMES which was utilized to perform device operando studies on molecular and MgO MTJs, respectively.

7.2.1 Introduction to synchrotron facility:

The fundamental idea behind the synchrotron was first realized by Oliphant [203] in 1943. A year later Veksler [204] independently discovered the new method of accelerating relativistic particles and Ed McMillan [205] coined the term synchrotron in 1945. The electromagnetic radiation called synchrotron radiation is emitted when charged particles are accelerated along a curved trajectory. Large scale facilities, namely a synchrotron machine (or synchrotron), are used to accelerate electrons to very high energy and these electrons are moving very close to the speed of light [206]. The Figure 7.3, gives a basic overview of the French SOLEIL synchrotron facility in the Paris area. Electrons are generated by the electron gun located in the center of the synchrotron. These electrons are accelerated to high speeds close to the speed of light by a linear accelerator or linac Figure 7.3[a]. Then the electrons are transferred to the booster ring Figure 7.3[b], where their energy is increased from 100MeV to 2.75GeV. Finally these high energy electrons are transferred to the outer storage ring Figure 7.3[c]. A series of magnets guide the electrons in circular path around the storage ring. As the electrons are deflected through the strong magnetic fields, they emit electromagnetic radiation that is manipulated by the bending magnets or insertion devices like wigglers, undulators located in the straight section of the storage ring. In the regions where the electrons change their direction,

synchrotron light is generated and this radiation branches off the storage ring and enters the beamlines. In the beamlines, this radiation is further refined with the help of monochromators and mirrors before it impinges on the sample under study.

A third generation synchrotron uses undulators as insertion devices. They are characterized by the *brilliance* of radiation produced by an undulator. The brilliance is defined as the number of photons emitted per second, per photon energy bandwidth, per solid angle and per unit source size. Usually, a third generation synchrotron has a brilliance of $10^{15} - 10^{21} \text{ photons}/(\text{s.mrad}^2.\text{mm}^2.0.1\%BW)$, which is beyond the possibilities of any laboratory-grade source.

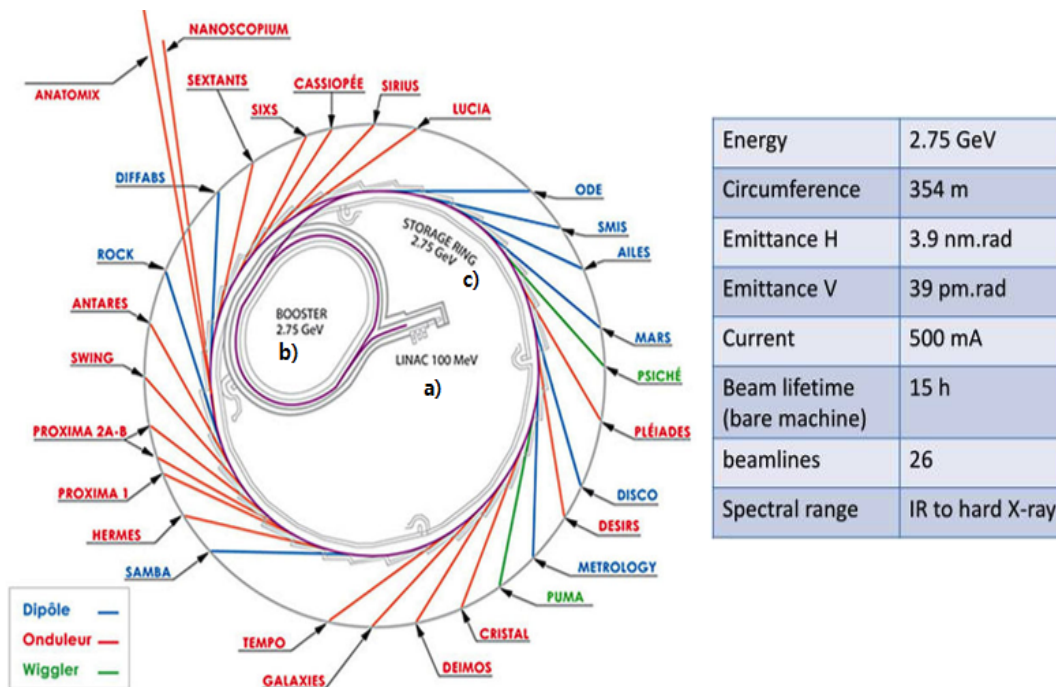


FIGURE 7.3: Outline of SOLEIL synchrotron facility is a 3rd generation source in Paris, France. Image adapted from Ref [207].

To summarize, there are several advantages of using synchrotron beamlines in comparison to the laboratory equipment. They offer high brilliance, wide-energy tunability, intense collimation and the emitted radiation is highly polarized linear, circular or elliptical and is tunable from infrared regime up to hard x-ray. The synchrotron-based experiments presented in this thesis utilized a third generation synchrotron SOLEIL's two technologically developed beamlines HERMES and DEIMOS, respectively.

7.2.2 Physics of X-ray absorption spectroscopy (XAS)

X-ray absorption spectroscopy is a powerful technique that is widely used to examine the atomic local structure and the electronic states of the samples [206]. The x-rays uniquely interact with the matter depending on the incident energy of the x-ray photons. Some of the prominent phenomena absorption, Rayleigh scattering, Compton scattering, see Figure 7.4, here we will only focus on x-ray absorption. When high energy ($\approx keV$) x-ray photons strike an atom, the core electron is either excited to a higher unoccupied energy level (LUMO) or unbound state known as the continuum. The former excitation is known as x-ray absorption near-edge (XANES) and the latter is known as x-ray absorption fine structure (EXAFS). The intensity of the XAS spectrum is given by the Fermi golden rule[208]. The probability of an excitation drastically increases when the energy of the incident x-ray photoelectron is equivalent to the binding energy of the core electron. This is referred as an *edge* in XAS. XANES and EXAFS are the two x-ray absorption edges; the former occurs in the range 50eV-100eV and for EXAFS it is several hundreds to $> 1000eV$ above the edge.

The edges in XAS follow a standard nomenclature, which uses the principal quantum number of the respective excited core electron. For example, $n=1$ corresponds to the K-edge, $n=2$ for L-edge, $n=3$ its M-edge and so on. The L-edge spectroscopy is more sensitive to electronic, structural and changes in spin states of the sample compared to the K-edge spectroscopy. The soft x-ray excitations provide strong resonance signals due to the dipole allowed transitions ($\Delta l = +1$) into the valence magnetic state. This region includes the 3d transition metals (Fe, Co), L- edges ($2p \rightarrow 3d = L_{2,3}$) and rare earths (lanthanides) M - edges ($3d \rightarrow 4f = M_{3,4}$), which are relevant for magnetic studies.

The excitation of core electrons in the atom requires very high x-ray energy $> 10^3 eV$. XAS is highly sensitive thanks to its element specificity obtained by tuning the energy of the incident x-ray photons to the resonance energy of core to valence shell transition. Hence, XAS is widely used to distinguish between the different layers in a thin film composed of diverse elements. In addition, it also enables to

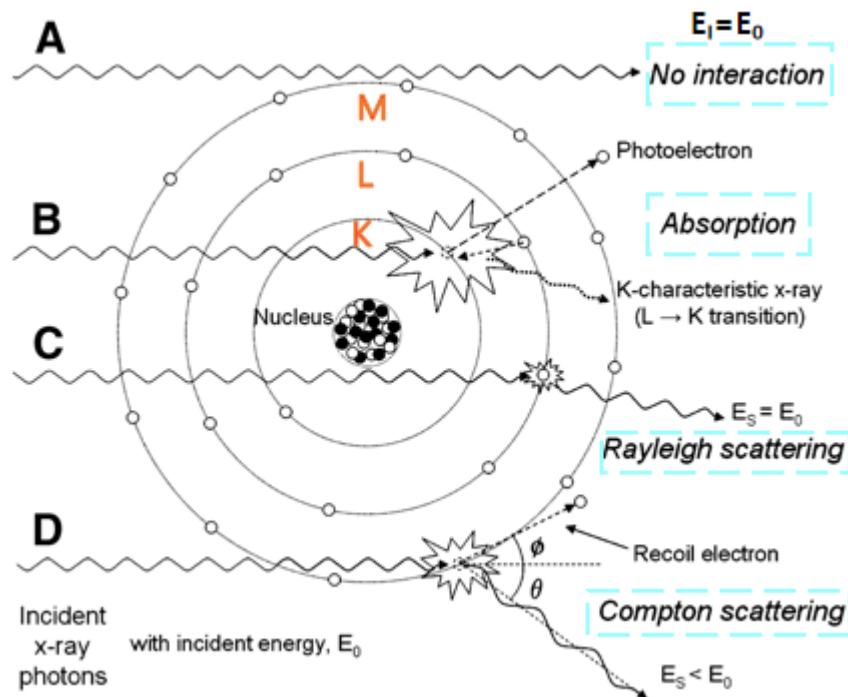


FIGURE 7.4: **Illustration summary of x-ray photon interactions with an atom.** A) The primary, attenuated x-ray beam does not interact with the matter. B) The high energy x-ray photons interact with the core electrons and transfers all its energy to the electron and subsequently the electron is ejected from the atom (photoelectron). The vacancy created in the core shell K by the loss of electron is filled by the other electron shells' resulting in the respective absorption lines. C) Elastic collision with a bound outer-shell electron leads to Rayleigh scattering. D) Inelastic collision with weakly bound outer-shell electron results in Compton scattering. E_I is the energy of the transmitted photon and E_s is the energy of the scattered photon. Image is adapted from Ref [209].

identify unequally populated zones which can be used to spatially map the respective elements in the sample.

7.2.2.1 The absorption coefficient $\mu(E)$

XAS is a technique to measure the linear absorption coefficient. When a narrow x-ray beam of incident intensity I_0 is impinged on a sample at 90° angle, I_0 experiences an exponential decay, see Figure 7.5. The x-ray intensity attenuation is given by,

$$I(d) = I_0 e^{-\mu(E)d} \quad (7.1)$$

where, I is the final intensity of the incident X-ray I_0 , $d(\text{cm})$ is the thickness of sample that is irradiated. For a uniform thickness of the sample, a plot of $\mu(E)$ vs. incident x-ray energy gives a fingerprint of the chemical character and electronic structure of the sample. The factor $\mu(E)(\text{cm}^{-1})$ is known as the linear x-ray absorption coefficient. $\mu(E)$ can be related to the x-ray absorption cross-section σ_a by the relationship:

$$\mu(E) = \rho_o \sigma_o = [N_A/A] \rho_m \sigma_o \quad (7.2)$$

where ρ_a is the atomic number density, ρ_m is the atomic mass density, N_A is the Avogadro's number, and A is the atomic mass number. The linear absorption coefficient has a characteristic value depending on the element and the number of atoms that are along the path of x-ray beam[210, 211]. Often, the x-ray mass absorption coefficient, $\mu(\text{cm}^2/\text{gm})$, is used, since it is independent of material density and is given by:

$$\mu_m = \frac{\mu(E)}{\rho} \quad (7.3)$$

The x-ray attenuation length λ is the inverse of the linear x-ray absorption coefficient, $\lambda = 1/\mu$. This is one of the limiting factors in synchrotron grade experiments, especially for strongly attenuated soft x-rays. Therefore, it might be useful to calculate the x-ray attenuation lengths of the materials used in the sample for a given photon energy. This can help to have a strong signal intensity for all the buried elements in the heterostructure.

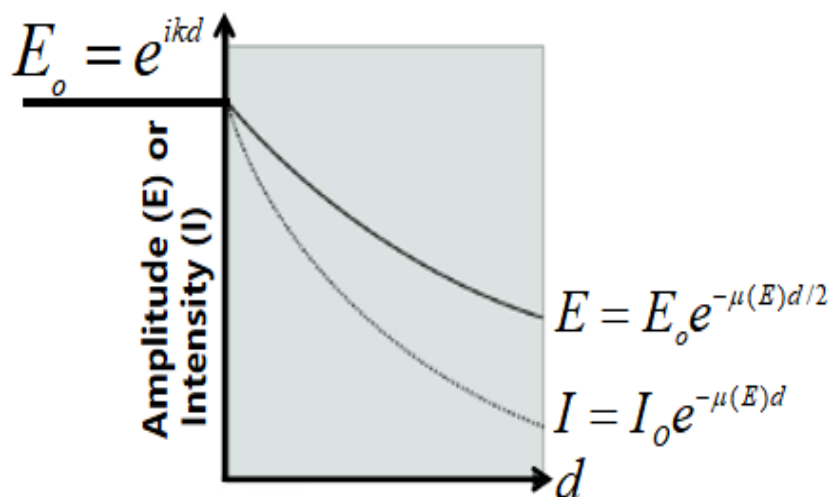


FIGURE 7.5: **Schematics of attenuation of x-ray photons.** The incident x-rays with intensity (I_0) when travelling through a material exponentially attenuates as $E = E_0 e^{-\mu(E)d/2}$ due to absorption. The factor $\mu(E)$ is the linear absorption coefficient and d is the distance travelled in the material by the x-rays. Figure redrawn from Ref [206].

7.2.2.2 Information extracted from XAS

The complex nature of interaction between the sample and incident x-rays results in several distinct features in the XAS spectrum. The x-ray absorption spectra of materials are characterized by a sharp rise in absorption at specific x-ray photon energies. These abrupt peaks in absorption are termed as absorption edges. The structure of absorption peaks can be interpreted as the electronic transitions to the unoccupied molecular orbital (LUMO) above the Fermi energy. An absorption edge allows to identify various elements.

The x-ray absorption spectra of isolated gas atoms show sharp rise and a smooth curve. For atoms in a solid and liquid show discontinuity even after the absorption

edge. After a close examination of these edges, it is clear that it is not simply a discontinuous rise in absorption. Instead, the edge displays a rich structure both in the immediate proximity of the edge jump, as well as above the edge [212, 213]. The Figure 7.6 represents a typical x-ray absorption spectra including the two spectral regions XANES (or NEXAFS: Near-edge X-ray Absorption Fine Structure) and EXAFS. The technique with the combination of XANES and EXAFS is known as x-ray absorption fine structure (XAFS). The XAFS measurements can provide direct structural information of any form of matter, isotope and spin state, and also determines the oxidation state of the element.

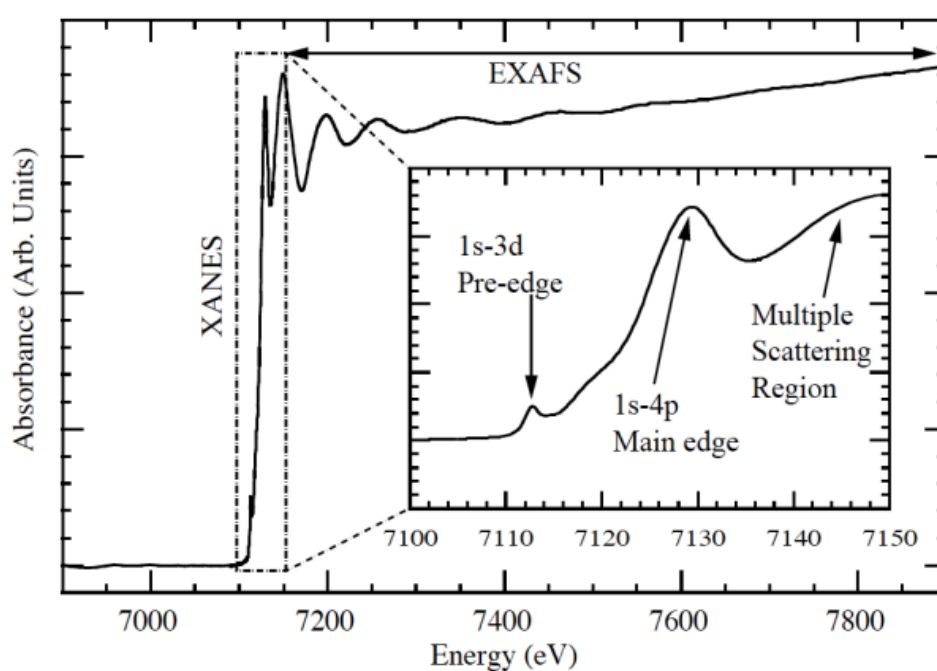


FIGURE 7.6: **XAS measurement near Fe K edge** illustrating the XANES and EXAFS of a typical X-ray Absorption Fine Structure (XAFS) spectrum. The insert describes the three regions of XANES spectra. Image adapted from Ref [214].

The XANES region provides wealth of information about the geometry and electronic structure of the absorbing atom. Since, a photo-electron is excited into an unoccupied orbital XANES mainly provides insight about the sample's unoccupied energy states. XANES can be analyzed in three sections, see inset of Figure 7.6.

1. The **pre-edge** intensity gives information on the covalency and electronic structure of the respective species under study.

2. At the **edge**, the oxidation state and site symmetry of the element can be extracted. The energy of the edge location does not vary for a given element, instead the peak shifts with the corresponding electron density.
3. In the **post edge** the coordination shells are examined as the emitted photoelectron scatters off the neighbouring atoms.

At higher energies, the scattering of the excited photoelectron from the neighboring atoms result in EXAFS fine structure due to the constructive and destructive interference of the excited and scattered electrons, see Figure 7.6. The EXAFS region provides local structural information such as types of ligands, distances to ligands and coordination number i.e., the respective neighboring atoms from the absorbing element [215, 216]. Some of the drawbacks of XAFS are that it is not compatible for bulk spectroscopy, gives little angular information, applicable only for local structural information and always requires a synchrotron x-ray source.

7.2.2.3 Detection methods of XAS

X-ray absorption spectra is measured by three methods, namely transmission, total electron yield (TEY) and total fluorescence yield (TFY). The choice of preferred detection method depends on the sample thickness and the concentration of the element being probed.

7.2.2.3.1 Transmission mode is performed by measuring the intensity of the incident x-ray beam before and after the transmission through a thin film. Conceptually this is one of the simplest methods as it is a direct measure of the x-ray absorption cross section of a sample using the Beer-Lambert law [210], see equation 7.1. Suppose the x-ray penetration depth exceeds the thickness of the sample d at all respective energies E , then the linear x-ray absorption coefficient $\mu(E)$ is a direct measure of the ratio of incident to transmitted intensity of x-rays. By solving the equation 7.1 we get the following $\mu(E)$ for the transmission mode.

$$\mu(E) = -\frac{1}{d} \ln \left(\frac{I_1(E)}{I_0(E)} \right) \quad (7.4)$$

Conventionally, the transmitted intensity is recorded using a photodiode or a channel-plate detector mounted along the beam direction. Transmission mode measurements work well with hard x-rays. However, for soft x-rays, this technique requires optimizing the sample thickness, which should not vary over the surface of the x-ray beam spot. In addition to this, nearly transparent samples which are sufficiently thin are important. Otherwise, the soft x-rays will be strongly attenuated. Since this method is quite restrictive, techniques like TEY and TFY are used which mostly rely on the by-products of the x-ray absorption.

7.2.2.3.2 Fluorescence yield is an indirect way to determine the absorption cross section is to measure the emitted photon directly using the total fluorescence yield (TFY). TFY is often employed parallel to TEY mode. Due to the long mean free path of the photons, TFY provides crucial information about the bulk of the sample with a probing depth $\approx 100\text{nm}-200\text{nm}$. When a high energy x-ray photon interacts with an atom, it promotes the core electron to an empty state near the Fermi level. The resulting vacancy in the core shell has a lifespan of femto seconds [217]. As shown in the Figure 7.7, there are two possibilities to fill the core hole. One is to emit a fluorescence x-ray photon, see Figure 7.7a; or to eject one or more Auger electrons with high kinetic energy (Figure 7.7b). The probability of either of their occurrence depends on the respective atomic shell involved and the atomic number of the atom [218, 219, 220]. By using an x-ray detector like a photodiode or a channeltron, the total yield of photons escaping the sample can be measured.

The different fluorescence lines are illustrated in the Figure 7.8. The $K\alpha$ spectral line is a characteristic energy of the emitted photon emitted when the electron vacancy in the K-shell is filled by an electron from the L-shell. When the K shell vacancy is filled by the electron from M-shell, the characteristic energy of the photon emitted is known as $K\beta$ line. The filling of K shell by an electron from L and/or M

shell creates an electron vacancy in the corresponding L and/or M shell, thus catalyzing an electrical flow, as electrons in the M and N shells emit photons in order to fill in the vacancies of the lower energy shells. In the fluorescence mode, the sample is fixed at a 45° angle relative to the incident x-rays, and the detector is located at right angle to the incident beam to collect the fluorescence x-rays. Even though TFY mode is bulk sensitive, it is limited by the self-absorption process, meaning the emitted photon during the radiative relaxation is reabsorbed by another atom. This results distortion of line-shape and poor intensity of the TFY spectrum.

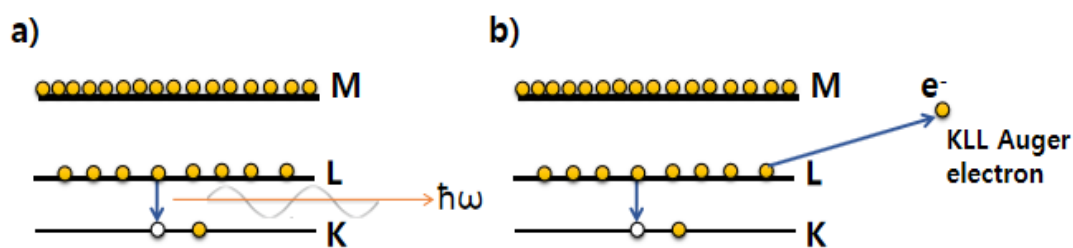


FIGURE 7.7: Schematic describes two possible ways to fill in the core hole (white sphere) created due to the excitation of the core electron due to interaction with high energy x-ray photon. (a) A radiative recombination leading to emission of a photon ($\hbar\omega$), (b) an Auger process backed by the emission of a photoelectron.

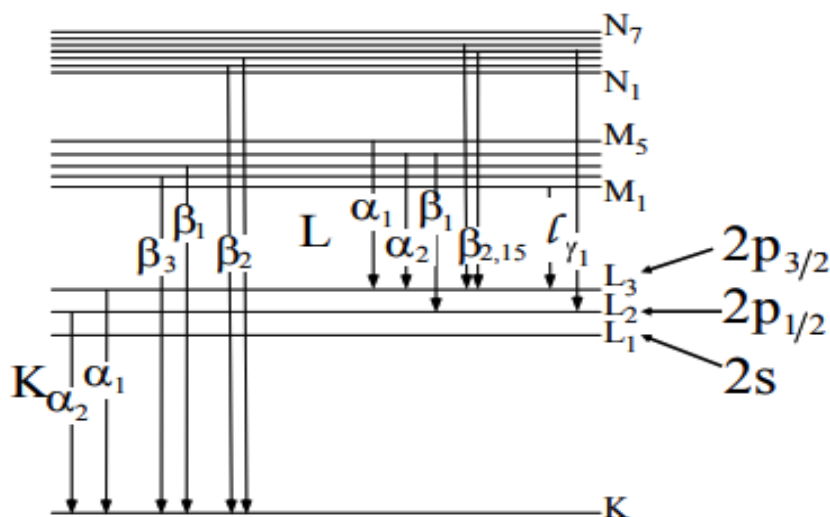


FIGURE 7.8: X-ray fluorescence lines formed by K, L, M and N shells of an atom. The splitting of higher energy shells L, M and N is due to spin orbital interaction. For example, the 2p state splits into $2p_{1/2}$ and $2p_{3/2}$ energy levels. The different positions of the bars correspond to the different occupation numbers of the $2p_{1/2}$ and $2p_{3/2}$. Same logic is applicable to other higher energy levels. Information taken from Ref [221].

7.2.2.3.3 Total electron yield is another indirect method to measure the absorption process. The TEY signal consists of total number of electrons which includes the contributions from photoelectrons, primary Auger electrons and low-energy secondary electrons emitted from the sample. In the TEY mode, the decaying excited electron may transfer its energy to a bound electron instead of emitting a photoelectron. When the bound electron is near the surface material it may be ejected from the thin film. This results in a net positive charge on the sample. For an electrically grounded and conductive sample, a current flows into the sample and fills the vacancies created by the aforementioned electron cascade and this current is used to measure the total electron yield. This method is practical because it requires only a sensitive ammeter connected between the ground and the sample. The TEY mode is highly surface sensitive with sampling depth ($\approx 3nm$) and hence, requires atomically clean sample surfaces [222]. TEY mode is best suited for mono-layer coverage. One of the drawbacks of the TEY technique is that the escape depth of the detected particles must be shorter than the mean absorption length, else it results in saturation effects which causes weak edge intensities and can hinder the quantitative analysis of the XAS spectra. Furthermore, TEY measurements are also sensitive to surface charge. Therefore, on non-conductive surfaces there can be some charging effect which can induce distortions in the TEY spectrum.

Altogether, the descending order of the mean probing depth for XAS measurements is, $TFY > TEY > \text{partial electron yield} > \text{ion yield}$. Irrespective of the type of sample under detection, both TEY and TFY have their own advantages and drawbacks. Interestingly, TEY and TFY show dependence on a atomic number Z and the absorption edge [223]. The Figure 7.9, demonstrates the impact of TEY and TFY at K-edge and L_3 -edge for different Z values. At the K-edge, the light elements ($Z < 20$) gives a strong signal in TEY mode than in TFY and vice-versa for heavy atoms ($Z > 20$). Similar contribution of TEY and TFY is observed for the L_3 -edge but with a dominating TEY up to $Z=87$.

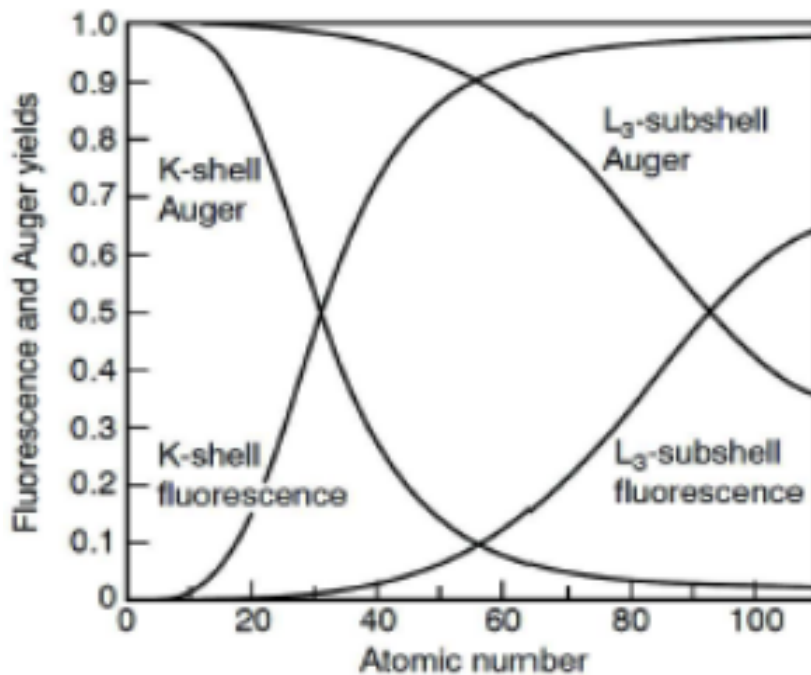


FIGURE 7.9: TEY and TFY dependence on the atomic number (Z) of various elements at K- and L_3 - edge. Image adapted from Ref [224].

7.2.2.4 X-ray magnetic circular dichroism (XMCD)

In general, x-ray absorption spectroscopy is carried out using polarized synchrotron radiation. In a synchrotron, the polarized x-rays originate from the bending magnets or the insertion devices along the storage ring. Similar to visible light, x-rays can be categorized as linearly polarized (LP) used in x-ray magnetic linear dichroism (XMLD), right circularly polarized (CR) or left circularly polarized (CL) used in x-ray magnetic circular dichroism (XMCD). A linearly polarized light can detect any anisotropy in the electronic charge in a sample; and the circularly polarized x-rays can measure the spin and orbital magnetic moments. XMCD is described as the difference spectrum of the x-ray absorption spectra acquired with CR and CL x-ray photons in an external magnetic field. One can imagine XMCD as the x-ray equivalent of Faraday or Kerr effects which occur in the optical regime.

Here, we focus on XMCD as it provides details on element-specific micro-scale origin the magnetic anisotropies such as magneto-crystalline effect, easy magnetization direction, magnetostriction, magnetic hysteresis and coercivity of a thin film.

The basis for XMCD is the fact that the density of the occupied states for a magnetically ordered material depends on the spin configuration. Therefore, any interaction of the left or the right circularly polarized x-ray photons with magnetic substance will give rise to a different transition probability [225]. XMCD has a surface sensitivity approaching better than 0.01 mono-layer and spatial resolution of tens of nm based on the incident x-ray spot size. Thanks to the simple detection methods like TEY and TFY, XMCD has been widely used to perform element specific studies.

XMCD is the only element specific technique that is able to draw a distinction between the spin and the orbital magnetic moments. This technique is powerful to independently determine the values and direction of the spin for each element of the sample on a per atom basis. For x-ray absorption, a circularly polarized x-rays propagating along the direction of macroscopic magnetization is used and depending on the x-rays helicity chosen, the photon angular momentum $+\hbar$ or $-\hbar$ is transferred to the sample once the photon is absorbed. This makes the XMCD technique a vector magnetometry where the dichroic intensity is proportional to the wave vector direction k and the magnetization of the sample \mathbf{M} , $(k \times \mathbf{M})$. The absorbed photon cannot directly couple to the electron spin, it is guided by a finite spin-orbit energy. For instance, in 3d transition metals the dipole selection rules allows for transitions from $2p_{3/2,1/2}$ ground states to the unoccupied 3d states by spin selectivity. The exchange splitting of the unoccupied 3d states creates an imbalance of empty states, which promotes a spin selective absorption and thus the information on spin polarization of the 3d states can be obtained.

7.2.2.4.1 One electron theory A two-step approach is often used to describe XMCD in a one-electron model [226]. In this model the absorption process occurs in two steps. In the first step of the absorption process, the circularly polarized x-ray photons partially transfer their angular momentum to the p-shell electrons through spin-orbit coupling (SOC). This results in the spin-polarization of the excited photoelectrons with a sign opposite to the helicity of the incident x-rays. The core shells can therefore be imagined as atom-specific, localized source of spin polarized electrons. Due to the opposite sign of SOC at energy levels $2p_{1/2} (l + s)$ and $2p_{3/2} (l - s)$,

the spin polarization for the two edges L_3 and L_2 have opposite signs (Figure 7.10). However, the spin polarization axis stays along the direction of the photon propagation direction k . Note that in the process of absorption of circularly polarized light, in addition to $\Delta l = +1$ another selection rule $\Delta m_l = +1$ should also be fulfilled, where Δm_l depends on the helicity of incident x-rays. The photon absorption process in terms of the x-ray helicity contribution is given as:

$$I^\pm = I_0^\pm e^{-\mu^\pm x} \quad (7.5)$$

where μ^+ and μ^- indicates the absorption coefficient for CR and CL x-rays. Hence, the spin polarization is highly dependent on the edge and the polarization of the incident x-rays. At L_2 edge the left circular polarized x-rays excites 25% spin up and 75% spin down electrons which is in contrast to the right circularly polarized x-rays. At L_3 edge, 62.5% (37.5%) spin up electrons and 37.5% (62.5%) spin down electrons are excited by μ^- (μ^+) x-rays respectively.

For a non magnetic material the total spin transition intensities are the same for CL and CR x-rays. Ferromagnetic, paramagnetic and ferri-magnetic materials have an imbalance in the number of available empty spin up and spin down electron states (Figure 7.10a). The absorption of the CL(μ^-) and CR(μ^+) x-rays will be with therefore be different and will have a difference which is opposite at L_2 and L_3 edges.

In the second step of the one-electron theory, the excited spin polarized electrons have to find its place in the unoccupied 3d band, and suppose there are less spin up than spin down vacancies then the XMCD spectra has a net negative L_3 edge and a positive L_2 edge peak. The XMCD difference ($\mu^+ - \mu^-$) is the intensity difference of the normalized XAS spectra to the atomic cross section, recorded for a parallel and anti-parallel magnetic orientation of the sample against the photon spin. This XMCD difference signal is directly proportional to the atomic magnetic moment strength and the magnetization along the k wave vector making it suitable for ferro-, ferri- and para-magnetic materials.

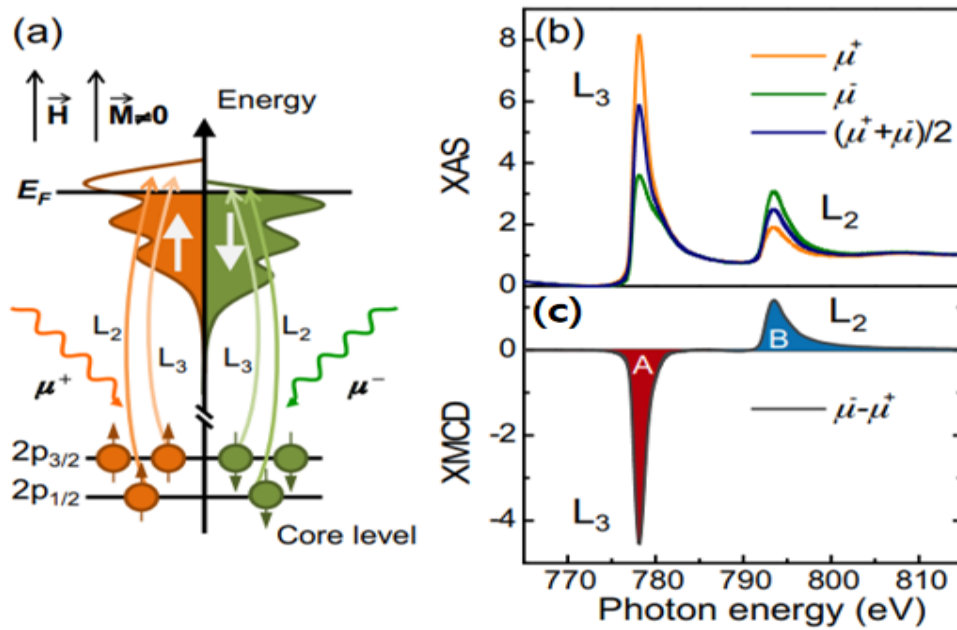


FIGURE 7.10: (a) Figurative representation of the two step picture of XMCD for a single electron in excitation process considered for a magnetic material. In the first step a circularly polarized x-ray photon causes excitation of a spin polarized electron from the spin-orbit split 2p level. (b) XAS and (c) XMCD spectra of cobalt at L_2 and L_3 edges for right (μ^+) and left (μ^-) circularly polarized x-rays. Image taken from Ref [227].

The XAS and XMCD spectra acquired at $L_{3,2}$ -edges of cobalt is described in Figure 7.10b,c. The two circular polarizations μ^+ , μ^- results in x-ray absorption process with spectral intensity high(low) for μ^+ (μ^-) at L_3 -edge and the converse at L_2 -edge, see Figure 7.10b. The resulting XMCD spectrum for Co has negative(positive) sign at the $L_3(L_2)$ -edge as shown in Figure 7.10c. During XAS and XMCD experiments, it is practical to sequentially reverse both the the x-ray photons polarizations and direction of magnetic fields such that μ^+ (+H) = μ^- (-H), to avoid any instrumental errors.

7.2.2.4.2 Sum Rules The sum rules [228, 229] and multipole moment analysis [230] can be used to obtain the spin and the orbital magnetic moments of atoms. This is done by analyzing the integrals of the XMCD spectra and the spectral shape.

Here, we will introduce the sum rules for a 3d transition metal by relating the dichroism integrals at $L_{2,3}$ -edges to the spin and the orbital magnetic moments. The absorption coefficients μ^+ , μ^- corresponds to left circularly - (CL) and right

circularly (CR) polarized x-ray photons and the x-ray propagation wave vector k is assumed to be parallel to the magnetization direction, \mathbf{M} i.e., $k \parallel \mathbf{M}$. To define the overall XAS intensity or white line across the edge as $(\mu^+ + \mu^- + \mu^0)$, the sum rules require three spectra μ^+ , μ^- and μ^0 , where μ^0 is the linear x-ray polarization [231]. The linear x-ray polarization, μ^0 can be approximated as $\mu^0 = (\mu^+ + \mu^-)/2$ and thus, the white line expression can be rewritten as $3/2(\mu^+ + \mu^-)$. From this information the sum rules for 3d transition metal $L_{2,3}$ - edges can be formulated as :

$$m_{orb} = -\frac{4 \int_{L_3+L_2} (\mu^+ - \mu^-) dE}{3 \int_{L_3+L_2} (\mu^+ + \mu^-) dE} (10 - \eta_{3d}) \quad (7.6)$$

$$m_{spin} = \frac{6 \int_{L_3} (\mu^+ - \mu^-) dE - 4 \int_{L_3+L_2} (\mu^+ - \mu^-) dE}{\int_{L_3+L_2} (\mu^+ + \mu^-) dE} (10 - \eta_{3d}) \left(1 + \frac{7 \langle T_z \rangle}{2 \langle S_z \rangle} \right)^{-1} \quad (7.7)$$

where, m_{orb} and m_{spin} refers to the orbital and spin magnetic moment in μ_B per atom units, n_{3d} is the number of electrons in the 3d state, $\langle T_z \rangle$ is the expectation value of the magnetic dipole operator and $\langle S_z \rangle$ is the expectation value of the z-component of the spin = $1/2 m_{spin}$ in Hartree units. For the spin sum rule the factor $\langle T_z \rangle$ is negligibly small for materials with high(cubic) symmetry like Fe, Co [232, 233]. However, $\langle T_z \rangle \neq 0$ for materials with lower symmetry (octahedral and tetrahedral), high atomic numbers (4f metals), ultra-thin films and surfaces [234, 235]. Based on the sign of $\langle T_z \rangle$ factor, the spin moment is either over/under-estimated. The integrals from eq. 7.6 and eq. 7.7 for the 3d transition metal at $L_{2,3}$ - edges can be simplified to:

$$p = \int_{L_3} (\mu^+ - \mu^-) dE \quad (7.8)$$

$$q = \int_{L_3+L_2} (\mu^+ - \mu^-) dE \quad (7.9)$$

$$r = \int_{L_3} (\mu^+ + \mu^-) dE \quad (7.10)$$

Thus, the sum rules can be reformulated by using p [7.8], q [7.9], r [7.10]. Finally, the following equations for orbital and spin magnetic moment for $L_{2,3}$ - edges of 3d transition metals can be obtained.

$$m_{orb} = -\frac{4q(10 - \eta_{3d})}{r} [\mu_B/atom] \quad (7.11)$$

$$m_{spin} = \frac{(6p - 4q)(10 - \eta_{3d})}{r} [\mu_B/atom] \quad (7.12)$$

The equations 7.11 and 7.12 are based on the assumption the saturation of material's magnetization, total circular polarization of the incident x-ray photons and $k \parallel \mathbf{M}$.

These sum rules, when applied to the XMCD spectra at the L edge, can exclusively determine the spin and orbital moments on per atom basis for rare earths and 3d transition metals. The distinct measurement of spin and orbital moment of a material is one of the unique privilege of XMCD method. The magnetic moments can be obtained by using the sum rule parameters generated from the integral XMCD spectra. However, care must be taken to account for the saturation effect and self absorption effects for ultra-thin films [236], else deviations of the spin and orbital moments from their real values by 20% and 100% can be observed.

Another approach to determine the orbital and spin moments is multipole moment analysis. It calculates the fine structures in the experimental XMCD and exclusively focuses on the actual spectroscopic details unlike the integral sum-rule analysis method described earlier. Nevertheless, the multipole moment analysis also yields the same values for the spin and orbital moments. For detailed information on multipole analysis readers can refer G. van der Laan [230].

7.3 Beamline DEIMOS

DEIMOS is an acronym for Dichroism Experimental Installation for Magneto-Optical Spectroscopy. It is a soft x-ray beamline at synchrotron SOLEIL that is designed to study the magnetic characteristics and electronic properties of materials using x-ray absorption spectroscopy. The x-ray spectroscopy measurements are performed using the total fluorescence mode or total electron yield technique and XMCD is conducted by changing the direction of the applied magnetic field and the trajectory of the incoming x-ray photons. The main interest of the beamline is to explore the in-situ magnetism of organic/inorganic materials at mono-layer growth level on the surface or interface, single molecular magnets super-paramagnetic molecules and much more. In this thesis we focus on the organic cobalt phthalocyanine paramagnetic centers in the device operando mode using XAS.

The beamline DEIMOS [237] generates photons in the soft x-rays energy regime between 350eV - 2500eV and has an energy resolution of $E/\Delta E$ between 6,000 and 10,000 over the whole energy range. A photon flux of $\sim 6 \times 10^{12}$ photons/s/0.1%BW at 750eV on the sample can be established with a predefined beam size of ($80\mu\text{m} \times 80\mu\text{m}$) or ($800\mu\text{m} \times 800\mu\text{m}$). The photons energy range in the beamline includes L-edges of 3d transition metals and 4f metals, M-edges of rare earths, and K-edges of C, N, O and S. This enables for element-specific investigation of heterostructure thin films by using XAS, XMCD.

Currently, the DEIMOS beamlines hosts two endstations. The first one is a cryo-magnet and the second setup is MK2T for electrical measurements, see Figure 7.11(a). The cryo-magnet uses superconducting coils to produce a magnetic field of $\pm 7\text{T}$ along the x-ray beam direction and $\pm 2\text{T}$ field perpendicular to the beam direction. The sample temperature range from 1.5K up to 350K. The second end station was designed to achieve high sample temperatures which is not possible in the former due to the presence of cryogenic liquids. The MK2T endstation utilizes electromagnetic coils to generate a magnetic field of $\pm 2\text{T}$ along the x-ray beam direction and offers a sample temperature of 20K-1000K. Both endstations allow for XAS studies using TEY and TFY methods. The beamline allows for in situ deposition of metals

and organic materials in UHV chambers having a base pressure in low e^{-10} mbar.

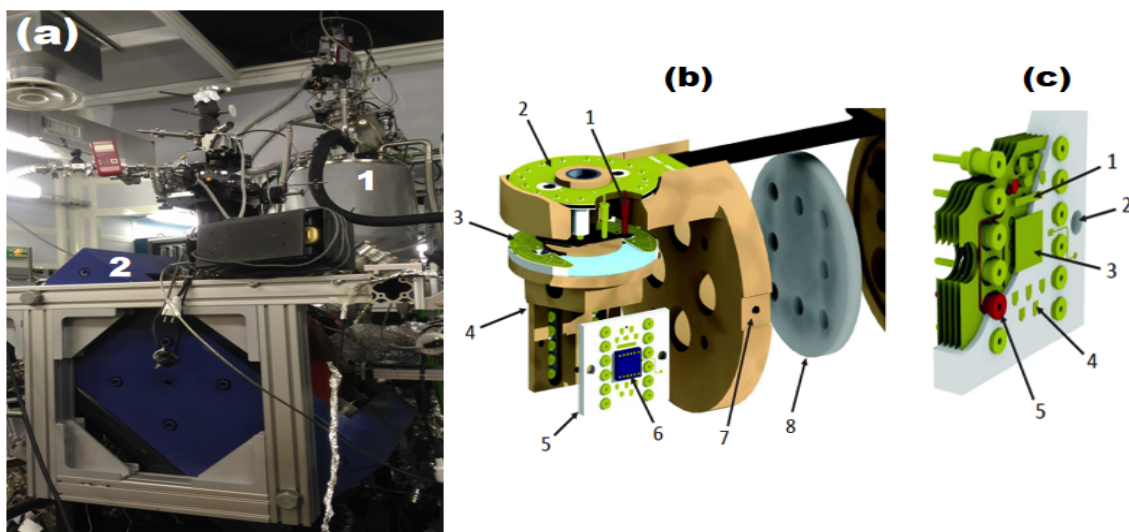


FIGURE 7.11: **Beamline DEIMOS.** (a) The two endstations of DEIMOS beamline in Synchrotron SOLEIL namely, 1) cryo-magnet endstation 2) MK2T endstation. (b) cross sectional view of Versatile Variable Temperature Insert (V^2TI) head with 1 - pin contacting the head and sample holders PCB, 2 - PCB head, 3 - PCB sample holder head, 4 - copper block sample holder, 5 - DEIMOS dedicated chip, 6 - sample glued on chip, 7 - temperature sensor diode position and 8 - sapphire disk. (c) Detailed description of the DEIMOS chip, namely: 1 - total electron yield (TEY) contact pad, 2 - screw holes for fixing the chip on to the sample holder, 3 - central thermal contact pad for sample, 4 - one of the gold coated electrical contact pads, 5 - one of the twelve tulip pins that cling on to the sample holder. Image (b) and (c) adapted from Ref [238].

In the framework of this thesis, the MK2T endstation was used to perform device-centric operando studies on organic MTJs, see Figure 7.11a(2). To make the endstation compatible for electrical measurements, a versatile variable temperature insert (V^2TI) set-up has been installed, which includes an electrical wiring and hence can be used to measure voltages, currents or electrically polarize the sample and many other applications[238], see Figure 7.11(b,c). In a standard operando technique, the device is placed in a given state and then one may read out its material properties. This is the materials-centric operando approach [238]. In the device-centric operando approach, one reads out the materials property within the device current (details in Chap. 2). This focuses the materials characterization onto those atoms which drive the device operation. In 2017, the IPCMS team demonstrated the use of V^2TI by conducting a joint XAS and electronic transport measurements on MgO

based MTJs and displayed the capabilities of the device operando approach by resolving contribution of specific atomic species in the MTJ operation [5] (details in Chap. 2, Sec. 2.7). As a continuation of this work, in the current thesis for the first time we performed device-centric operando studies on molecular CoPc based MTJs under x-rays. The goal was to better understand the role of Co paramagnetic centers in spin-transport measurements. Specifically, we aimed to utilize the magnetic element sensitivity of XMCD at beamline DEIMOS to probe the spintronic properties of the CoPc spin chains (Chap. 3, Sec. 3.3.1.2) within nanoscale vertical devices.

Here, we will walk through the steps involved in introducing the sample into the measurement setup. The fabricated devices are glued on to DEIMOS chips which are compatible with the (V^2TI) sample holder, see Figure 7.11b. The sample is wire bonded to the gold pads of the chip and the bar contacting pad which is used for TEY detection. The sample holder head (Figure 7.11b-3) is cleaned with ethanol using a cotton stub and electrically qualified using the standard multi-meter. The wire bonded chip is fixed on the copper block using molybdenum screws and is introduced into the UHV load-lock chamber of the beamline. Before transferring the sample on to the (V^2TI) the electrostatically fragile device is set to floating during all manipulation until the start of the electrical measurements.

The in situ transfer of the copper block sample holder on to the (V^2TI) arm is done as shown in Figure 7.11b. This creates a contact between the sample holder head and the PCB head through conducting pins and thus forms an electrical link between the sample and outside, see Figure 7.11b(3-2). Care should be taken so as to not under/over tighten the screw while mounting the copper block on to the (V^2TI) arm, else a bad electrical contact with the PCB pads is possible. Out of the sixteen wires present on the PCB head, twelve of them are connected to the chip via holder. Choice of the sample holder can be done based on the measurement requirement. For instance, there are V02, V03 copper block holders which offer $\theta = 45^\circ$ with respect to the incident photon beam such that XMCD shall be sensitive to in-plane and out-of-plane magnetization. The sample is in UHV condition and sample cooling is done by introducing helium externally in the presence of an applied magnetic field. The temperature can be monitored using the a diode which is located beside the (V^2TI)

insert's head Figure 7.11b(7). The temperature is controlled by heaters in the setup. The lowest stabilized temperature on the sample was 40K and the highest was 360K.

7.3.1 Device operando at DEIMOS beamline

As detailed earlier, the x-ray absorption spectrum can yield information about the number of atoms, their charge, chemical environment, and thus the resulting electronic and magnetic properties in materials. A synchrotron x-ray source opens up opportunities to study the atoms which are buried in complex heterostructure thin films devices. On electrically operating the device, while at the same time shining the x-rays and exciting specific atoms, changes in the operation can provide information into those atoms that contribute to electrical transport.

In our studies we focus on Co paramagnetic centers of CoPc molecule based MTJs devices whose operation involves spin-polarized transport across a presumed nanoscale hotspot containing a CoPc-based spin chain (Chap. 3, Sec. 3.3.1.2). Therefore, we focus the XAS studies only on those Co PM centers by performing the magneto-transport measurements as x-rays with an energy tuned to the Co L-edge are absorbed by the cobalt atoms. The device composition studied includes $Si/SiO_x/Cr(5)/Fe(50)/CoPc(10)/Fe(10)/Cr(5)$ and $Si/SiO_x/Cr(5)/Fe(50)/C_{60}(nML)/CoPc(3ML)/C_{60}(5ML)/Fe(10)/Cr(100)$, where (n = 1, 2, 3) mono layers and rest in nm. The processed stacks have a passivation SiO_2 layer of thickness of 135nm and a bi-layer capping of $Al(110nm)/Au(35nm)$. The Figure 7.12(a) shows the sample glued on to DEIMOS chip. The wire bonded organic samples are fixed on 45° or (0°) sample holder (see Fig.7.12b) and transferred to the V^2TI arm in the MK2T endstation of DEIMOS beamline. In our samples the FM electrode magnetization is in-plane and since there is no ready copper block holder that offers in-plane magnetisation for the mounted sample, the V^2TI arm is rotated by an additional angle ϕ . This enables the device's FM electrode magnetization M to be aligned along the applied magnetic field H . Extra care is taken to make sure that the V^2TI is not in contact with the chamber or the magnet, to avoid any electrical short circuit.

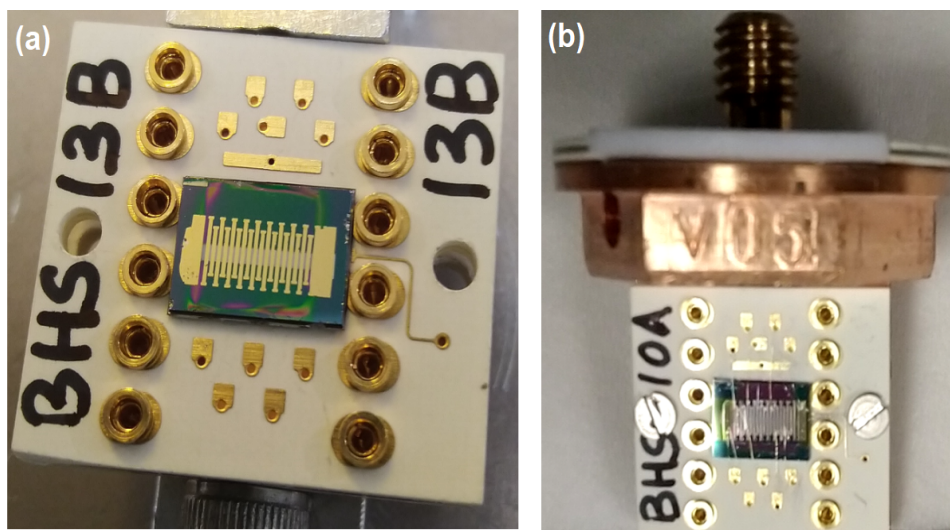


FIGURE 7.12: Molecular devices mounted on DEIMOS (a) chip and (b) copper block sample holder V05 which makes sample 0° to x-ray beam & is out-of-plane to applied magnetic field .

All these arrangements ensures the sample is placed almost in-plane to the applied magnetic field. Note, the sample is $(\theta + \phi)$ degrees w.r.t the incident x-ray photon beam, where θ is the angle offered by the copper block sample holder and ϕ is additional angle gained by rotation of the V^2TI . The electrical set up consists of a Keithley 2636 sourcemeter which is used to source voltage/current integrated via Python into the DEIMOS control station, see Figure 7.13. Using the commands in Python beamline operations such as the applied magnetic field, x-ray beam characteristics and sample temperature can be controlled. This development by L. Joly is significant as it simplifies V^2TI usage and does not demand any additional hardware equipment to be plugged into the endstation. The x-ray absorption spectra were recorded in total electron yield and total fluorescence yield with the MTJ electrode grounded. It is in principle nice to simultaneously record the device current and TEY current by connecting the MTJ to the TEY pad of the chip, which is then connected to a separate electrometer. But, our experience in the beamline taught us that doing so heavily degrades the TEY and TFY mapping of the device. Hence, the TEY pad is connected to the edge of the substrate (avoiding the MTJ) using silver paste to fix the wire.

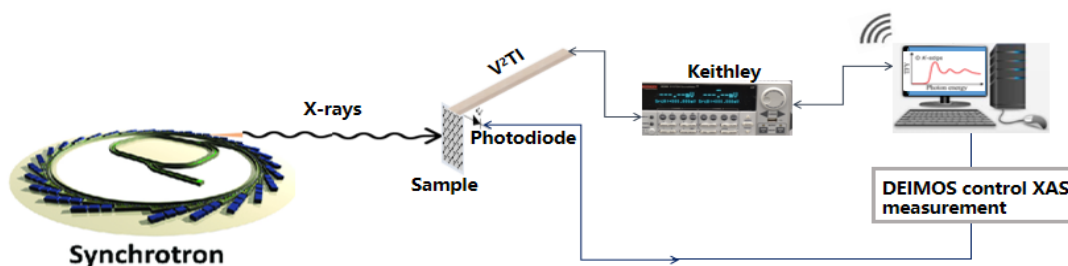


FIGURE 7.13: **Integrated XAS and electrical measurement using MK2T endstation at DEIMOS beamline.** All manipulations such as electrical, magnetic, incident beam polarization, temperature stabilization to the device is done by Python commands at measurement station.

7.3.2 Device mapping using x-rays

To perform synchrotron based device operando, it is crucial to precisely align the x-ray beam on to the MTJ and perform XAS and electrical studies on the junction. The device-centric XAS was performed by measuring the device current $I(E)$ as a photon energy function while sweeping the Co L-edges present in the CoPc film. The nano-lithography process in organic device does not have an optical opening in the top electrical contact. Due to electron escape lengths and the thickness of our top electrode, these spectra will therefore not include a photocurrent coming from the junction center. To acquire magnetic information, we tried to study the Co L-edge using circularly polarized x-rays for different applied bias, applied magnetic fields before and after spin-flip excitations at 40K.

The measurement was done by recording the x-ray absorption intensity in TFY mode with fixed photon energy at Co L_3 - edge along the sample surface. Using a (800×800) micron beam it was difficult to pinpoint any features of lithography on the sample, only the side gold pins of the chip were distinguishable in the scans, see Figure 7.14a. On switching to a smaller x-ray beam sized (80×80) micron, the features in the sample were much clearer. The TFY mapping reveals the patterning of the metallic capping electrodes and the passivation oxide layer features of the sample, see Figure 7.14b.

The experiment's biggest challenge was to localize the 300nm device using an (80×80) micron x-ray beam. We were partially successful in completing this task

by recording the precise coordinates of the areal intersection between the thin film and electrical electrodes (Al/Au) that encloses the nano-pillar device, which is operated electronically, see Figure 7.15. We successfully performed magneto-transport measurements on several organic MTJs. The resistance vs field $R(H)$ curves reveal low- H magnetoresistance, which is associated with switching the top free FM electrode, and the high- H magnetoresistance associated with the bottom FM electrode. We have also recorded the spin-flip excitations in conductance, a signature of the CoPc molecules in action. These measurements were crucial in the publication of Katcko et al.(2021) [11].

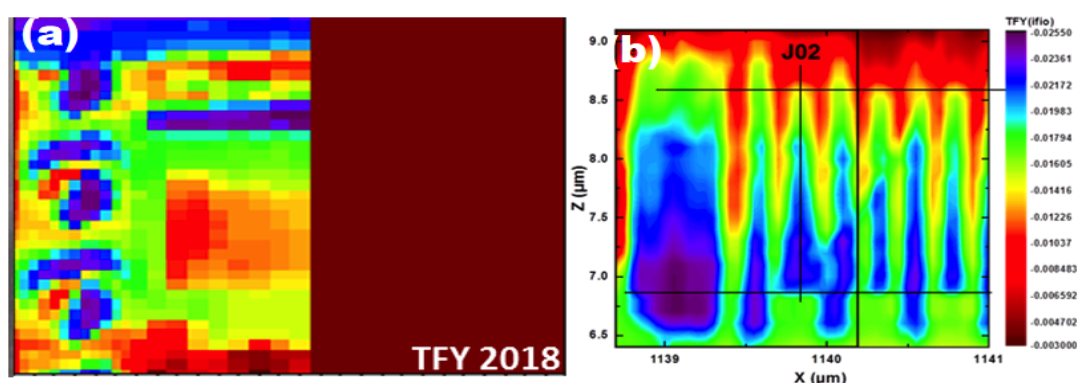


FIGURE 7.14: **TFY maps of on-chip CoPc based device coordinates** recorded with : (a) (800×800) micron x-ray beam shows only the gold pins of the DEIMOS chip but hardly any features of the device (b) (80×80) micron x-ray beam clearly distinguishes the individual top electrodes of the respective junctions. Here junction 02 coordinates is localized using total florescence mode. Compare this image with Fig. 7.12(a) Au pins and electrode patterns.

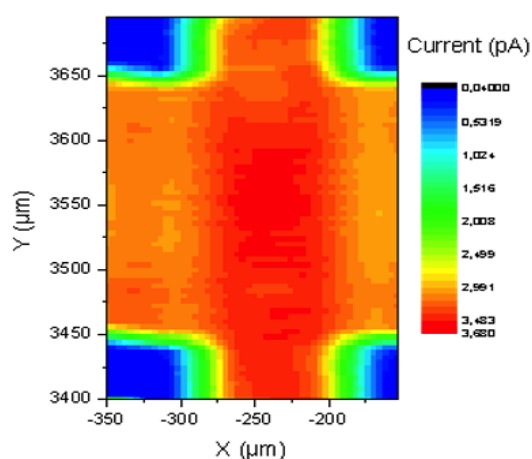


FIGURE 7.15: **Areal view of the top electrical (Al/Au) bi-layer electrode** which encloses the 300nm vertical device obtained by TFY map. XAS scans at Co edge is performed in the entire area of the bright red color zone as the CoPc device cannot be localized due to absence of optical opening.

For device operando studies, the entire intersection area was scanned at Co-edge with CL and CR x-ray beam by performing $I(V)$ s and $R(H)$ s on the junction.. Despite successfully localizing the prospective device location (see Fig. 7.15) & accumulating several XAS scans, averaging out the spectra the bigger challenge was to see any device response to the tuned x-rays. Below is a quick run down for the estimated total electron yield value for the buried Co atoms. To find the estimation for the TEY value, we assume the initial number of photons to be $6e^{12}$ photons/s, for simplicity we consider full Co layers instead of CoPc and the absorption coefficient calculated from Ref. [239]. The case (1) corresponds to a thin film of Co layer (Fig. 7.16). The graph of TEY current (A) vs. x-ray energy (eV) shows a jump in TEY at the Co edge (780eV) from $2.29e^{-7}$ A to $2.39e^{-7}$ A, which is 4.4% with respect to the background.

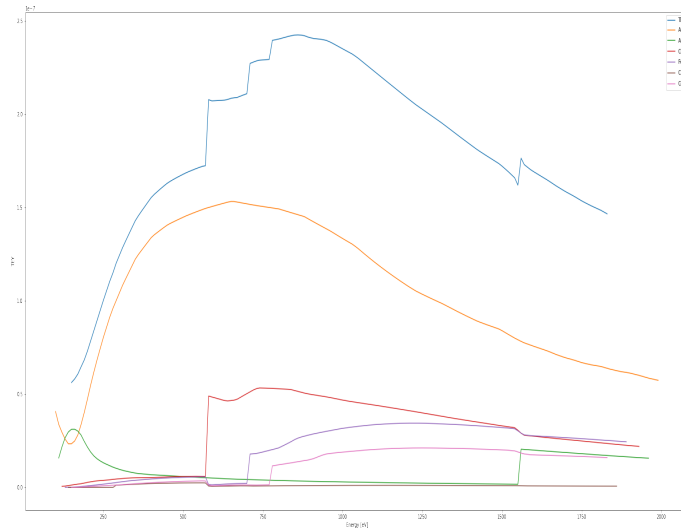


FIGURE 7.16: Case (1) Estimated TEY current for all layers stacked Co(3)/C₆₀(5)/Fe(10)/Cr(100)/Al(110)/Au(35) nm scale. At Co edge 780eV jump in signal (blue curve).

In case (2), the Co layer within the nano junction area has similar TEY but its divided by the junction shape w.r.t the beam with jump in $3.29e^{-12}$ A to $3.39e^{-12}$ (see Fig. 7.17). Overall, this TEY value is in the DEIMOS beamline measurable range i.e., within 100fA. But, these estimations are for Co thin film, in our devices Co signal is only coming from CoPc which has reduced Co density, hence the TEY jump is strongly decreased. Our present signal should be probably multiplied by a factor of 10-100 to detect any changes with TEY detection mode. Also, with $6e^{12}$ photons/s produced by the (80×80)micron beam in DEIMOS, the amount of photons reaching the 300nm sized devices is estimated to be $1.4e^7$ photons/s, which is extremely

low. All these factors are challenges to be addressed to see any change in the device measurements contributed by Co atoms when x-rays are incident on the device.

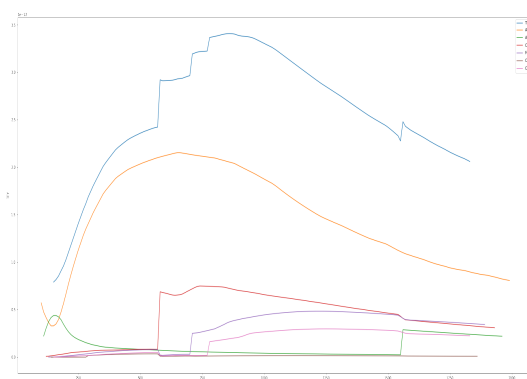


FIGURE 7.17: Case (2) - estimated TEY current for 300nm device for all layers stacked Co(3)/C₆₀(5)/Fe(10)/Cr(100)/Al(110)/Au(35) nm scale. At Co edge 780eV jump in signal (blue curve).

Nevertheless, out of the multiple challenges involved in this work we have tackled most of them. Firstly, MgO MTJs enjoy a huge fabrication success rate (in a $(5 \times 6) \text{mm}^2$ surface out of 144 devices, 80% were working) but a low success rate when studied at DEIMOS, presumably due to electrostatic issues [5]. In the lithography of molecular stacks, only ~ 20 organic devices can be made on a similar surface, i.e., with a low fabrication success rate. Despite this downside, we successfully mounted several electrostatically fragile Fe/molecule-based organic nano junctions under x-rays, see the histogram 7.18.

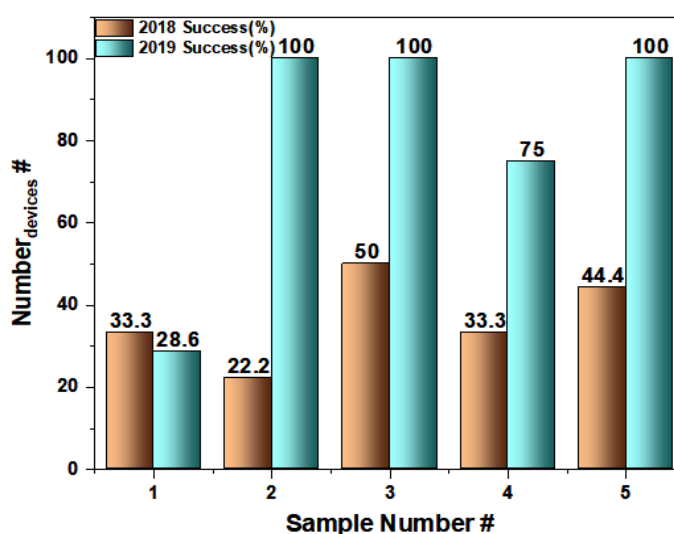


FIGURE 7.18: The histogram represents the success rate of organic nano devices that were qualified in lab setup and reproduced in the DEIMOS experimental setup.

Altogether, our team is the first to successfully mount a nm-sized molecular solid-state device and record a high device success rate under x-rays. We have optimized the device mapping protocol, which adds to the efficient usage of the beam-time. Overall, the magneto-transport results recorded at DEIMOS added to our understanding of the CoPc molecular chains Chapter 8. Measurements on molecular spintronic engine molecular nano devices were performed at DEIMOS are presented in Chapter 9.

7.4 Beamline HERMES

HERMES is an acronym for High Efficiency and Resolution x-ray Microscopy and Electron Spectroscopy [240]. The beamline is dedicated to soft x-ray microscopy with and is made up of two microscopy methods namely: scanning transmission x-ray microscopy (STXM) and x-ray photo emitted electron microscopy (XPEEM). The STXM is a photon-photon microscopy technique which is used to probe the samples' volume properties, offering depth analysis up to few hundred nm's. The XPEEM is a photon-electron microscopy, which is a surface sensitive technique useful to scan the top few nm's of the sample surface under UHV environment. The two techniques are not just limited to imaging the samples but also can perform local spectroscopy like XAS, XANES at a nano-scale. In this thesis, the STXM endstation, see Figure 7.19a, available in the HERMES beamline was used to locally image the oxygen defects in MgO based MTJ, using synchrotron x-rays and probe its direct impact on the device magnetoresistance. This work was done with close collaboration with IJL, Nancy along with significant involvement of our former IPCMS colleague Dr.Katcko.

The HERMES beamline covers a wide energy range from 2.5eV to 2.5keV, starting below the Si 2p-edge, K-edges of C, N, O and many other light elements, L-edges of transition metals, M-edges of rare earths and K-edge of Si, S and P. HERMES has an energy resolution of $E/\Delta E > 5000$ on the entire energy range and the photon flux on the sample is $> 1.1011Ph/s$. Key highlight of the beamline is that it offers a spatial resolution below 20nm and the STXM technique has the beam size of $\sim 25nm$

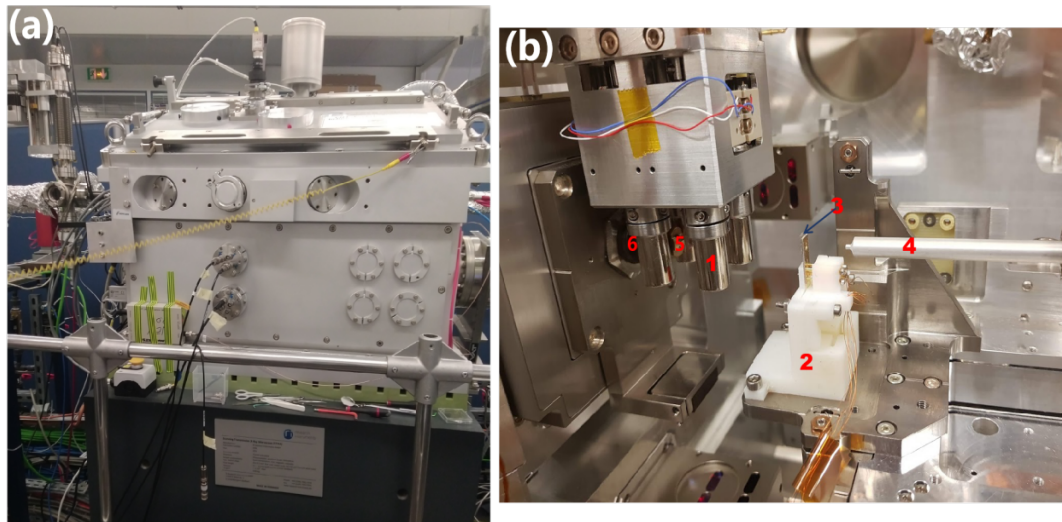


FIGURE 7.19: **Beamline HERMES experimental setup.** (a) Scanning transmission x-ray microscopy (STXM) endstation of the HERMES beamline at SOLEIL synchrotron. (b) Interior of the STXM chamber with : 1) four permanent magnets, 2) sample stage, 3) MgO MTJ sample fixed to the sample stage using a PCB sample chip, 4) photon detector, 5) order selecting aperture (OSA) and 6) zone plate (ZP) in close contact with the x-ray source.

on the sample. In the STXM chamber the sample is in secondary vacuum condition with pressure $< 1\text{ barr}$ (see Figure 7.19b). The sample temperature can be controlled between 150K-600K and a magnetic field up to 2kOe can be applied to realize parallel and anti-parallel magnetic states in the sample. In the current thesis, the STXM endstation is used to perform device operando studies on MgO MTJs.

7.4.1 Experimental procedure

To perform device operando studies at HERMES beamline, the MgO samples with composition glass//Ta(5)/Co(10)/IrMn(7.5)/CoFeB(4)/MgO(2.5)/CoFeB(3)/Ta(1)/Pt(1) were fabricated and processed using photolithography techniques. The prepared samples have $20\mu\text{m}$ sized MgO MTJs with a $10\mu\text{m}$ optical access to the device. The electrically characterized MTJs were glued on HERMES printed circuit sample holder and wire bonded, see Figure 7.20a,b. The sample is mounted onto the sample stage to perform operando studies, see Figure 7.20c.

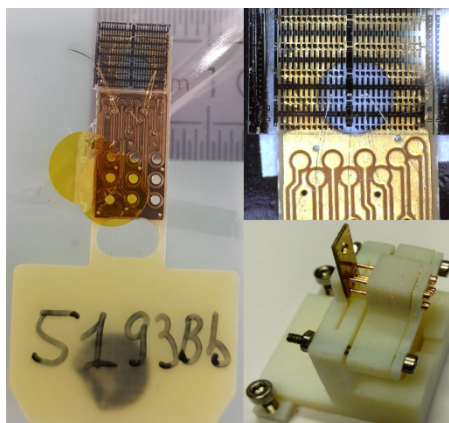


FIGURE 7.20: **Samples on HERMES PCB chip.** To the left hand-side the image of MgO MTJ is glued onto PCB chip and wire bonded to Au pads. The top right image is a close up view of the MTJ and bottom is sample mounted on the 3D printed sample stage.

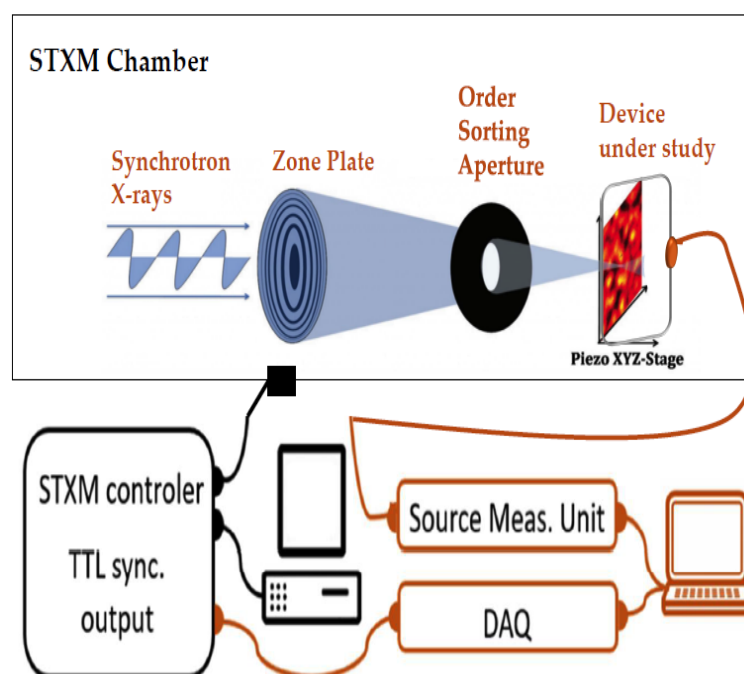


FIGURE 7.21: **HERMES goes operando - electrical connections.** The standard STXM set up is in black and the orange represents the operando extension. To record the TEY and MTJs conductance while scanning the x-ray nano beam hardware and home built software was connected to the standard STXM end station. The sourceme-ter records TEY current and sample conductance. The dual analog-digital input/output board (DAQ) allows TTL acquisition to establish live condition for TEY and sample's conductance x-ray maps.

An illustration of the operando setup in the scanning transmission x-ray microscopy (STXM) endstation is shown in Figure 7.21. In the device operando technique, the x-ray photons energy is selectively tuned to match the oxygen atoms absorption on core electron levels and simultaneously study the change in device response. The synchrotron studies were performed using two indigenous techniques

described below.

1. Imaging using the total electron yield in STXM is a relatively established technique which provides information based on the contrast of sample's geometry, chemical composition, and electrical conductivity. The TEY-STXM signals come from the x-ray ejected electrons from the sample. Our experiment's first step involved the simultaneous recording of the TEY and the MTJs conductance while scanning with x-rays. This method is termed scanning total electron yield microscopy (STEYM), which we developed on the HERMES beamline to localize the device using x-rays.
2. In the second step, the set-up was re-configured, where the bottom electrode and respective device to be studied is connected to perform device operando measurements. This allows to record the MTJ resistance while being scanned by x-rays and hence the name operando scanning x-ray microscopy (OSXM).

To perform the experiment, firstly the x-ray beam's spot size is centered on the transparent membrane for easy transmission. Once the spot size is optimized the MgO sample is introduced into the STXM chamber. Usually care is taken while gluing the sample such that the potential working devices are closer to the circular hole in the holder (Fig. 7.20). Because the initial optimization of the beam size is done with respect to the membrane which is comparable to this circular hole in the holder. Of course, one would want to drill a tiny hole in the sample itself using FIB for easy focalization of the junction. But since the substrate is glass it might get worse than better. Several TEY maps are collected to confirm the exact coordinates of the optical opening of optical opening of the MTJ.

7.4.2 Device operando at HERMES beamline

One of the challenging aspects of this experiment is to locate the exact coordinates of the $12\mu\text{m}$ optical opening of the MgO tunneling junction using a narrow x-ray spot sized $\approx 30\text{nm}$. A scanning total electron yield microscopy (STEYM) technique

is employed. The technique is advantageous as it does not work in the transmission mode, which ensures an ease to study industrial samples. The imaging does not require the sample to be mounted on an ultra-thin membrane holder. Instead a more rigid PCB can be used. The electrical connections for the STEYM involves connecting the MTJs to a Keithley sourcemeter, see Figure 7.22a. The STEYM image of three MTJs recorded at energy 660eV can be clearly confirmed by its optical counterpart, see Figure 7.22b,c and the electrically connected top and the bottom electrodes of the device are well resolved.

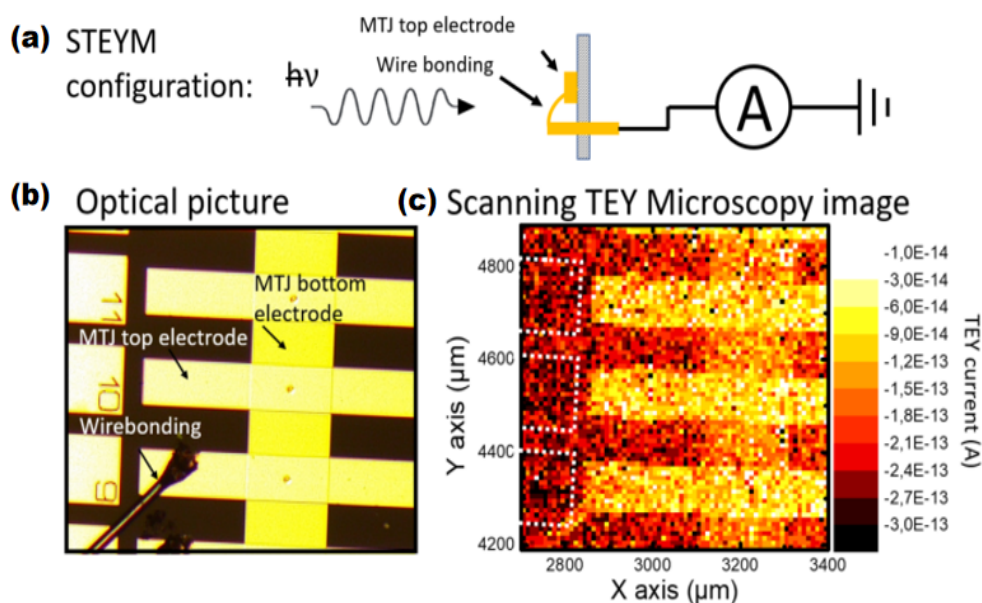


FIGURE 7.22: **Scanning Total Electron Yield Microscopy.** (a) The electrical connections for a STEYM where the device is connected to a digital pico-ammeter. (b) An optical image revealing the three MTJs and (c) The STEYM image of the same three MTJs recorded at 660eV, OSA bias = 10V. Only the electrically connected regions of the top and bottom electrodes are visible in the STEYM image.

Following this, to gain more insight into the STEYM technique, the image was recorded for different energies. For instance, the Figure 7.23a represents the STEYM scans at energies 660eV and 530eV of top and bottom electrode of the sample. The extent of contrast in these images certainly is linked to the photon energy and therefore to the chemical nature of the examined atoms. The imaging was done with the order selecting aperture (OSA) grounded. Lack of publications on such unique microscopy technique allowed us to discover that a positively biased OSA can be applied to avoid its electronic emissions when it is illuminated by x-rays. The unwanted electronic emissions can result in an additional parasitic sample current which can cause

a total loss of image contrast. This has been tested and confirmed during our beam time. An increase in the OSA bias sharpens the imaging resolutions and enhances the signal to noise (S/N) ratio by a factor of 2, see Figure 7.23b.

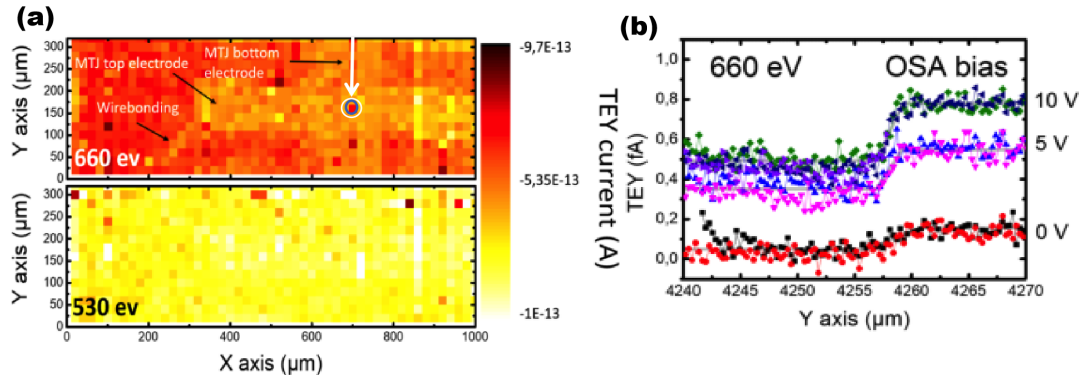


FIGURE 7.23: **Impact of x-ray energy and OSA bias on STEYM image scan.** (a) The two STEYM images recorded at the same region at 660eV and 530eV, shows lack of contrast for the top and bottom electrodes of the MTJ, specifically for the latter x-ray energy value. (b) For applied OSA bias : 0V, 5V and 10V at 660eV the TEY line scans of an electrode when crossing the MgO MTJ (white circle in panel-a), shows a sharp signal at OSA bias = 10V. Each line scan was repeated twice.

To perform device operando it is vital to know the exact coordinates of the 12 micron diameter optical opening located on top of the MgO MTJ, see Figure 7.24a,b. After multiple attempts with many strategies and accumulated knowledge from previous beamtimes, we were successful in mapping the MTJ opening, see Figure 7.24c. Now that the junction is localized using STEYM, we can switch to operando mode.

The set-up was re-configured to perform device operando measurements using the operando scanning x-ray microscopy (OSXM) method, see Figure 7.25a. Here, the resistance of the MTJ is recorded when the x-rays are scanned across the junction. The line scans were conducted over the optical opening of one MTJ at three different x-ray photon energies, see Figure 7.25b. At 660eV a clear resistance plateau is observed for a scanning across the 12 micron MTJ optical window yields an increase in device resistance when the photon energy is 660eV, i.e., above the oxygen K-edge. When the energy is 520eV which is below the O K-edge, this resistance increase is strongly reduced. Thus, the OSXM technique factually reveals the involvement of oxygen atoms in electronic transport across the MgO MTJ.

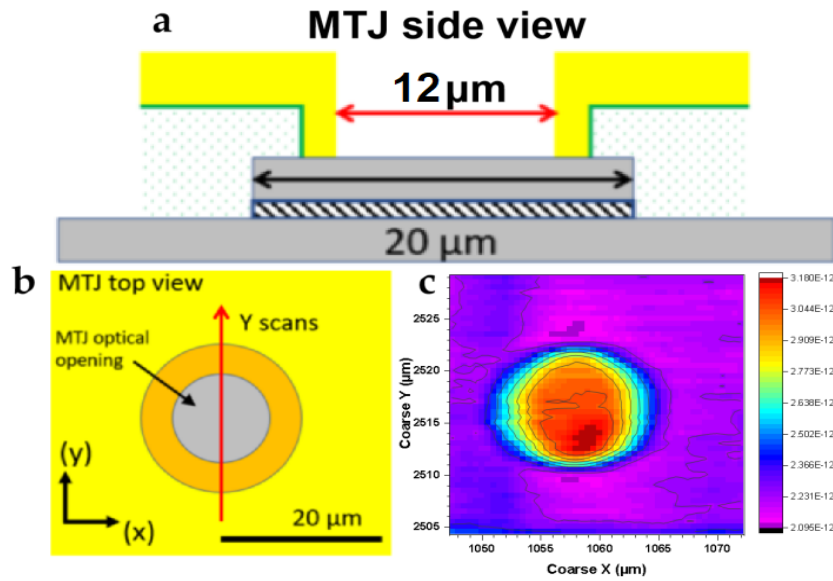


FIGURE 7.24: Exclusive STEYM map of MgO MTJ. (a) Diagrammatic representation of the 20 micron MgO MTJ with an optical opening of 12 micron, (b) Top cross section of the MTJ and (c) STEYM mapping of the MgO MTJ, optical opening in the top technological contact.

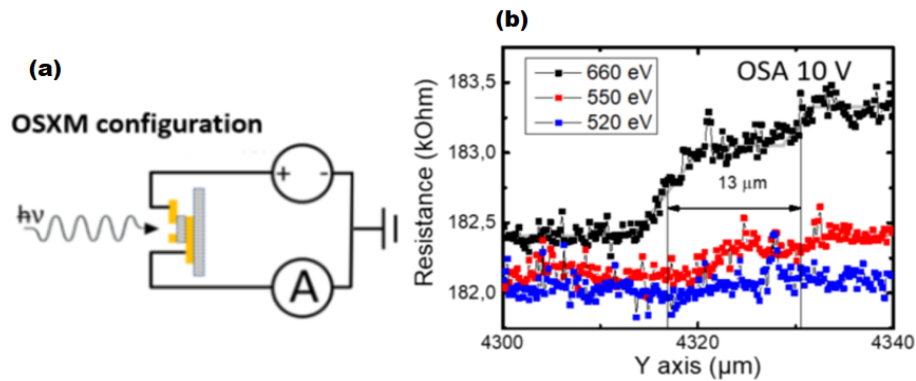


FIGURE 7.25: Operando Scanning X-ray Microscopy mode of operation. (a) Electrical connections for OSXM mode : MgO junction contact is connected to Keithley and bottom electrode is connected to pico-ammeter, the set up is grounded. (b) A typical resistance amplitude recorded on MgO MTJ for a OSA bias value of 10V at three different x-ray energies. The sudden rise in the resistance on hitting the MgO junction is clearly visible at 660eV (black).

After the time consuming focalization, we attempted to map the oxygen defects/hotspots within the device for a given bias and field values. As we already know from Chap. 2 Sec. 2.7 that MgO MTJs anti-parallel orientation shows significant change to x-rays compared to parallel state we recorded the variation in resistance for AP state when scanned with x-rays of energies corresponding to oxygen atoms, see Fig.7.26. Similar study at 570eV for P state showed poor contrast due to

small resistance change with incident x-rays. The Figure 7.27 shows the MTJ mapping for 570eV i.e., above the O K-edge in the AP state. This mapping is the flatten plot of three TEY data sets at same position and energy. The highlighted green box could be a region which includes the hotspots. Since hotspots are in the range of nm scale (Ref. 2, Sec. 2.7), ideally, energy scans in this green boxed zone with steps of nano scale when performed can lead to prospective candidate for hotspot. The challenge is to observe a substantial resistance change ($\sim k\Omega$'s) to the tuned x-ray energies. However, due to limited beamtime, we were unable to get reproducible map the nano hotspots.

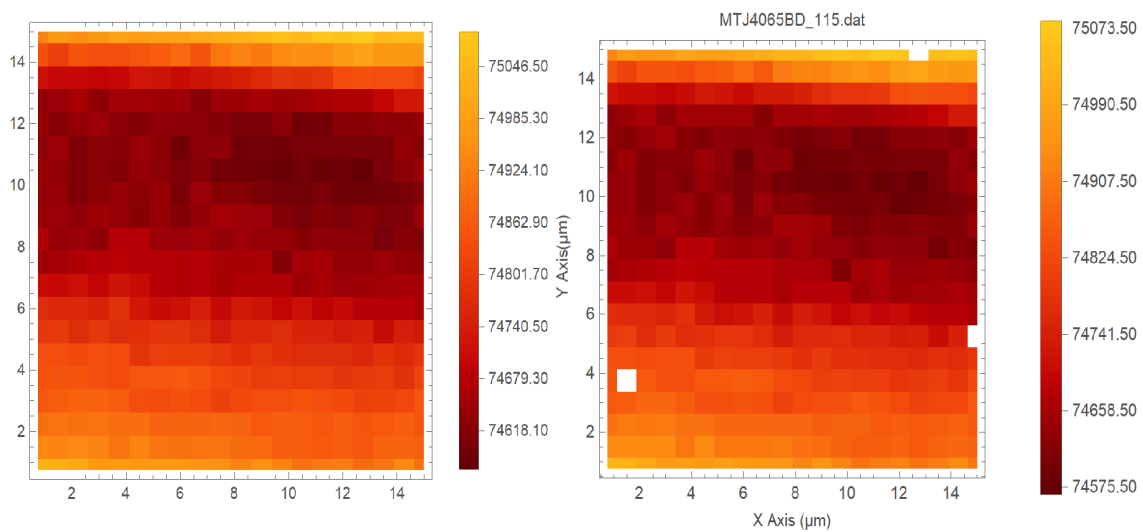


FIGURE 7.26: **MgO device resistance maps.** The two images are resistance maps of MTJ for same (x,y) coordinates recorded above O K-edge 570eV for AP state. The 2 datasets were acquired consecutively within the MgO optical opening. The color scale is the resistance in Ohm.

On a positive note, the progress in the work is commendable. We have successfully defined an experimental protocol to obtain a high-resolution STEYM image of a $12\mu\text{m}$ optical opening of an industrial-grade FeCoB/MgO MTJ using synchrotron grade x-rays. The resistance variations observed in OSXM mode when x-rays were locally illuminated on to MgO MTJs is inspiring to explore device operando method. These first-hand results shall perk interest in researchers to explore novel methods to study defects in devices, especially when the lateral dimensions of MgO MTJs are shrinking to less than 20nm, closer to the dimension of the defect. To conclude, this work's progress can bring better insights about the role of oxygen vacancies within

MgO in magneto-transport.

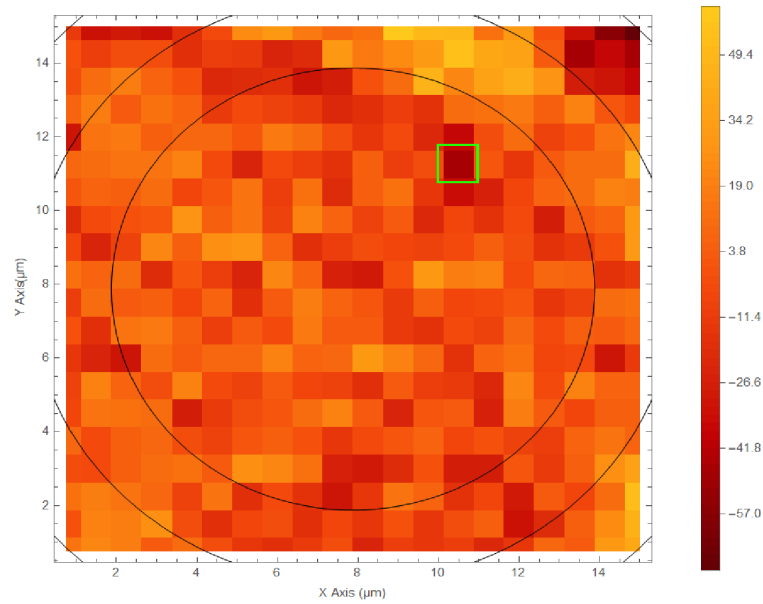


FIGURE 7.27: The TEY image at O K-edge for devices' AP state for OSA bias 10V within the $\sim 12\mu\text{m}$ optical opening of the MTJ displays varied range of resistance at room temperature color scale. This image is obtained after overlapping and flattening three consecutive TEY scans recorded at same coordinates and energy. The green box is the region which seems to be common in all three scans and shows a resistance change of $\sim 57\Omega$. This zone could be a prospective candidate for hotspot. The black circles are a visual guide to the size of the MgO MTJ. Inner most circle is in size of the optical opening $\sim 12\mu\text{m}$.

Chapter 8

Encoding information on the excited state of a molecular spin chain

Traditionally, spintronic solid state devices encode information as "0" and "1" in the form of parallel (P) and anti-parallel (AP) states of the two neighbouring magnetic electrodes, which converts the respective magnetic information into two distinct values of resistance, that can be detected and processed in an electrical circuit. This effect is called magnetoresistance (MR), which is the basis for information encoding and transmission using electron spins [241]. Hence, storage of new memory data requires the switching of the magnetization of only one electrode i.e., the free layer, while the second electrode is unperturbed and acts as a reference layer. The reference layer is fixed (/pinned) by coupling the layer with an antiferromagnetic (AFM) layer. Such spin-polarized transport across a device's metallic/ semi-conducting antiferromagnetic layer can foster macroscale effects such as tunneling anisotropic magnetoresistance (TAMR) [242] and interface charging effects [243, 244] as discussed in Chapter 3.

Experiments suggest that magnetoresistance of a solid state device could be used to explore the evolution of AFM molecular spin chain's quantum states [9, 8], details in Chap. 3. It is interesting to design spintronic devices that utilize these discrete

spin states as it would boost the current strategies of quantum information encoding and transmission [6, 245, 246, 247, 248, 249, 10, 250], and also thermal energy harvesting [17]. In this thesis, we have integrated the spin states of CoPc paramagnetic molecules in a solid state device by using solvent- and resist-free nano-sphere lithography technique (see Appendix A). As a result of this integration, we have several important findings that will be discussed in the current and in the following Chapter 9.

8.1 Device architecture

The basic structure of any magnetic memory device consists of a ultra-thin insulator sandwiched between two magnetic spin injector/analyzer electrodes (see Chap. 1). Here, molecular CoPc paramagnetic centers are sandwiched between Fe and (or) Co ferromagnetic (FM) electrodes. The CoPc layer is the device's active spintronic spacer. The standalone magnetic orientation of the CoPc spin chain is not fixed because the spins are paramagnetic, so it can be influenced by a local [245, 247, 250] or an external [251, 252] magnetic field (see Chap.3). Besides, the excited spin chains states are dynamical. They normally are short-lived before the transfer of spin angular momentum to the transport electron triggers the molecular chain to return to its quantum ground state [96]. Here, we propose to encode the information in the CoPc molecular spin chain's (MSCs) quantum ground and excited states. To realize this, it is necessary to have a magnetic steady state within the chain that can be independently controlled (concept from Chap. 3, Sec. 3.5.1). This is done by the FM electrode, which maintains a spin referential of a MSC [124, 253]. A UHV fabricated stack is developed into an on-chip memory device. More details on the processes, experimental setup can be found in Chapter 5 and Chapter 6.

To ensure the quality of multi-layers in the stack, x-ray reflectometry (XRR), x-ray diffraction (XRD) and transmission electron microscopy (TEM) were done to characterize the layers, for details on techniques see Chap. 5. The XRR measurements for a stack of composition $Si/SiO_2//Cr(5)/Fe(50)/CoPc(20)$ (nm units) is shown in Figure 8.1a. The rms roughness (σ) of iron is less than 0.5nm, indicating a smooth

interface with the Cr buffer layer. The excellent fit to the measured data with low $\chi^2=0.0049$ signifies the overall structural quality of the entire stack. The x-ray diffraction scan shows a sharp peak at $\sim 45^\circ$ that is tabulated to the bcc(110) structure of Fe, Figure 8.1b. The iron sputtered on Cr buffer thus exhibits a bcc(110) texture. The TEM measurements on the entire stack Si/SiO₂//Cr(5)/Fe(50)/CoPc(20)/Co(10)/Cr(5) (nm units) reveal the expected nominal thickness of the various layers and the XRRs' low rms roughness confirms the clear interfaces in the TEM, Figure 8.1c. Despite the metal/molecule interfacial roughness, the wide field-of-view image confirms the continuity of the layers. The molecular vertical devices sized 500nm were crafted using nano-sphere lithography, a novel technique described in Appendix A. This technique preserves the interfacial structural and magnetic properties of the device.

8.2 Impact of in-plane magnetic field cooling

In our vertical organic nano device-A: Si/SiO₂//Cr(5)/Fe(50)/CoPc(20)/Fe(10)/Cr(5), Fe is the bottom electrode, the top electrode is Co and CoPc is the insulating barrier. The metal/molecule interface, i.e. the spinterface [101, 102] which gives rise to the exchange bias effect, needs to be activated via field cooling (HFC) (details in Chap. 3, Sec. 3.5.2). So, a large static magnetic field is applied to saturate the ferromagnet (FM) iron layer, while cooling down the sample below the blocking temperature (T_B) of AFM CoPc. Prior to field cooling, the bulk FM layer is magnetically ordered while the CoPc AFM layer is random. During FC process, the spins of Fe and CoPc interact with each other and the 1st mono-layer (ML) of CoPc aligns with the underlying Fe (due to FM-FM interactions at the spinterface), while the successive layers of the CoPc molecular spin chain are aligned anti-parallel to each other. Therefore, the field cooling procedure generates magnetic order within the anti-ferromagnetic CoPc chain and at the spinterface. The data in Figure 8.2 records the evolution of device resistance (R) over a range of temperature (T) at a constant applied bias voltage (V) and external magnetic field (H). The R(T) plot is useful to determine the nature of transport through the nano junction. A change in device

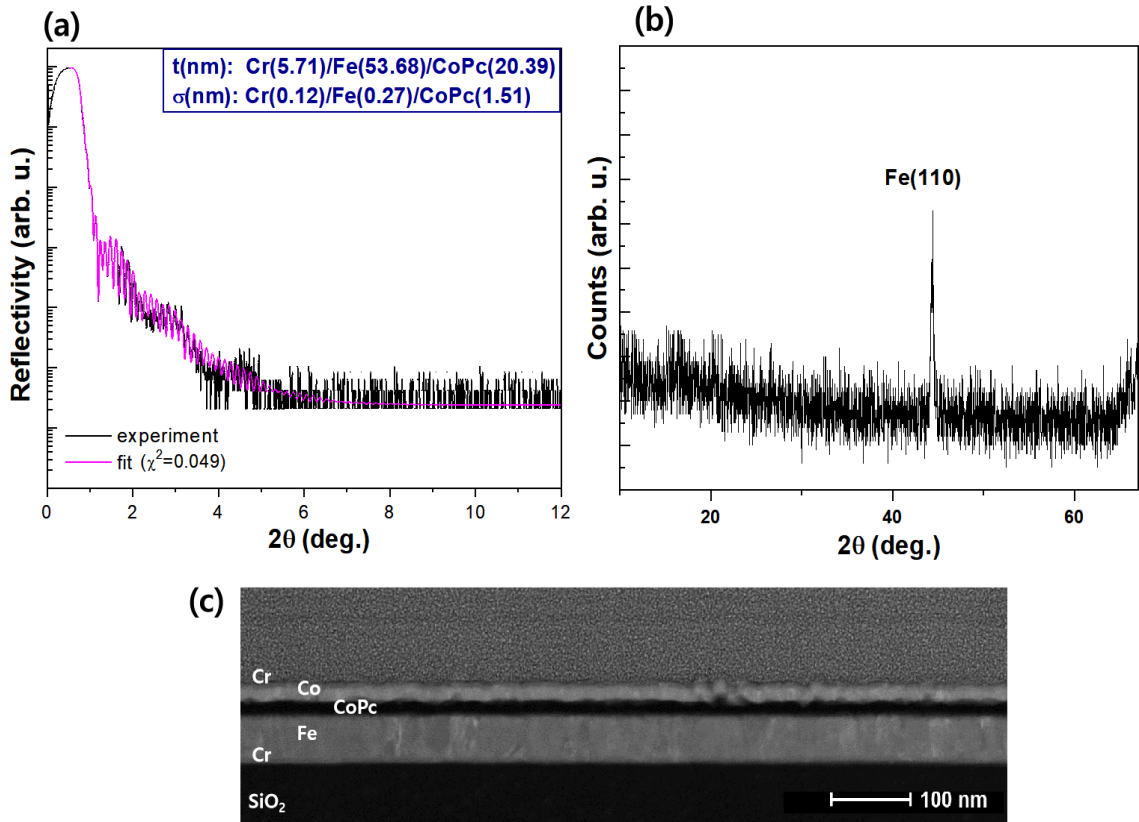


FIGURE 8.1: **Structural characterization.** (a) XRR data displays a good fit (magenta) for the measurement (black) on a $\text{Si}/\text{SiO}_2//\text{Cr}(5)/\text{Fe}(50)/\text{CoPc}(20)$ (nm scale) stack, with a low fit error function (0.049) indicating smooth layers in the overall heterostructure. (b) The x-ray diffraction peak at $\sim 45^\circ$ is for bcc (110) Fe sputtered on Cr. (c) The cross-sectional TEM image of the entire $\text{Si}/\text{SiO}_2//\text{Cr}(5)/\text{Fe}(50)/\text{CoPc}(20)/\text{Fe}(10)/\text{Cr}(5)$ (nm scale) stack, shows nominal thickness of the all the layers, which are in agreement with the actual deposition thicknesses.

resistance from $R(300\text{K}) = 32\text{k}\Omega$ to $R(17\text{K}) = 11\text{G}\Omega$ at 20mV underscores thermally activated hopping regime of transport across the CoPc spin chains.

Once field cooled, the magnetoresistance response of the device A induced by the application of an external field is recorded by imposing a fixed bias voltage to the metallic FM electrodes. The corresponding resistance (or current) of the device is measured as a function of the external magnetic field \mathbf{H} . The Figure 8.3 shows the magnetoresistance loops measured at ($T = 60\text{K}$, $V = 58\text{mV}$). Interestingly, a three resistance level symmetric $R(\mathbf{H})$ loop is observed. As the positive field is increased, the first resistance jump occurs near $\mathbf{H} = 0\text{T}$ (Fig. 8.3 gray dotted line), the second resistance change is centered at $\mathbf{H} = 1.17\text{T}$ (Fig. 8.3 magenta dotted line) and a third resistance change is observed for higher positive field sweeps $\mathbf{H} = 1.9\text{T}$ (Fig. 8.3

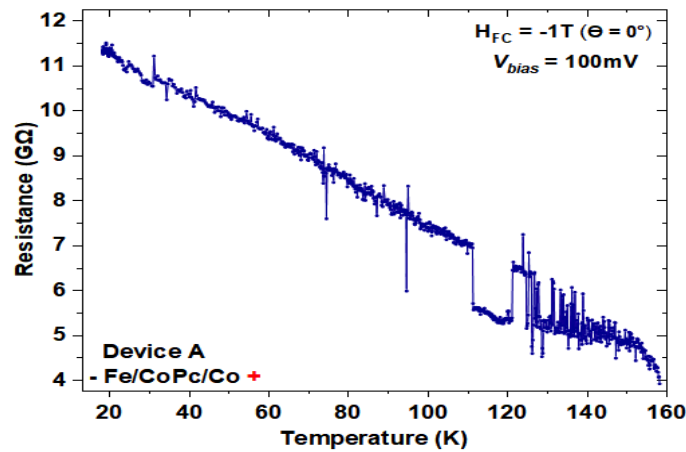


FIGURE 8.2: Resistance vs. Temperature, $R(T)$ plot of nano device-A : Fe/CoPc(20nm)/Co measured at bias $V = 100\text{mV}$ for in-plane magnetic field $H = -1\text{T}$. The positive lead of Keithley is connected to top Co and negative lead to Fe electrode.

black dotted line). To determine the origin of these resistance levels, it is crucial to understand the role of each layer in the device heterostructure.

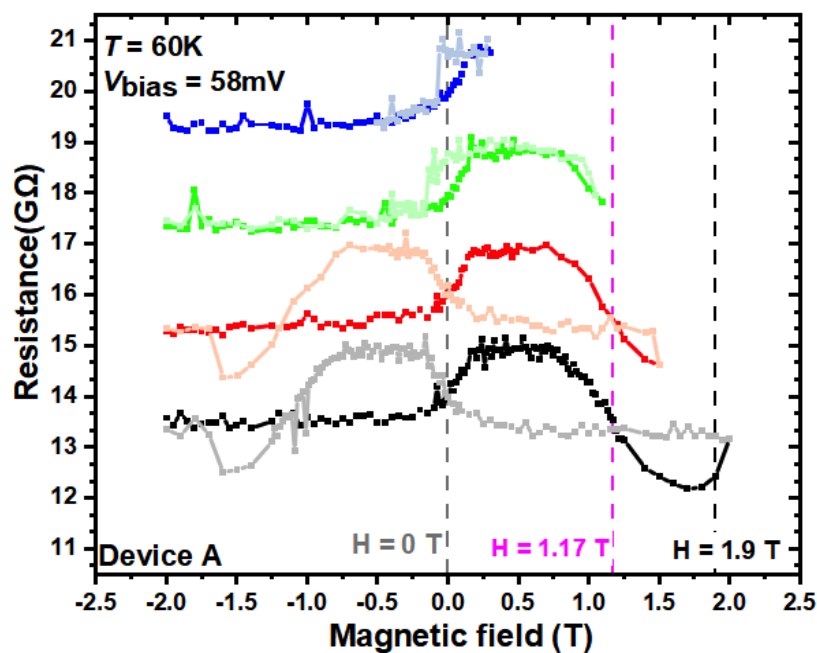


FIGURE 8.3: $R(H)$ data for device-A Fe/CoPc(20nm)/Co measured at 60K and 58mV. Minor (blue,green,red) and major (black) $R(H)$ loops show three resistance levels at $H = 0\text{T}$ (gray), $H = 1.17\text{T}$ (magenta) and $H = 1.9\text{T}$ (black). The return cycle of the field sweep i.e., from $H = +2\text{T}$ to -2T of the $R(H)$ is given by the gray, light colors of red, green and blue.

From our previous discussion in Chapter 3 we know that CoPc molecules deposited on top of the lower Fe electrode forms a chain-like channel for the spin-polarized transport (Figure 8.4a-e). The length of the arrows (magenta, cyan) within the green box (see Figure 8.4b) corresponds to the magnitude of the spin up and spin down channels in the bulk Fe FM, spinterface [101, 102] and the molecular spin chains. The spin polarization (P) of the current changes its sign [100] and its amplitude becomes very high when propagating from bulk FM metal to metal/molecule interface, detailed in Chap. 3, Sec. 3.4. The Fe/CoPc spinterface has $P < 0$ [100] and this spin-polarized current flows across the molecular spin chains' ground state (larger cyan arrow in solid green box). This is accompanied by a current with $P > 0$ across the MSCs' excited state (magenta arrow within the striped yellow/green box) because of molecular spin-flip excitations, see Chapter 3, Sec. 3.3.1.2. The inelastic excitation can result in the increase in current flow through the conjugated electron system by invoking the electronic transitions ($\Delta S = 0$ & $\Delta l = \pm 1$) in the CoPc spin chains from its ground to excited state. As a result of sign change of P , the spin-polarized currents generate magnetoresistance (MR) at ground state (MR_{GS}) and excited state (MR_{ES}) of the molecular spin chains respectively.

The functional parts of the heterostructure stack can be divided into three magnetic units namely: (a) The magnetically hard bottom unit (Fig. 8.4e lower green box), (b) top magnetic unit (Fig. 8.4e top green box) and (c) central unit (Fig. 8.4e mid striped box). The magnetically hard bottom unit comprises of bottom FM layer that is coupled across the spinterface to a molecular spin chain through exchange bias [108, 123, 124, 253, 254, 255, 256, 257]. In the spin chain's ground state, the bottom unit includes the MSC and represents one magnetic unit (thick green arrow in Fig. 8.4d). But, in the experimental conditions (Figure 8.5), the AFM spin chain is in the electrically excited state (Fig. 8.4c) and forms the central magnetic unit, see Figure 8.4e striped green/yellow (arrow+box). This excited MSC acts as a distinct steady-state magnetic unit and exhibits a low magnetic anisotropy and is exchange-coupled with energy J_{12}^{MSC} to the bottom FM layer. At the top interface, often times the metal atoms diffuse [258] into the molecular layers showcasing different molecular stacking [123] compared to the devices' bottom interface. This results in a slight

magnetic anisotropy and it is structurally complex. This is shown as faded region in the Figure 8.4e. The top magnetic unit's reversal occurs relative to the magnetically hard bottom unit since the latter has well-characterized physical properties. The three magnetic units are exchange coupled to one another through ECTop and J_{12}^{MSC} (Fig. 8.4e). ECTop is the exchange coupling between the top and the central magnetic units.

Using these three magnetic units we can understand the three resistance levels in the $R(\mathbf{H})$ of Figure 8.5, measured at (60K,58mV). The resistance level near $\mathbf{H} = 0\text{T}$ occurs due to the magnetization reversal of the top magnetic unit (top green arrow in Fig. 8.5). The resistance change at $\mathbf{H} = 1.17\text{T}$ is due to the excited spin chain switching its magnetic orientation due to exchange bias [108, 123, 124, 253, 254, 255, 256, 257] (striped green/yellow arrow in Fig. 8.5). Finally, the bottom magnetic unit switches at higher magnetic field values (bottom green arrow in Fig. 8.5). Therefore, the spin transport path in FM/CoPc/FM proceeds across the molecular Pc spin chains' ground and excited states relative to the corresponding magnetic units. With this understanding, we will explore in depth the system and see what interesting information can be unraveled about their ground and excited states within a device.

8.3 Effect of applied bias voltage on device transport.

8.3.1 Bias dependence of magnetoresistance:

The magnetotransport measurement of device-A at 17K for bias voltage $20 < V(\text{mV}) < 115$ shows interesting features in the $R(\mathbf{H})$ loops (Fig. 8.6a-e & Fig. 8.18). Unlike the $R(\mathbf{H})$ at 60K, the magnetoresistance loop is no longer symmetric at this low temperature and the final reversal now occurs at a much higher field $|\mathbf{H}| > 2T$. The magnetoresistance at the spin chain's ground state and excited state can be experimentally defined as : $MR_{GS} = [R(2T)/R(-2T)] - 1$ and $MR_{ES} = [R(H_f)/R(2T)] - 1$, where $H_f = 1\text{T}$ for $17 < T(\text{K}) < 50$ and $H_f < 1\text{T}$ for $T > 50\text{K}$. These MR contributions are sketched in the $R(\mathbf{H})$ loop for $T = 17\text{K}$, $V = 80\text{mV}$, see Figure 8.6a.

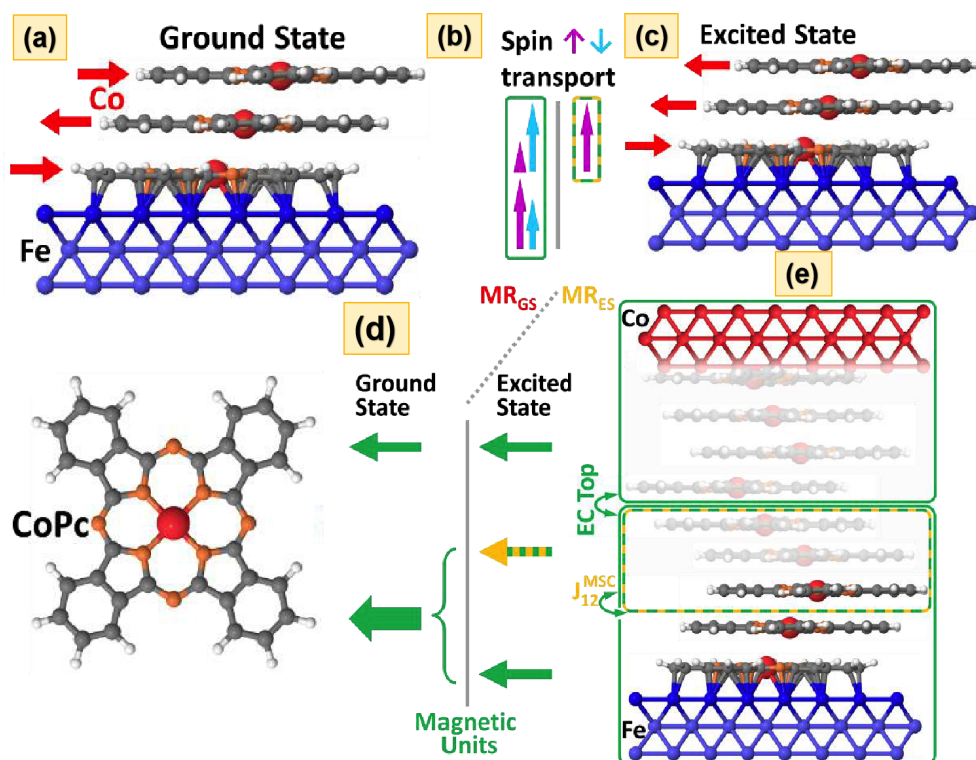


FIGURE 8.4: **Spin-flip magnetoresistance.** (a) CoPc has cobalt as the central metal atom with spin $1/2$ (red). CoPc molecular spin chain on top of an iron electrode. The first monolayer (ML) of CoPc deposited on Fe layer forms the metal/molecular interface. In the ground state the spinterface has FM-FM interaction while the rest of the spin chain has AFM order. (b) The colored arrows represent the spin up (purple) and down (cyan) channel: bottom arrows (long magenta+cyan) for bulk FM electrode, top arrows for molecular spin chains in ground (within green box) and excited (inside striped green/yellow box) states. Spin polarized transport across the spinterface and the MSC is given by the length of the arrows, with $P < 0$ in the MSC's ground state (large cyan arrow inside green box), which is increased by transport with $P > 0$ in its excited state (magenta arrow in the striped green/yellow box). (c) The excited MSC state can be electrically manipulated with respect to the spinterface. (d) Sketch of the magnetic units that promote the MR at ground (MR_{GS}) and excited (MR_{ES}). Transport across the ground state involves two magnetic units (thick green arrow) and top green arrow, while in the excited state an additional third magnetic unit (striped green/yellow arrow) which only contributes to the (MR_{ES}). (e) In the ground state transport involves two magnetic units containing the FM electrodes (only green boxes) coupled by ECTop. In the excited state the central magnetic unit (striped green/yellow box) is coupled to the lower magnetic unit by exchange energy J_{12}^{MSC} .

We observe that the magnetoresistance (MR_{ES}) at 17K decreases as the applied bias is reduced and vanishes for $V = 20\text{mV}$, see Fig. 8.6e, which shows only two resistance plateaus. So, for bias values $V < 20\text{mV}$, the nano transport channel is dominated by the ground state of the molecular spin chains. The $R(H)$ curves measured at

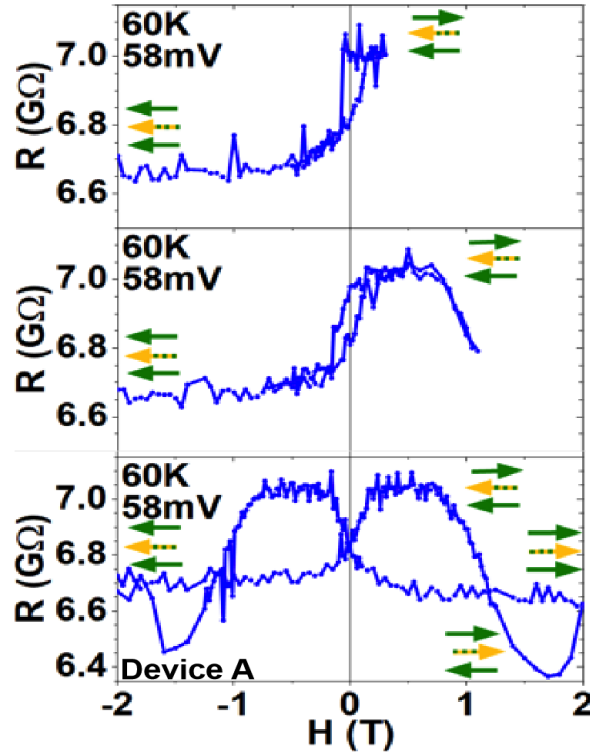


FIGURE 8.5: (a) The $R(H)$ loops at $T = 60\text{K}$ and $V = 58\text{mV}$ has three R levels due to the magnetization reversal of three magnetic units (green and striped green/yellow arrows).

negative bias values also exhibit similar behaviour at 17K , proving that the direction of applied bias does not affect our device magnetotransport (Fig. 8.7). Although, one might argue that at $\pm 100\text{mV}$ the MR_{GS} in the negative bias is less pronounced. This is because the current is driven from top Co to the bottom Fe electrode direction, where the CoPc arrangement is complex (see Fig. 8.4e top green box). Despite of the complex top interface the features observed for \pm bias are comparable. With this understanding, we opted to study our system in the positive bias voltages.

8.3.2 Bias dependence of differential conductance:

The device conductance can be studied by taking the first derivative of the current with respect to voltage bias (dI/dV). The bias dependence of dI/dV at 17K reveals a constant amplitude for $|V| < 35\text{mV}$ and large increase for $|V| > 35\text{mV}$ associated with peaks at $|V| \approx 70\text{mV}$, see Figure 8.8a (gray curve). The amplitude and jumps in conductance increase at higher bias voltages. These features in conductance are the signature of spin flip excitations, which has been reported in STM experiments [6, 7]

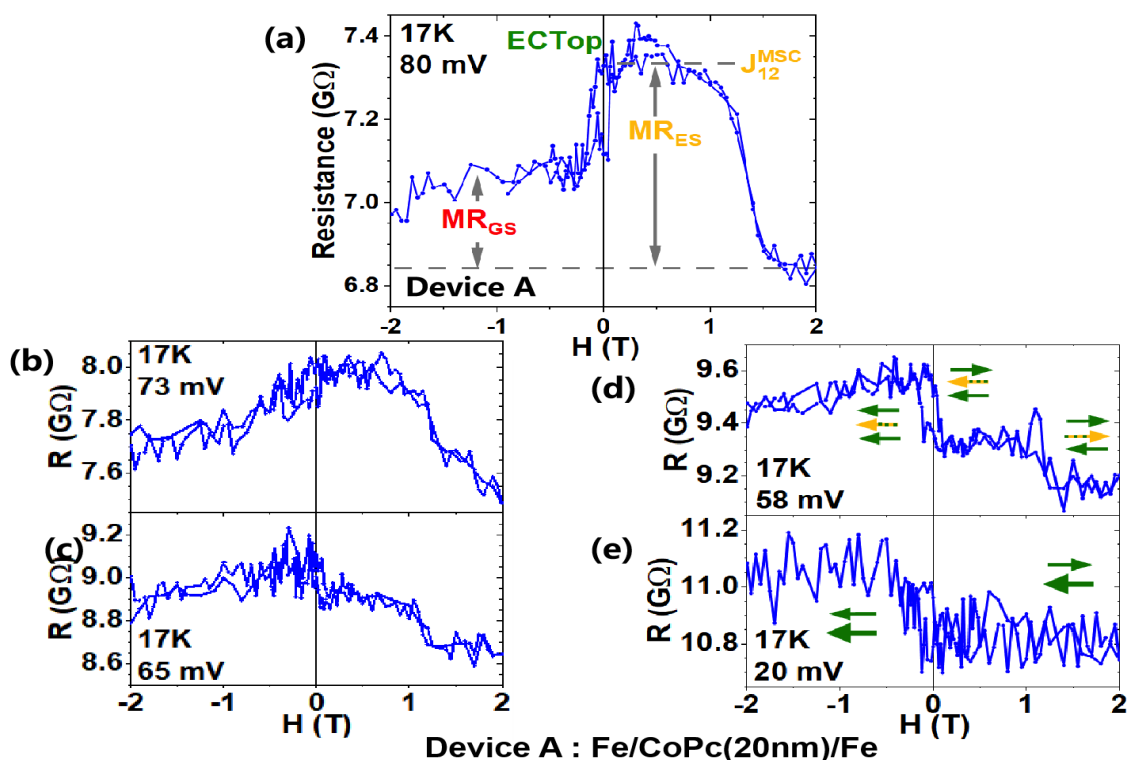


FIGURE 8.6: **Bias voltage dependence on $R(H)$ s.** (a-e) Experimental $R(H)$ loops measured at 17K for voltage bias $20 < V(\text{mV}) < 80$ between $H = \pm 2T$. The solid green and striped green/yellow arrows refer to the respective magnetic units in the system. The big green arrow in panel (e) includes both lower units in the absence of MSC excitations.

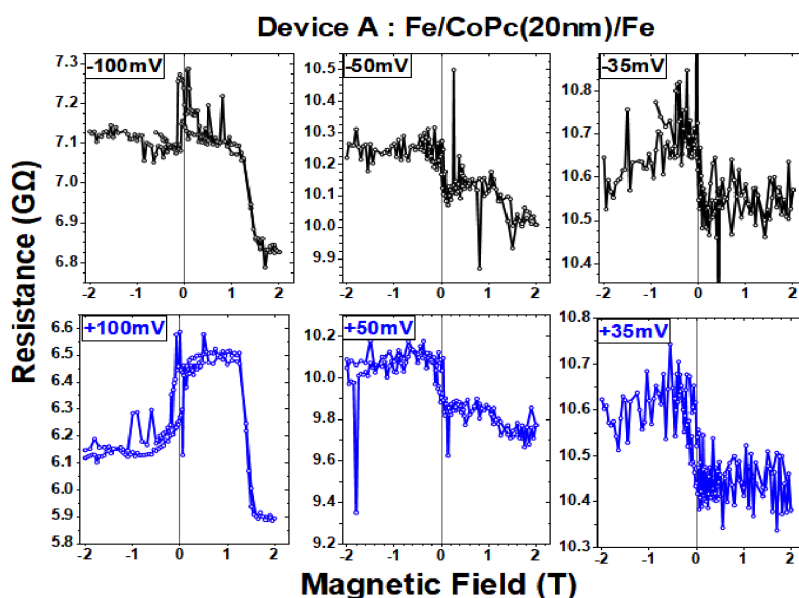


FIGURE 8.7: The $R(H)$ curves measured for a negative (black) and positive (blue) applied bias voltage at 17K.

and is clearly visible in our solid state device (details in Chap. 3, Sec. 3.3.1.2). The higher bias onset in our device compared to STM studies could be explained by the

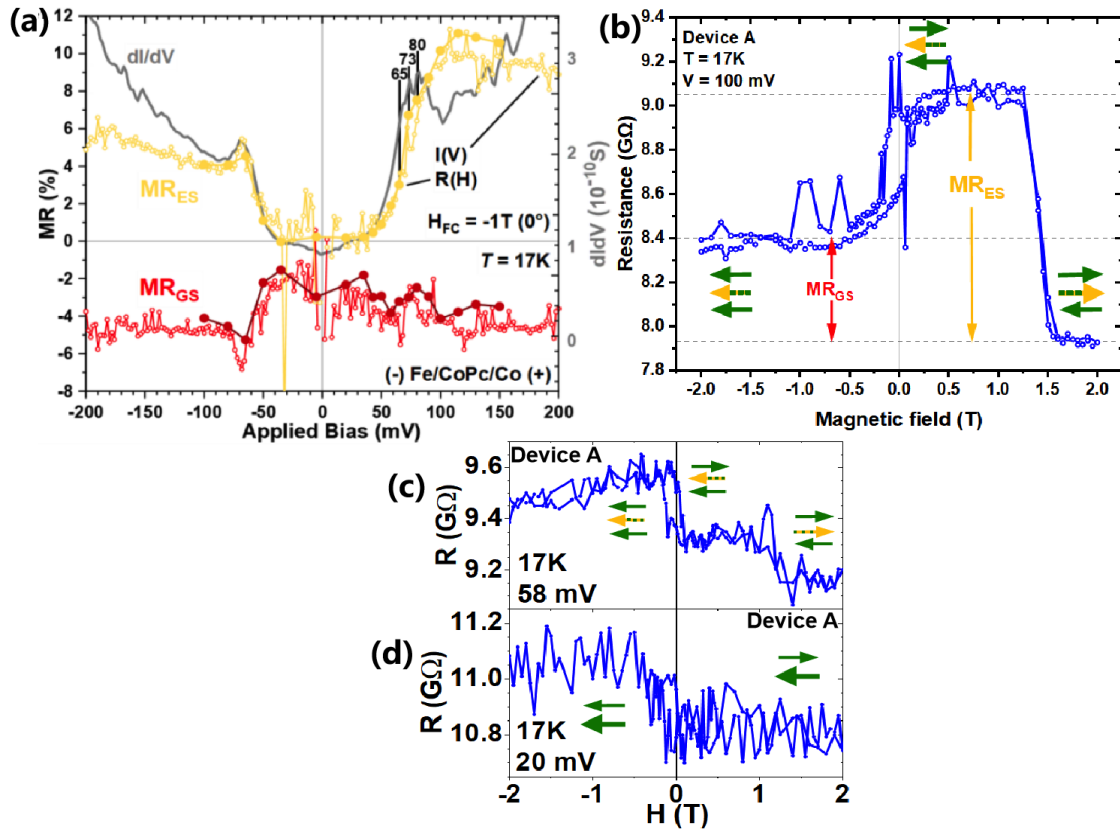


FIGURE 8.8: **Electrical onset of spin-flip magnetoresistance.** (a) The differential conductance (dI/dV -gray) as a function of applied bias voltage at 17K measured after a field cooling, $H_{Fc} = -1T$ in-plane magnetization. The bias dependence of MR_{GS} (red) and MR_{ES} (mustard) extracted from $I(V)$ (solid circles) and $R(H)$ (empty circles) data. (b) Example of MRs extracted from $R(H)$ at (17K, 100mV). The transport across the MSC in (c) ground and (d) excited states are described in the $R(H)$ s with two and three arrows respectively, to represent the magnetization units.

complex bias drop due to hopping transport across 20nm thick CoPc junction. This could also be the reason for the asymmetric differential conductance with different peak amplitudes for $V > 0$ and $V < 0$, alongside the spin-polarized transport explanation. Altogether, the features observed in the dI/dV are a direct proof that our organic devices' nano transport path involves the CoPc molecular spin chains.

The magnetoresistance of the excited (MR_{ES}) and ground (MR_{GS}) state spin chain is extracted from the $R(H)$ and $I(V)$ data at 17K, see Figure 8.8a. The respective resistance levels considered to extract MR from $R(H)$ is described in Figure 8.8b. Interestingly the extracted MR_{ES} tracks the dI/dV increase (Fig. 8.8a). This trace is a key highlight as it's the first observation of a specific MR signal being driven by a bias voltage and whose amplitude tracks the devices' conductance increase.

This is not expected for an electrically driven [259, 260] generation of interfacial MR at a spinterface because of magnetic hardening effect [108, 123, 124, 253, 254, 255, 256, 257] (refer Chap. 3. Sec. 3.5.1), above an electric field threshold to yield a MR term that scales with dI/dV . Following our interpretation of dI/dV , we conclude that MR_{ES} originates from the opening of spin-flip channels of transport across the molecular spin chains. The opposite sign of spin polarization of the spin-flip transport channel compared to the ground-state magnetotransport channel is manifested in the opposite signs of MR_{GS} (red -ve) and (MR_{ES}) (mustard +ve).

Suppose the excited MSC state merely opened a conductance channel with opposite P, then the MR in Figure 8.8a would eventually switch signs but the shape of $R(H)$ would remain identical. The presence of the resistance change at $H = +1.17T$ occurs only when a spin excitation current is present (compare Fig. 8.8c, 8.8d). This points out that a third magnetic unit (see fig.8.4e central striped green/yellow box) is responsible for the resistance change and its involvement in the magnetotransport across the spin chain in its excited state, and not in its ground state. This is cartooned in the magnetoresistance loops in Figure 8.8c, 8.8d, where the two magnetic units are for the transport across the spin chain's ground state and three units are for transport across the spin chain's excited state. Therefore, the excited MSC magnetic unit is responsible for MR_{ES} , which is electrically driven above a voltage bias threshold and also exhibits effective magnetostatic properties like its own coercive field (H_C).

8.4 Device characteristics as a function of temperature

8.4.1 Temperature dependence of conductance

Along with bias dependence, the $I(V)$ s were also studied as a function of temperature $17 < T(K) < 90$ at $H = +2T$, see Figure 8.9. The bias position of the kink in the $I(V)$ due to spin-flip excitation's decreases with increasing temperatures. This is more evident in the dI/dV data, where the kink begins to fade at $T \geq 72K$, see Figure 8.10. The changes in the conductance peaks can be due to the thermal smearing and thermally activated hopping effects.

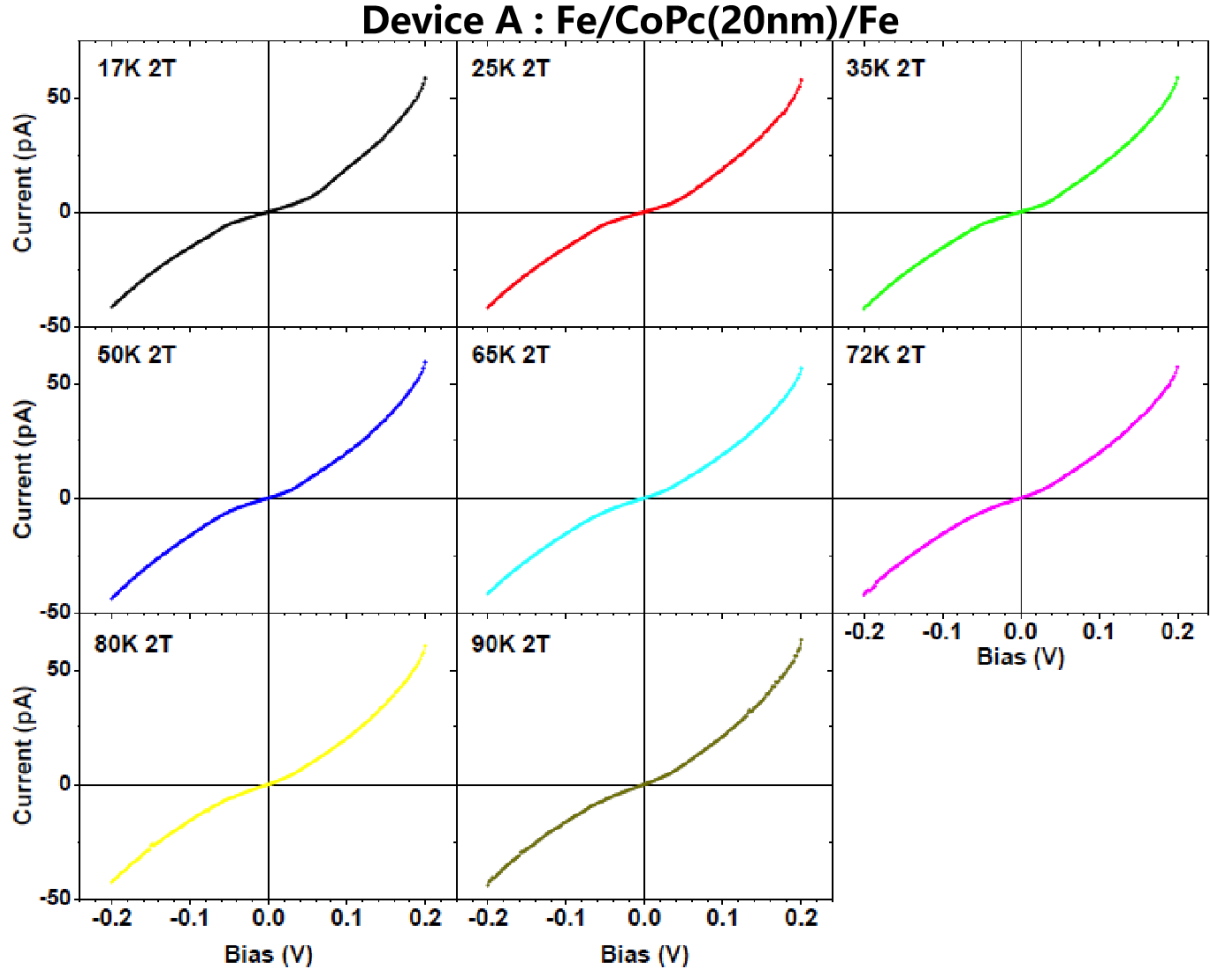


FIGURE 8.9: Temperature dependence of $I(V)$ data recorded on device-A for $17 < T(K) < 90$ at $\mathbf{H} = +2T$.

8.4.2 Temperature dependence of magnetoresistance

To explore the energetics of the excited spin chains, we performed temperature dependent magnetotransport studies for temperatures $17 < T(K) < 90K$ at $100mV$, see Figure 8.11. In the magnetoresistance plot (Fig. 8.11a) for $17 < T(K) < 55$, the same top and central magnetic units flipping is observed for $|\mathbf{H}| \leq 2T$. A symmetric $R(\mathbf{H})$ is observed for $60 \leq T(K) < 72$ (Fig. 8.11b, 8.11c) and here, along with top and central magnetic units the bottom magnetic unit also flips for $|\mathbf{H}| \leq 2T$. A sharp change in the \mathbf{H} dependence of MR_{ES} contribution is observed at $T = 72K$. For $T \geq 80K$, the $R(\mathbf{H})$ loop collapses and only low-field MR is observed up to $100K$.

The MR for the excited (MR_{ES}) and the ground (MR_{GS}) state of molecular spin

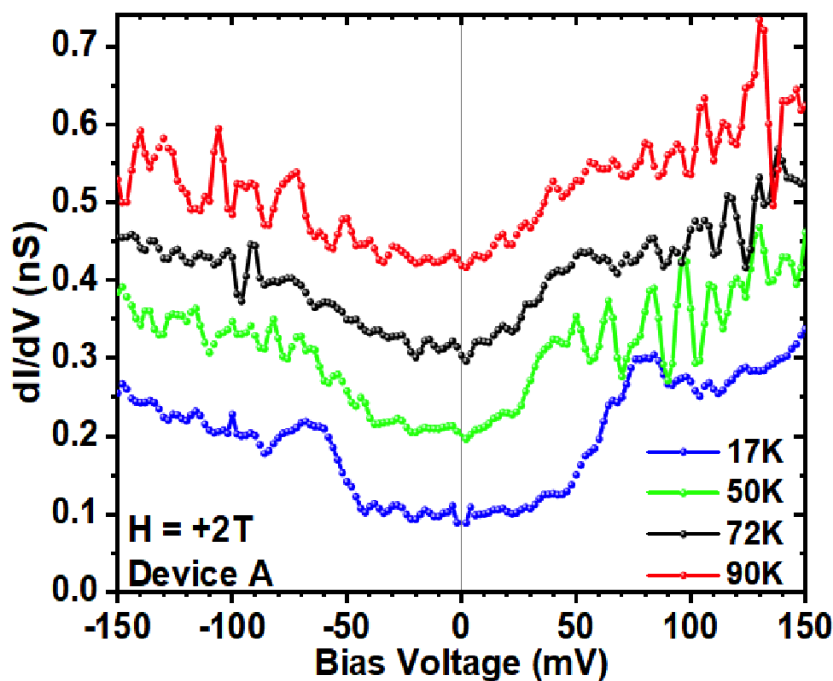


FIGURE 8.10: Differential conductance at various T for $H = +2T$ displays jumps above $\sim \pm 50\text{mV}$, which smooths out with increasing temperature.

chain is plotted for bias voltage 100mV at $17 < T(K) < 120$ (Figure 8.12). Throughout the explored temperature range the MR_{ES} has positive decreasing value and MR_{GS} has a negative increasing value. Both these MR's saturate above 90K . As already seen in Chap. 3. Sec. 3.3.1.1, the blocking temperature of CoPc spin chains in thin films is around $T_B = 100\text{K}$ [7], above which the AFM coupling is weakened, this explains the vanishing MR terms. This is a confirmation for spin-polarized transport across the spinterface and the MSC (ground & excited spin state). Along with temperature characteristics of excited states of MSC, the plot also shows the magnetostatic property i.e., coercive field (H_C) dependence between $17 < T(K) < 120$ (Figure 8.12). The coercive field decreases as the temperature approaches $T_B = 100\text{K}$ [7] of the CoPc MSC (details in Chap. 3. Sec. 3.3.1.1). All these results unambiguously point at the excited MSC being an independent magnetic unit.

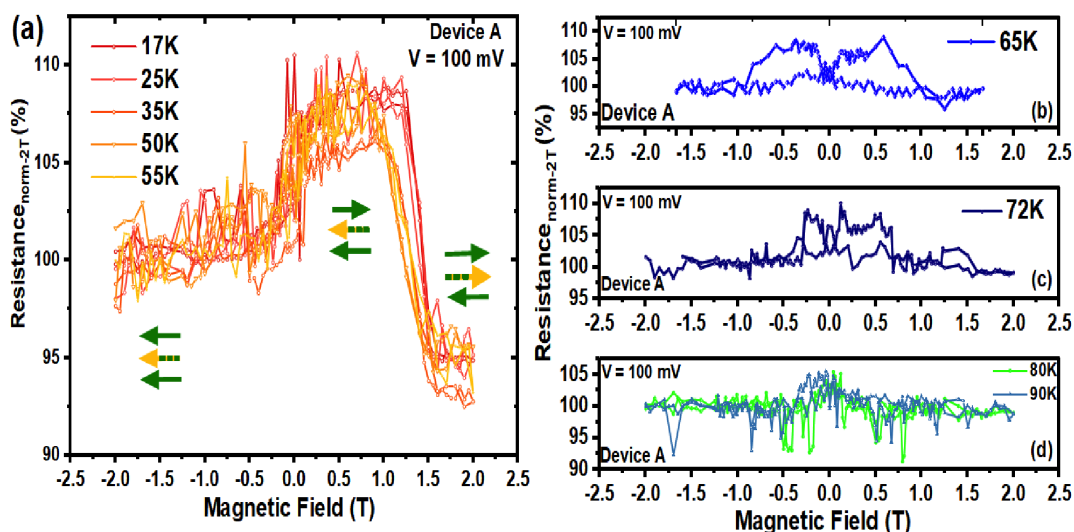


FIGURE 8.11: **Thermal stability of spin-flip magnetoresistance.** (a-d) $R(H)$ loops at 100mV for $17 < T(K) < 90$. The colored arrows represent the respective magnetic units flips. Solid green arrows are the top and bottom magnetic units and central striped yellow /green arrow is the excited MSC (same arrow notations as Fig. 8.4).

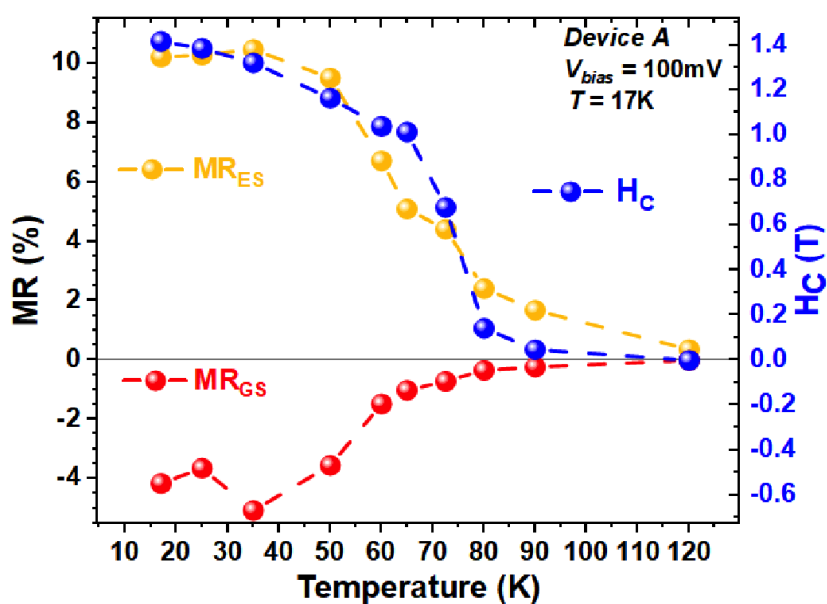


FIGURE 8.12: Temperature dependence of MRs of molecular spin chains at ground MR_{GS} (red), excited MR_{ES} (mustard) states and the coercive field (H_C) (blue) of the excited MSC

8.5 Additional CoPc based devices exhibiting MR

Besides the above discussed Fe/CoPc(20nm)/Co stack we also studied stack composition Fe/CoPc(10nm)/Fe. The change in the in the stack composition was intended to study the Co PM centers at SOLEIL synchrotron, so we made sure the Co signal

to be studied is coming only from the molecules hence the switch to the top Fe FM electrodes. Although our initial goal was to study the CoPc spin chain state using XAS/XMCD, but due the challenges already described in Chap. 7, Sec. 7.3.2 we turned our focus on to magneto-transport measurements.

We fabricated, processed and studied > 100 Fe/CoPc based MTJs and observed a range of resistances (Figure 8.13). All these results were possible thanks to our group's novel nano sphere lithography technique (see Appendix A). Here, we will see 300nm sized Fe/CoPc/Fe vertical MTJs which were studied in DEIMOS beam-line that exhibit unique MR characteristics and reproducible effects recorded previously in device-A : Fe/CoPc(20nm)/Co.

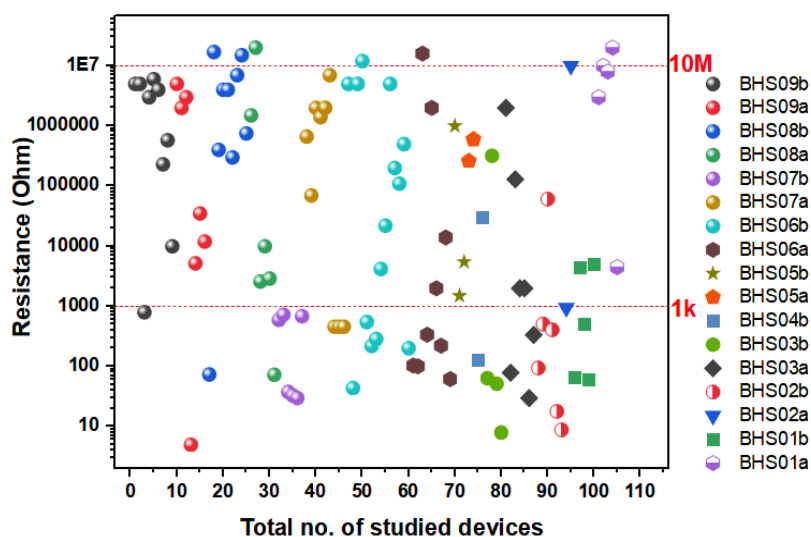


FIGURE 8.13: Scatter plot of few device resistances measured at $T = 300\text{K}$, $V = +10\text{mV}$ before wire-bonding. On sampling the $R\Omega <$ bottom electrode resistance and $R = \text{open circuit}$ were discarded and the rest were studied in the magnetotransport bench. Respective colored shapes correspond to the sample names on the right.

The $I(V)$ recorded in device B: $Si/SiO_x//Cr(5)/Fe(50)/CoPc(10nm)/Fe(10)/Cr(5)$ shows non-linear behaviour for an applied magnetic field almost in-plane to the device's electrode magnetization, Figure 8.14(a), for details on sample mount at DEIMOS see Chap. 7. The bias dependence of conductance is presented in Figure 8.14b. The device-B also exhibits a bias-asymmetric conductance plateau around $V = 0$, and jumps above $\pm 60\text{mV}$ indicating the opening of the spin channel transport (Figure 8.14b), thus reproducing the results observed previously in device-A:

Fe/CoPc(20nm)/Co (fig.8.8a). These results are for the first time recorded in a technologically advanced experimental MK2T set-up of the beamline DEIMOS (for details on set up refer Chap. 7. Sec. 7.3). It would have been nice to have detailed studies especially $R(\mathbf{H})$ data sets on this device-B, unfortunately the device state changed and became highly resistive due to external intervention during the measurements. This is one of the many experiences which taught us how fragile these devices are to any static electric currents.

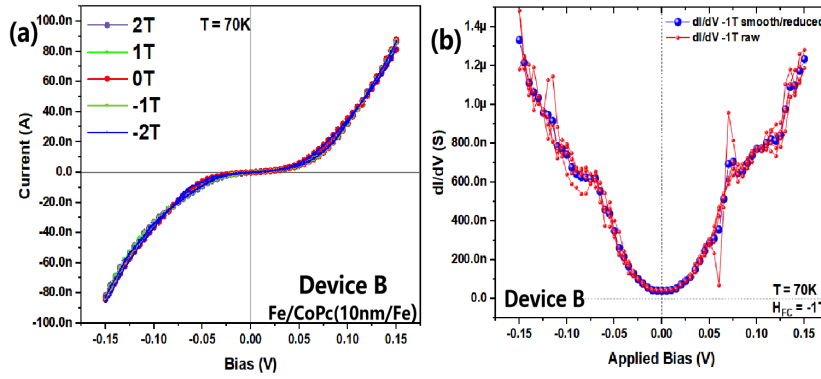


FIGURE 8.14: **Magnetotransport on Device-B : Fe/CoPc(10nm)/Fe.** (a) Non-linear, Ohmic IV at 70K for almost in-plane magnetic field values. (b) Bias dependence of conductance curve exhibits flat region then sudden jumps with increasing bias values signature of spin-flip excitations.

Nevertheless, we were able to successfully perform magnetotransport measurements on another sample at DEIMOS, namely, device-C : $Si/SiO_x//Cr(5)/Fe(50)/CoPc(10nm)/Fe(10)/Cr(5)$. The MR extracted from $I(V)$ s (Fig. 8.15a) follows the rising conductance at 60K, see Figure 8.15b. While describing the Fe/CoPc(20nm)/Co device-A, we experimentally observed that a MR term at $\mathbf{H} > 1T$ is electrically driven to appear across the device. This effect is reproduced on device - C : Fe/CoPc(10nm)/Fe, see Figure 8.15b. The dI/dV at $T = 60K$ shows a $\sim 20mV$ -wide conductance plateau around $V = 0$, followed at higher bias by a large increase in conductance (Figure 8.15b). The $R(\mathbf{H})$ performed within this plateau, precisely at $V = 10mV$, exhibits a fairly flat trace for $|\mathbf{H}| > 0.7T$, see Figure 8.15c. On the contrary, the $R(\mathbf{H})$ recorded at $V = -100mV$ (Fig. 8.15d) displays three resistance levels just like device-A and has a MR term around $\mathbf{H} \sim \pm 1.6T$. The sign change of all MR terms between the device-A : Fe/CoPc(20nm)/Co, and device-C : Fe/CoPc(10nm)/Fe is interpreted as the contribution from the sign change of spin polarization at the top spinterface

[100] (details in Chap. 3, Sec. 3.4). One of the objective of this thesis was to procreate the results of device-A. With the reproducible $I(V)$ s, dI/dV , $R(H)$ s recorded on devices -B (Fig. 8.14) and -C (Fig. 8.15) successfully validated the previous results on device-A.

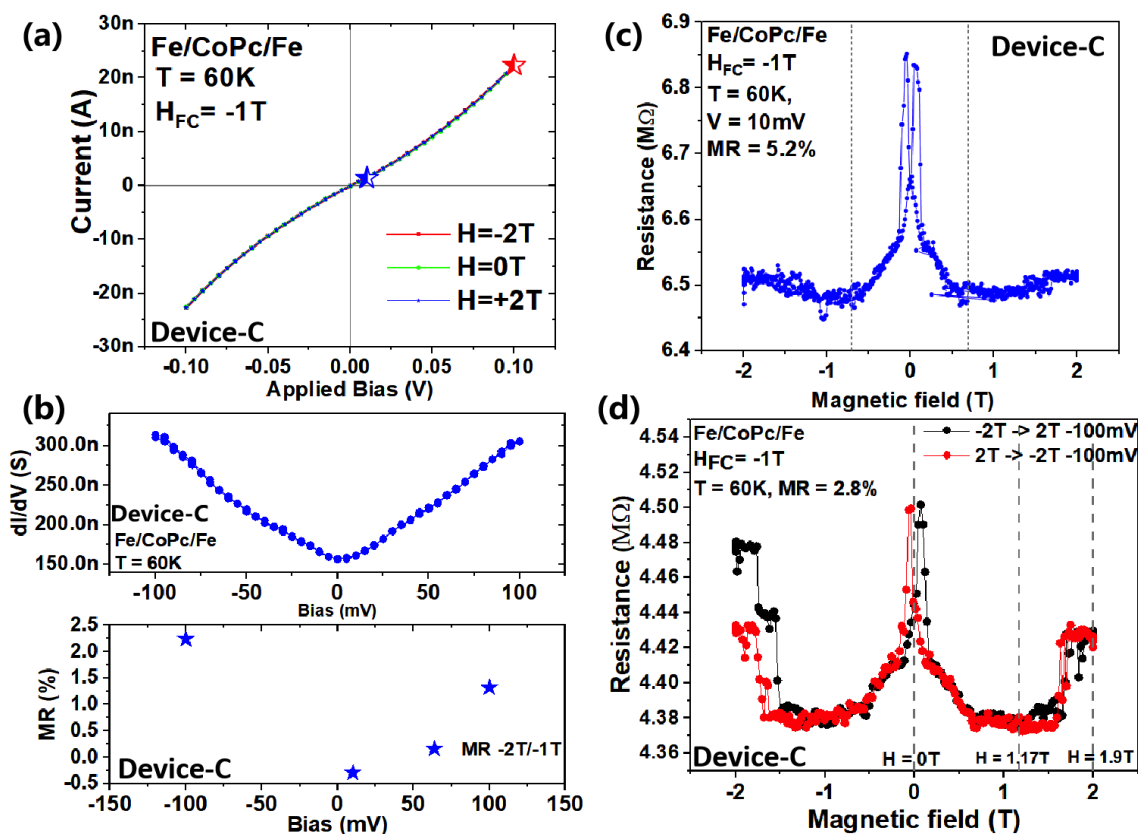


FIGURE 8.15: Magnetotransport on Device-C : Fe/CoPc(10nm)/Fe. (a) Non-linear, Ohmic $I(V)$ for almost in-plane applied magnetic fields at 60K. (b) differential conductance at 60K for 2T along with the MR extracted from $R(H)$ s following the increasing bias voltage similar to device-A. The $R(H)$ s recorded at (c) : 10mV and, (d): -100mV respectively after field cooling at -1T for $T = 60K$. The two $R(H)$ s are easily distinguishable by the huge jump in resistance above $|H| = 1.5T$ observed for -100mV. The red (blue) stars in $I(V)$ correspond to data points at which $R(H)$ s are performed.

8.6 The three macro-spin transport model

To verify our earlier interpretation of the experimental data set on Fe/CoPc(20nm)/Co, we propose a model using three magnetic units, namely : (1) top magnetic unit : top FM + neighbouring MSC's, (2) bottom magnetic unit : Fe coupled with spinterface to the MSC and (3) central magnetic unit comprises the portion of the AFM spin

chain in its electrically excited state. Together these 3 magnetic units form the basis of the three macro-spin model (Fig. 8.4e). This model is used to fit the experimental data on magnetotransport. The three macrospin model has the following parameters : two for each magnetic unit (top unit = t, central unit = c, bottom unit = b; anisotropy field = K and angle = θ), two coupling terms ECTop and J_{12}^{MSC} and two magnetoresistance coefficients MR_{GS} and MR_{ES} . The three magnetic units are coupled to one another such that the exchange coupling between the bottom and the top magnetic unit is named ECTop and the exchange coupling between the excited spin chains and bottom magnetic unit is J_{12}^{MSC} (Fig. 8.4e). The magnetoresistance MR_{GS} is associated with flipping the magnetization of the top magnetic unit relative to the bottom magnetic unit (MR Top/Bottom), and MR_{ES} is the MR between the top and central magnetic units (MR Top/Central).

To model the magnetotransport data in a phenomenological manner, the effective anisotropy field K of the nano-transport path across the top (i = t), central (i = c), bottom (i = b) units are written as :

$$K = -\mu_0 \sum_{i=t,c,b} H \cdot m_i + \frac{1}{2} \sum_{i=t,c,b} K_i \sin^2(\theta_M - \theta_K) - \sum_{i=t,b} C_{ci} m_c \cdot m_i \quad (8.1)$$

where, $\mathbf{H}(T)$ is the external magnetic field and for each unit, m_i is the reduced magnetization, θ_{Mi} the magnetization angle, $K_i(T)$ is uniaxial anisotropy field with an easy axis angle θ_{Ki} . Note, here we treat the magnetizations of the two FM units as identical and large compared to the magnetization of CoPc, which is neglected because, as an AFM spin chain, it has a very low magnetization at remanence, if any. Finally, C_{ci} is the coupling strength between the central (c) and outer (b,t) magnetic units and $C_{ci} = \text{ECTop}$ and $C_{cb} = J_{12}^{MSC}$. At each field step K is minimized to yield for each magnetic unit the magnetization's in-plane orientation. The resistance $R(\Omega)$, due to the non-collinear reduced magnetizations \mathbf{m}_t , \mathbf{m}_c and \mathbf{m}_b is given as :

$$R = R_0 \cdot \left[1 - \frac{MR_{GS}}{2} \cdot (m_t m_b - 1) - \frac{MR_{ES}}{2} \cdot (m_t m_c - 1) \right] \quad (8.2)$$

The modelling proceeds from the experimental data of $R(H)$ s at 17K (Fig. 8.16 a-e) and 60K (figure 8.5) assuming the sequential magnetization reversal of the three magnetic units. In the model the three MR terms potentially define the effective $R(H)$ data, Figure 8.17. Each MR term has a specific magnetic field (H) dependent signature (Fig. 8.17a). The $R(H)$ data sets can be fitted using MR Top/Central and MR Top/Bottom terms (i.e. MR_{ES} and MR_{GS} , respectively). As illustrated in Figure 8.17b, the data for (17K, 20mV) can be fitted using only MR Top/Bottom trace (compare with Fig. 8.16e). Additionally, the experiment data shows that the MR upon reversing the top magnetic unit is made to switch its sign as the spin excitation conductance channel is opened with the increasing bias voltage. This is true for the MR term upon flipping the bottom magnetic unit's magnetization. These two aspects are sketched in Fig. 8.17b, for case of 17K, 100mV which is experimentally observed at 80mV (Fig. 8.16a). Thus $R(H)$ data for (17K, 80mV) is reproduced by adding a MR Top/Central trace to the MR Top/Bottom trace.

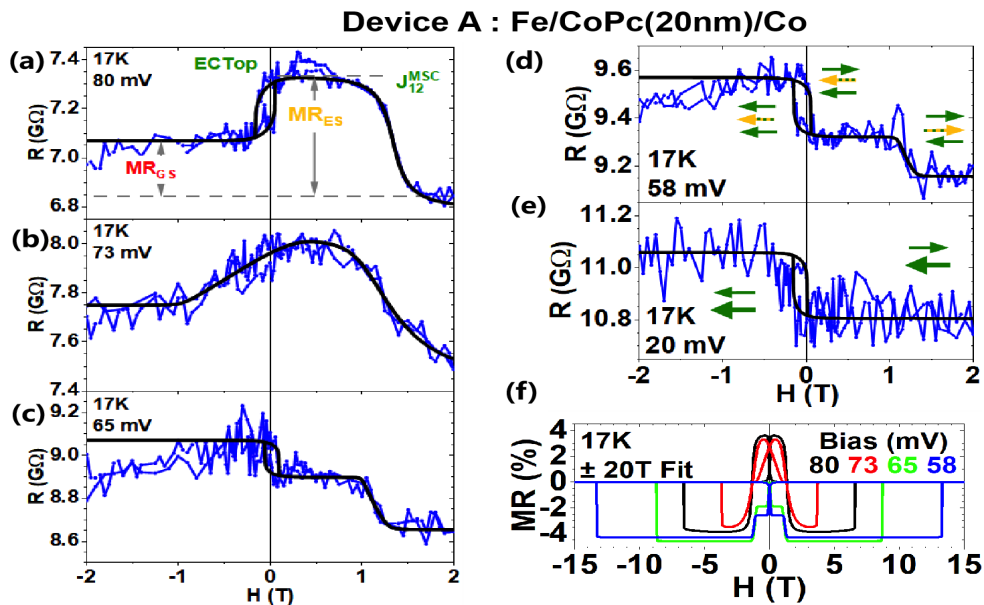


FIGURE 8.16: Macrospin Model Fit of bias dependent $R(H)$ s. (a-e) Experiment (blue) and fit (black) $R(H)$ loops at 17K for $20 < V(\text{mV}) < 80$. The green and striped green/yellow arrows are for the magnetic units in the system. For 20mV panel (e), only two magnetic units are sufficient compared to panel (d), the thick green arrow accommodates both lower units in the absence of spin excitations. (f) This panel represents all the fits upto $\pm 20\text{T}$ at 17K for bias $20 < V(\text{mV}) < 80$.

While modelling, the 'free layer' property was imposed to the central magnetic unit : $K_c = 5\text{mT}$. This aspect is exhibited in the experimental data set of $R(H)$ for

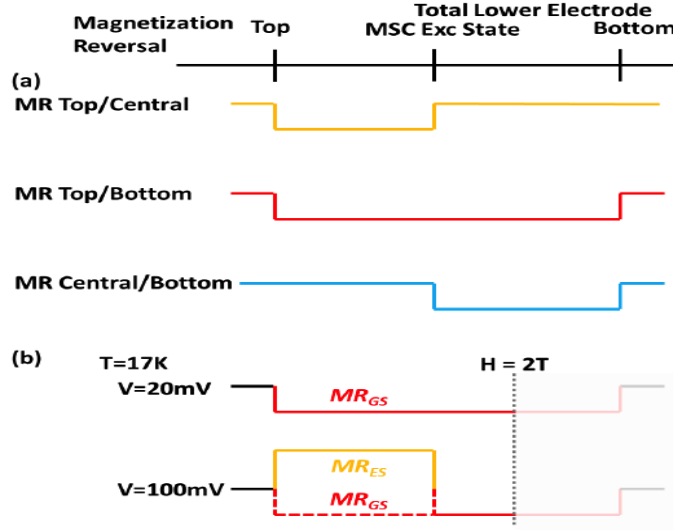


FIGURE 8.17: **Rationalization of magnetization reversals and magnetoresistance (MR) terms.** (a) Corresponding MR traces upon flipping pairs of the magnetic units in the system. For simplicity MR is assumed to be less than zero in all cases. (b) Two examples of the sequence followed in fitting the experimental MR data at 17K for 20mV and 100mV. At 20mV only one MR Top/Bottom term is used to fit the experimental MR data. At $V = 100\text{mV}$, the R change upon flipping the top unit magnetization, switches from a decrease to an increase as V is increased, so the MR trace is fitted by combining two terms MR Top/Bottom and MR Top/Central terms.

(17K, 115mV), see Figure 8.18a. The external magnetic field at which the magnetization of the central magnetic unit reverses is mostly driven by its coupling (J_{12}^{MSC}) to the bottom magnetic unit (Fig. 8.18g). The bottom layer's anisotropy field K_b defines the shape of the central magnetic units magnetization reversal, i.e., sharpness of the onsets and slope of the reversal; θ_b is mostly constant, see Figure 8.18(f,g). In agreement with the previous reports [9, 8, 256] the exchange biased Fe layer is magnetically hard at 17K with $K_b \sim 10\text{-}20\text{T}$, which tracks the spin-flip current amplitude (compare Fig. 8.8a with Fig. 8.19c), while its temperature dependence (8.19i) follows the exchange bias amplitude previously observed [9, 8, 256].

A minimum value of $K_b \approx 10\text{T}$ is necessary to avoid the symmetric $R(H)$ for $V < 35\text{mV}$. Finally, the minor loops due to the two magnetization reversals at low fields (0.22T, 0.3T) were reproduced by fitting the top magnetic unit's K_t and θ_t , see Figure 8.18b,c. Since, the top magnetic unit's $K_t \sim 0.2\text{T}$ which is over an order of magnitude stronger than that of the free layer (Fig. 8.19a), we infer that it contains not only the top Co FM electrode but also MSC (Fig. 8.5). During the curve fit, care was taken

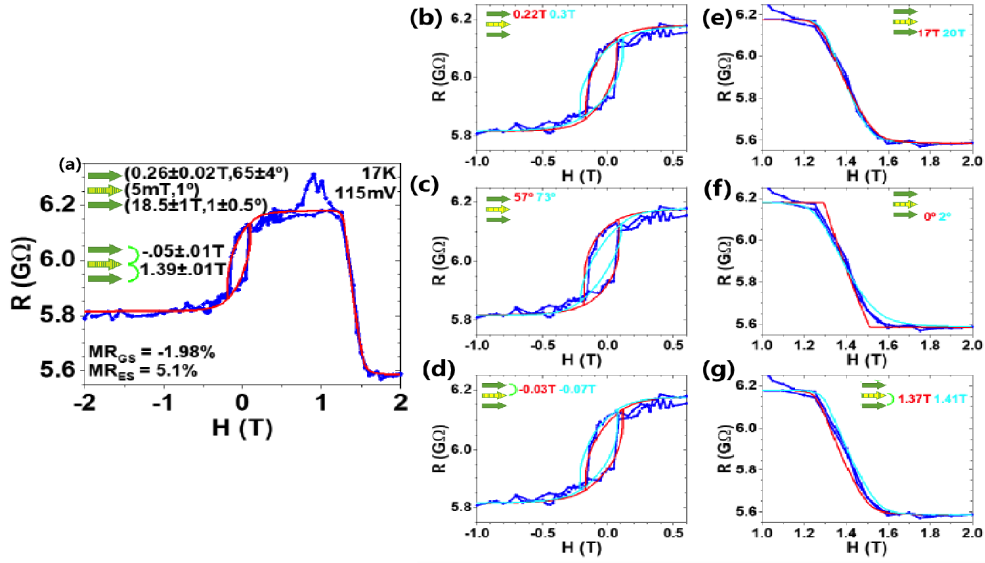


FIGURE 8.18: **R(H) fitting procedure using three macrospin model.** (a) The experiment (blue) data and the fit (red) for $R(H)$ at 17K and 115mV. The parameters with error bars of the fit are shown with focus on experimental data (blue) and two fits outside the error margin (cyan, red) for (b) K_t (T); (c) θ_t (degree); (d) $ECTop$ (T); (e) K_b (T); (f) θ_b (degree) and (g) J_{12}^{MSC} (T).

to respect the squareness of the loop and the evolution of $R(H)$ from saturation to remanence. The $R(H)$ loop's voltage bias shift was set using $ECTop$, see Figure 8.18d. The Figure 8.19(a-i) has the error bars depicted with all the parameters constant, the parameter range within which the fit is still considered correct after visual inspection.

Along with bias dependence, the temperature dependence of $R(H)$ is also modelled using the three macrospin model. As per our magnetotransport model, the change in magnetic field H dependence of MR_{ES} (see Fig. 8.20a-f) is associated with a sudden decrease in J_{12}^{MSC} for $T > 65K$ (Fig. 8.19h). This corresponds to a magnetic anisotropy energy barrier, $E_{SF} = 5.9 \pm 0.3 meV$, i.e., a threshold thermal energy to magnetically decouple the MSC in its excited state from the exchange-biased Fe layer and spinterface.

To fit the experimental MR values, the $R(H)$ data was fitted using MR_{GS} and MR_{ES} terms. But, as we have already seen in the bias dependence section, the $R(H)$ loop does not necessarily assure a full magnetization reversal within the $|H| < 2T$ experimental window. Hence, the fitting was done starting with high voltage bias

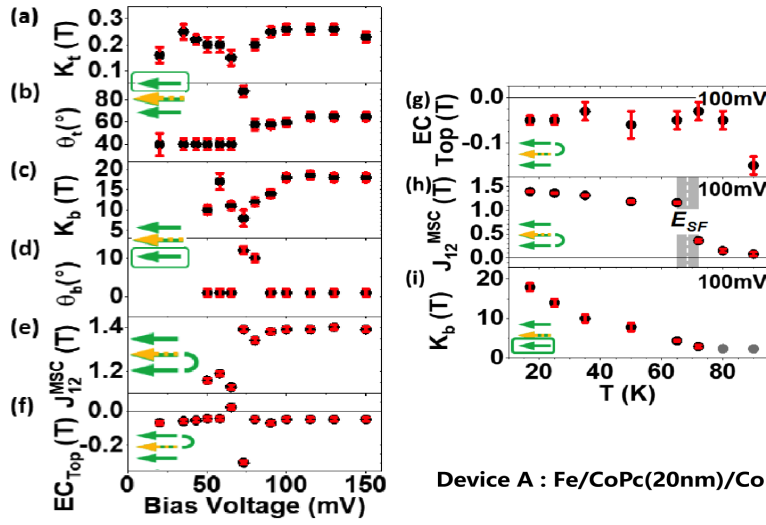


FIGURE 8.19: **Bias and Temperature dependence of fitting parameters.** (a-f) Bias dependencies of anisotropy fields' strength (K) and angle (θ) for (a-b) top and (c-d) central magnetic units. Bias dependency of the exchange coupling terms (e) J_{12}^{MSC} and (f) EC_{Top} . The fitting parameters K_t and θ_t are for top magnetic unit (a,b) ; K_b and θ_b are for bottom magnetic unit. (g-i) Temperature dependencies of (g) EC_{Top} , (h) J_{12}^{MSC} , and (i) K_b . The vertical gray zone in panel (h) is the magnetic anisotropy energy barrier, $E_{SF} = 5.9 \pm 0.3 \text{ meV}$ for $T \equiv 70 \text{ K}$. Black are the data points, red is the error bars and the two gray data points in panel (i) for $T > 80 \text{ K}$ are the minimum values needed to achieve $R(-2T) \neq R(2T)$. These error bars (a-i) provide a range to model the transport measurements so the fit can be acceptable after visual inspection. Note that an example of the values of the parameters can be found in

Fig. 8.18a.

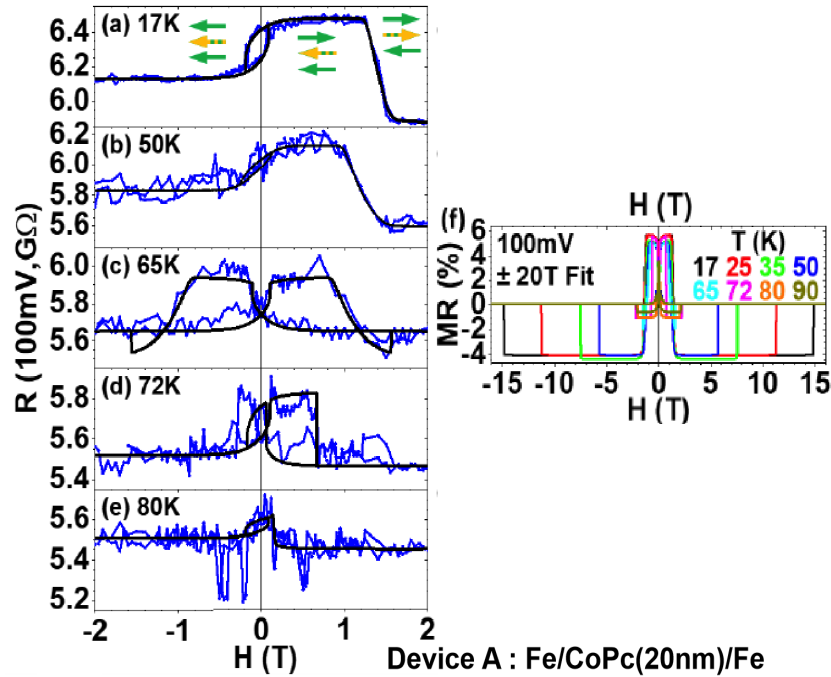


FIGURE 8.20: **Model fit of temperature dependence of $R(H)$ for device-A.** (a-e) The $R(H)$ experimental (blue) and fitted (black) curves for $17 < T(K) < 80$ at 100mV & $H = \pm 2\text{T}$. The arrows represent the three magnetic units observed in these T ranges. (f) Summary of fitted $R(H)$ s for high magnetic field $H = \pm 20\text{T}$, 100mV & $17 < T(K) < 90$.

data set (17K, 115mV), see Figure 8.18. For this $R(H)$ data, the resistance is mostly flat for $H < 0$ and also for $1.7 < H(\text{T}) < 2$, assuming that these plateaus imply full magnetization reversal. As the voltage bias or the temperature was altered, the evolution of the plateau at $1.7 < H(\text{T}) < 2$ was closely monitored, and the respective MR_{GS} and MR_{ES} values were adjusted accordingly to imitate the $R(H)$ trace in this magnetic field range. The Figure 8.21 presents the experimental and the fitted MR values observed for $V > 0$. The fitted MR terms tracks their experimental counterparts with only slight deviations. This endorses the 3-macrospin model's initial assumption relating to the initial fully aligned magnetic state at $H = -2\text{T}$, and the definitions of MR_{GS} and MR_{ES} terms.

8.7 Magnetic anisotropies along CoPc nano-transport path

To examine the conditions for and the symmetry of magnetic anisotropies along the nano-transport path, we first investigated the field cooling settings. For this we

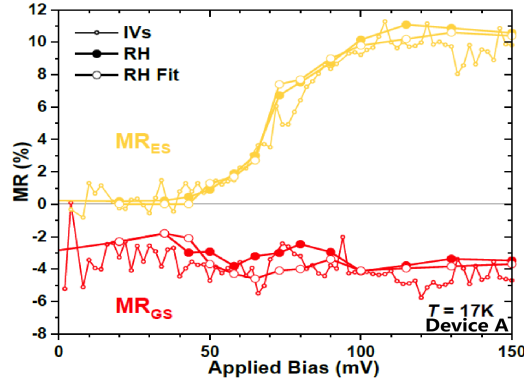


FIGURE 8.21: **Experimental and fitted magnetoresistance terms.** The experimental MR_{GS} (red) and MR_{ES} (mustard) obtained from IV and $R(H)$ data and fitted (empty circles) MR_{GS} and MR_{ES} parameters.

present the $R(H)$ data in Figure 8.22a, which was recorded after field cooling (FC) the junction from 120K to 25K at 100mV, while maintaining the in-plane angle of the external magnetic field, $\theta_H = 0^\circ$. The red $R(H)$ loop is for FC at $H = -1T$. The blue $R(H)$ curve is for zero field cooling (ZFC), which is achieved by initially applying a +2T field at 120K and then cooling down to 25K with $H = 0^+T$, this results in flipping of the $R(H)$ curve about the $H = 0$ axis. The same effect is also observed at 17K, when θ_H is switched from 0° to 180° (Figure 8.22b).

The angular dependence of MR_{GS} at 17K (Figure 8.23) reveals unidirectional behaviour for both with (100mV) and without (-50mV) the spin-flip excitations along the molecular spin chains observed in the conductance graph (Fig. 8.8a). Due to the additional MR_{ES} term at 100mV and our $|H| < 2T$ measurement window, it is not possible to follow the angular dependence of MR_{GS} for angles $30^\circ < \theta_H < 135^\circ$, as there is no resistance plateau in the $R(H)$ at 17K for $1.7 < H(T) < 2$. Along with this reason and the fact that the 1T resistance level becomes undetermined at intermediate angles, are also a reason to be unable to study the angular dependence of MR_{ES} . We also varied the amplitude of the applied bias voltage which is applied during field cooling. The $R(H)$ loop does not show any significant changes (Figure 8.24). Overall, it is quite evident from the above discussed data sets that it is the orientation of magnetization of the ferromagnetic electrodes during the field cooling that determined a unidirectional anisotropy along the nano-transport channel, which is in agreement with our discussion in Chap. 3, Sec. 3.5.2.

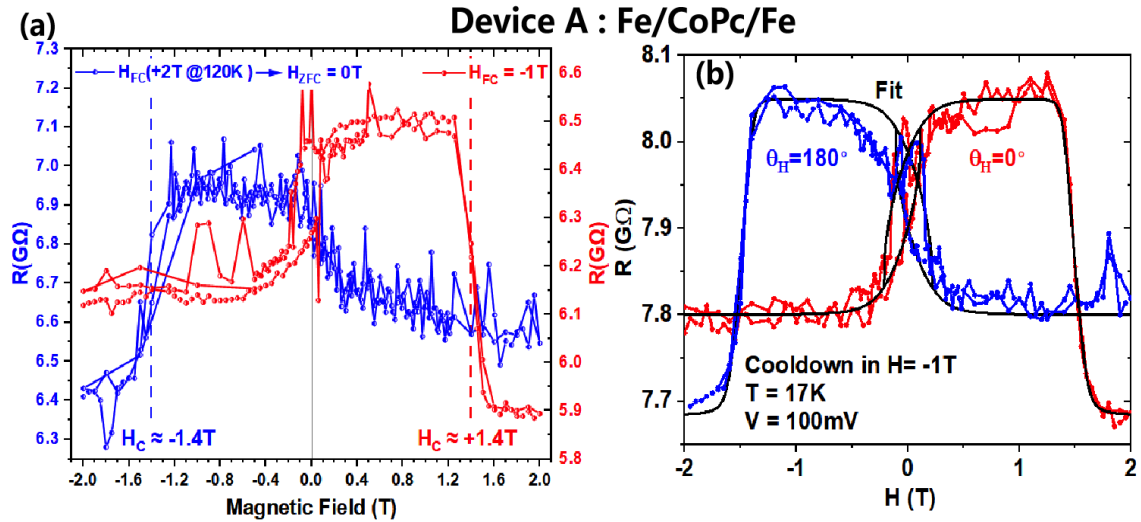


FIGURE 8.22: **Establishing the magnetic anisotropy from magnetotransport.** (a) $R(H)$ curves recorded for in-plane angle $\theta=0$ at 25K for 100mV after field cooling in $H = -1T$ (red) and $H = +0T$ (blue). (b) $R(H)$ acquired at 17K at 100mV for $H_{FC} = -1T$ at $\theta_H = 0^\circ$ (red) and 180° (blue). The black curve is the fitted data. First the $\theta_H = 0^\circ$ data was fitted then the same parameter set was used but the simulation was launched for $\theta_H = 180^\circ$. The change in resistance for $H = +2T$ to $-2T$ between the panels (a & b) is due to the minor evolution of device resistance during the ~ 100 hrs measurement and the associated field cooling procedures. The fitting parameters in panel (b) are as follows : $K_t = 0.28T$, $\theta_t = 70^\circ$, $K_b = 21T$, $\theta_b = -1^\circ$, $E_{CTop} = -0.05T$, $J_{12}^{MSC} = 1.49T$, $R_o = 7.8G\Omega$, $MR_{GS} = -1.4\%$ and $MR_{ES} = 4.8\%$. Small differences between the parameters reflect the evolution in device magnetotransport during the measurement cycles.

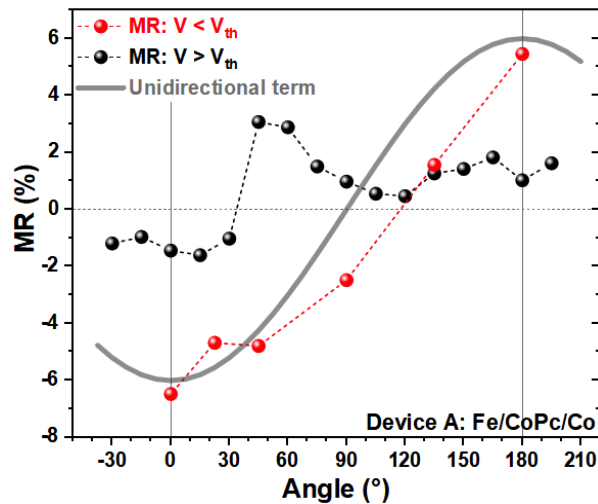


FIGURE 8.23: **Angular dependence of MR_{GS} at 17K** : for $V = -50mV$ (blue) and $V = +100mV$ (red). Note that at $V = -50mV$ no spin excitations along MSCs and $V = +100mV$ with spin excitations along the MSCs observed in the device conductance.

The Figure 8.25, presents the experimental and the fitted $R(H)$ data at (17K,

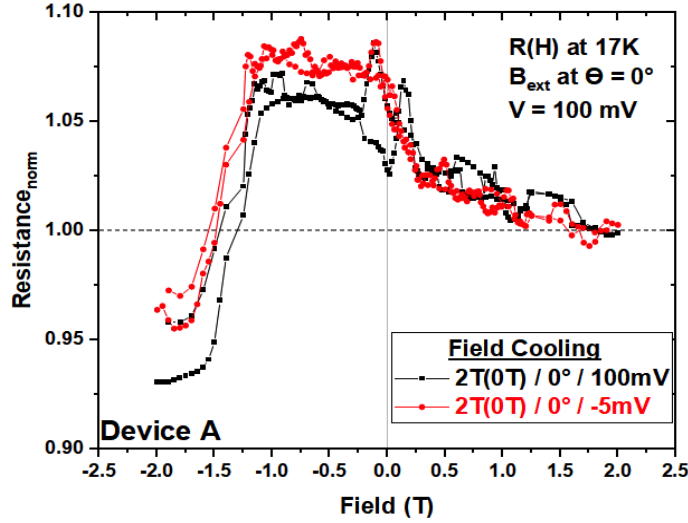


FIGURE 8.24: $R(H)$ loops measured in-plane angle at 17K for a field cooling initial $H = +2T$ for two applied bias values. (a) 100mV black curve and (b) -5mV red curve. The applied bias does not affect the magnetotransport while field cooling. The $R(H)$ loops were recorded at 100mV.

100mV; i.e. with the additional spin-flip conductance channel) for significant values of the in-plane angle θ_H of the external magnetic field. The $R(H)$ fit was done by adjusting the in-plane angle of H while preserving the same parameters. We thus only qualitatively reproduce features of the experimental $R(H)$ at intermediate angles, whereas an exact fit is obtained when the fitting parameters found for $\theta_H = 0^\circ$ are used for $\theta_H = 180^\circ$ (see Fig. 8.22b). This might reflect the limitations of our three macro-spin model's assumption, or the presence of higher-order terms within a more complicated model.

Most of the magnetotransport features observed in our experiment can be successfully fitted using our three macrospin model, however, best models are all imperfect. The compartmentalization of our model's parameters to $R(H)$ features fails at three critical points, namely, point A : 17K, 73mV (Fig. 8.16b) and point B : 17K, 80mV (Fig. 8.16a) on the dI/dV peaks of Figure 8.8 a; and point C : at 72K, 100mV (Fig. 8.11c). At critical points B and C, it is impossible to maintain 'free layer' properties for the central magnetic unit : $K_c \sim 3000Oe$ and $\theta_c = 13^\circ$. At critical points A and B, we have $\theta_c = 11^\circ$. There are also deviations in $ECTop$ and θ_t at critical point A, which are associated with a jump in exchange coupling energy J_{12}^{MSC} to a higher molecular chain, nearly constant value. These deviations are observed in the Figure

8.19a, which gives the bias dependence of the parameters used to fit the $R(H)$ at 17K. Interestingly, the K_b scales with dI/dV and MR_{ES} . This emphasizes the origin of the spin referential that the molecular spin chain in its excited state has inherited to become a comprehensive magnetic unit. The mutual couplings of otherwise independent model parameters indicate that the three magnetic units become dynamically coupled at these above mentioned critical points. Mainly due to two reasons, namely, first because of the changes induced by the spin polarized (SP) current in the spin-flip conductance channel's fully SP current, via spintronic anisotropy [261] (critical points A and B) and secondly, by the thermal fluctuations [262] - critical point C. This is also a feature of the exchange-bias systems near criticality [262].

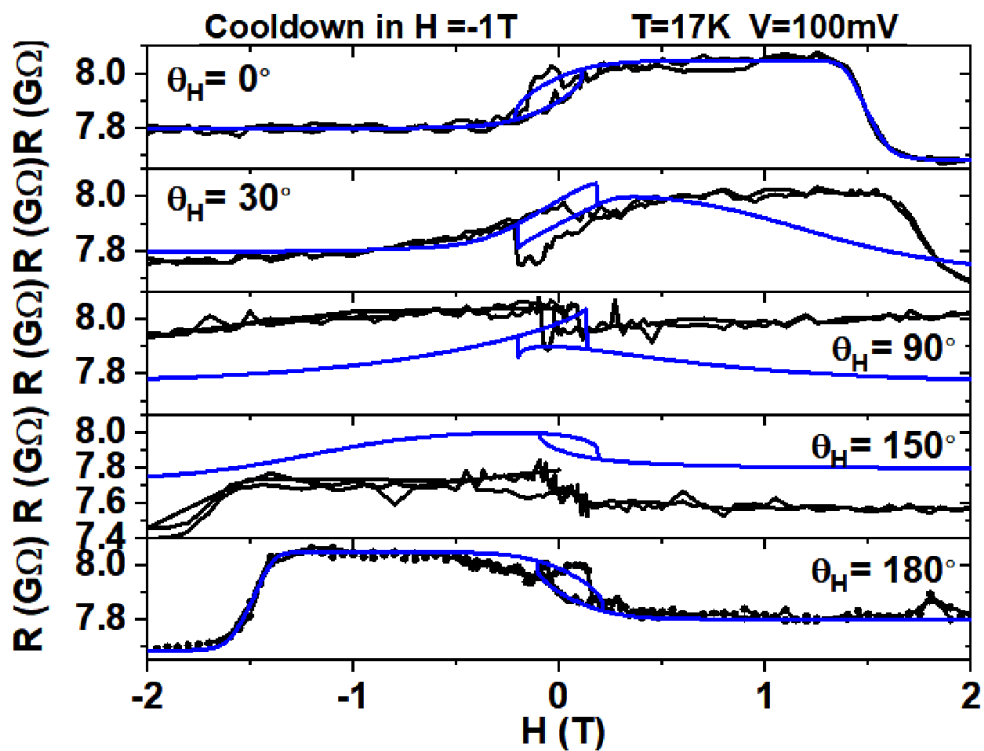


FIGURE 8.25: Angle dependent $R(H)$ of device-A at 17K, 100mV for $HFC = -1T$ for in-plane angle θ_H of the external magnetic field $0^\circ < \theta_H < 180^\circ$. Blue curves are the experimental data and modelled data is in black.

8.8 Study of structural and magnetic properties of Fe/CoPc spinterface using DFT calculations

To review the structural and magnetic properties of the CoPc molecular spin chain on top of our bcc Fe(110) layer (fig. 8.1), and to confirm the identification of the third magnetic unit as the excited state of our MSC, our collaborators in IPCMS performed density functional theory (DFT) calculations. This was done by using the Vienna ab-initio simulation packages [263] (VASP) and utilized the projector augmented waves (PAW) pseudopotentials as provided by VASP.

In Chap. 3, Sec. 3.5.1 we have already witnessed the magnetic hardening scenario [108], where the first molecular monolayer and the topmost monolayer of the FM electrode become anti-aligned relative to the underlying monolayers of the FM layer. Raman et al. [108] calculated the inter-atomic magnetic exchange coupling between the surface Co atoms and found to be reduced from 8.54meV per atom to 1.34meV per atom upon molecular adsorption. Due to this strong molecule-induced change to the surface magnetism, ΔE , the energy difference per atom upon anti-alignment, is reduced [108] from $\Delta E = 190.9\text{meV}$ to $\Delta E = 26.4\text{meV}$. This enables, without any external electric field, the magnetic decoupling of the topmost Co layer and ZMP molecule from the underlying Co film.

But in our bcc Fe(110)/CoPc system the molecular adsorption does minor changes to the surface magnetic properties. We see that for Fe bcc(110)(5ML)/CoPc(1ML), the adsorption of CoPc onto Fe reduces the magnetic moment of the iron surface atoms only by a little i.e., from $2.67\mu\text{B}$ to $2.51\mu\text{B}$. As a result, anti-aligning the magnetization of the surface monolayer of Fe (and the FM coupled CoPc layer) relative to the buried FM monolayers increases the system's energy by $\Delta = 200.5\text{ meV}$ per Fe atom. This value is marginally reduced compared to $\Delta E = 242\text{meV}$ for a naked Fe layer. For $\Delta E = 200.5\text{meV}$ per Fe atom, the corresponding [264] thermal energy of $\sim 2400\text{K}$ that is highly incompatible with the 70K thermal energy (Fig.8.19 h) at which the electrically spawned magnetic unit becomes coupled to the underlying FM electrode. Adding molecular layers on top of it will not drastically modify this

picture. Hence, we conclude that this ‘magnetic hardening’ [108] scenario cannot explain our experimental data.

To examine the impact of the molecular spin chains on the magnetic properties, the number of Fe layers were reduced from 5ML to 3ML in order to maintain a reasonable supercell size. Initially, we considered a geometry in which the 2nd CoPc molecule is centered atop of the 1st CoPc molecule with 45° rotation. This is the ‘on-top’ case, which is depicted in Figure 8.26a. In the second geometry taken into consideration the 2nd CoPc molecule is shifted, without rotation, relative to the 1st CoPc molecule, see Figure 8.26b.

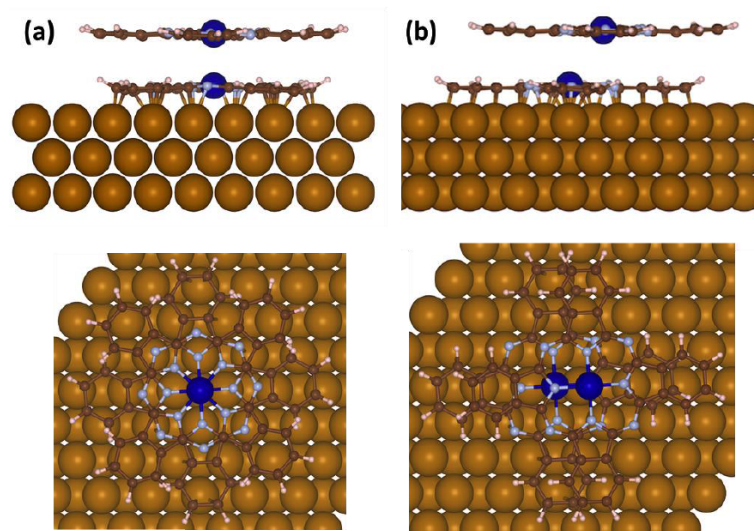


FIGURE 8.26: Top and side view of the adsorption geometries considered for bcc Fe(110)/CoPc(2ML) system. (a) ‘on-top’ and (b) ‘shifted’. The shifted case has lower energy, hence it is more energetically favorable.

The tables [Case (a) 8.1, Case (b) 8.2] offers the calculated energy of the bcc Fe(110)/ CoPc(2ML) system for both ‘on-top’ (console 8.26a) and ‘shifted’ (console 8.26b) cases, and also the intermolecular distance that minimizes the energy in each case. One can notice that, at energy minimization conditions obtained by varying the intermolecular distance, the ‘shifted’ scenario displays a lower energy than the ‘on-top’ scenario, and therefore is energetically more favorable. Moving on to the magnetic anisotropy, a 11.8meV energy difference between the AFM ground state and the excited FM state is observed.

Adding the third CoPc molecule to the system gives the final bcc Fe(110)/CoPc(3ML)

$d_{\text{CoPc-CoPc}}(\text{\AA})$	$E_{\text{AFM}}(\text{meV})$	$E_{\text{FM}}(\text{meV})$	$\Delta E(\text{meV})$
2.8	-448.20	-361.40	-86.81
2.9	-618.39	-536.20	-82.18
3.0	-681.14	-606.38	-74.76
3.1	-672.66	-607.52	-65.15
3.2	-616.76	-561.84	-54.92
3.3	-528.56	-483.22	-45.34
3.4	-420.51	-383.55	-36.96

TABLE 8.1: The total energies calculated for the ground AFM state and excited state of the bcc Fe(110)/CoPc(2ML) system. The intermolecular distance between two CoPc molecules is varied. The total energy of the system is shown when the top CoPc molecule's magnetic referential is aligned (FM) or anti-aligned (AFM) with that of the underlying CoPc and the Fe layer. The two cases are for the two scenarios for the second CoPc layer. Case (a) : when the second CoPc lies on top of the first one rotated by $\pi/2$.

$d_{\text{CoPc-CoPc}}(\text{\AA})$	$E_{\text{AFM}}(\text{meV})$	$E_{\text{FM}}(\text{meV})$	$\Delta E(\text{meV})$
2.9	-918.12	-902.26	-15.86
3.0	-1030.35	-1016.63	-13.72
3.1	-1054.52	-1042.73	-11.80
3.2	-1019.19	-1009.09	-10.10
3.3	-945.09	-936.48	-8.60
3.4	-846.83	-839.52	-7.30

TABLE 8.2: In case (b) the second CoPc layer is shifted with respect to the first one. The total energy is with respect to a reference energy of -2743 eV.

system, see Figure 8.27. The ground state has lowest energy when the molecules are shifted with respect to each other. The adsorption distances are shown in Fig. 8.27, and the magnetic moments for each transition metal atomic type are presented in Table 8.3.

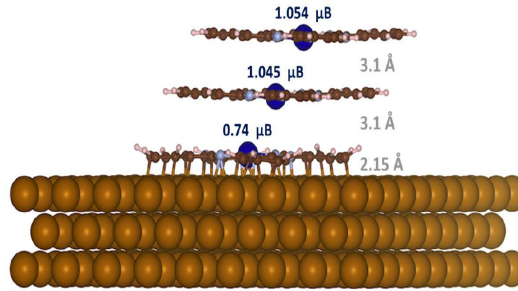


FIGURE 8.27: **Adsorption geometry of bcc Fe(110)/CoPc(3ML).** Molecular adsorption distances (\AA) and the magnitude of the magnetic moment (μ_B) of the cobalt atom of the respective ML of CoPc.

	Ferromagnetic Layer			Molecular Layer		
	Fe (bottom)	Fe (middle)	Fe (top)	Co (bottom)	Co (middle)	Co (top)
Magnetic moment (μ_B)	2.68	2.46	2.57	0.74	1.05	1.05

TABLE 8.3: Magnetic Moment on Fe and Co atoms in the FM layer and the molecular layers

The on-site spin density in the ground and the first excited states is described in Figure 8.28(a,b). The first spin flip of the third CoPc molecule with respect to the lower two molecules is about 6.14meV and is rationally agreeable with the 5.9meV thermal energy threshold for magnetic decoupling that was observed experimentally, more details in Table 8.4. Since the 1st CoPc is chemisorbed onto Fe [6, 265], the 1st CoPc molecules of the MSC is the 2nd CoPc ML atop of Fe. Thus the energy $E = 6.1\text{meV}$ is $E \approx E_{crit}$, when the magnetization of the 3rd CoPc molecule is reversed relative to that of the 1st and 2nd CoPc MLs atop of Fe (Fig. 8.4c). Using this knowledge, if we revisit the experimental $R(H)$ dataset in Figure 8.11, the sharp change in the field dependence of the MR_{ES} contribution is observed at $T = 72\text{K}$ i.e, $E_{crit} = k_B T = 6.14\text{meV}$ (compare Fig. 8.11a-c with 8.11d). Also, our argument of the disappearance of the conductance peaks at $T = 72\text{K}$ (Fig. 8.10) due to the thermal smearing and thermally activated hopping regime is justified by the DFT calculated 5.9meV thermal energy of the MSC. In addition in our magnetotransport

model we associated the change in \mathbf{H} dependence of MR_{ES} (see Fig. 8.16a-e) to a sudden decrease in the exchange coupling J_{12}^{MSC} for $T > 65K$ (Fig. 8.19h) [6] which corresponds to the anisotropy energy barrier, E_{SF} . This energy E_{SF} is a threshold thermal energy required to magnetically decouple the MSC in its excited state from the exchange-biased Fe layer and the spinterface. The calculated value of E_{SF} was found to be $5.9 \pm 0.3 meV$. This is in agreement with the DFT-calculated $\Delta E = 6.1 meV$, the energy difference between the molecular spin chains ground and excited spin states when coupled to the ferromagnet.

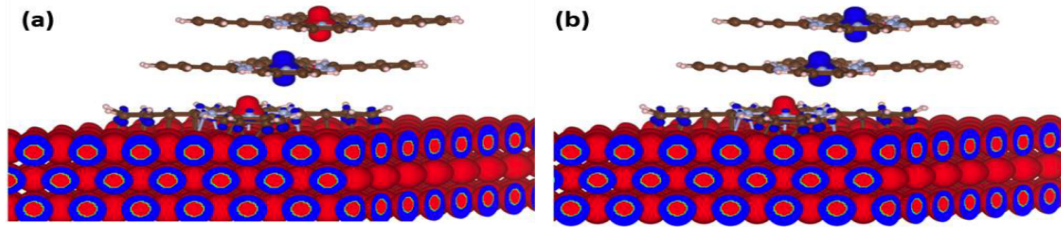


FIGURE 8.28: **Spin density plots of bcc Fe(110)/CoPc(3ML) for shifted scenario.** The spin are color coded the spin up (\uparrow) is red and spin down (\downarrow) is blue. (a) The panel represents the anti-ferromagnetic spin alignment ($\uparrow\downarrow\uparrow$) for the ground state. (b) The panel represents the lowest excited state with spin alignment ($\uparrow\downarrow\downarrow$). The energy cost to flip the upper CoPc spin is $6.14 meV$.

Configuration	$E_{\uparrow\downarrow\uparrow}(eV)$	$E_{\uparrow\downarrow\downarrow}(eV)$	$\Delta E(meV)$
On-top	-3167.92256	-3167.91951	-3.05
Shifted	-3168.04920	-3168.04306	-6.14

TABLE 8.4: **DFT calculated total energies for the AFM ground and the first excited state of the bcc Fe(110)/ CoPc (3ML) system,** as seen in the previous Fig. 8.28 for the ‘shifted’ case. The first row is for the case (a) wherein three CoPc molecules are on-top of each other. The second row represents the case (b) where the molecules are shifted (‘shifted’ case) with respect to one another.

8.9 Summary

Using a novel resist- and solvent-free nano-sphere lithography technique, we designed spintronic nano devices made up of molecular spin chains of CoPc molecular barriers sandwiched between FM electrodes. By performing magnetotransport measurements for varied (T, V, θ) , we have extracted the fundamental properties of the excited spin chains within a solid state device. The electrically spawned excited state

promotes a change in sign of the current's spin polarization and also has its own coercive field, making it an magnetically distinct unit. This generates a MR contribution (MR_{ES}) against the FM electrodes within a fixed spin reference, which exhibits a temperature dependence. This enables information to be encoded at magnetic remanence in the magnetic orientation of the spin chain's excited quantum state in a solid-state device. The DFT calculations clearly identify the excited spin state as the source of the encoding by comparing its thermal stability with experiment. Additionally, our three macrospin transport model elaborates the role of magnetic coupling between the spin chain and the FM electrode in promoting the encoding capability. We found $J/k_B = 72\text{K}$ for Fe/CoPc system as the calculated value of anisotropy energy barrier, $E_{SF} = 5.9 \pm 0.3\text{meV}$ is consistent with the DFT-calculated $\Delta E = 6.1\text{meV}$ energy difference between the molecular spin chains ground and excited spin states when coupled to the FM. Altogether, our model can help to better understand most intricate features of magnetotransport observed in FM/CoPc/FM solid state device.

The magnetotransport results across these devices have successfully implemented the exchange bias concept [266] at FM/molecule interfaces [123, 124, 254] within the device's active CoPc MSC spintronic layer, and resonate with the concepts of spin-flip spectroscopy [96] and spintronic anisotropy [17, 261] adds to the progress in molecular spintronics discussed in Chap. 3. This work extends the former magnetotransport research across AFM materials [242, 267, 268, 243, 244] into quantum regime, and suggests towards interesting magnetometry studies [161] of the MSC ground and excited states.

Although the electric alteration [259, 260] of the charge transfer that results in the spinterface [102] and interfacial MR [108] is appealing, our strategy of electrically manipulating the quantum states of CoPc molecular spin chains away from the spinterface is advantageous. Indeed, this opens the ability to electrically manipulate the amplitude/sign of MR using low-voltage addressing, and to transmit spin-wave encoded [250] information across an CoPc barrier using antiferromagnetic molecular spin chains in a pulsed voltage method. This encoding scheme is robust and can be technologically viable. Electrically controlling the quantum state of a MSC could help mature antiferromagnetic spintronics [269] at the quantum level.

Chapter 9

Large spintronic harvesting of thermal fluctuations using paramagnetic molecular centers

Multifunctional devices are always in demand, especially those that can add smart functionalities while being environmentally friendly. After successfully encoding information using a novel lithography process in organic devices (Chap. 8), in the current chapter we will explore how a multifunctional device can be realized by tweaking the materials of our previous FM/CoPc/FM stack composition.

Some of the exotic properties, like quantum superposition, quantum coherence, entanglement in quantum mechanics can, if tapped, solve several of society's existing problems. For example, increasing interest in quantum communications [270] (satellite, internet), quantum computers [271] are all based on the above mentioned quantum properties, and will soon dominate the technology market. However, one field that has needed a fresh, 'quantum' perspective is thermodynamics. Work has thus progressed on model quantum heat engines, in order to understand and utilize the quantum advantage here too. However, the low level of maturity has entailed the study of quantum engines mainly with a complex design and external control parameters (microwave/laser sources) that are required to operate the engine's cycle (see Chap. 4). Generally, the cycle of a classical engine involves the conversion

of heat into work by the transfer of heat from hot to cold thermal bath using a working fluid or substance (WS). The process increases the entropy of the system, and the temperature ratio of the thermal baths gives the engine's maximum efficiency at zero power output. This is called Carnot efficiency and it encompasses the second law of thermodynamics.

In Chapter 4, we have seen quantum engines performing close to Carnot efficiency [151, 150] and even surpassing [152] classical limit by refurbishing its underlying concepts. The quantum properties (e.g. quantum coherence) of engines' baths and WS comprises the 'quantum resources' that can provide 'ergotropy' which is the maximum amount of work extracted from a quantum system at a given state [272, 273]. Here, the working substance cannot merely exhibit internal coherence [274], instead a coherent superposition of quantum states are created during the operation of the engine [152]. So, the return from the non-passive state for instance a population inversion to the passive state channels ergotropy into actual work. Thus the quantum working substance can store useful energy just like a flywheel [275, 154] or battery [276].

A working substance with many-body quantum correlations can result a finite power at Carnot efficiency [277]. In this case, the power correlates with heat capacity, which is reduced when coupled to a thermal bath [278], and deviates when the WS undergoes a phase transition [277]. Interestingly, there exist non thermal baths that are also quantum resource. Generally, two varieties of non-thermal baths are known. The first type is a squeezed bath, meaning that the bath is unable to fully thermalize the WS on the time frame of the interaction due to a small energy spectral density [279]. In this type the Carnot limit becomes irrelevant, but it can generate a local non-passive state of the WS viz. ergotropy. In the second type of a non-thermal bath, the bath can inject quantum coherence into the WS, which increases ergotropy such that work can be extracted from a single bath [280]. With this and the brief understanding provided in Chap. 4, we try in the present chapter to expand the thermodynamics field and propose a molecular solid-state spintronic engine that integrates most of the above discussed quantum resources.

9.1 Design and operation of the spintronic engine

Underscoring that heat capacity of a correlated body diverges at a phase transition, we design our spintronic engine around the magnetic phase transition of one-dimensional CoPc molecular chains. To experimentally explore the concept of spintronic engine we fabricated multi-layered stacks of Fe/C₆₀/CoPc/C₆₀/Fe in UHV conditions (refer Chap. 6) and processed them into vertical nanodevices using nano sphere lithography technique (see Appendix A). In our vertical nano-device, the top and the bottom Fe/C₆₀ spinterface [101, 102] (spintronic selectors) acts as a thermal decoupler, leading to a non-thermal bath with the PM centers. The baths operate at and beyond room temperatures to block the undesired transport fluctuations (gray crosses in Fig. 9.1a). An ensemble of Co PM centers of CoPc molecule is the working substance of our engine.

In the film fabrication the lower C₆₀ layer is intentionally kept thin so the bottom spinterface drives the spin-splitting on the paramagnetic (PM) centers through spintronic anisotropy [17, 166, 261] (arrow thickness in Fig. 9.1a), thus allowing the spin ensemble to fluctuate while preserving its partial magnetic orientation. Also, the bottom Fe/C₆₀ spinterface is closer to the CoPc spin chain than the top spinterface to avoid any cancellation effects. In accordance with [281, 282] the spin-based potential landscape profile across the nano-device (Fig. 9.1b), the highest occupied molecular orbital (HOMO) of CoPc has a strong d character and contains an unpaired electron in the z^2 orbital that points out of the molecular plane [6, 7]. This orbital is almost aligned with the Fe and Fe/C₆₀ Fermi levels E_F , thus involving the molecules in the transport.

The operation of our spintronic quantum engine proceeds as follows. The interactions between the working substance (Co PM centers of CoPc) and the baths (spin polarized Fe/C₆₀ electrodes) are moderated by means of spin-polarized charge transport fluctuations, i.e spintronics. The working substance (WS) of our engine is a collection of spins that can mutually fluctuate below a magnetic phase transition [7] (detailed in Chap. 3, Sec. 3.3.1.1), which accounts for a quantum resource. The Co atoms of the CoPc molecules have S=1/2 spins that form one-dimensional spin

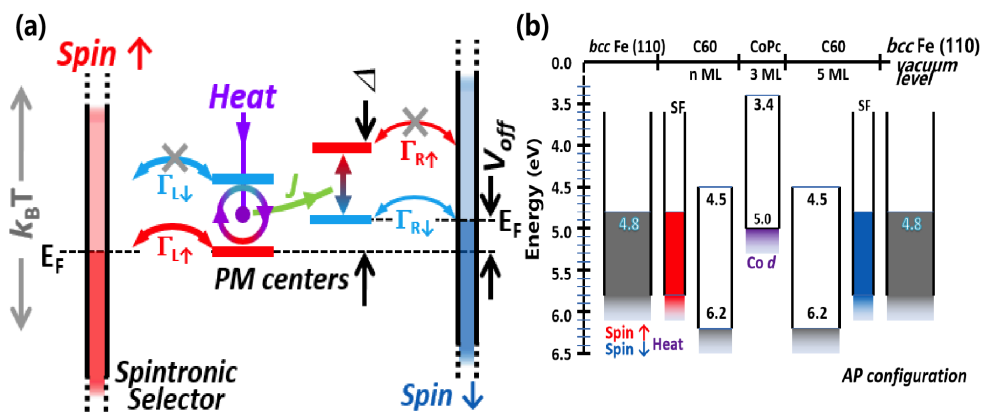


FIGURE 9.1: **Theoretical model of quantum spintronic engine.** (a) The spintronic engine schematic combines the baths (red & blue) with discrete spin states of the exchange-coupled (J) paramagnetic (PM) centers. Here Δ is the spin-splitting of Co $S = 1/2$ PM center and $\Delta < k_B T$ enable stochastic population of both spin up (down) states on PM center which is rectified by the two baths. The vertical arrows on PM center indicates the spin occupation, circular arrows indicates the thermal fluctuations on one PM center and the blue (red) arched arrows' thickness indicate the spin based asymmetries in transport fluctuations. The gray crosses are the forbidden transport fluctuations. The voltage offset V_{off} is induced because of spin-polarized charge transfer between the corresponding PM centers levels with different energies. Only two PM centers are shown for simplicity, when in reality the spintronic engine has an ensemble of PM centers whose thermal fluctuations are magnetically coupled (J). (b) The energy landscape of the nano device with Co PM centers from molecular CoPc and the spin polarized Fe/ C_{60} interface in anti-parallel state.

chains [6, 7]. The molecular paramagnetic fluctuations become antiferromagnetically (AFM) coupled between nearest neighbors when the thermal energy ($k_B T$) is below the magnetic exchange coupling (J) [7], i.e., $k_B T < J$. The AFM phase transition while maintaining the partial fluctuations on the PM centers is achieved by placing the CoPc spin chains in an effective magnetic field and hence lifting the spin degeneracy. Thanks to the spinterface [101, 102] it is possible to execute this effective magnetic field and include new quantum resources. The interface can spintronically implement both types of non-thermal baths with the spin ensemble. In our discussion on interface spin polarization (Chap. 3, Sec.3.5.1), it was evident that the spin-polarized charge transfer across the Fe/ C_{60} spinterface generates a low density of highly spin-polarized states [100] (DOS). So, one can imagine the spinterface's interface-localized low DOS as a transport quantum dot [17] that effectively screens the PM center from the thermalized DOS of the FM electrode. Logically, the spinterface is a squeezed bath of spintronic transport [279, 280]. The working substance's thermodynamic state is crafted by the transport fluctuations between the highly spin-polarized spinterface and the molecular spin chain (MSC). The spin degeneracy can be lifted by spintronic anisotropy [17, 261, 166] and the quantum coherence [145] is injected by the spinterface into the fluctuating spin chain. This results in gaining control [283] over the WS's thermodynamic state which in turn helps to improve [284] its ergotropy during the engine's operation.

The thermal spin fluctuations of the molecular spin ensemble are initially stochastic in origin, which interestingly also constitutes a quantum resource [285] by stimulating the superposition of the discrete energy states of the Co PM centers, i.e. contribute to a population inversion. This non-passive state is bound to the spinterface-injected quantum coherence. Note that these spintronic-enabled quantum resources do not lead to a perpetual motion. For example, the ergotropy generated due to coherence injection into the PM centers is in competition with the resistive losses, primarily due to the spinterface (Fe/ C_{60}), which spin filters the moderately spin-polarized current from the Fe FM electrode. The spin-resistance increases the entropy of the FM layer, i.e. its temperature, and the FM layer can advantageously decrease the resulting spin-based entropy by reverting to the FM's ground state.

Hence it is clear from the above discussion that our of spintronic engine's operation is different from the classical spin caloritronics which we discussed in Chap. 4. Altogether, this section gives a flavor of how the quantum spintronic engine ties the spintronic features of the engine to several quantum resources.

9.1.1 Structural and magnetic characterization of stacks

For quality assurance of multi-layers in the stack, x-ray reflectometry (XRR) and x-ray diffraction (XRD) was done to characterize the layers. The XRR measurements for a stack of composition $Si/SiO_2//Ta(5)/Fe(50)/C_{60}(6nm)$ (nm units) is shown in Figure 9.2a. The rms roughness (σ) of iron is less than 0.6nm indicating a smooth interface with the Ta buffer layer. The excellent fit to the measured data with low $\chi^2 = 0.0051$ signifies the overall structural quality of the entire stack. Ta has strong peaks due to x-ray diffraction at (002) and (330) planes (Fig. 9.2b). The iron sputtered on Ta buffer shows a sharp XRD peak at $\sim 45^\circ$ that is tabulated to the bcc(110) structure of Fe, Fig. 9.2c. The C_{60} and CoPc layers were carefully calibrated using XRR to ensure reproducible rate of thermal deposition of 0.005ML/s for CoPc and 0.0036ML/s for C_{60} at room temperature. Generally, 1ML of CoPc is $\sim 0.35nm$ and for C_{60} 1ML $\sim 0.9nm$. You will notice that the XRD and the SQUID+AGFM data is based on Ta buffer (Co electrode), the idea behind using Ta as buffer and capping was to perform spin transfer torque (STT) measurements on organic nano devices. We fabricated, optimized the spacer thickness using magnetometry and processed (>20) nano vertical devices using nano sphere lithography.

In our devices we maintained the overall thickness of the spacer to be nearly $\sim 10nm$. So, AGFM and SQUID measurements were done to calibrate the minimum C_{60} thickness required to decouple the FM electrodes (Fig. 9.3a-d). For this FM(50nm)/ $C_{60}(n)$ /FM(10nm) with $n = (3ML, 4ML, 5ML, 6ML)$ stacks used. The studies show 4ML of C_{60} is sufficient to decouple the FM electrodes, since a plateau is seen at low H (Fig. 9.3b). In ideal case one would expect a ratio of nominal jump to be around 1/6 of the hysteresis loop, the reduction of kink/jump in our stacks FM(50)/ $C_{60}(nML)$ /FM(10) is due to top FM electrode dead layer FM = Co(or Fe)

calculated to be $\sim 6\text{nm}$ ($\sim 8\text{nm}$), respectively.

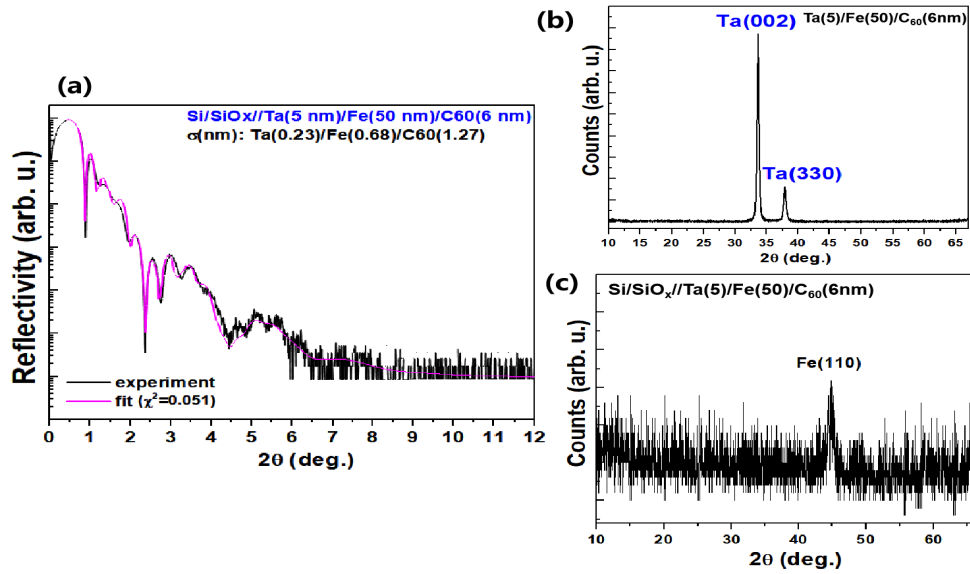


FIGURE 9.2: (a) XRR measurement on the stack $\text{Si}/\text{SiO}_2//\text{Ta}(5)/\text{Fe}(50)/\text{C}_{60}(6)$ (nm units) with a low error fit (magenta) function ~ 0.051 that points at smooth layers in the multi-structure. (b), (c) the XRD patterns for tantalum and iron. A strong diffraction peak at (002) is seen for Ta accompanied by a minor peak at (330). For iron a peak at $\sim 45^\circ$ is for bcc(110) structure for Fe sputtered on Ta buffer.

A thickness of 3ML CoPc was sandwiched between C₆₀ layers with a fixed top interface thickness C₆₀ = 5ML, and the bottom C₆₀ varied between (n = 1, 2, 3) MLs. A complex heterostructure of Fe(50)/C₆₀(2ML)/CoPc(3ML)/C₆₀(5ML)/Fe(10) studied in SQUID shows a weak temperature dependence after field cooling at 6T. Nevertheless, the electrodes are partly decoupled, with a distinct plateau at low field and has a top Fe electrode dead layer of 6.5nm (Figure 9.4).

During the electrical characterization of the stacks $\text{Ta}(5)/\text{Fe}(50)/\text{C}_{60}(n\text{ML})/\text{CoPc}(3\text{ML})/\text{C}_{60}(5\text{ML})/\text{Fe}(10)/\text{Ta}$ (x = 5, 10, 20, 100nm) in prober (procedure detailed in Chap. 6, Sec. 6.2.1), the device yield was lower than expected (>50% were OC, rest shorted). To track down this low yield we closely looked into various factors such as continuity of the top technological electrode (Prober), deposition and lift off steps in nano sphere lithography, quality of the nano-spheres used in lithography (see Appendix B) and conformity of the stack (XRR). There is no drastic structural change observed in XRD of Fe which retains its bcc character when sputtered on Ta buffer. This should eliminate the argument of change of Fe and C₆₀

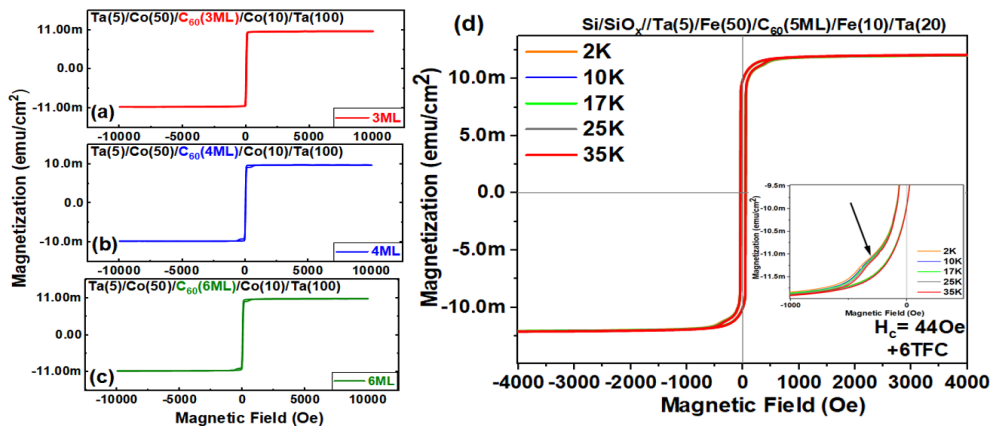


FIGURE 9.3: **Magnetometry measurements on FM/C₆₀(nML)/FM** where FM = Co or Fe and n = (3, 4, 5) MLs. (a) Room temperature parallel AGFM measurements shows no visible sign of decoupling of FM electrodes with n = 3ML but (b) and (c) show kinks or plateau at low field values indicating the FM electrodes are separated by C₆₀ monolayers respectively. A very small coercive field is recorded ~12Oe for all the Co/C₆₀/Co stacks. (d) The dc SQUID measurements for Fe/C₆₀(5ML)/Fe was done after field cooling from 300K to 2K with field at 6T. The parallel measurements were done at 2 < T(K) < 35 shows decoupling of electrodes with plateau pointed in the lower inset. The coercive field, $H_c = 44\text{Oe}$ and has rather negligible T dep. The magnetometry was only done to qualify the minimum thickness required of C₆₀ spacer required to decouple the FM electrodes.

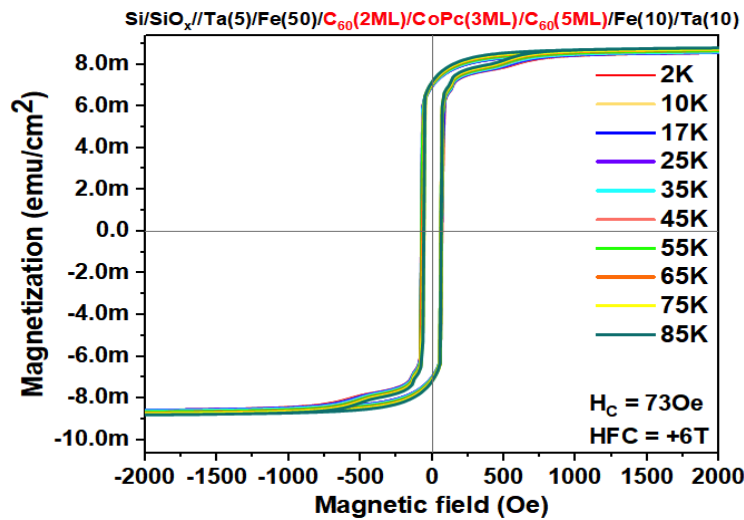


FIGURE 9.4: **Temperature dependent SQUID measurements** on heterostructure of Fe/C₆₀(2ML)/CoPc(3ML)/C₆₀(5ML)/Fe at 2 < T(K) < 85 shows visible kinks at lower field and smooths out at $|\mathbf{H}| = 500\text{Oe}$. This is recorded after the sample was field cooled at 6T from 300K to 2K. The coercive field is ~70Oe and has a weak T dependence.

subsequent layers being the reason for low yield. On close examination, firstly the nano spheres used for the Ta study had evolved structurally (Appendix B) forming

agglomerates which affects the lift off process and the RA of the device. If agglomerates of silica spheres are being deposited then the device size will be much higher than 300nm and device is shorted. The surface chemistry might also play a role, previous devices (Chap. 8) the nano spheres were deposited on chromium. If one looks at the electro-negativity which is the strength of an atom to attract e^- density towards itself, Cr has 1.66 [286] and Ta 1.5 [286] in Pauling scale. This could mean Cr surface may provide a better vdW bond with silica spheres compared to Ta. So if only few or no silica spheres were binding to the Ta surface then the device is open circuited. Therefore, we reverted to Cr buffer as we already had evidenced success working with it in Chap. 8. Moreover, the XRD (& TEM) analysis of Cr/Fe (see Chap. 4) and in current chapter the XRD of Fe/ C_{60} show smooth continuous layers so, structurally switching from Ta to Cr buffer should not alter the stack growth. Altogether, from the above discussions, in this chapter all devices studied have the following stack composition $Si/SiO_x//Cr(5)/Fe(50)/C_{60}(nML)/CoPc(3ML)/C_{60}(5ML)/Fe(10)/Cr(100)$ where $n = 1, 2,$ and 3 mono layers.

9.2 Magnetotransport results across nanodevices

The stacks $Si/SiO_x//Cr(5)/Fe(50)/C_{60}(nML)/CoPc(3ML)/C_{60}(5ML)/Fe(10)/Cr(100)$ where $n(ML) = 1, 2, 3$ were processed using the team's solvent-free SiO_2 nanobead lithography technique, resulting in 300nm sized devices that were wire bonded on to the sample chips. For details on the process, refer Chap. 5. As per our device statistics, out of 173 devices processed, 10 were neither open circuit (OC) nor short-circuit (SC), and 8 among them jointly exhibited current and voltage offset, not less than an order of magnitude higher than those observed on our measurement set-up using a calibrated standard resistance of similar amplitude (Fig. 9.5a,b). The fabricated devices were mounted on a cryostat in a technologically advanced setup in the DEIMOS beamline of the SOLEIL synchrotron facility, see Chapter 6 for details. Care was taken to maintain the experimental set up to be in a dark cryostat that is electrically grounded. Long metallic wires are used to connect the device to the setup [238]

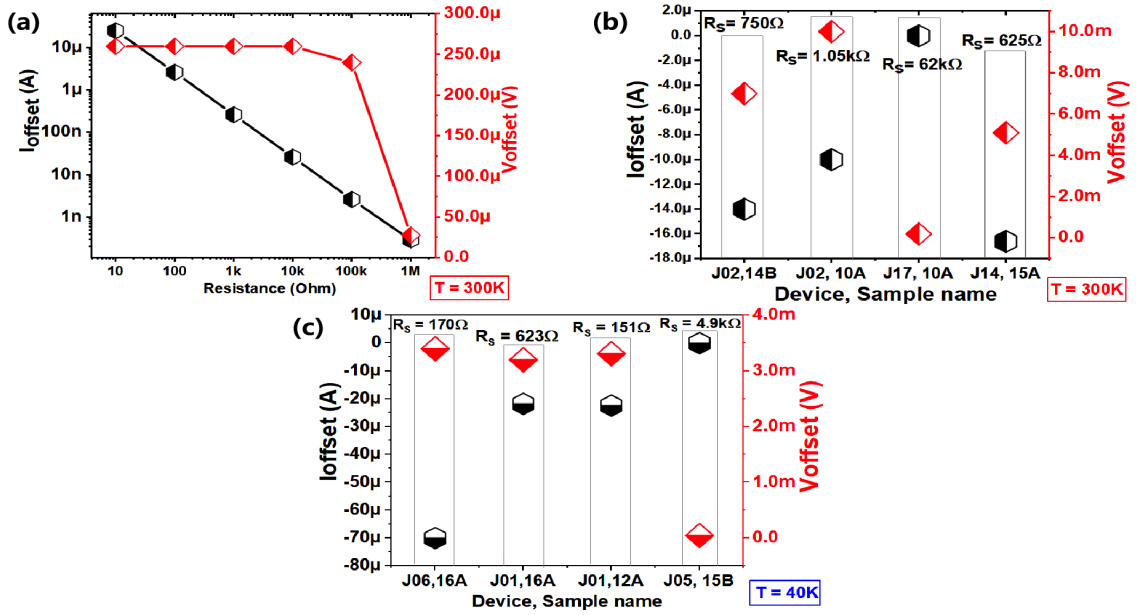


FIGURE 9.5: **Graph of Current and Voltage offsets.** (a) The current (I_{offset} -black) and voltage (V_{offset} -red) offsets measured at room temperature using a standard resistances $10 < R(\Omega) < 1\text{M}$ in DEIMOS experimental setup. For the smallest resistance $R = 10\Omega$ $I_{\text{offset}} = 25\mu\text{A}$ and $V_{\text{offset}} = 260\mu\text{V}$. I_{offset} decreases for higher resistances whereas the V_{offset} remains nearly unchanged upto $100\text{k}\Omega$ and decreases thereafter. The I_{offset} (black) and V_{offset} (red) recorded on eight MTJ devices at (b) 300K and (c) 40K . The MTJs device composition is $\text{Fe}(50\text{nm})/\text{C}_{60}(\text{nML})/\text{CoPc}(3\text{ML})/\text{C}_{60}(5\text{ML})/\text{Fe}(10\text{nm})$, ($n = 1, 2, 3$) MLs. The sample : device names are - 14B: $J02(n=3\text{ML})$, 10A: $J02$ & $J17(n=1\text{ML})$, 15A: $J14(n=2\text{ML})$, 16A: $J01$ & $J06(n=1\text{ML})$ and 12A : $J01(n=3\text{ML})$. The slope resistances are noted on top of the respective devices (gray pillar is visual guide). These devices have resistances at least 20x greater than the smallest standard resistance, so both I_{offset} s and V_{offset} s are always above the experimental error.

Unlike the regular quantum engine operations discussed in Chap. 4, Sec. 4.2.2.1, in this experiment there is no need for an external microwave excitation [152]. The entire data set was recorded at a uniform temperature T maintained on the sample. In the following sections we will look closely into three nano devices, one semi-conducting device-A : $\text{Si}/\text{SiO}_x//\text{Cr}(5)/\text{Fe}(50)/\text{C}_{60}(1\text{ML})/\text{CoPc}(3\text{ML})/\text{C}_{60}(5\text{ML})/\text{Fe}(10)/\text{Cr}(50)$ and two metallic device-B: $\text{Si}/\text{SiO}_x//\text{Cr}(5)/\text{Fe}(50)/\text{C}_{60}(3\text{ML})/\text{CoPc}(3\text{ML})/\text{C}_{60}(5\text{ML})/\text{Fe}(10)/\text{Cr}(10)$ & device-C: $\text{Si}/\text{SiO}_x//\text{Cr}(5)/\text{Fe}(50)/\text{C}_{60}(1\text{ML})/\text{CoPc}(3\text{ML})/\text{C}_{60}(5\text{ML})/\text{Fe}(10)/\text{Cr}(100)$.

9.2.1 Semiconducting device - A

At room temperature, the device-A : $Fe/C_{60}(1ML) / CoPc(3ML) / C_{60}(5ML) / Fe$ exhibits a linear $I(V)$ with a current offset of $\sim -10\mu A$, (Fig. 9.6). The device was mounted on a sample holder which allows the magnetization of the FM electrodes to be normal to the external magnetic field (details Chap.7, Sec. 7.3). Due to this out-of-plane orientation, the applied H has no strong impact on the device's $I(V)$ (Fig. 9.6). This limited our access to device's parallel and anti-parallel magnetic states. It is interesting to note that the I_{offset} exists despite $H = 0T$, which means external magnetic field is not the source of this current offset. As described earlier the standard calibrated resistances were used to determine the experimental bias and current and voltage offsets (Fig. 9.5a). The current and the voltage offsets observed in device-A are plotted in Figure 9.7, they are much higher than our experimental offsets, compare Fig. 9.5a with Fig. 9.7. Notably, we obtained ($1k\Omega$, $260\mu V$, $263nA$) and ($10k\Omega$, $260\mu V$, $26.3nA$). These experimental offsets are much smaller than the device offsets, compare the magenta crosspoint with gray dashed line in Fig. 9.6.

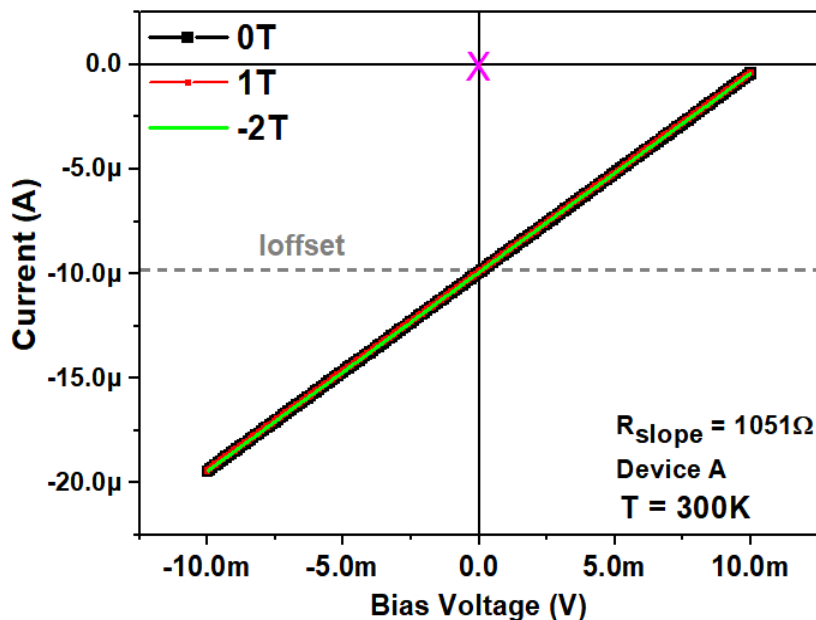


FIGURE 9.6: **Room Temperature $I(V)$ characteristics.** A linear behavior with current offset $-10\mu A$ and slope resistance of 1051Ω . External H is applied out-of-plane to the sample with in-plane magnetization. The magenta cross is the experimental error.

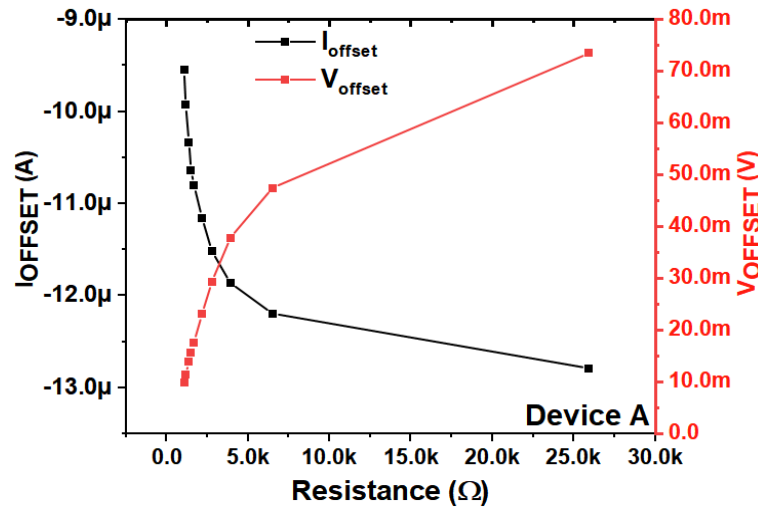


FIGURE 9.7: **Current and Voltage offsets of device-A.** The I_{offset} (black) and V_{offset} (red) offsets for various resistances are much higher than the experimental error. Compare this figure with fig. 9.5a.

On decreasing the device temperature, the linear $I(V)$ becomes highly non-linear and the device slope resistance (R_s at $\pm 10mV$) increases from $1.05k\Omega$ (300K) to $25.9k\Omega$ (40K). Therefore, device-A is said to be semi-conducting (compare Fig. 9.6 with Fig. 9.8). The device is subjected to a fixed magnetic field when decreasing the temperature. The I_{offset} (V_{offset}) show only minor changes depending on the field cooling protocol (**HFC** and **ZFC**). This again indicates that the magnetic field is not the source of this spontaneous current (voltage) recorded in the device, see Figure 9.8.

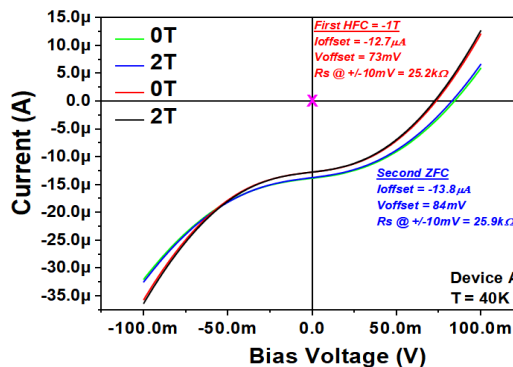


FIGURE 9.8: **IV characteristics at 40K.** H is applied out-of-plane to the sample with in-plane magnetization. The black (red) and the blue (green) non-linear $I(V)$ curves are measured at $T = 40K$ for out-of-plane FC = $-1T$ (ZFC) respectively. The slope resistance R_s for $\pm 10mV$ is found to be $25.2k\Omega$ ($25.9k\Omega$). The magenta cross is the experimental offset.

To closely study the evolution of current and voltage offsets, we performed a temperature-dependent study on device-A. The field cooled sample was stabilized at 40K and warmed up in the presence of zero field. The I(V) was recorded at $40 < T(K) < 360$, see Figure 9.9. The non-linear I(V) becomes highly linear as the temperature is increased. The current and the voltage offsets are found to be orders of magnitude greater than the experimental error for the R_s observed at all temperatures (see Fig. 9.10a, b). Both the offsets show a strong temperature dependence.

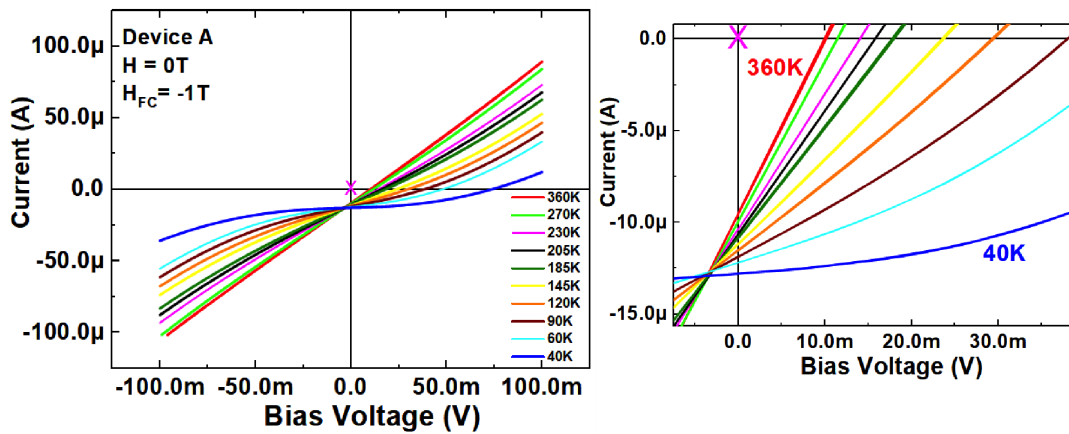


FIGURE 9.9: **Temperature dependent I(V) characteristics.** The I(V) recorded for $360 < T(K) < 40$ has a strong Tdep with linear I(V) at 360K (red curve) becoming non-linear as temperature is decreased at $H = 0T$. The right close up view looks at the low bias to display the voltage offsets, current offsets and the magenta crosspoint represents the experimental error.

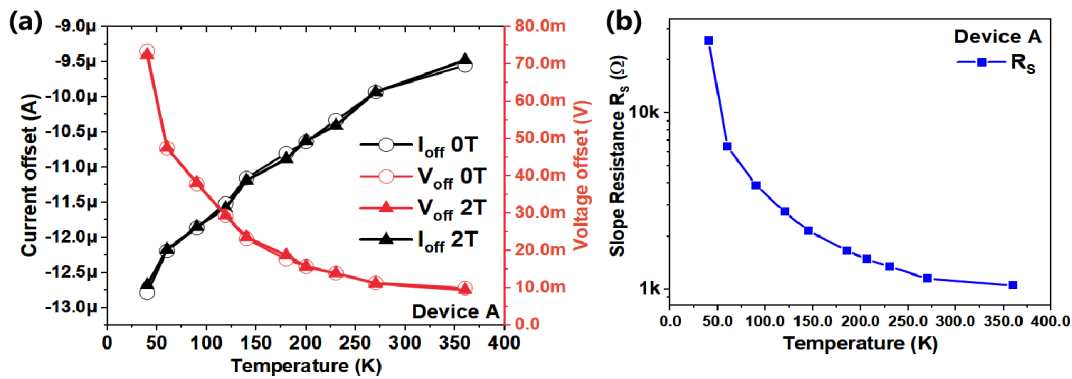


FIGURE 9.10: **Temperature and magnetic field dependence of (I, V) offsets and slope resistance R_s .** (a) Temperature has a strong impact on both I_{off} and V_{off} values unlike the magnetic field which has rather negligible effect on the (I,V)offsets. The circles represent the offsets at $H = 0T$ and solid triangles are for $H = 2T$ for $40 < T(K) < 360$. (b) Slope resistance R_s calculated for $40 < T(K) < 360$ at $H = 0T$. For rising temperatures the resistance falls down i.e., at 40K (360K) the R_s is calculated to be $25.9k\Omega$ ($1.05k\Omega$).

For instance the offsets reach nearly $(-13\mu A, 80mV)$ at 40K. Not only are these V

and I offsets orders of magnitude greater than those measured using a calibrated resistance, but the temperature trend of both offsets doesn't match that of a calibrated resistance. Indeed, when the amplitude of the calibrated resistance is decreased, the bias offset remains nearly constant, while the current offset increases (see Fig. 9.5a). However, for device-A, when the slope resistance R_s decreases with increasing T (Fig. 9.10b), we observe that the current offset also decreases. This is the opposite trend of that found for the calibrated resistance. Also, once permanent electrostatic degradation causes R_s to decrease from 23.9k Ω to 8.1k Ω at 40K, the offsets are recovered within these boundaries. The power characteristics of device-A is plotted for $40 < T(K) < 360$, shows 450nWatt at 40K for $H = 0T$, see Figure 9.11.

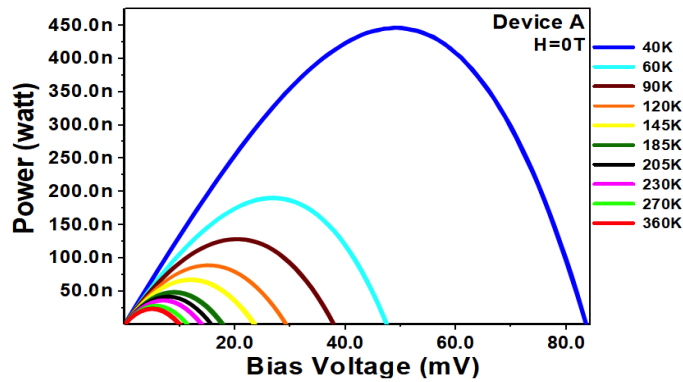


FIGURE 9.11: **Power characteristics as a function of temperature.** The $P(V)$ data shows maximum power $P_{Max} = 450nW$ at 40K which decreases as the temperature is increased beyond room temperature. At 360K, the $P_{Max} = 24nW$. The data set was recorded for stable temperature with applied magnetic field $H = 0T$.

Squeezed baths or SS	PM Center	T (K)	P_{max} (nW)	Ref.
FM Metal	MnAs FM QDs in GaAs matrix	3	1	Hai 2009 [13]
Spin filter tunnel barrier	Al QDs	1	10^{-5}	Miao 2014 [18]
Co/C spinterface	C PM dimer in MgO	295	0.1	Katcko 2019 [17]
Fe/ C_{60} spinterface	CoPc, between C_{60} layers	360	24	Current thesis work
		295	27	
		40	450	

TABLE 9.1: Analogy between the various reported experimental spin engines. PM = paramagnetic center and QD = quantum dot.

A combined graph of $\ln. R_s$, V_{off} and P_{Max} temperature dependence plots is described in Figure 9.12. The $\ln. R_s$ vs. $1/T$ plot (Fig. 9.12a) shows the decrease in

resistance with increasing T which can be fitted using the thermal activation law of the form, $R = R_0 e^{-\frac{E_a}{k_B T}}$ with a single activation energy of E_a over $40 < T(K) < 360$. On the contrary, V_{off} and P_{Max} have two activation regimes with a crossover at 120K (purple vertical line Fig. 9.12-b,-c).

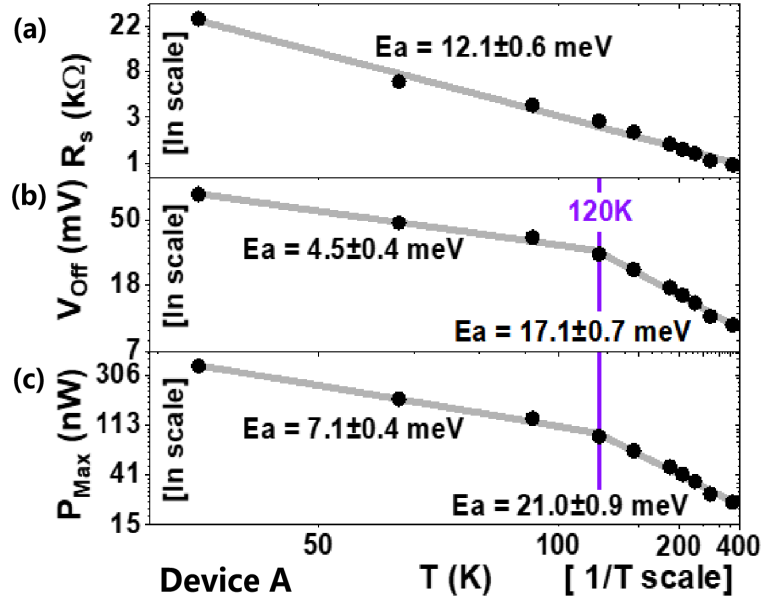


FIGURE 9.12: **Thermally activated, large output electrical power across the nano-harvester.** The \ln vs $1/T$ plots of (a) slope resistance R_s , (b) voltage offset V_{off} and (c) maximum power P_{Max} . (a) The calculated slope resistance is found to decrease with increasing T with thermal activation energy $E_a = 12\text{meV}$. (b) & (c) V_{off} and P_{Max} decrease with rising temperature but have two distinct regimes with respective E_a . The crossover temperature 120K could be associated with the exchange coupling between the Co PM centers of the CoPc molecular spin chains, based on prior literature from crystals [7] and ultrathin films [6]. The black dots are the experimental data points and the gray line is the fit.

Interestingly, this thermal energy is quantitatively similar to $J/k_B = 105\text{K}$ found for CoPc in crystal [7] and ultrathin film [6] forms. When thermal energy is decreased below J , the partly oriented, fluctuating magnetic moments in the spin chain become antiferromagnetically coupled. A magnetic phase transition to an antiferromagnetic state with on-site fluctuations occurs at $J/k_B = T = 120\text{K}$ and the fluctuations become correlated i.e., $J > k_B T$. As a result, P_{Max} is strongly altered when the partly fluctuating working substance (PM centers) undergo a magnetic phase transition at $T = 120\text{K}$, see Fig. 9.12c. The lower zone from $40 < T(K) < 120$ (Fig. 9.12 b,c) displays thermally activated decrease in V_{off} and P_{Max} which is due to the spin

depolarization transport processes [287]. When the AFM order of the partly fluctuating PM centers begins to disappear above 120K, a faster thermally activated fall in V_{off} and P_{Max} is observed, see Fig. 9.12(-b,-c). This sharp decrease is expected considering the predicted [17, 177, 179, 178] significance of the magnetic correlations between PM centers in the spintronic engine, which are thermally wiped out for $T > 120K$. The key take way from this result is that the output power tracks the antiferromagnetic fluctuation phase transition of the CoPc spin chains. This is the engines' first thermodynamic signature involving the quantum resource (WS) and magnetic phase transition in a solid state spintronic device.

9.2.2 Metallic device - B

The second device-B : $Fe/C_{60}(3ML)/CoPc(3ML)/C_{60}(5ML)/Fe$ was mounted on a 45° sample holder and an additional angle $\phi = 37^\circ$ was added by rotating the arm of the V^2TI setup. Since our device's FM electrode's magnetization is in-plane this rotation allowed for an in-plane external magnetic field on the device-B. The device shows a large stable non-zero spontaneous current $I_{sp} \sim -26\mu A$ recorded at 60K (Fig. 9.13). The I_{sp} amplitude endures over nearly two hours, and is not heavily affected by the back & forth sweeps of an almost in-plane external magnetic field $\mathbf{H} = 2T$. The weak impact of the field on the spontaneous current can be explained by the metallic character of the device-B which leads to ferromagnetic coupling. Hence, it is impossible to alter the device's magnetic state even with a mostly in-plane magnetic field. This is aligned with our previous conclusion that the external magnetic field is not our engine's primary energy source [13, 177, 14].

The persistent spontaneous currents (Fig. 9.13) can probably be explained as follows. Firstly, we discard the Joule heating within the metallic pinholes in the device. Instead, 'quantum friction' viz. quantum fluctuations between eigen states leading to decoherence could be low. Certainly, spin excitations on the molecular CoPc PM centers are long-lived due to the weak spin-lattice and spin-orbit interactions which is unique to organic semiconductors [288, 289, 290], while any spin relaxation to the electrodes is weakened due to their high spin polarized transport [17].

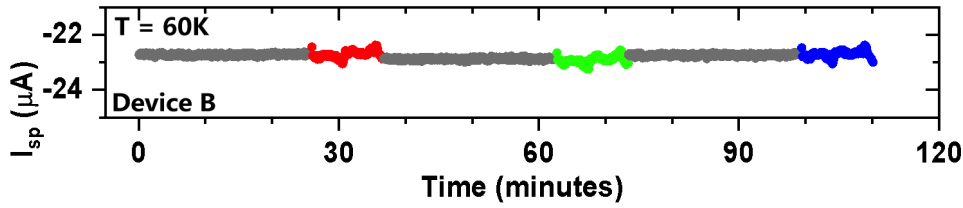


FIGURE 9.13: **Persistent spontaneous current** at $T = 60\text{K}$ which has weak field dependence when $\mathbf{H} = 2\text{T}$ is applied almost in-plane. The gray data points are when the field is off and colored data points are for the I_{sp} recorded with $\mathbf{H} = 2\text{T}$. The effect is stable and continuous for more than 90 minutes.

The $I(V)$ characteristics of device-B for $40 < T(\text{K}) < 240$ at $\mathbf{H} = 0\text{T}$ shows a linear behaviour throughout the T range (Fig. 9.14a). The calculated slope resistance R_s for $\pm 10\text{mV}$ is 157Ω and the maximum output power is 26nW at 240K , see insert 9.14a. The devices' spontaneous current and voltage offset values measured at 240K are much higher than the experimental offsets. Note that the time dependence of I_{sp} and the current offset at $V=0\text{V}$ (compare Fig. 9.14a with Fig. 9.14b) is the same i.e, $I_{off} = I_{sp} = -26\mu\text{A}$. Thus supplying bias voltage $V=0$ does not grant energy to the device. The I_{off} and the complementary voltage offset $V_{off} = 4.05\text{mV}$ at $I=0$ (Figure 9.14b) are $230\times$ and $100\times$ greater than the experimental offset errors observed on a 100Ω calibrated standard resistance magneta crosspoint (compare Fig. 9.5 with Fig. 9.14).

The $I(V)$ s hysteric divergence from a linear response closely depends on the sweep direction (red and black arrows in Fig. 9.14c). On taking the differential derivative of current the conductance (Fig. 9.15a) in the 1.4mV bias window reveals unique features with a full width half maxima (FWHM) as low as 0.3meV despite $k_B T = 20.7\text{meV}$. This sub - $k_B T$ resolution exists regardless of the expected thermal smearing of $2-3k_B T$ upon transport and is hardly changed upon reducing thermal fluctuations by a factor of 6 of the main spectral features (A, B, and C in Fig. 9.15b) from 40K to 240K . This is the second quantum thermodynamical signature where sub- $k_B T$ spectral features are recorded due to the squeezed bath which is a quantum resource.

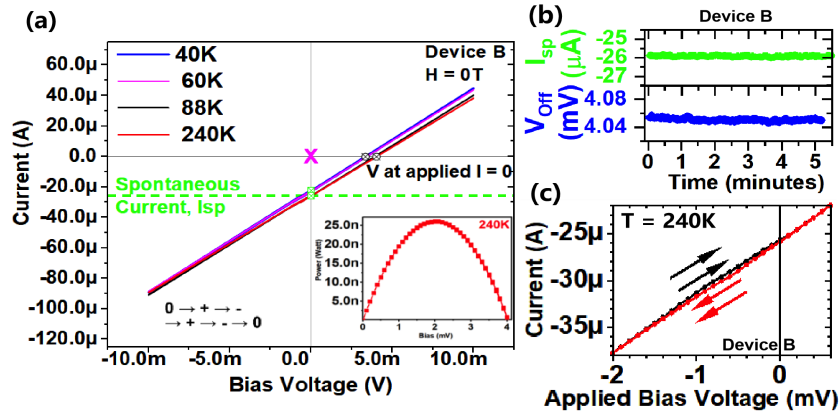


FIGURE 9.14: **Current vs. Voltage characteristics of device-B** for $40 < T(K) < 240$ at $H = 0T$. The current is swept from $0V$ to high $+V$ then traversed to high $-V$ and back to $+V$. Finally the cycle ends at $0V$. (a) IV shows current and voltage offsets. The IV is linear and non-ohmic. The magenta crosspoint is the experimental error. Note that Ioffset and I_{sp} are the same. The lower inset is the plot of maximum power output $P_{Max} = 26.12nW$ at $240K$ (b) Time dependence of $I_{sp} = -26\mu A$ and $V_{offset} = 4.06mV$ at $240K$. They are constant over at least 5 minutes. (c) IVs from $-V$ to $+V$ (black) and from $+V$ to $-V$ in red near $V=0$.

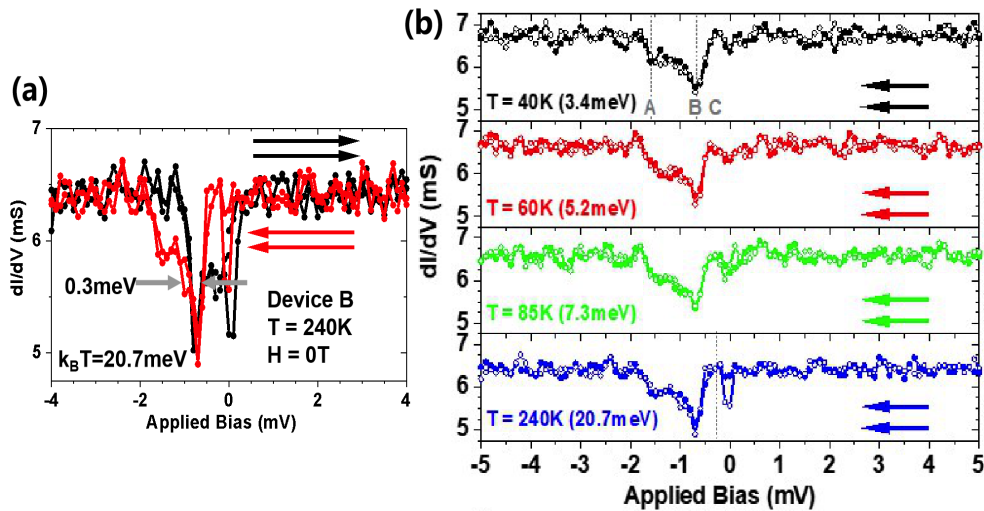


FIGURE 9.15: **Temperature dependence of differential conductance of device-B.** (a) The dI/dV for $H = 0T$ shows hysteresis behaviour at $240K$. The $k_B T$ at $240K$ is calculated to be $20.7meV$ and the dataset shows sub- $k_B T$ spectral resolution i.e., $0.3meV$ (gray arrows). The red and black arrows determine the current's sweep direction. The temperature dependent study of the dI/dV for $40K$, $60K$, $85K$ and $240K$ shows that the sub- $k_B T$ features are not drastically altered. The markings A, B, C serve as reference to track the trace and the arrows represent the dI/dV 's return trace respectively.

As device-B exhibits a slight decrease in its conductance with raising temperature, it is categorized as a metallic junction. Studies on tunneling spintronic devices suggest that, due to quantized states within the tunnel barrier [64, 65, 66], one

can witness coexisting spintronic regimes involving metallic and semiconducting nanochannels [291] within the device.

9.2.3 Metallic device - C

To demonstrate the spintronic nature of our thermal energy harvester we will look into the key features of device-C : Fe/C₆₀(1ML)/CoPc(3ML)/C₆₀(5ML)/Fe evidenced in Figure 9.16 where the applied magnetic field was almost in-plane with the magnetization of device's FM electrodes giving access to its magnetic P and AP states. The I(H) data acquired on device-C at 40K with the applied magnetic field almost in-plane reveals a strong H dependence of device current (Fig. 9.16). We infer that the parallel configuration of the FM electrode magnetization is reached at |H| = 0.5T. The device current can be suppressed at H = 0 and H = -0.5T for V_{off} = 2.76mV and V_{off} = 2.13mV respectively. This indicates the device's two magnetic states promote separate V_{off}. Interestingly, they also drives a sign change in current at V = 2.67mV with ΔI = ±1A. These voltage, current pairs are orders of magnitude higher than our experimental offset errors confirmed using a standard resistance.

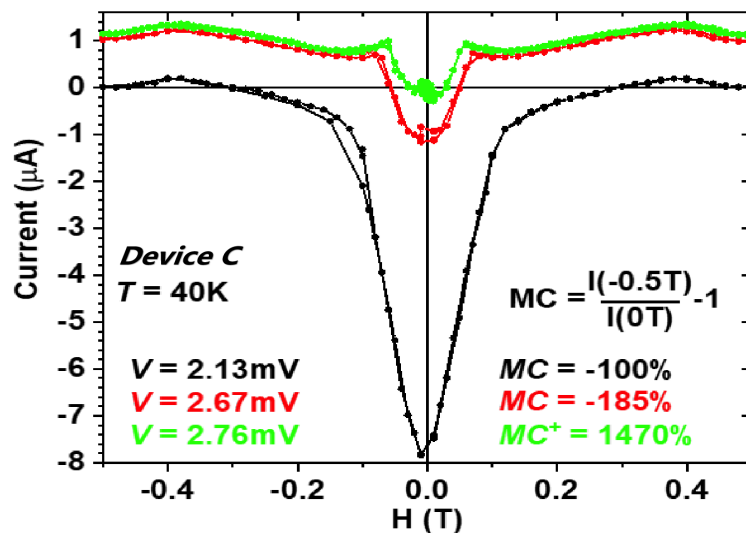


FIGURE 9.16: **Spintronic switch.** Current vs magnetic field I(H) plot for device C at 40K for three voltages values 2.13mV, 2.67mV and 2.76mV respectively. The calculated magneto-current MC is more than 1000% showing a strong magneto-transport contribution. The current is suppressed when H = 0T for Voffset = 2.76mV (green) and when H = -0.5T for Voffset = 2.13mV (black). This property could be used as a spintronic switch.

In Figure 9.17, we confirm these V_{off} through multiple IV data sets. The slope resistance R_s calculated using $I(H)$ data from Figure 9.16 is studied for its H dependence (Fig. 9.18). Concurrent data points between the three figures (9.16, 9.17, 9.18) are visualized by blue crosses in Fig. (9.17 and Fig. 9.18).

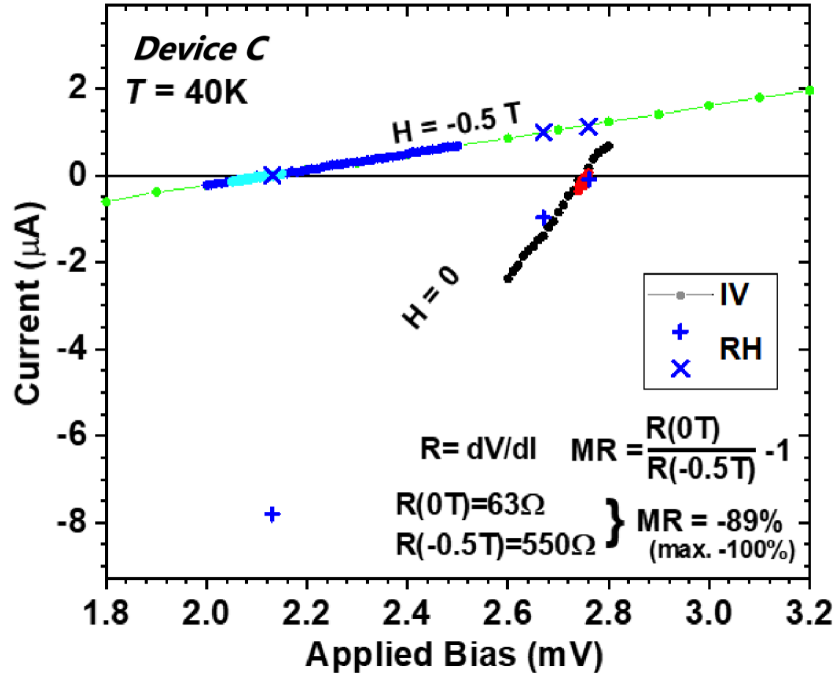


FIGURE 9.17: The combined IV plots registered at $H = 0T$ (black, red) and $H = -0.5T$ (cyan, green, blue) shows a linear behaviour with slope resistances $R_s = 63\Omega$ and $R_s = 550\Omega$ focus on $V_{offset} = 2.13mV$ and $V_{offset} = 2.76mV$, respectively. The $I(H)$ data points (blue crosses) are extracted from Fig. 9.16 which seems to follow the IV curve.

The magnetoresistance MR is calculated using $MR = \frac{R_s(0T)}{R_s(-0.5T)} - 1$ and the MR range is $-100 < MR(\%) < \infty$, reaches -89% . The 'optimistic' $MR = \frac{R_s(-0.5T)}{R_s(0T)} - 1 = 770\%$. This indicates an average transport spin polarization $P = 89.1\%$ of the two Fe/C_{60} spintronic selectors [100] according to the Julliere model [3]. The magnetocurrent MC is calculated as $\frac{I(-0.5T)}{I(0T)} - 1$. The MC 's measured at each V_{off} viz. $MC = -100\%$ and $MC = 1470\%$ supports the experimental verification of the expected range $-100 < MC(\%) < \infty$ when the currents in each magnetic state are of same sign. Note that at $V = 2.67mV$, the MC is -185% (Fig. 9.16) this is due to the opposite signs of the current. Therefore, we can conclude that this device class behaves as a spintronically controlled switch of current flow and its direction.

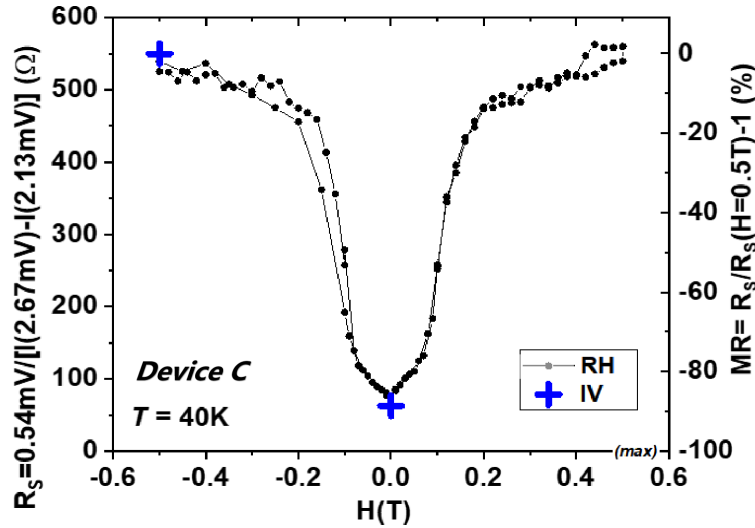


FIGURE 9.18: **Dominant spintronic properties in energy harvester.** Magnetic field dependence of the slope resistance (RH) and magnetoresistance (MR). The slope resistances (solid curve) are calculated using the $I(H)$ datasets of Fig. 9.16 and the blue crosses represent the R_s inferred from the IV graphs of Fig. 9.17. The MR calculated at two Voffsets 2.67mV and 2.13mV exhibits very high values of magnetocurrent $-100 < MC(\%) < \infty$ calculated from the $I(H)$ data and the magnetoresistance of the R_s yields $-100 < MR(\%) < \infty$.

9.3 Summary

We have experimentally seen how a solid-state device autonomously harvests collective thermal fluctuations on PM centers around its magnetic phase transition based on spin-polarized charge transport between highly spin polarized Fe/ C_{60} non-thermal baths coupled to entropy sinks. Our experimental data sets evidence two quantum thermodynamical signatures [152] namely: (1) sub - $k_B T$ spectral resolution due to the squeezed baths 9.15; (2) power output that traces the antiferromagnetic fluctuation magnetic phase transition (at $J/k_B = T = 120K$) of the working substance CoPc molecular spin chains 9.12. These thermodynamical signatures confirm the presence of multiple quantum resources in our spintronic engine, namely non-thermal baths (Fe/ C_{60} spinterface), spintronic anisotropy, and a spin ensemble working substance around a magnetic phase transition.

Our spintronic engines exhibit a large electrical power generation without a nominal thermal gradient, which we ascribe to the spintronic harvesting of the paramagnetic fluctuations due to its surrounding temperature. A maximum power of

450nWatt at 40K is recorded and the output power is associated with the magnetic correlations between fluctuation paramagnetic centers around a magnetic phase transition. This power output can be controlled spintronically and is stable even beyond room temperature, which is a big advantage for practical applications. Several improvements can be pursued to get enhanced device power output by tuning specific elements of the spintronic engine, starting from the magnetic coupling strength between PM centers to the spintronic anisotropy exerted on these centers by the spintronic selectors (or baths), to the number of centers. Finally, this device can encode information and also acts as a spintronically controlled switch of current flow, and of its direction, thus making it a multifunctional device.

To eliminate any skepticism for all previously reported spintronic engines [17, 13, 18] and CoPc based engine which generate electrical output power despite of all the device components (bath and PM centers) at nominal thermal equilibrium. In our experiment we have carefully considered all possible artifacts. For instance the sign change of current with \mathbf{H} (see Fig. 9.16) and the voltage amplitude (upto 74mV in Fig. 9.17) both indicate against a thermal voltage drop along the device leads. This effect persists at $T = 40\text{K}$ when the sample heater is turned off, and decreases with increasing temperature. Thus casts aside a black-body radiation effect, as well as any stray T gradient between the cryostats cold finger and sample. Device electrostatic breakdown to lower resistances leads to IVs with offsets similar to those found using a calibrated resistance. This indicates that the large offsets measured originate from the device, and not the experimental environment. Also, from the previous Chapter 8, devices with only a CoPc spacer devices yield current and bias offsets within the range found using calibrated resistances.

Additionally, at the magnetic transition i.e., $k_B T = J$, the thermalization of the disordered many-body quantum system can fail if it is isolated [292]. Generally, a quantum engine which exploits a phase transition can output finite power even at Carnot efficiency [277]. The efficiency of the spintronic quantum engine as the spintronic engine operates, the electron charge deposited onto the spin chain due to transport fluctuations can dynamically promote the magnetic phase transition. When the PM fluctuations become correlated $k_B T < J$, a prior report [145] claims

that this quantum coherence can foster extraction of work from a single thermal bath. Hence, earlier reports on atomic quantum engines specifically highlight the possibility to surpass classical thermodynamical limits when a phase transition is engaged, which is aligned with our experimental results.

Spintronics engines [17, 13, 18] are advantageous for three important reasons : (1) the regime of interaction is electronic in character - no laser or microwave interactions [152] like in an atomic engine, (2) it involves discrete atomic levels, rather n and $n+1$ electron levels in mesoscopic system, finally, (3) it merges multiple quantum resources. Since classical or meso-engines [147, 129, 293] operate using many electrons their efficiency can never exceed Carnot limit. To conclude, this chapter of the thesis highlights and tries to steer the direction of research in quantum engines from atomic [138, 280] and mesoscopic [147, 129, 293] implementations to an industrially advantageous spintronic implementation. This should stimulate interest to understand closely this phenomenon at the intersection between spintronics and quantum thermodynamics.

Chapter 10

General conclusion and perspectives

This thesis discusses the crucial role of magnetic tunnel junctions and the physics of spintronics for two demanding applications namely, memory and low power devices, see Chap. 1. We emphasized the origin and the nature of structural imperfections of two types of spintronic devices. After reviewing, it became clear that oxygen vacancies within the MgO spacer have a direct impact on the device performance, details in Chap. [2, 3]. Similarly, in organic spintronic junctions, the cobalt paramagnetic centers serve as the transport path. Taking advantage of intriguing properties of organic semiconductors we designed multifunctional devices.

The overall objective of this thesis was to explore the nano transport paths involved in MgO and organic based MTJs for information encoding and energy harvesting. Specifically our idea was to unambiguously identify the direct role of oxygen defects and Co PM centers in the device operation and performance. For this we performed electrical measurements in the laboratory and at dedicated synchrotron beamlines (see Chap. 7). The thesis represents a balance of work accomplished along the process chain starting from 1) thin film deposition and characterization, 2) technological processing into solid-state devices, and 3) measurement of devices in challenging environments, detailed in Chapters 5, 6, & 7. In addition to this, much time was spent in designing, testing and optimizing the shadow masks used for fabrication of organic MTJs. The following discussion of the scientific results

demonstrates the added value to the pool of knowledge in the field of spintronics and thermodynamics that was achieved in the course of this thesis.

In our experiment on organic devices, we discovered that the excited spin state of a CoPc spin chain consists of a unique magnetic unit that exists in the steady state within the solid state device, see Chap. 8. These properties are due to the FM exchange coupling between the excited spin chain and the underlying FM electrode, concept details in Chap. 3, Sec. 3.5.2. Our solid-state device approach instead of the traditional model experimental (STM) (Chap. 3, Sec. 3.3.1.2) path gives insights into how a spin chain's ground and excited states interact with a FM electrode. This work should stimulate interest to exploit the functional property of magnetic molecules to transfer data across molecular films using spin waves. Additionally, this nanoscale engineering of quantum states of the spin chains should also propel involvement of oxide material and antiferromagnetic researchers, who have mostly focused on macroscale properties of AFM and ferroic orders, rather than at the quantum level. Finally, this exceptional combination of a fundamental development along with technological advancement illustrates how crucial it is to reveal the quantum nature of functional materials within a solid state device.

Following along the lines of quantum properties of materials we explored the special type of quantum engines known as spintronic engines, see Chapter 9. This spintronic engine consists of Fe/C_{60} electrodes acting as non-thermal baths. It operates by autonomously harvesting thermal fluctuations on cobalt PM centers around the magnetic phase transition due to the spin-polarized electron transport between the baths coupled to FM metallic electrodes that act as entropy sinks, concepts in Chapters 4 & 9. One of the milestones in this work is the observation of 770% MR across this class of device (compare reported MRs in Chap 1). This record MR for a molecular spintronic device confirms the high spin polarization ($P = 89\%$ according to Julliere model [3] of the spinterface [101, 102], in the footsteps of the 300% TMR (i.e., $P = 77\%$) using Co/C interfaces that our group previously reported [17] (details in Chap. 3, Sec. 3.4).

A second milestone is the large persistent non-zero spontaneous current, operating at and beyond room temperature with power output $P_{Max} = 24\text{nW}$ at 360K, see Chap. 9, Sec. 9.2.2 & Sec.9.2.1. Most importantly, the solid-state device implementation compares favorably with other quantum engines implementations (see Chap. 4). It does not require the substantial auxiliary equipment (e.g. microwave sources) of an atomic implementation, and its spintronic underpinnings enable the presence of several quantum resources, in part because it operates using discrete energy levels instead of electron puddles as in mesoscopic quantum engines [147, 129, 293]. These spintronic underpinnings and advantages enable a path toward real world applications that the mesoscopic and atomic implementations cannot follow.

As a perspective, it would be nice to have a thermodynamic modelling [17, 177, 179, 178, 171] of the spintronic quantum engine containing, among several ingredients that amount to quantum resources, the non-thermal bath properties of the spinterfaces, PM centers around a magnetic fluctuation phase transition [168, 277], spin entropy sinking by the FM electrodes [294] and their weak coupling to the PM centers, and also examine the long-lived [295] dynamics of this magnetic coupling as a result of spintronic anisotropy.

After exploring the CoPc nano objects in molecular devices (Chap. 8, Chap. 9), it is evident that the CoPc molecular chain is complex beyond three mono layers, especially when the thickness is $\sim 20\text{nm}$ ($\sim 57\text{MLs}$) which limits our understanding of the top interface. Indeed, it is not a challenge to fabricate thin layers of spacers and perform similar magnetotransport studies. But, our technique of nano lithography method (see Appendix A) has its limitations to readily provide high yield devices. This is because of lack of control over the number of silica spheres being deposited during the lithography process. Possibly, one could improve the method of deposition of these silica spheres. As a perspective, advanced droplet micro-positioning technique can be a breakthrough to achieve localized devices. Since it is a relatively long processing chain it would be nice to get a quick confirmation on deposition of spheres using optical methods rather than SEM imaging. For this one could have an additional functionality to the spheres (e.g. fluorescent spheres) allowing for easy detection.

Concerning the study of two nano-objects namely : O vacancies (see Chap. 7, Sec. 7.4) and Co PM centers (see Chap. 7, Sec. 7.3.1) in device operando mode using synchrotron radiation. At HERMES beamline, we were able to hone in on the 20 micron MgO MTJ, with its 12 micron optical opening using $\sim 30\text{nm}$ x-ray spot size. We successfully managed to record the resistance maps at the oxygen edge inside the MTJ's optical opening, see Chap. 7, Sec. 7.4.2. Our analysis revealed a region of sized (0.5×0.5) micron that could be a prospective zone of hotspots. Due lack of beam time, we were not able to confirm this point. This progress will nevertheless enable future operando experiments during beam time to provide us with a factual understanding of how oxygen defects within the MgO barrier of a MTJ impact its operation.

At beamline DEIMOS, we established a protocol to mount these electrically fragile devices and performed TEY maps & T dependent transport measurements, see Chap. 7, Sec. 7.3. The results recorded during the beam time added weight to the publication Katcko et al. [11] by reproducing the spin flip excitation in solid state devices (Chap. 8, Sec. 8.5) and measurement of spintronic engines, see Chap. 9. We unambiguously mapped the intersection of the technological electrode and the bottom electrode within which the device lies, see Chap. 7, Sec. 7.3.2. Unlike MgO MTJs, due to our nano sphere lithography **A** the organic devices have no optical opening, which is one of the bottleneck in device operando study. Also, the Co PM centers are buried below the metallic overlayers (details of device structure in Chapters [5, 6]), so the TEY and TFY signals from the Co edge is below the detection threshold and there is only a 0.1% change directly in device current at the Co edge (see Chap. 7, Sec. 7.3.2).

To probe the PM center's nanotransport path one could be try to perform Electron Paramagnetic Resonance (EPR) operando measurements, which is analogous to nuclear magnetic resonance (NMR) where the former studies the materials with unpaired electron spins that are excited instead of the nuclear spins. This could give information on the coupling constant J of CoPc molecules which could be compared to our DFT calculations [11] (J concept in Chap. 8), thus factually determining the properties of the nano transport path within the solid state device.

Appendix A

Nano sphere lithography

The main ingredient for solvent and resist free nano lithography is silica nano spheres. The nano particles were fabricated by colleague L.Kandpal as a cross department collaboration with D.Mertz. The recipe is optimized to get the desired size of beads.

The fabricated silica spheres were stored in ethanol solvent to avoid contact with moisture which could increase their size. 1ml of the solution is heated slowly from 40C-80°C to accelerate the solvent evaporation and the dry powder is used for processing. The thin films were deposited with the nano spheres using a handcrafted apparatus and ultrasonic bath. The apparatus consists of TEM mesh with a 10micron opening that can block the adsorption of agglomerates from the silica powder. The sample is fixed behind the TEM mesh of the apparatus and placed inside the ultrasonic bath. A continuous ultrasonic power is applied for 7sec which provides kinetic energy to the dry silica spheres, which then hop to adsorption onto the sample surface.

Appendix B

Imaging the silica nano spheres

In order to get to the bottom of the failure in devices based on Ta capping one approach was to qualify the nano sphere solution. So, Dynamic Light Scattering (DLS) was performed on three types of silica in ethanol solutions namely, A, B and C see Figures [B.1, B.2]. From DLS it is clear the solution C is contaminated as its particle size is beyond the range of fabricated silica spheres. To check the structure of the spheres TEM measurements were performed on solution A and B. Interestingly, the TEM image of the silica nanoparticles showed bridges between them see Fig. B.3. This is due to the long term storage (>4months) in ethanol. The silanol functions continue to condense into silica with a very slow kinetics. Therefore, for optimum yield it is advisable to use freshly prepared nano particle solution or use up the batch before three months. SEM imaging enables to see single and agglomerates of silica spheres on Cr(100nm) surface, see Figures [B.4, B.5]

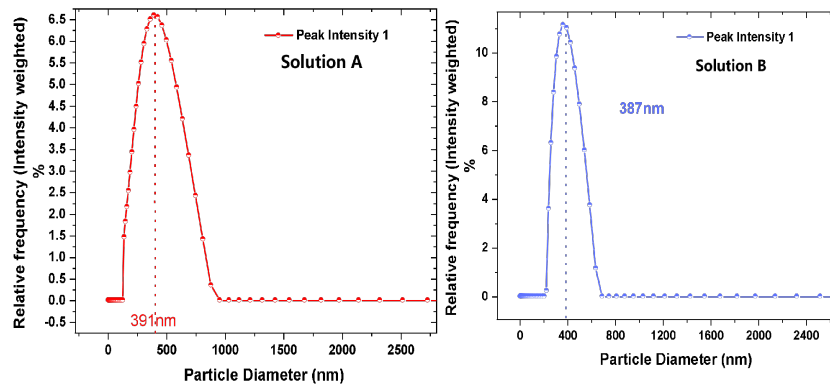


FIGURE B.1: The intensity vs. Particle diameter graph of DLS measurement indicates that solution A has nano spheres of size 391nm and solution-B has 387nm sized silica spheres dispersed in the solution.

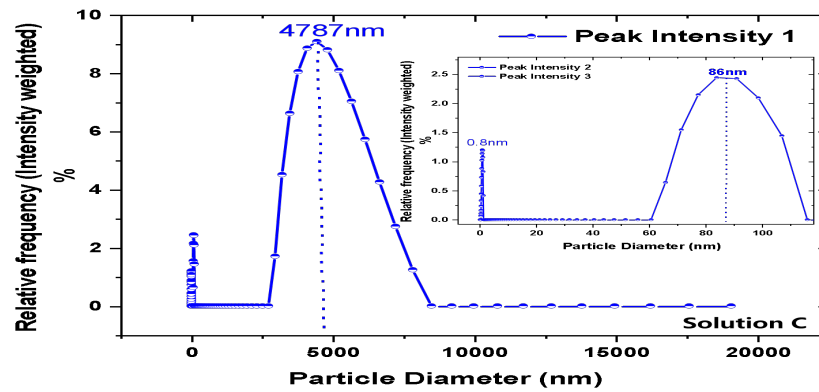


FIGURE B.2: The solution C is contaminated as it shows three different peaks with sizes incomparable to the silica spheres. The inset shows the extra peaks with small sizes <100nm.

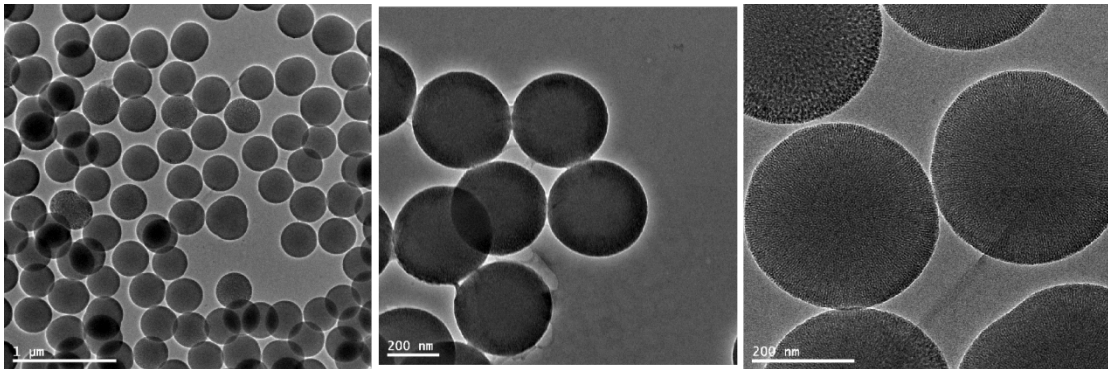


FIGURE B.3: The TEM measurements on solution A shows independent spheres and also some spheres forming bridges see the middle image.

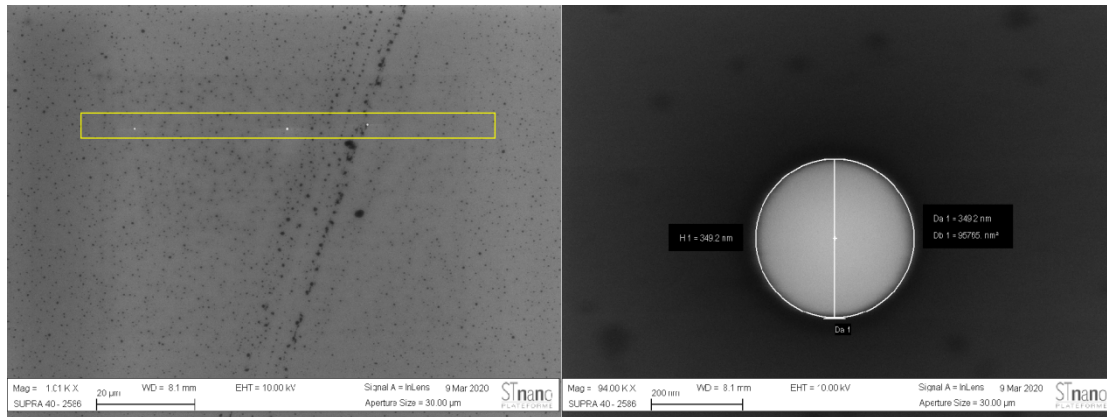


FIGURE B.4: The SEM scan in a 20micron window shows well distanced three spheres (yellow box) sized 500nm. The right image is a zoom one of the spheres.

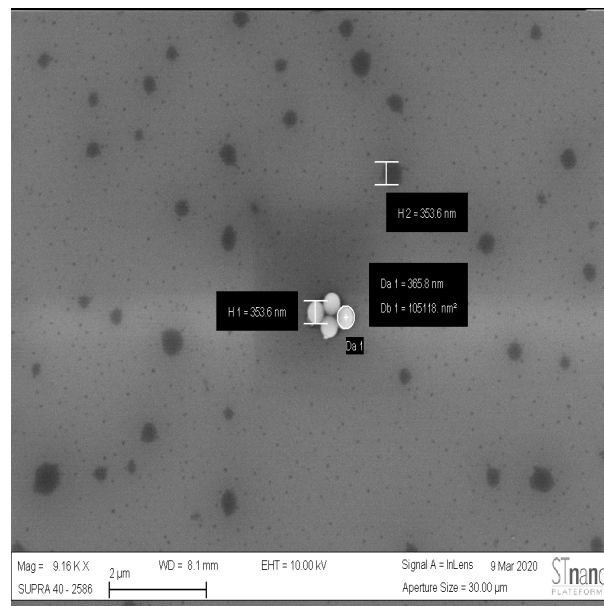


FIGURE B.5: SEM image in 2micron scale showing a agglomerate of four nano silica spheres

Bibliography

- [1] Albert Fert. "Origin, Development, and Future of Spintronics (Nobel Lecture)". In: *Angewandte Chemie International Edition* 47.32 (2008), pp. 5956–5967. DOI: [10.1002/anie.200801093](https://doi.org/10.1002/anie.200801093). eprint: <https://onlinelibrary.wiley.com/doi/pdf/10.1002/anie.200801093>. URL: <https://onlinelibrary.wiley.com/doi/abs/10.1002/anie.200801093>.
- [2] M. N. Baibich, J. M. Broto, A. Fert, F. Nguyen Van Dau, F. Petroff, P. Etienne, G. Creuzet, A. Friederich, and J. Chazelas. "Giant Magnetoresistance of (001)Fe/(001)Cr Magnetic Superlattices". In: *Phys. Rev. Lett.* 61 (21 Nov. 1988), pp. 2472–2475. DOI: [10.1103/PhysRevLett.61.2472](https://doi.org/10.1103/PhysRevLett.61.2472). URL: <https://link.aps.org/doi/10.1103/PhysRevLett.61.2472>.
- [3] M. Julliere. "Tunneling between ferromagnetic films". In: *Physics Letters A* 54.3 (Sept. 1975), pp. 225–226. DOI: [10.1016/0375-9601\(75\)90174-7](https://doi.org/10.1016/0375-9601(75)90174-7).
- [4] Prashanth Barla, Vinod Joshi, and Somashekara Bhat. "Spintronic devices: a promising alternative to CMOS devices". In: *Journal of Computational Electronics* 20 (Apr. 2021). DOI: [10.1007/s10825-020-01648-6](https://doi.org/10.1007/s10825-020-01648-6).
- [5] Michał Studniarek, Ufuk Halisdemir, Filip Schleicher, Beata Taudul, Etienne Urbain, Samy Boukari, Marie Hervé, Charles-Henri Lambert, Abbass Hamadeh, Sebastien Petit-Watelot, Olivia Zill, Daniel Lacour, Loïc Joly, Fabrice Scheurer, Guy Schmerber, Victor Da Costa, Anant Dixit, Pierre André Guitard, Manuel Acosta, Florian Leduc, Fadi Choueikani, Edwige Otero, Wulf Wulfhekel, François Montaigne, Elmer Nahuel Montebancho, Jacek Arabski, Philippe Ohresser, Eric Beaurepaire, Wolfgang Weber, Mébarek Alouani, Michel Hehn, and Martin Bowen. "Probing a Device's Active Atoms". In: *Advanced Materials* 29.19 (2017), p. 1606578. DOI: [10.1002/adma.201606578](https://doi.org/10.1002/adma.201606578). eprint: <https://www>.

- onlinelibrary.wiley.com/doi/pdf/10.1002/adma.201606578. URL: <https://www.onlinelibrary.wiley.com/doi/abs/10.1002/adma.201606578>.
- [6] Xi Chen, Ying-Shuang Fu, Shuai-Hua Ji, Tong Zhang, Peng Cheng, Xu-Cun Ma, Xiao-Long Zou, Wen-Hui Duan, Jin-Feng Jia, and Qi-Kun Xue. "Probing Superexchange Interaction in Molecular Magnets by Spin-Flip Spectroscopy and Microscopy". In: *Physical Review Letters* 101.19, 197208 (Nov. 2008), p. 197208. DOI: [10.1103/PhysRevLett.101.197208](https://doi.org/10.1103/PhysRevLett.101.197208).
- [7] Michele Serri, Wei Wu, Luke R. Fleet, Nicholas M. Harrison, Cyrus F. Hirjibehedin, Christopher W. M. Kay, Andrew J. Fisher, Gabriel Aeppli, and Sandrine Heutz. "High-temperature antiferromagnetism in molecular semiconductor thin films and nanostructures". In: *Nature Communications* 5, 3079 (Jan. 2014), p. 3079. DOI: [10.1038/ncomms4079](https://doi.org/10.1038/ncomms4079).
- [8] C. Barraud, K. Bouzehouane, C. Deranlot, D. J. Kim, R. Rakshit, S. Shi, J. Arab-ski, M. Bowen, E. Beaurepaire, S. Boukari, F. Petroff, P. Seneor, and R. Mattana. "Phthalocyanine based molecular spintronic devices". In: *Dalton Trans.* 45 (42 2016), pp. 16694–16699. DOI: [10.1039/C6DT02467J](https://doi.org/10.1039/C6DT02467J). URL: <http://dx.doi.org/10.1039/C6DT02467J>.
- [9] Clément Barraud, Karim Bouzehouane, Cyrille Deranlot, Stéphane Fusil, Hashim Jabbar, Jacek Arabski, Rajib Rakshit, Dong-Jik Kim, Christophe Kieber, Samy Boukari, Martin Bowen, Eric Beaurepaire, Pierre Seneor, Richard Mattana, and Frédéric Petroff. "Unidirectional Spin-Dependent Molecule-Ferromagnet Hybridized States Anisotropy in Cobalt Phthalocyanine Based Magnetic Tunnel Junctions". In: *Physical Review Letters* 114.20, 206603 (May 2015), p. 206603. DOI: [10.1103/PhysRevLett.114.206603](https://doi.org/10.1103/PhysRevLett.114.206603).
- [10] Sebastian Loth, Kirsten von Bergmann, Markus Ternes, Alexander F. Otte, Christopher P. Lutz, and Andreas J. Heinrich. "Controlling the state of quantum spins with electric currents". In: *Nature Physics* 6.5 (May 2010), pp. 340–344. DOI: [10.1038/nphys1616](https://doi.org/10.1038/nphys1616).
- [11] Kostantine Katcko, Etienne Urbain, Franck Ngassam, Lalit Kandpal, Bhavishya Chowrira, Filip Schleicher, Ufuk Halisdemir, Di Wang, Torsten Scherer, Damien Mertz, Benoit Leconte, Nicolas Beyer, Daniel Spor, Pierre Panissod,

- Arnaud Boulard, Jacek Arabski, Christophe Kieber, Emmanuel Sternitzky, Victor Costa, and Martin Bowen. "Encoding Information on the Excited State of a Molecular Spin Chain". In: *Advanced Functional Materials* (Feb. 2021), p. 2009467. DOI: [10.1002/adfm.202009467](https://doi.org/10.1002/adfm.202009467).
- [12] Haiming Tu Sa Yu. "Record thermopower found in an IrMn-based spintronic stack". In: *Nature Communications* 11, 2023 (Apr. 2020), p. 2023. DOI: [10.1038/s41467-020-15797-6](https://doi.org/10.1038/s41467-020-15797-6).
- [13] Pham Nam Hai, Shinobu Ohya, Masaaki Tanaka, Stewart E. Barnes, and Sadamichi Maekawa. "Electromotive force and huge magnetoresistance in magnetic tunnel junctions". In: *Nature* 458.7237 (Mar. 2009), pp. 489–492. DOI: [10.1038/nature07879](https://doi.org/10.1038/nature07879).
- [14] Daniel Ralph. "The electromotive force of MnAs nanoparticles". In: *Nature* 474 (June 2011), E6. DOI: [10.1038/nature10142](https://doi.org/10.1038/nature10142).
- [15] Kensaku Chida, Katsuhiko Nishiguchi, Gento Yamahata, Hirotaka Tanaka, and Akira Fujiwara. "Thermal-noise suppression in nano-scale Si field-effect transistors by feedback control based on single-electron detection". In: *Applied Physics Letters* 107.7 (2015), p. 073110. DOI: [10.1063/1.4928656](https://doi.org/10.1063/1.4928656).
- [16] Seng Ghee Tan and Mansoor B.A. Jalil. *Introduction to the Physics of Nanoelectronics*. 2012. ISBN: 978-0-85709-588-6.
- [17] K. Katcko, E. Urbain, B. Taudul, F. Schleicher, J. Arabski, E. Beaurepaire, B. Vilenó, D. Spor, W. Weber, D. Lacour, S. Boukari, M. Hehn, M. Alouani, J. Fransson, and M. Bowen. "Spin-driven electrical power generation at room temperature". In: *Communications Physics* 2.1, 116 (Sept. 2019), p. 116. DOI: [10.1038/s42005-019-0207-8](https://doi.org/10.1038/s42005-019-0207-8). arXiv: [1809.09836](https://arxiv.org/abs/1809.09836) [[cond-mat.mes-hall](https://arxiv.org/abs/1809.09836)].
- [18] Guo-Xing Miao, Joonyeon Chang, Badih A. Assaf, Donald Heiman, and Jagadeesh S. Moodera. "Spin regulation in composite spin-filter barrier devices". In: *Nature Communications* 5, 3682 (Apr. 2014), p. 3682. DOI: [10.1038/ncomms4682](https://doi.org/10.1038/ncomms4682).
- [19] G. Binasch, P. Grünberg, F. Saurenbach, and W. Zinn. "Enhanced magnetoresistance in layered magnetic structures with antiferromagnetic interlayer

- exchange". In: *Phys. Rev. B* 39 (7 Mar. 1989), pp. 4828–4830. DOI: [10.1103/PhysRevB.39.4828](https://doi.org/10.1103/PhysRevB.39.4828). URL: <https://link.aps.org/doi/10.1103/PhysRevB.39.4828>.
- [20] P. M. Tedrow and R. Meservey. "Spin-Dependent Tunneling into Ferromagnetic Nickel". In: *Physical Review Letters* 26.4 (Jan. 1971), pp. 192–195. DOI: [10.1103/PhysRevLett.26.192](https://doi.org/10.1103/PhysRevLett.26.192).
- [21] Mary Beth Stearns. "Simple explanation of tunneling spin-polarization of Fe, Co, Ni and its alloys". In: *Journal of Magnetism and Magnetic Materials* 5.2 (1977), pp. 167–171. ISSN: 0304-8853. DOI: [https://doi.org/10.1016/0304-8853\(77\)90185-8](https://doi.org/10.1016/0304-8853(77)90185-8). URL: <http://www.sciencedirect.com/science/article/pii/0304885377901858>.
- [22] J. C. Slonczewski. "Conductance and exchange coupling of two ferromagnets separated by a tunneling barrier". In: *Phys. Rev. B* 39 (10 Apr. 1989), pp. 6995–7002. DOI: [10.1103/PhysRevB.39.6995](https://doi.org/10.1103/PhysRevB.39.6995). URL: <https://link.aps.org/doi/10.1103/PhysRevB.39.6995>.
- [23] J. S. Moodera, Lisa R. Kinder, Terrilyn M. Wong, and R. Meservey. "Large Magnetoresistance at Room Temperature in Ferromagnetic Thin Film Tunnel Junctions". In: *Physical Review Letters* 74.16 (Apr. 1995), pp. 3273–3276. DOI: [10.1103/PhysRevLett.74.3273](https://doi.org/10.1103/PhysRevLett.74.3273).
- [24] T. Miyazaki and N. Tezuka. "Giant magnetic tunneling effect in Fe/Al₂O₃/Fe junction". In: *Journal of Magnetism and Magnetic Materials* 139.3 (Jan. 1995), pp. L231–L234. DOI: [10.1016/0304-8853\(95\)90001-2](https://doi.org/10.1016/0304-8853(95)90001-2).
- [25] Dexin Wang, C. Nordman, J. M. Daughton, Zhenghong Qian, and J. Fink. "70% TMR at room temperature for SDT sandwich junctions with CoFeB as free and reference Layers". In: *IEEE Transactions on Magnetics* 40.4 (2004), pp. 2269–2271.
- [26] J. H. Park, E. Vescovo, H. J. Kim, C. Kwon, R. Ramesh, and T. Venkatesan. "Direct evidence for a half-metallic ferromagnet". In: *Nature* 392.6678 (Apr. 1998), pp. 794–796. DOI: [10.1038/33883](https://doi.org/10.1038/33883).

- [27] K. Schwarz. "CrO₂ predicted as a half-metallic ferromagnet". In: *Journal of Physics F Metal Physics* 16.9 (Sept. 1986), pp. L211–L215. DOI: [10.1088/0305-4608/16/9/002](https://doi.org/10.1088/0305-4608/16/9/002).
- [28] M Bowen, A Barthélémy, M Bibes, E Jacquet, J P Contour, A Fert, D Wortmann, and S Blügel. "Half-metallicity proven using fully spin-polarized tunnelling". In: *Journal of Physics: Condensed Matter* 17.41 (Sept. 2005), pp. L407–L409. DOI: [10.1088/0953-8984/17/41/102](https://doi.org/10.1088/0953-8984/17/41/102). URL: <https://doi.org/10.1088/0953-8984/17/41/102>.
- [29] M. Bowen, M. Bibes, A. Barthélémy, J. P. Contour, A. Anane, Y. Lemaître, and A. Fert. "Nearly total spin polarization in La_{2/3}Sr_{1/3}MnO₃ from tunneling experiments". In: *Applied Physics Letters* 82.2, 233 (Jan. 2003), p. 233. DOI: [10.1063/1.1534619](https://doi.org/10.1063/1.1534619). arXiv: [cond-mat/0211158](https://arxiv.org/abs/cond-mat/0211158) [[cond-mat.mtrl-sci](https://arxiv.org/abs/cond-mat/0211158)].
- [30] H. Itoh, T. Ohsawa, and J. Inoue. "Magnetoresistance of Ferromagnetic Tunnel Junctions in the Double-Exchange Model". In: *Phys. Rev. Lett.* 84 (11 Mar. 2000), pp. 2501–2504. DOI: [10.1103/PhysRevLett.84.2501](https://doi.org/10.1103/PhysRevLett.84.2501). URL: <https://link.aps.org/doi/10.1103/PhysRevLett.84.2501>.
- [31] W. H. Butler, X.-G. Zhang, T. C. Schulthess, and J. M. MacLaren. "Spin-dependent tunneling conductance of Fe|MgO|Fe sandwiches". In: *Phys. Rev. B* 63 (5 Jan. 2001), p. 054416. DOI: [10.1103/PhysRevB.63.054416](https://doi.org/10.1103/PhysRevB.63.054416). URL: <https://link.aps.org/doi/10.1103/PhysRevB.63.054416>.
- [32] J. Mathon and A. Umerski. "Theory of tunneling magnetoresistance of an epitaxial Fe/MgO/Fe(001) junction". In: *Phys. Rev. B* 63.22, 220403 (June 2001), p. 220403. DOI: [10.1103/PhysRevB.63.220403](https://doi.org/10.1103/PhysRevB.63.220403).
- [33] P. Paufler. "Landolt-Börnstein, New Series, K. H. Hellwege (ed.), Group III: Crystal and Solid State Physics, Vol. 12: Magnetic and Other Properties of Oxides and Related Compounds, Part c: Hexagonal Ferrites. Special Lanthanide and Actinide Compounds. Springer-Verlag Berlin, Heidelberg, New York: 1982, XI + 604 Seiten, 1034 Figuren Leinen DM 980.–, etwa. US \$ 392.00". In: *Crystal Research and Technology* 18.12 (1983), pp. 1546–1546. DOI: [10.1002/crat.2170181220](https://doi.org/10.1002/crat.2170181220). eprint: <https://onlinelibrary.wiley.com/doi/pdf/10.1002/crat.2170181220>.

- 1002/crat.2170181220. URL: <https://onlinelibrary.wiley.com/doi/abs/10.1002/crat.2170181220>.
- [34] Yan Wang, Jia Zhang, X. G. Zhang, Hai-Ping Cheng, and X. F. Han. "First-principles study of Fe/MgO based magnetic tunnel junctions with Mg interlayers". In: *Phys. Rev. B* 82.5, 054405 (Aug. 2010), p. 054405. DOI: [10.1103/PhysRevB.82.054405](https://doi.org/10.1103/PhysRevB.82.054405).
- [35] Andrew Gibson, Roger Haydock, and John P. Lafemina. "Stability of vacancy defects in MgO: The role of charge neutrality". In: *Phys. Rev. B* 50.4 (July 1994), pp. 2582–2592. DOI: [10.1103/PhysRevB.50.2582](https://doi.org/10.1103/PhysRevB.50.2582).
- [36] R. C. Whited and W. C. Walker. "Exciton Spectra of CaO and MgO". In: *Physical Review Letters* 22.26 (June 1969), pp. 1428–1430. DOI: [10.1103/PhysRevLett.22.1428](https://doi.org/10.1103/PhysRevLett.22.1428).
- [37] G. H. Rosenblatt, M. W. Rowe, Jr. Williams G. P., R. T. Williams, and Y. Chen. "Luminescence of F and F⁺ centers in magnesium oxide". In: *Phys. Rev. B* 39.14 (May 1989), pp. 10309–10318. DOI: [10.1103/PhysRevB.39.10309](https://doi.org/10.1103/PhysRevB.39.10309).
- [38] Philipp Haas, Fabien Tran, and Peter Blaha. "Erratum: Calculation of the lattice constant of solids with semilocal functionals [Phys. Rev. B 79, 085104 (2009)]". In: *Physical Review B* 79 (May 2009). DOI: [10.1103/PhysRevB.79.209902](https://doi.org/10.1103/PhysRevB.79.209902).
- [39] F. Bonell, S. Andrieu, A. M. Bataille, C. Tiusan, and G. Lengaigne. "Consequences of interfacial Fe-O bonding and disorder in epitaxial Fe/MgO/Fe(001) magnetic tunnel junctions". In: *Phys. Rev. B* 79.22, 224405 (June 2009), p. 224405. DOI: [10.1103/PhysRevB.79.224405](https://doi.org/10.1103/PhysRevB.79.224405).
- [40] H. L. Meyerheim, R. Popescu, J. Kirschner, N. Jedrecy, M. Sauvage-Simkin, B. Heinrich, and R. Pinchaux. "Geometrical and Compositional Structure at Metal-Oxide Interfaces: MgO on Fe(001)". In: *Physical Review Letters* 87.7, 076102 (Aug. 2001), p. 076102. DOI: [10.1103/PhysRevLett.87.076102](https://doi.org/10.1103/PhysRevLett.87.076102).
- [41] S Yuasa and D D Djayaprawira. "Giant tunnel magnetoresistance in magnetic tunnel junctions with a crystalline MgO(001) barrier". In: *Journal of Physics D:*

- Applied Physics* 40.21 (Oct. 2007), R337–R354. DOI: [10.1088/0022-3727/40/21/r01](https://doi.org/10.1088/0022-3727/40/21/r01). URL: <https://doi.org/10.1088/0022-3727/40/21/r01>.
- [42] C. Kittel. *Introduction to Solid State Physics, 6th edition*. Wiley, New York, 1986.
- [43] N. W. Ashcroft and N. D. Mermin. *Solid State Physics*. Philadelphia: Saunders College, 1976.
- [44] M. Bowen, V. Cros, F. Petroff, A. Fert, C. Martinez Boubeta, J. L. Costa-Krämer, J. V. Anguita, A. Cebollada, F. Briones, J. M. de Teresa, L. Morellón, M. R. Ibarra, F. Güell, F. Peiró, and A. Cornet. “Large magnetoresistance in Fe/MgO/FeCo(001) epitaxial tunnel junctions on GaAs(001)”. In: *Applied Physics Letters* 79.11 (2001), pp. 1655–1657. DOI: [10.1063/1.1404125](https://doi.org/10.1063/1.1404125). eprint: <https://doi.org/10.1063/1.1404125>. URL: <https://doi.org/10.1063/1.1404125>.
- [45] J. Faure-Vincent, C. Tiusan, E. Jouguelet, F. Canet, M. Sajieddine, C. Bellouard, E. Popova, M. Hehn, F. Montaigne, and A. Schuhl. “High tunnel magnetoresistance in epitaxial Fe/MgO/Fe tunnel junctions”. In: *Applied Physics Letters* 82.25 (2003), pp. 4507–4509. DOI: [10.1063/1.1586785](https://doi.org/10.1063/1.1586785). eprint: <https://doi.org/10.1063/1.1586785>. URL: <https://doi.org/10.1063/1.1586785>.
- [46] Shinji Yuasa, Taro Nagahama, Akio Fukushima, Yoshishige Suzuki, and Koji Ando. “Giant room-temperature magnetoresistance in single-crystal Fe/MgO/Fe magnetic tunnel junctions”. In: *Nature Materials* 3.12 (Dec. 2004), pp. 868–871. DOI: [10.1038/nmat1257](https://doi.org/10.1038/nmat1257).
- [47] Stuart S. P. Parkin, Christian Kaiser, Alex Panchula, Philip M. Rice, Brian Hughes, Mahesh Samant, and See-Hun Yang. “Giant tunnelling magnetoresistance at room temperature with MgO (100) tunnel barriers”. In: *Nature Materials* 3.12 (Dec. 2004), pp. 862–867. DOI: [10.1038/nmat1256](https://doi.org/10.1038/nmat1256).
- [48] S. Ikeda, J. Hayakawa, Y. Ashizawa, Y. M. Lee, K. Miura, H. Hasegawa, M. Tsunoda, F. Matsukura, and H. Ohno. “Tunnel magnetoresistance of 604% at 300 K by suppression of Ta diffusion in CoFeB/MgO/CoFeB pseudo-spinal valves annealed at high temperature”. In: *Applied Physics Letters* 93.8, 082508 (Aug. 2008), p. 082508. DOI: [10.1063/1.2976435](https://doi.org/10.1063/1.2976435).

- [49] H. Sato, E. C. I. Enobio, M. Yamanouchi, S. Ikeda, S. Fukami, S. Kanai, F. Matsukura, and H. Ohno. "Properties of magnetic tunnel junctions with a MgO/CoFeB/Ta/CoFeB/MgO recording structure down to junction diameter of 11nm". In: *Applied Physics Letters* 105.6 (2014), p. 062403. DOI: [10.1063/1.4892924](https://doi.org/10.1063/1.4892924). eprint: <https://doi.org/10.1063/1.4892924>. URL: <https://doi.org/10.1063/1.4892924>.
- [50] K. Watanabe, B. Jinnai, S. Fukami, H. Sato, and H. Ohno. "Shape anisotropy revisited in single-digit nanometer magnetic tunnel junctions". In: *Nature Communications* 9, 663 (Feb. 2018), p. 663. DOI: [10.1038/s41467-018-03003-7](https://doi.org/10.1038/s41467-018-03003-7). arXiv: [1712.08774](https://arxiv.org/abs/1712.08774) [[physics.app-ph](https://arxiv.org/abs/1712.08774)].
- [51] H. L. Meyerheim, R. Popescu, N. Jedrecy, M. Vedpathak, M. Sauvage-Simkin, R. Pinchaux, B. Heinrich, and J. Kirschner. "Surface x-ray diffraction analysis of the MgO/Fe(001) interface: Evidence for an FeO layer". In: *Phys. Rev. B* 65.14, 144433 (Apr. 2002), p. 144433. DOI: [10.1103/PhysRevB.65.144433](https://doi.org/10.1103/PhysRevB.65.144433).
- [52] X. G. Zhang, W. H. Butler, and Amrit Bandyopadhyay. "Effects of the iron-oxide layer in Fe-FeO-MgO-Fe tunneling junctions". In: *Phys. Rev. B* 68.9, 092402 (Sept. 2003), p. 092402. DOI: [10.1103/PhysRevB.68.092402](https://doi.org/10.1103/PhysRevB.68.092402).
- [53] J. Mathon and A. Umerski. "Theory of resonant tunneling in an epitaxial Fe/Au/MgO/Au/Fe (001) junction". In: *Phys. Rev. B* 71.22, 220402 (June 2005), p. 220402. DOI: [10.1103/PhysRevB.71.220402](https://doi.org/10.1103/PhysRevB.71.220402).
- [54] H. X. Yang, M. Chshiev, B. Dieny, J. H. Lee, A. Manchon, and K. H. Shin. "First-principles investigation of the very large perpendicular magnetic anisotropy at Fe|MgO and Co|MgO interfaces". In: *Phys. Rev. B* 84.5, 054401 (Aug. 2011), p. 054401. DOI: [10.1103/PhysRevB.84.054401](https://doi.org/10.1103/PhysRevB.84.054401). arXiv: [1011.5667](https://arxiv.org/abs/1011.5667) [[cond-mat.mtrl-sci](https://arxiv.org/abs/1011.5667)].
- [55] J. W. Koo, S. Mitani, T. T. Sasaki, H. Sukegawa, Z. C. Wen, T. Ohkubo, T. Niizeki, K. Inomata, and K. Hono. "Large perpendicular magnetic anisotropy at Fe/MgO interface". In: *Applied Physics Letters* 103.19, 192401 (Nov. 2013), p. 192401. DOI: [10.1063/1.4828658](https://doi.org/10.1063/1.4828658).

- [56] A. Hallal, H. X. Yang, B. Dieny, and M. Chshiev. "Anatomy of perpendicular magnetic anisotropy in Fe/MgO magnetic tunnel junctions: First-principles insight". In: *Phys. Rev. B* 88.18, 184423 (Nov. 2013), p. 184423. DOI: [10.1103/PhysRevB.88.184423](https://doi.org/10.1103/PhysRevB.88.184423). arXiv: [1308.2909](https://arxiv.org/abs/1308.2909) [[cond-mat.mtrl-sci](#)].
- [57] J. Okabayashi, J. W. Koo, H. Sukegawa, S. Mitani, Y. Takagi, and T. Yokoyama. "Perpendicular magnetic anisotropy at the interface between ultrathin Fe film and MgO studied by angular-dependent x-ray magnetic circular dichroism". In: *Applied Physics Letters* 105.12, 122408 (Sept. 2014), p. 122408. DOI: [10.1063/1.4896290](https://doi.org/10.1063/1.4896290).
- [58] S. H. Liang, T. T. Zhang, P. Barate, J. Frougier, M. Vidal, P. Renucci, B. Xu, H. Jaffrès, J. M. George, X. Devaux, M. Hehn, X. Marie, S. Mangin, H. X. Yang, A. Hallal, M. Chshiev, T. Amand, H. F. Liu, D. P. Liu, X. F. Han, Z. G. Wang, and Y. Lu. "Large and robust electrical spin injection into GaAs at zero magnetic field using an ultrathin CoFeB/MgO injector". In: *Phys. Rev. B* 90.8, 085310 (Aug. 2014), p. 085310. DOI: [10.1103/PhysRevB.90.085310](https://doi.org/10.1103/PhysRevB.90.085310). arXiv: [1404.4527](https://arxiv.org/abs/1404.4527) [[cond-mat.mtrl-sci](#)].
- [59] J.G. Park, Tae-Hun Shim, K.S. Chae, D.Y. Lee, Y. Takemura, S.E. Lee, M.S. Jeon, Jong Baek, S.O. Park, and J.P. Hong. "Challenging Issues for Terra-bit-level Perpendicular STT-MRAM". In: *Technical Digest - International Electron Devices Meeting, IEDM 2015* (Feb. 2015), pp. 19.2.1–19.2.4. DOI: [10.1109/IEDM.2014.7047081](https://doi.org/10.1109/IEDM.2014.7047081).
- [60] S. X. Huang, T. Y. Chen, and C. L. Chien. "Spin polarization of amorphous CoFeB determined by point-contact Andreev reflection". In: *Applied Physics Letters* 92.24, 242509 (June 2008), p. 242509. DOI: [10.1063/1.2949740](https://doi.org/10.1063/1.2949740).
- [61] Ulrike Diebold. "The Surface Science of Metal Oxides: A Step Towards More 'Realistic' Model Systems". In: *APS Southeastern Section Meeting Abstracts*. APS Meeting Abstracts. Nov. 1998, IA.01.
- [62] G. X. Miao, Y. J. Park, J. S. Moodera, M. Seibt, G. Eilers, and M. Münzenberg. "Disturbance of Tunneling Coherence by Oxygen Vacancy in Epitaxial Fe/MgO/Fe Magnetic Tunnel Junctions". In: *Phys. Rev. Lett.* 100 (24 June

- 2008), p. 246803. DOI: [10.1103/PhysRevLett.100.246803](https://doi.org/10.1103/PhysRevLett.100.246803). URL: <https://link.aps.org/doi/10.1103/PhysRevLett.100.246803>.
- [63] D. J. Kim, W. S. Choi, F. Schleicher, R. H. Shin, S. Boukari, V. Davesne, C. Kieber, J. Arabski, G. Schmerber, E. Beaurepaire, W. Jo, and M. Bowen. “Control of defect-mediated tunneling barrier heights in ultrathin MgO films”. In: *Applied Physics Letters* 97.26, 263502 (Dec. 2010), p. 263502. DOI: [10.1063/1.3531652](https://doi.org/10.1063/1.3531652). arXiv: [1010.2473](https://arxiv.org/abs/1010.2473) [cond-mat.mtrl-sci].
- [64] F. Schleicher, U. Halisdemir, D. Lacour, M. Gallart, S. Boukari, G. Schmerber, V. Davesne, P. Panissod, D. Halley, H. Majjad, Y. Henry, B. Leconte, A. Boulard, D. Spor, N. Beyer, C. Kieber, E. Sternitzky, O. Cregut, M. Ziegler, F. Montaigne, E. Beaurepaire, P. Gilliot, M. Hehn, and M. Bowen. “Localized states in advanced dielectrics from the vantage of spin- and symmetry-polarized tunnelling across MgO”. In: *Nature Communications* 5, 4547 (Aug. 2014), p. 4547. DOI: [10.1038/ncomms5547](https://doi.org/10.1038/ncomms5547).
- [65] Beata Taudul, Elmer Nahuel Montebianco, Ufuk Halisdemir, Daniel Lacour, Filip Schleicher, François Montaigne, Eric Beaurepaire, Samy Boukari, Michel Hehn, Mébarek Alouani, and Martin Bowen. “Tunneling Spintronics across MgO Driven by Double Oxygen Vacancies”. In: *Advanced Electronic Materials* 3.7 (2017), p. 1600390. DOI: [10.1002/aelm.201600390](https://doi.org/10.1002/aelm.201600390). eprint: <https://onlinelibrary.wiley.com/doi/pdf/10.1002/aelm.201600390>. URL: <https://onlinelibrary.wiley.com/doi/abs/10.1002/aelm.201600390>.
- [66] F. Schleicher, B. Taudul, U. Halisdemir, K. Katcko, E. Montebianco, D. Lacour, S. Boukari, F. Montaigne, E. Urbain, L. M. Kandpal, J. Arabski, W. Weber, E. Beaurepaire, M. Hehn, M. Alouani, and M. Bowen. “Consolidated picture of tunnelling spintronics across oxygen vacancy states in MgO”. In: *Journal of Physics D Applied Physics* 52.30, 305302 (July 2019), p. 305302. DOI: [10.1088/1361-6463/ab1f4d](https://doi.org/10.1088/1361-6463/ab1f4d).
- [67] R. W. Dave, G. Steiner, J. M. Slaughter, J. J. Sun, B. Craigo, S. Pietambaram, K. Smith, G. Grynkewich, M. DeHerrera, J. Akerman, and S. Tehrani. “MgO-based tunnel junction material for high-speed toggle magnetic random access

- memory". In: *IEEE Transactions on Magnetics* 42.8 (2006), pp. 1935–1939. DOI: [10.1109/TMAG.2006.877743](https://doi.org/10.1109/TMAG.2006.877743).
- [68] Zhongchang Wang, Mitsuhiro Saito, Keith P. McKenna, Shunsuke Fukami, Hideo Sato, Shoji Ikeda, Hideo Ohno, and Yuichi Ikuhara. "Atomic-Scale Structure and Local Chemistry of CoFeB-MgO Magnetic Tunnel Junctions". In: *Nano Letters* 16.3 (Mar. 2016), pp. 1530–1536. DOI: [10.1021/acs.nanolett.5b03627](https://doi.org/10.1021/acs.nanolett.5b03627).
- [69] Filip Schleicher, Michał Studniarek, Kuppusamy Senthil Kumar, Etienne Urbain, Kostantine Katcko, Jinjie Chen, Timo Frauhammer, Marie Hervé, Ufuk Halisdemir, Lalit Mohan Kandpal, Daniel Lacour, Alberto Riminucci, Loic Joly, Fabrice Scheurer, Benoit Gobaut, Fadi Choueikani, Edwige Otero, Philippe Ohresser, Jacek Arabski, Guy Schmerber, Wulf Wulfhekel, Eric Beaurepaire, Wolfgang Weber, Samy Boukari, Mario Ruben, and Martin Bowen. "Linking Electronic Transport through a Spin Crossover Thin Film to the Molecular Spin State Using X-ray Absorption Spectroscopy Operando Techniques". In: *ACS Applied Materials & Interfaces* 10.37 (2018). PMID: 30136570, pp. 31580–31585. DOI: [10.1021/acsami.8b11495](https://doi.org/10.1021/acsami.8b11495). eprint: <https://doi.org/10.1021/acsami.8b11495>. URL: <https://doi.org/10.1021/acsami.8b11495>.
- [70] Bernhard Mann and Hans Kuhn. "Tunneling through Fatty Acid Salt Monolayers". In: *Journal of Applied Physics* 42.11 (Oct. 1971), pp. 4398–4405. DOI: [10.1063/1.1659785](https://doi.org/10.1063/1.1659785).
- [71] Arieh Aviram and Mark A. Ratner. "Molecular rectifiers". In: *Chemical Physics Letters* 29.2 (Nov. 1974), pp. 277–283. DOI: [10.1016/0009-2614\(74\)85031-1](https://doi.org/10.1016/0009-2614(74)85031-1).
- [72] V. Dediu, M. Murgia, F. C. Matocotta, C. Taliani, and S. Barbanera. "Room temperature spin polarized injection in organic semiconductor". In: *Solid State Communications* 122.3 (Apr. 2002), pp. 181–184. DOI: [10.1016/S0038-1098\(02\)00090-X](https://doi.org/10.1016/S0038-1098(02)00090-X).
- [73] Z. H. Xiong, Di Wu, Z. Valy Vardeny, and Jing Shi. "Giant magnetoresistance in organic spin-valves". In: *Nature* 427.6977 (Feb. 2004), pp. 821–824. DOI: [10.1038/nature02325](https://doi.org/10.1038/nature02325).

- [74] T L Francis, Ö Mermer, G Veeraraghavan, and M Wohlgenannt. "Large magnetoresistance at room temperature in semiconducting polymer sandwich devices". In: *New Journal of Physics* 6 (Dec. 2004), pp. 185–185. DOI: [10.1088/1367-2630/6/1/185](https://doi.org/10.1088/1367-2630/6/1/185). URL: <https://doi.org/10.1088%2F1367-2630%2F6%2F1%2F185>.
- [75] Ö. Mermer, G. Veeraraghavan, T. L. Francis, Y. Sheng, D. T. Nguyen, M. Wohlgenannt, A. Köhler, M. K. Al-Suti, and M. S. Khan. "Large magnetoresistance in nonmagnetic π -conjugated semiconductor thin film devices". In: *Phys. Rev. B* 72.20, 205202 (Nov. 2005), p. 205202. DOI: [10.1103/PhysRevB.72.205202](https://doi.org/10.1103/PhysRevB.72.205202). arXiv: [cond-mat/0504738](https://arxiv.org/abs/cond-mat/0504738) [[cond-mat.mtrl-sci](https://arxiv.org/abs/cond-mat/0504738)].
- [76] Clément Barraud, Pierre Seneor, Richard Mattana, Stéphane Fusil, K. Bouzouane, Cyrille Deranlot, Patrizio Graziosi, Luis Hueso, Ilaria Bergenti, Alek Dediu, Frederic Petroff, and Albert Fert. "Unravelling the role of the interface for spin injection into organic semiconductors". In: *Nature Physics* 6 (May 2010). DOI: [10.1038/nphys1688](https://doi.org/10.1038/nphys1688).
- [77] Marta Galbiati. *Molecular Spintronics: From Organic Semiconductors to Self-Assembled Monolayers*. 2016. ISBN: 978-3-319-22611-8.
- [78] M. Pope, C.E. Swenberg, and P.D.C.E. Swenberg. *Electronic Processes in Organic Crystals and Polymers*. Monographs on the Physics & Ch. Oxford University Press, 1999. ISBN: 9780195129632. URL: <https://books.google.fr/books?id=AZVUAAAAMAAJ>.
- [79] J. Eiduss and E.A. Silinsh. *Organic Molecular Crystals: Their Electronic States*. Springer Series in Solid-State Sciences. Springer Berlin Heidelberg, 2012. ISBN: 9783642814648. URL: <https://books.google.fr/books?id=3uLnCAAQBAJ>.
- [80] V. Alek Dediu, Luis E. Hueso, Ilaria Bergenti, and Carlo Taliani. "Spin routes in organic semiconductors". In: *Nature Materials* 8.9 (Sept. 2009), pp. 707–716. DOI: [10.1038/nmat2510](https://doi.org/10.1038/nmat2510).
- [81] V. I. Krinichnyi, S. D. Chemerisov, and Ya. S. Lebedev. "EPR and charge-transport studies of polyaniline". In: *Phys. Rev. B* 55.24 (June 1997), pp. 16233–16244. DOI: [10.1103/PhysRevB.55.16233](https://doi.org/10.1103/PhysRevB.55.16233).

- [82] S Pramanik, Cg Stefanita, Sreehari Patibandla, Supriyo Bandyopadhyay, K. Garre, N Harth, and M. Cahay. "Spin relaxation in a nanowire organic spin valve: Observation of extremely long spin relaxation times". In: *Nature nanotechnology* 2 (Apr. 2007), pp. 216–9. DOI: [10.1038/nnano.2007.64](https://doi.org/10.1038/nnano.2007.64).
- [83] Kazuhito Tsukagoshi, Bruce W. Alphenaar, and Hiroki Ago. "Coherent transport of electron spin in a ferromagnetically contacted carbon nanotube". In: *Nature* 401.6753 (Oct. 1999), pp. 572–574. DOI: [10.1038/44108](https://doi.org/10.1038/44108).
- [84] Xikang Zhao, Saadia T. Chaudhry, and Jianguo Mei. "Chapter Five - Heterocyclic Building Blocks for Organic Semiconductors". In: *Heterocyclic Chemistry in the 21st Century*. Ed. by Eric F.V. Scriven and Christopher A. Ramsden. Vol. 121. Advances in Heterocyclic Chemistry. Academic Press, 2017, pp. 133–171. DOI: <https://doi.org/10.1016/bs.aihch.2016.04.009>. URL: <http://www.sciencedirect.com/science/article/pii/S0065272516300320>.
- [85] Greg Szulczewski, Stefano Sanvito, and Michael Coey. "A spin of their own". In: *Nature materials* 8 (Oct. 2009), pp. 693–5. DOI: [10.1038/nmat2518](https://doi.org/10.1038/nmat2518).
- [86] Dali Sun, Eitan Ehrenfreund, and Z. Vally Vardeny. "The first decade of organic spintronics research". In: *Chem. Commun.* 50 (15 2014), pp. 1781–1793. DOI: [10.1039/C3CC47126H](https://doi.org/10.1039/C3CC47126H). URL: <http://dx.doi.org/10.1039/C3CC47126H>.
- [87] Michael G. Walter, Alexander B. Rudine, and Carl C. Wamser. "Porphyrins and phthalocyanines in solar photovoltaic cells". In: *Journal of Porphyrins and Phthalocyanines* 14.09 (2010), pp. 759–792. DOI: [10.1142/S1088424610002689](https://doi.org/10.1142/S1088424610002689). eprint: <https://doi.org/10.1142/S1088424610002689>. URL: <https://doi.org/10.1142/S1088424610002689>.
- [88] Akitaka Hoshino, Yoshiko Takenaka, and Hideki Miyaji. "Redetermination of the crystal structure of α -copper phthalocyanine grown on KCl". In: *Acta Crystallographica Section B* 59.3 (June 2003), pp. 393–403. DOI: [10.1107/S010876810300942X](https://doi.org/10.1107/S010876810300942X). URL: <https://doi.org/10.1107/S010876810300942X>.
- [89] Meng-Sheng Liao and Steve Scheiner. "Electronic structure and bonding in metal phthalocyanines, Metal=Fe, Co, Ni, Cu, Zn, Mg". In: *The Journal of Chemical Physics* 114.22 (2001), pp. 9780–9791. DOI: [10.1063/1.1367374](https://doi.org/10.1063/1.1367374).

- eprint: <https://doi.org/10.1063/1.1367374>. URL: <https://doi.org/10.1063/1.1367374>.
- [90] R. C. Jaklevic and J. Lambe. "Molecular Vibration Spectra by Electron Tunneling". In: *Phys. Rev. Lett.* 17 (22 Nov. 1966), pp. 1139–1140. DOI: [10.1103/PhysRevLett.17.1139](https://doi.org/10.1103/PhysRevLett.17.1139). URL: <https://link.aps.org/doi/10.1103/PhysRevLett.17.1139>.
- [91] B. C. Stipe, M. A. Rezaei, and W. Ho. "Single-Molecule Vibrational Spectroscopy and Microscopy". In: *Science* 280.5370 (1998), pp. 1732–1735. ISSN: 0036-8075. DOI: [10.1126/science.280.5370.1732](https://doi.org/10.1126/science.280.5370.1732). eprint: <https://science.sciencemag.org/content/280/5370/1732.full.pdf>. URL: <https://science.sciencemag.org/content/280/5370/1732>.
- [92] X. H. Qiu, G. V. Nazin, and W. Ho. "Vibrationally Resolved Fluorescence Excited with Submolecular Precision". In: *Science* 299.5606 (Jan. 2003), pp. 542–546. DOI: [10.1126/science.1078675](https://doi.org/10.1126/science.1078675).
- [93] A. J. Heinrich, J. A. Gupta, C. P. Lutz, and D. M. Eigler. "Single-Atom Spin-Flip Spectroscopy". In: *Science* 306.5695 (2004), pp. 466–469. DOI: [10.1126/science.1101077](https://doi.org/10.1126/science.1101077). eprint: <https://science.sciencemag.org/content/306/5695/466.full.pdf>. URL: <https://science.sciencemag.org/content/306/5695/466>.
- [94] Cyrus F. Hirjibehedin, Christopher P. Lutz, and Andreas J. Heinrich. "Spin Coupling in Engineered Atomic Structures". In: *Science* 312.5776 (2006), pp. 1021–1024. DOI: [10.1126/science.1125398](https://doi.org/10.1126/science.1125398). eprint: <https://science.sciencemag.org/content/312/5776/1021.full.pdf>. URL: <https://science.sciencemag.org/content/312/5776/1021>.
- [95] Cyrus F. Hirjibehedin, Chiung-Yuan Lin, Alexander F. Otte, Markus Ternes, Christopher P. Lutz, Barbara A. Jones, and Andreas J. Heinrich. "Large Magnetic Anisotropy of a Single Atomic Spin Embedded in a Surface Molecular Network". In: *Science* 317.5842 (2007), pp. 1199–1203. ISSN: 0036-8075. DOI: [10.1126/science.1146110](https://doi.org/10.1126/science.1146110). eprint: <https://science.sciencemag.org/content/317/5842/1199.full.pdf>. URL: <https://science.sciencemag.org/content/317/5842/1199>.

- [96] Sebastian Loth, Christopher Lutz, and Andreas Heinrich. "Spin-polarized spin excitation spectroscopy". In: *New Journal of Physics* 12 (Dec. 2010), p. 125021. DOI: [10.1088/1367-2630/12/12/125021](https://doi.org/10.1088/1367-2630/12/12/125021).
- [97] Taeyoung Choi. "Studies of single atom magnets via scanning tunneling microscopy". In: *Journal of Magnetism and Magnetic Materials* 481 (2019), pp. 150–155. ISSN: 0304-8853. DOI: <https://doi.org/10.1016/j.jmmm.2019.03.007>. URL: <https://www.sciencedirect.com/science/article/pii/S0304885318331718>.
- [98] H. Vázquez, R. Oszwaldowski, P. Pou, J. Ortega, R. Pérez, F. Flores, and A. Kahn. "Dipole formation at metal/PTCDA interfaces: Role of the Charge Neutrality Level". In: *EPL (Europhysics Letters)* 65.6 (Mar. 2004), pp. 802–808. DOI: [10.1209/epl/i2003-10131-2](https://doi.org/10.1209/epl/i2003-10131-2). arXiv: [cond-mat/0405527](https://arxiv.org/abs/cond-mat/0405527) [[cond-mat.mtrl-sci](https://arxiv.org/abs/cond-mat/0405527)].
- [99] Mickael L. Perrin, Christopher J. O. Verzijl, Christian A. Martin, Ahson J. Shaikh, Rienk Eelkema, Jan H. van Esch, Jan M. van Ruitenbeek, Joseph M. Thijssen, Herre S. J. van der Zant, and Diana Dulić. "Large tunable image-charge effects in single-molecule junctions". In: *Nature Nanotechnology* 8.4 (Apr. 2013), pp. 282–287. DOI: [10.1038/nnano.2013.26](https://doi.org/10.1038/nnano.2013.26). arXiv: [1403.4266](https://arxiv.org/abs/1403.4266) [[cond-mat.mes-hall](https://arxiv.org/abs/1403.4266)].
- [100] Fatima Djeghloul, Manuel Gruber, Etienne Urbain, Dimitra Xenioti, Loic Joly, Samy Boukari, Jacek Arabski, Hervé Bulou, Fabrice Scheurer, François Bertran, Patrick Le Fèvre, Amina Taleb-Ibrahimi, Wulf Wulfhekel, Guillaume Garreau, Samar Hajjar-Garreau, Patrick Wetzels, Mebarek Alouani, Eric Beaurepaire, Martin Bowen, and Wolfgang Weber. "High Spin Polarization at Ferromagnetic Metal–Organic Interfaces: A Generic Property". In: *The Journal of Physical Chemistry Letters* 7.13 (2016). PMID: 27266579, pp. 2310–2315. DOI: [10.1021/acs.jpcllett.6b01112](https://doi.org/10.1021/acs.jpcllett.6b01112). eprint: <https://doi.org/10.1021/acs.jpcllett.6b01112>. URL: <https://doi.org/10.1021/acs.jpcllett.6b01112>.
- [101] Stefano Sanvito. "Surface science: Seeing the spin through". In: *Nature* 467 (Oct. 2010), pp. 664–5. DOI: [10.1038/467664a](https://doi.org/10.1038/467664a).

- [102] Sophie Delprat, Marta Galbiati, Sergio Tatay, Benoit Quinard, Clément Barraud, Frédéric Petroff, Pierre Seneor, and Richard Mattana. “Molecular spintronics: The role of spin-dependent hybridization”. In: *Journal of Physics D: Applied Physics* 51 (Nov. 2018), p. 473001. DOI: [10.1088/1361-6463/aad9dc](https://doi.org/10.1088/1361-6463/aad9dc).
- [103] C. Iacovita, M. V. Rastei, B. W. Heinrich, T. Brumme, J. Kortus, L. Limot, and J. P. Bucher. “Visualizing the Spin of Individual Cobalt-Phthalocyanine Molecules”. In: *Physical Review Letters* 101.11, 116602 (Sept. 2008), p. 116602. DOI: [10.1103/PhysRevLett.101.116602](https://doi.org/10.1103/PhysRevLett.101.116602). arXiv: 0805.0485 [cond-mat.mtrl-sci].
- [104] Stefan Schmaus, Alexei Bagrets, Yasmine Nahas, Toyo K. Yamada, Annika Bork, Martin Bowen, Eric Beaupaire, Ferdinand Evers, and Wulf Wulfhekel. “Giant magnetoresistance through a single molecule”. In: *Nature Nanotechnology* 6.3 (Mar. 2011), pp. 185–189. DOI: [10.1038/nnano.2011.11](https://doi.org/10.1038/nnano.2011.11). arXiv: 1102.2630 [cond-mat.mes-hall].
- [105] Stefan Lach, Anna Altenhof, Kartick Tarafder, Felix Schmitt, Md Ehesan Ali, Michael Vogel, Jens Sauther, Peter M. Oppeneer, and Christiane Ziegler. “Metal-Organic Hybrid Interface States of A Ferromagnet/Organic Semiconductor Hybrid Junction as Basis For Engineering Spin Injection in Organic Spintronics”. In: *Advanced Functional Materials* 22.5 (2012), pp. 989–997. DOI: [10.1002/adfm.201102297](https://doi.org/10.1002/adfm.201102297).
- [106] F. Djeghloul, F. Ibrahim, M. Cantoni, M. Bowen, L. Joly, S. Boukari, P. Ohresser, F. Bertran, P. Le Fèvre, P. Thakur, F. Scheurer, T. Miyamachi, R. Mattana, P. Seneor, A. Jaafar, C. Rinaldi, S. Javaid, J. Arabski, J. P. Kappler, W. Wulfhekel, N. B. Brookes, R. Bertacco, A. Taleb-Ibrahimi, M. Alouani, E. Beaupaire, and W. Weber. “Direct observation of a highly spin-polarized organic spinterface at room temperature”. In: *Scientific Reports* 3, 1272 (Feb. 2013), p. 1272. DOI: [10.1038/srep01272](https://doi.org/10.1038/srep01272). arXiv: 1209.1267 [cond-mat.mtrl-sci].
- [107] L. Schulz, L. Nuccio, M. Willis, P. Desai, P. Shakya, T. Kreouzis, V. K. Malik, C. Bernhard, F. L. Pratt, N. A. Morley, A. Suter, G. J. Nieuwenhuys, T. Prokscha, E. Morenzoni, W. P. Gillin, and A. J. Drew. “Engineering spin propagation across a hybrid organic/inorganic interface using a polar layer”. In: *Nature Materials* 10.3 (Mar. 2011), p. 252. DOI: [10.1038/nmat2962](https://doi.org/10.1038/nmat2962).

- [108] Karthik V. Raman, Alexander M. Kamerbeek, Arup Mukherjee, Nicolae Atodiresei, Tamal K. Sen, Predrag Lazić, Vasile Caciuc, Reent Michel, Dietmar Stalke, Swadhin K. Mandal, Stefan Blügel, Markus Münzenberg, and Jagadeesh S. Moodera. "Interface-engineered templates for molecular spin memory devices". In: *Nature* 493.7433 (Jan. 2013), pp. 509–513. DOI: [10.1038/nature11719](https://doi.org/10.1038/nature11719).
- [109] Kenji Yoshida, Ikutaro Hamada, Shuichi Sakata, Akinori Umeno, Masaru Tsukada, and Kazuhiko Hirakawa. "Gate-Tunable Large Negative Tunnel Magnetoresistance in Ni-C₆₀-Ni Single Molecule Transistors". In: *Nano Letters* 13.2 (2013). PMID: 23327475, pp. 481–485. DOI: [10.1021/nl303871x](https://doi.org/10.1021/nl303871x). eprint: <https://doi.org/10.1021/nl303871x>. URL: <https://doi.org/10.1021/nl303871x>.
- [110] T. L. A. Tran, P. K. J. Wong, M. P. de Jong, W. G. van der Wiel, Y. Q. Zhan, and M. Fahlman. "Hybridization-induced oscillatory magnetic polarization of C₆₀ orbitals at the C₆₀/Fe(001) interface". In: *Applied Physics Letters* 98.22, 222505 (May 2011), p. 222505. DOI: [10.1063/1.3595269](https://doi.org/10.1063/1.3595269).
- [111] K. Bairagi, A. Bellec, V. Repain, C. Chacon, Y. Girard, Y. Garreau, J. Lagoute, S. Rousset, R. Breitwieser, Yu-Cheng Hu, Yen Cheng Chao, Woei Wu Pai, D. Li, A. Smogunov, and C. Barreateau. "Tuning the Magnetic Anisotropy at a Molecule-Metal Interface". In: *Physical Review Letters* 114.24, 247203 (June 2015), p. 247203. DOI: [10.1103/PhysRevLett.114.247203](https://doi.org/10.1103/PhysRevLett.114.247203).
- [112] Oscar Ma'Mari Cespedes. "Beating the Stoner criterion using molecular interfaces". In: *Nature* 524.7563 (Aug. 2015), pp. 69–73. DOI: [10.1038/nature14621](https://doi.org/10.1038/nature14621).
- [113] W. H. Meiklejohn and C. P. Bean. "New Magnetic Anisotropy". In: *Phys. Rev.* 105 (3 Feb. 1957), pp. 904–913. DOI: [10.1103/PhysRev.105.904](https://doi.org/10.1103/PhysRev.105.904). URL: <https://link.aps.org/doi/10.1103/PhysRev.105.904>.
- [114] J Nogués and Ivan K Schuller. "Exchange bias". In: *Journal of Magnetism and Magnetic Materials* 192.2 (1999), pp. 203–232. ISSN: 0304-8853. DOI: [https://doi.org/10.1016/S0304-8853\(98\)00266-2](https://doi.org/10.1016/S0304-8853(98)00266-2). URL: <https://www.sciencedirect.com/science/article/pii/S0304885398002662>.
- [115] Masakiyo Tsunoda, Yoshihiro Tsuchiya, Takahiko Hashimoto, and Migaku Takahashi. "Magnetic anisotropy and rotational hysteresis loss in exchange coupled Ni-Fe/Mn-Ir films". In: *Journal of Applied Physics* 87.9 (2000), pp. 4375–

4388. DOI: [10.1063/1.373081](https://doi.org/10.1063/1.373081). eprint: <https://doi.org/10.1063/1.373081>. URL: <https://doi.org/10.1063/1.373081>.
- [116] B. Dieny, V. S. Speriosu, S. S. P. Parkin, B. A. Gurney, D. R. Wilhoit, and D. Mauri. “Giant magnetoresistive in soft ferromagnetic multilayers”. In: *Phys. Rev. B* 43.1 (Jan. 1991), pp. 1297–1300. DOI: [10.1103/PhysRevB.43.1297](https://doi.org/10.1103/PhysRevB.43.1297).
- [117] E. Jiménez, J. Camarero, J. Sort, J. Nogués, A. Hoffmann, F. J. Teran, P. Perna, J. M. García-Martín, B. Dieny, and R. Miranda. “Highly asymmetric magnetic behavior in exchange biased systems induced by noncollinear field cooling”. In: *Applied Physics Letters* 95.12, 122508 (Sept. 2009), p. 122508. DOI: [10.1063/1.3236768](https://doi.org/10.1063/1.3236768).
- [118] C. Leighton, M. Song, J. Nogués, M. C. Cyrille, and Ivan K. Schuller. “Using magnetoresistance to probe reversal asymmetry in exchange biased bilayers”. In: *Journal of Applied Physics* 88.1 (2000), pp. 344–347. DOI: [10.1063/1.373665](https://doi.org/10.1063/1.373665). eprint: <https://doi.org/10.1063/1.373665>. URL: <https://doi.org/10.1063/1.373665>.
- [119] S. Giri, M. Patra, and S. Majumdar. “Exchange bias effect in alloys and compounds”. In: *Journal of Physics Condensed Matter* 23.7, 073201 (Feb. 2011), p. 073201. DOI: [10.1088/0953-8984/23/7/073201](https://doi.org/10.1088/0953-8984/23/7/073201). arXiv: [1107.1978](https://arxiv.org/abs/1107.1978) [cond-mat.mtrl-sci].
- [120] Garen Avedissian. *Role of interfaces on the magnetic properties of ferromagnetic metal/organic heterostructures: Exchange bias and interlayer exchange coupling in Co/metal tetra-phenyl porphyrin*. 2020.
- [121] Miguel Kiwi. “Exchange bias theory”. In: *Journal of Magnetism and Magnetic Materials* 234.3 (2001), pp. 584–595. ISSN: 0304-8853. DOI: [https://doi.org/10.1016/S0304-8853\(01\)00421-8](https://doi.org/10.1016/S0304-8853(01)00421-8). URL: <https://www.sciencedirect.com/science/article/pii/S0304885301004218>.
- [122] J. Brede and R. Wiesendanger. “Spin-resolved characterization of single cobalt phthalocyanine molecules on a ferromagnetic support”. In: *Phys. Rev. B* 86.18, 184423 (Nov. 2012), p. 184423. DOI: [10.1103/PhysRevB.86.184423](https://doi.org/10.1103/PhysRevB.86.184423).

- [123] Manuel Gruber, Fatima Ibrahim, Samy Boukari, and Martin Bowen. “Exchange bias and room-temperature magnetic order in molecular layers”. In: *Nature Materials* 14.10 (Oct. 2015), pp. 981–984. DOI: [10.1038/nmat4361](https://doi.org/10.1038/nmat4361).
- [124] Samy and Boukari. “Disentangling Magnetic Hardening and Molecular Spin Chain Contributions to Exchange Bias in Ferromagnet/Molecule Bilayers”. In: *Nano Letters* 18.8 (Aug. 2018), pp. 4659–4663. DOI: [10.1021/acs.nanolett.8b00570](https://doi.org/10.1021/acs.nanolett.8b00570). arXiv: [1712.07450](https://arxiv.org/abs/1712.07450) [[cond-mat.mtrl-sci](https://arxiv.org/abs/1712.07450)].
- [125] Junhyeon Jo, Jinho Byun, Inseon Oh, Jungmin Park, Mi-Jin Jin, Byoung-Chul Min, Jaekwang Lee, and Jung-Woo Yoo. “Molecular Tunability of Magnetic Exchange Bias and Asymmetrical Magnetotransport in Metalloporphyrin/Co Hybrid Bilayers”. In: *ACS Nano* 13.1 (2019), pp. 894–903. DOI: [10.1021/acsnano.8b08689](https://doi.org/10.1021/acsnano.8b08689). eprint: <https://doi.org/10.1021/acsnano.8b08689>. URL: <https://doi.org/10.1021/acsnano.8b08689>.
- [126] Junhyeon Jo, Jinho Byun, Jaebyeong Lee, Daeseong Choe, Inseon Oh, Jungmin Park, Mi-Jin Jin, Jaekwang Lee, and Jung-Woo Yoo. “Emergence of Multispininterface and Antiferromagnetic Molecular Exchange Bias via Molecular Stacking on a Ferromagnetic Film”. In: *Advanced Functional Materials* 30.11 (2020), p. 1908499. DOI: <https://doi.org/10.1002/adfm.201908499>. eprint: <https://onlinelibrary.wiley.com/doi/pdf/10.1002/adfm.201908499>. URL: <https://onlinelibrary.wiley.com/doi/abs/10.1002/adfm.201908499>.
- [127] Quentin Arnoux, Camille Blouzon, Dongzhe Li, Yannick J. Dappe, Alexander Smogunov, Pierre Bonville, Ludovic Torteck, and Jean-Baptiste Moussy. “Controlling the magnetic exchange coupling in hybrid heterojunctions via spacer layers of π -conjugated molecules”. In: *Phys. Rev. B* 99.14, 144405 (Apr. 2019), p. 144405. DOI: [10.1103/PhysRevB.99.144405](https://doi.org/10.1103/PhysRevB.99.144405).
- [128] Victoria E. Campbell, Monica Tonelli, Irene Cimatti, Jean-Baptiste Moussy, Ludovic Torteck, Yannick J. Dappe, Eric Rivière, Régis Guillot, Marie-Anne Delprat, Philippe Saintavit, and Talal Mallah. “Engineering the magnetic

- coupling and anisotropy at the molecule-magnetic surface interface in molecular spintronic devices". In: *Nature Communications* 7, 13646 (Dec. 2016), p. 13646. DOI: [10.1038/ncomms13646](https://doi.org/10.1038/ncomms13646).
- [129] T. E. Humphrey and H. Linke. "Quantum, cyclic, and particle-exchange heat engines". In: *Physica E Low-Dimensional Systems and Nanostructures* 29.1 (Oct. 2005), pp. 390–398. DOI: [10.1016/j.physe.2005.05.038](https://doi.org/10.1016/j.physe.2005.05.038). arXiv: [cond-mat/0407508](https://arxiv.org/abs/cond-mat/0407508) [[cond-mat](https://arxiv.org/abs/cond-mat).[stat-mech](https://arxiv.org/abs/stat-mech)].
- [130] Thomas Johann Seebeck. *Magnetische Polarisation der Metalle und Erze durch Temperatur-Differenz*. 1895, pp. 265–373. ISBN: 978-0-85709-588-6. eprint: [urn:oclc:record:1049682994](https://nbn-resolving.org/urn:oclc:record:1049682994).
- [131] K. Uchida, S. Takahashi, K. Harii, J. Ieda, W. Koshibae, K. Ando, S. Maekawa, and E. Saitoh. "Observation of the spin Seebeck effect". In: *Nature* 455.7214 (Oct. 2008), pp. 778–781. DOI: [10.1038/nature07321](https://doi.org/10.1038/nature07321).
- [132] John C. Slonczewski. "Initiation of spin-transfer torque by thermal transport from magnons". In: *Phys. Rev. B* 82 (5 Aug. 2010), p. 054403. DOI: [10.1103/PhysRevB.82.054403](https://doi.org/10.1103/PhysRevB.82.054403). URL: <https://link.aps.org/doi/10.1103/PhysRevB.82.054403>.
- [133] A.R. Mackintosh and L. Sill. "The thermoelectric power in chromium and vanadium". In: *Journal of Physics and Chemistry of Solids* 24.4 (1963), pp. 501–506. ISSN: 0022-3697. DOI: [https://doi.org/10.1016/0022-3697\(63\)90145-8](https://doi.org/10.1016/0022-3697(63)90145-8). URL: <https://www.sciencedirect.com/science/article/pii/0022369763901458>.
- [134] Jannis Maiwald and Philipp Gegenwart. "Interplay of 4f and 3d moments in EuFe₂As₂ iron pnictides". In: *physica status solidi (b)* 254.1 (2017), p. 1600150. DOI: <https://doi.org/10.1002/pssb.201600150>. eprint: <https://onlinelibrary.wiley.com/doi/pdf/10.1002/pssb.201600150>. URL: <https://onlinelibrary.wiley.com/doi/abs/10.1002/pssb.201600150>.
- [135] Giuliano Benenti, Giulio Casati, Keiji Saito, and Robert S. Whitney. "Fundamental aspects of steady-state conversion of heat to work at the nanoscale". In: *Physics Reports* 694 (2017). Fundamental aspects of steady-state conversion of heat to work at the nanoscale, pp. 1–124. ISSN: 0370-1573. DOI: <https://doi.org/10.1016/j.physrep.2017.05.001>.

- [//doi.org/10.1016/j.physrep.2017.05.008](https://doi.org/10.1016/j.physrep.2017.05.008). URL: <https://www.sciencedirect.com/science/article/pii/S0370157317301540>.
- [136] H. E. D. Scovil and E. O. Schulz-DuBois. “Three-Level Masers as Heat Engines”. In: *Phys. Rev. Lett.* 2 (6 Mar. 1959), pp. 262–263. DOI: [10.1103/PhysRevLett.2.262](https://doi.org/10.1103/PhysRevLett.2.262). URL: <https://link.aps.org/doi/10.1103/PhysRevLett.2.262>.
- [137] J. E. Geusic, E. O. Schulz-Dubios, and H. E. Scovil. “Quantum Equivalent of the Carnot Cycle”. In: *Physical Review* 156.2 (Apr. 1967), pp. 343–351. DOI: [10.1103/PhysRev.156.343](https://doi.org/10.1103/PhysRev.156.343).
- [138] Giovanni Barontini and Mauro Paternostro. “Ultra-cold single-atom quantum heat engines”. In: *New Journal of Physics* 21.6, 063019 (June 2019), p. 063019. DOI: [10.1088/1367-2630/ab2684](https://doi.org/10.1088/1367-2630/ab2684). arXiv: [1812.10929](https://arxiv.org/abs/1812.10929) [quant-ph].
- [139] Ting Zhang, Wei-Tao Liu, Ping-Xing Chen, and Cheng-Zu Li. “Four-level entangled quantum heat engines”. In: *Phys. Rev. A* 75.6, 062102 (June 2007), p. 062102. DOI: [10.1103/PhysRevA.75.062102](https://doi.org/10.1103/PhysRevA.75.062102).
- [140] Holger Thierschmann, Rafael Sánchez, Björn Sothmann, Fabian Arnold, Christian Heyn, Wolfgang Hansen, Hartmut Buhmann, and Laurens W. Molenkamp. “Three-terminal energy harvester with coupled quantum dots”. In: *Nature Nanotechnology* 10.10 (Oct. 2015), pp. 854–858. DOI: [10.1038/nnano.2015.176](https://doi.org/10.1038/nnano.2015.176). arXiv: [1603.08570](https://arxiv.org/abs/1603.08570) [cond-mat.mes-hall].
- [141] Y. S. Liu, X. F. Yang, X. K. Hong, M. S. Si, F. Chi, and Y. Guo. “A high-efficiency double quantum dot heat engine”. In: *Applied Physics Letters* 103.9, 093901 (Aug. 2013), p. 093901. DOI: [10.1063/1.4819852](https://doi.org/10.1063/1.4819852).
- [142] Bitan De and Bhaskaran Muralidharan. “Thermoelectric study of dissipative quantum-dot heat engines”. In: *Phys. Rev. B* 94.16, 165416 (Oct. 2016), p. 165416. DOI: [10.1103/PhysRevB.94.165416](https://doi.org/10.1103/PhysRevB.94.165416). arXiv: [1605.09195](https://arxiv.org/abs/1605.09195) [cond-mat.mes-hall].
- [143] Rafael Sánchez and Markus Büttiker. “Optimal energy quanta to current conversion”. In: *Phys. Rev. B* 83.8, 085428 (Feb. 2011), p. 085428. DOI: [10.1103/PhysRevB.83.085428](https://doi.org/10.1103/PhysRevB.83.085428). arXiv: [1008.3528](https://arxiv.org/abs/1008.3528) [cond-mat.mes-hall].

- [144] Martin Josefsson, Artis Svilans, Adam M. Burke, Eric A. Hoffmann, Sofia Fahlvik, Claes Thelander, Martin Leijnse, and Heiner Linke. “A quantum-dot heat engine operating close to the thermodynamic efficiency limits”. In: *Nature Nanotechnology* 13.10 (July 2018), pp. 920–924. DOI: [10.1038/s41565-018-0200-5](https://doi.org/10.1038/s41565-018-0200-5). arXiv: [1710.00742](https://arxiv.org/abs/1710.00742) [cond-mat.mes-hall].
- [145] Marlan O. Scully, M. Suhail Zubairy, Girish S. Agarwal, and Herbert Walther. “Extracting Work from a Single Heat Bath via Vanishing Quantum Coherence”. In: *Science* 299.5608 (2003), pp. 862–864. ISSN: 0036-8075. DOI: [10.1126/science.1078955](https://doi.org/10.1126/science.1078955). eprint: <https://science.sciencemag.org/content/299/5608/862.full.pdf>. URL: <https://science.sciencemag.org/content/299/5608/862>.
- [146] Tova Feldmann and Ronnie Kosloff. “Performance of discrete heat engines and heat pumps in finite time”. In: *Phys. Rev. E* 61 (5 May 2000), pp. 4774–4790. DOI: [10.1103/PhysRevE.61.4774](https://doi.org/10.1103/PhysRevE.61.4774). URL: <https://link.aps.org/doi/10.1103/PhysRevE.61.4774>.
- [147] T. E. Humphrey, R. Newbury, R. P. Taylor, and H. Linke. “Reversible Quantum Brownian Heat Engines for Electrons”. In: *Phys. Rev. Lett.* 89 (11 Aug. 2002), p. 116801. DOI: [10.1103/PhysRevLett.89.116801](https://doi.org/10.1103/PhysRevLett.89.116801). URL: <https://link.aps.org/doi/10.1103/PhysRevLett.89.116801>.
- [148] Seth Lloyd. “Quantum-mechanical Maxwell’s demon”. In: *Phys. Rev. A* 56 (5 Nov. 1997), pp. 3374–3382. DOI: [10.1103/PhysRevA.56.3374](https://doi.org/10.1103/PhysRevA.56.3374). URL: <https://link.aps.org/doi/10.1103/PhysRevA.56.3374>.
- [149] J. E. Geusic, E. O. Schulz-Du Bois, R. W. De Grasse, and H. E. D. Scovil. “Three Level Spin Refrigeration and Maser Action at 1500 mc/sec”. In: *Journal of Applied Physics* 30.7 (July 1959), pp. 1113–1114. DOI: [10.1063/1.1776991](https://doi.org/10.1063/1.1776991).
- [150] John P. S. Peterson, Tiago B. Batalhão, Marcela Herrera, Alexandre M. Souza, Roberto S. Sarthour, Ivan S. Oliveira, and Roberto M. Serra. “Experimental Characterization of a Spin Quantum Heat Engine”. In: *Physical Review Letters* 123.24, 240601 (Dec. 2019), p. 240601. DOI: [10.1103/PhysRevLett.123.240601](https://doi.org/10.1103/PhysRevLett.123.240601). arXiv: [1803.06021](https://arxiv.org/abs/1803.06021) [quant-ph].

- [151] W. B. Wang, X. Y. Chang, F. Wang, P. Y. Hou, Y. Y. Huang, W. G. Zhang, X. L. Ouyang, X. Z. Huang, Z. Y. Zhang, H. Y. Wang, L. He, and L. M. Duan. “Realization of Quantum Maxwell’s Demon with Solid-State Spins*”. In: *Chinese Physics Letters* 35.4, 040301 (Apr. 2018), p. 040301. DOI: [10.1088/0256-307X/35/4/040301](https://doi.org/10.1088/0256-307X/35/4/040301). arXiv: [1711.10101](https://arxiv.org/abs/1711.10101) [quant-ph].
- [152] James Klatzow, Jonas N. Becker, Patrick M. Ledingham, Christian Weinzetl, Krzysztof T. Kaczmarek, Dylan J. Saunders, Joshua Nunn, Ian A. Walmsley, Raam Uzdin, and Eilon Poem. “Experimental Demonstration of Quantum Effects in the Operation of Microscopic Heat Engines”. In: *Physical Review Letters* 122.11, 110601 (Mar. 2019), p. 110601. DOI: [10.1103/PhysRevLett.122.110601](https://doi.org/10.1103/PhysRevLett.122.110601).
- [153] Arjun Mani, Subhajit Pal, and Colin Benjamin. “Designing a highly efficient graphene quantum spin heat engine”. In: *Scientific Reports* 9, 6018 (Apr. 2019), p. 6018. DOI: [10.1038/s41598-019-42279-7](https://doi.org/10.1038/s41598-019-42279-7).
- [154] D. von Lindenfels, O. Gräß, C. T. Schmiegelow, V. Kaushal, J. Schulz, Mark T. Mitchison, John Goold, F. Schmidt-Kaler, and U. G. Poschinger. “Spin Heat Engine Coupled to a Harmonic-Oscillator Flywheel”. In: *Physical Review Letters* 123.8, 080602 (Aug. 2019), p. 080602. DOI: [10.1103/PhysRevLett.123.080602](https://doi.org/10.1103/PhysRevLett.123.080602). arXiv: [1808.02390](https://arxiv.org/abs/1808.02390) [quant-ph].
- [155] Jizhou He, Jincan Chen, and Ben Hua. “Quantum refrigeration cycles using spin-1/2 systems as the working substance”. In: *Physical Review E* 65.3, 036145 (Mar. 2002), p. 036145. DOI: [10.1103/PhysRevE.65.036145](https://doi.org/10.1103/PhysRevE.65.036145).
- [156] Jincan Chen, Bihong Lin, and Ben Hua. “The performance of a quantum heat engine working with spin systems”. In: *Journal of Physics D Applied Physics* 35.16 (Aug. 2002), pp. 2051–2057. DOI: [10.1088/0022-3727/35/16/322](https://doi.org/10.1088/0022-3727/35/16/322).
- [157] Feng Wu, Lingen Chen, Shuang Wu, Fengrui Sun, and Chih Wu. “Performance of an irreversible quantum Carnot engine with spin 1/2”. In: *The Journal of Chemical Physics* 124.21 (June 2006), pp. 214702–214702. DOI: [10.1063/1.2200693](https://doi.org/10.1063/1.2200693).

- [158] G. F. Zhang. “Entangled quantum heat engines based on two two-spin systems with Dzyaloshinski-Moriya anisotropic antisymmetric interaction”. In: *European Physical Journal D* 49.1 (Aug. 2008), pp. 123–128. DOI: [10.1140/epjd/e2008-00133-0](https://doi.org/10.1140/epjd/e2008-00133-0). arXiv: [0808.2409](https://arxiv.org/abs/0808.2409) [quant-ph].
- [159] S. E. Barnes. “Spin motive forces, “measurements”, and spin-valves”. In: *Journal of Magnetism and Magnetic Materials* 310.2 (Mar. 2007), pp. 2035–2037. DOI: [10.1016/j.jmmm.2006.10.944](https://doi.org/10.1016/j.jmmm.2006.10.944).
- [160] Jagadeesh S Moodera, Tiffany S Santos, and Taro Nagahama. “The phenomena of spin-filter tunnelling”. In: *Journal of Physics: Condensed Matter* 19.16 (Apr. 2007), p. 165202. DOI: [10.1088/0953-8984/19/16/165202](https://doi.org/10.1088/0953-8984/19/16/165202). URL: <https://doi.org/10.1088/0953-8984/19/16/165202>.
- [161] B. Verlhac, N. Bachellier, L. Garnier, M. Ormaza, P. Abufager, R. Robles, M. L. Bocquet, M. Ternes, N. Lorente, and L. Limot. “Atomic-scale spin sensing with a single molecule at the apex of a scanning tunneling microscope”. In: *Science* 366.6465 (Nov. 2019), pp. 623–627. DOI: [10.1126/science.aax8222](https://doi.org/10.1126/science.aax8222). arXiv: [1901.04862](https://arxiv.org/abs/1901.04862) [cond-mat.mes-hall].
- [162] Fabian D. Natterer, Kai Yang, William Paul, Philip Willke, Taeyoung Choi, Thomas Greber, Andreas J. Heinrich, and Christopher P. Lutz. “Reading and writing single-atom magnets”. In: *Nature* 543.7644 (Mar. 2017), pp. 226–228. DOI: [10.1038/nature21371](https://doi.org/10.1038/nature21371). arXiv: [1607.03977](https://arxiv.org/abs/1607.03977) [cond-mat.mes-hall].
- [163] JOEL S. MILLER, ARTHUR J. EPSTEIN, and WILLIAM M. REIFF. “Molecular/Organic Ferromagnets”. In: *Science* 240.4848 (1988), pp. 40–47. ISSN: 0036-8075. DOI: [10.1126/science.240.4848.40](https://doi.org/10.1126/science.240.4848.40). eprint: <https://science.sciencemag.org/content/240/4848/40.full.pdf>. URL: <https://science.sciencemag.org/content/240/4848/40>.
- [164] J. V. Koski, A. Kutvonen, I. M. Khaymovich, T. Ala-Nissila, and J. P. Pekola. “On-Chip Maxwell’s Demon as an Information-Powered Refrigerator”. In: *Physical Review Letters* 115.26, 260602 (Dec. 2015), p. 260602. DOI: [10.1103/PhysRevLett.115.260602](https://doi.org/10.1103/PhysRevLett.115.260602). arXiv: [1507.00530](https://arxiv.org/abs/1507.00530) [cond-mat.mes-hall].

- [165] Alvaro Núñez and Rembert Duine. “Effective temperature and Gilbert damping of a current-driven localized spin”. In: *Physical Review B* 77 (June 2007). DOI: [10.1103/PhysRevB.77.054401](https://doi.org/10.1103/PhysRevB.77.054401).
- [166] Jonas Fransson, Jie Ren, and Jian-Xin Zhu. “Electrical and Thermal Control of Magnetic Exchange Interactions”. In: *Physical Review Letters* 113.25, 257201 (Dec. 2014), p. 257201. DOI: [10.1103/PhysRevLett.113.257201](https://doi.org/10.1103/PhysRevLett.113.257201). arXiv: [1401.5592](https://arxiv.org/abs/1401.5592) [[cond-mat.mes-hall](https://arxiv.org/abs/1401.5592)].
- [167] Turab Saygun, Johan Bylin, Henning Hammar, and Jonas Fransson. “Voltage-Induced Switching Dynamics of a Coupled Spin Pair in a Molecular Junction”. In: *Nano letters* 16 (Mar. 2016). DOI: [10.1021/acs.nanolett.6b00628](https://doi.org/10.1021/acs.nanolett.6b00628).
- [168] Juan Vasquez Jaramillo and Jonas Fransson. “Charge Transport and Entropy Production Rate in Magnetically Active Molecular Dimer”. In: *The Journal of Physical Chemistry C* 121 (Nov. 2017). DOI: [10.1021/acs.jpcc.7b10350](https://doi.org/10.1021/acs.jpcc.7b10350).
- [169] Andrei Zholud, Ryan Freeman, R. Cao, Ajit Srivastava, and Sergei Urazhdin. “Spin transfer due to quantum fluctuations of magnetization”. In: *Physical Review Letters* 119 (Mar. 2017). DOI: [10.1103/PhysRevLett.119.257201](https://doi.org/10.1103/PhysRevLett.119.257201).
- [170] Alireza Qaiumzadeh and Arne Brataas. “Quantum magnetization fluctuations via spin shot noise”. In: *Physical Review B* 98 (Dec. 2018). DOI: [10.1103/PhysRevB.98.220408](https://doi.org/10.1103/PhysRevB.98.220408).
- [171] J.-E Wegrowe, Mihaela-Cristina Ciornei, and H-J Drouhin. “Spin transfer in an open ferromagnetic layer: From negative damping to effective temperature”. In: *Journal of Physics Condensed Matter* 19 (Nov. 2006). DOI: [10.1088/0953-8984/19/16/165213](https://doi.org/10.1088/0953-8984/19/16/165213).
- [172] S. Patitsas. “Thermodynamic Induction Effects Exhibited in Nonequilibrium Systems with Variable Kinetic Coefficients”. In: *Physical review. E, Statistical, nonlinear, and soft matter physics* 89 (Jan. 2014), p. 012108. DOI: [10.1103/PhysRevE.89.012108](https://doi.org/10.1103/PhysRevE.89.012108).
- [173] S. Patitsas. “Cooling by Thermodynamic Induction”. In: *Journal of Low Temperature Physics* 186 (Mar. 2017). DOI: [10.1007/s10909-016-1711-9](https://doi.org/10.1007/s10909-016-1711-9).

- [174] J. Grollier, D. Querlioz, and M. D. Stiles. “Spintronic Nanodevices for Bioinspired Computing”. In: *Proceedings of the IEEE* 104.10 (2016), pp. 2024–2039.
- [175] Ilaria Bergenti, Alberto Riminucci, E. Arisi, Mauro Murgia, Massimiliano Cavallini, Massimo Solzi, Francesca Casoli, and Alek Dediu. “Magnetic properties of Cobalt thin films deposited on soft organic layers”. In: *J. Magn. Magn. Mater.* 316 (Sept. 2007), E987–E989. DOI: [10.1016/j.jmmm.2007.03.165](https://doi.org/10.1016/j.jmmm.2007.03.165).
- [176] Weihao Xu, Jonathan Brauer, Greg Szulczewski, M. Driver, and A. Caruso. “Electronic, magnetic, and physical structure of cobalt deposited on aluminum tris(8-hydroxy quinoline)”. In: *Applied Physics Letters* 94 (Dec. 2008), p. 233302. DOI: [10.1063/1.3148665](https://doi.org/10.1063/1.3148665).
- [177] Krzysztof Ptaszyński. “Autonomous quantum Maxwell’s demon based on two exchange-coupled quantum dots”. In: *Phys. Rev. E* 97 (1 Jan. 2018), p. 012116. DOI: [10.1103/PhysRevE.97.012116](https://doi.org/10.1103/PhysRevE.97.012116). URL: <https://link.aps.org/doi/10.1103/PhysRevE.97.012116>.
- [178] Gaomin Tang, Juzar Thingna, and Jian Wang. “Thermodynamics of energy, charge, and spin currents in a thermoelectric quantum-dot spin valve”. In: *Phys. Rev. B* 97.15, 155430 (Apr. 2018), p. 155430. DOI: [10.1103/PhysRevB.97.155430](https://doi.org/10.1103/PhysRevB.97.155430). arXiv: [1802.06549](https://arxiv.org/abs/1802.06549) [cond-mat.mes-hall].
- [179] Krzysztof Ptaszyński and Massimiliano Esposito. “Thermodynamics of Quantum Information Flows”. In: *Physical Review Letters* 122.15 (Apr. 2019), p. 150603. DOI: [10.1103/PhysRevLett.122.150603](https://doi.org/10.1103/PhysRevLett.122.150603).
- [180] J A Venables, G D T Spiller, and M Hanbucken. “Nucleation and growth of thin films”. In: *Reports on Progress in Physics* 47.4 (Apr. 1984), pp. 399–459. DOI: [10.1088/0034-4885/47/4/002](https://doi.org/10.1088/0034-4885/47/4/002). URL: <https://doi.org/10.1088/0034-4885/47/4/002>.
- [181] I. N. Stranski and L. Krastanow. In: *Sitzungsber. Wien. Akad. Wiss Math.-Nat. Kl* 2B.146 (1938).
- [182] J.E. Greene. “Thin Film Nucleation, Growth, and Microstructural Evolution: An Atomic Scale View”. In: Dec. 2010, pp. 554–620. ISBN: 9780815520313. DOI: [10.1016/B978-0-8155-2031-3.00012-0](https://doi.org/10.1016/B978-0-8155-2031-3.00012-0).

- [183] Milan Králik. "Adsorption, chemisorption, and catalysis". In: *Chemical Papers* 68 (Sept. 2014). DOI: [10.2478/s11696-014-0624-9](https://doi.org/10.2478/s11696-014-0624-9).
- [184] Arthur W. Adamson and Alice P. Gast. *Physical Chemistry of Surfaces*. 6th ed. 1997. ISBN: 9780471148739.
- [185] S Swann. "Magnetron sputtering". In: *Physics in Technology* 19.2 (Mar. 1988), pp. 67–75. DOI: [10.1088/0305-4624/19/2/304](https://doi.org/10.1088/0305-4624/19/2/304). URL: <https://doi.org/10.1088/0305-4624/19/2/304>.
- [186] J. E. Greene. "Review Article: Tracing the recorded history of thin-film sputter deposition: From the 1800s to 2017". In: *Journal of Vacuum Science & Technology A* 35.5 (2017), p. 05C204. DOI: [10.1116/1.4998940](https://doi.org/10.1116/1.4998940). eprint: <https://doi.org/10.1116/1.4998940>. URL: <https://doi.org/10.1116/1.4998940>.
- [187] adnano tek. *UHV Magnetron Sputtering Deposition (SPUTTER-16)*. URL: http://www.adnano-tek.com/uploads/1/6/5/3/16533032/msd-x_orig.jpg.
- [188] Masahiko Hara, Hiroyuki Sasabe, Akira Yamada, and Anthony F. Garito. "Epitaxial Growth of Organic Thin Films by Organic Molecular Beam Epitaxy". In: *Japanese Journal of Applied Physics* 28.Part 2, No. 2 (Feb. 1989), pp. L306–L308. DOI: [10.1143/jjap.28.1306](https://doi.org/10.1143/jjap.28.1306). URL: <https://doi.org/10.1143/jjap.28.1306>.
- [189] S. FORREST. "ChemInform Abstract: Ultrathin Organic Films Grown by Organic Molecular Beam Deposition and Related Techniques". In: *Cheminform* 28 (Dec. 2010). DOI: [10.1002/chin.199752310](https://doi.org/10.1002/chin.199752310).
- [190] Marian A. Herman and Helmut Sitter. *Molecular beam epitaxy : Fundamentals and current status*. 2nd ed. 1996, pp. 33–36. ISBN: 978-3-642-80062-7.
- [191] MBE KOMPONENTEN, Dr. EBERL, *Applied EPI, St. Paul, MN (USA)*. URL: https://www.mbe-komponenten.de/glossary/hotlip-filament-hl__110.php.
- [192] J. Bernos, M. Hehn, F. Montaigne, C. Tiusan, D. Lacour, M. Alnot, B. Negulescu, G. Lengaigne, E. Snoeck, and F. G. Aliev. "Impact of electron-electron interactions induced by disorder at interfaces on spin-dependent tunneling

- in Co-Fe-B/MgO/Co-Fe-B magnetic tunnel junctions". In: *Phys. Rev. B* 82.6, 060405 (Aug. 2010), p. 060405. DOI: [10.1103/PhysRevB.82.060405](https://doi.org/10.1103/PhysRevB.82.060405).
- [193] Shinji Yuasa, Yoshishige Suzuki, Toshikazu Katayama, and Koji Ando. "Characterization of growth and crystallization processes in CoFeB /MgO/CoFeB magnetic tunnel junction structure by reflective high-energy electron diffraction". In: *Applied Physics Letters* 87.24, 242503 (Dec. 2005), p. 242503. DOI: [10.1063/1.2140612](https://doi.org/10.1063/1.2140612).
- [194] Y. S. Choi, K. Tsunekawa, Y. Nagamine, and D. Djayaprawira. "Transmission electron microscopy study on the polycrystalline CoFeB /MgO/CoFeB based magnetic tunnel junction showing a high tunneling magnetoresistance, predicted in single crystal magnetic tunnel junction". In: *Journal of Applied Physics* 101.1, 013907-013907-4 (Jan. 2007), pp. 013907–013907–4. DOI: [10.1063/1.2407270](https://doi.org/10.1063/1.2407270).
- [195] M. Mizuguchi, Y. Suzuki, T. Nagahama, and S. Yuasa. "In situ scanning tunneling microscopy observations of polycrystalline MgO(001) tunneling barriers grown on amorphous CoFeB electrode". In: *Applied Physics Letters* 91.1, 012507 (July 2007), p. 012507. DOI: [10.1063/1.2754372](https://doi.org/10.1063/1.2754372).
- [196] W. G. Wang, C. Ni, G. X. Miao, C. Weiland, L. R. Shah, X. Fan, P. Parson, J. Jordan-Sweet, X. M. Kou, Y. P. Zhang, R. Stearrett, E. R. Nowak, R. Opila, J. S. Moodera, and J. Q. Xiao. "Understanding tunneling magnetoresistance during thermal annealing in MgO-based junctions with CoFeB electrodes". In: *Phys. Rev. B* 81.14, 144406 (Apr. 2010), p. 144406. DOI: [10.1103/PhysRevB.81.144406](https://doi.org/10.1103/PhysRevB.81.144406).
- [197] Joachim Mayer, Lucille Giannuzzi, Takeo Kamino, and Joseph Michael. "TEM sample preparation and FIB-induced damage". In: *MRS Bulletin* 32 (May 2007). DOI: [10.1557/mrs2007.63](https://doi.org/10.1557/mrs2007.63).
- [198] Goldstein J. *Scanning Electron Microscopy and X-Ray Microanalysis*. 2003. ISBN: 978-0-306-47292-3.
- [199] Valparaiso University. *X-ray Reflectivity*. URL: <http://physics.valpo.edu/staff/arichter/XRR.htm>.

- [200] W. E. Gifford and H. O. McMahon. "The Gifford-McMahon Cycle". In: *Advances in Cryogenic Engineering* 11 (Aug. 1966), pp. 152–159. DOI: [10.1007/978-1-4757-0522-5_16](https://doi.org/10.1007/978-1-4757-0522-5_16).
- [201] Ufuk Halisdemir. *Probing the impact of structural defects on spin dependent tunneling using photons*. 2016. URL: <http://www.theses.fr/2016STRAE018>.
- [202] Vincent Davesne. *Organic spintronics : an investigation on spin-crossover complexes from isolated molecules to the device*. 2013. URL: <http://www.theses.fr/2013STRAE005>.
- [203] M. O. Oliphant. *The acceleration of particles to very high energies*. 1943.
- [204] V. I. Veksler. "A new method of acceleration of relativistic particles". In: *J. Phys.* 9 (1945), pp. 153–158. URL: <https://cds.cern.ch/record/109364>.
- [205] Edwin M. McMillan. "The Synchrotron—A Proposed High Energy Particle Accelerator". In: *Phys. Rev.* 68 (5-6 Sept. 1945), pp. 143–144. DOI: [10.1103/PhysRev.68.143](https://doi.org/10.1103/PhysRev.68.143). URL: <https://link.aps.org/doi/10.1103/PhysRev.68.143>.
- [206] J. StohrHans and C. Siegmann. *Magnetism*. Vol. 52. 2006. ISBN: 978-3-540-30282-7.
- [207] *Synchrotron SOLEIL*. URL: <https://www.synchrotron-soleil.fr/en>.
- [208] Grant Henderson, Frank De Groot, and Benjamin Moulton. "X-ray Absorption Near-Edge Structure (XANES) Spectroscopy". In: *Reviews in Mineralogy and Geochemistry* 78 (Feb. 2014), pp. 75–138. DOI: [10.2138/rmg.2014.78.3](https://doi.org/10.2138/rmg.2014.78.3).
- [209] James Seibert and John Boone. "X-Ray Imaging Physics for Nuclear Medicine Technologists. Part 2: X-Ray Interactions and Image Formation". In: *Journal of nuclear medicine technology* 33 (Apr. 2005), pp. 3–18.
- [210] Giorgio Margaritondo. *Introduction to synchrotron radiation / Giorgio Margaritondo*. English. Oxford University Press New York, 1988, xi, 280 p. : ISBN: 0195045246. URL: <http://www.loc.gov/catdir/enhancements/fy0639/87022028-t.html>.

- [211] “Photoelectric absorption”. In: *Elements of Modern X-ray Physics*. John Wiley & Sons, Ltd, 2011. Chap. 7, pp. 239–273. ISBN: 9781119998365. DOI: <https://doi.org/10.1002/9781119998365.ch7>. eprint: <https://onlinelibrary.wiley.com/doi/pdf/10.1002/9781119998365.ch7>. URL: <https://onlinelibrary.wiley.com/doi/abs/10.1002/9781119998365.ch7>.
- [212] H.G.J. Moseley M.A. “XCIII. The high-frequency spectra of the elements”. In: *The London, Edinburgh, and Dublin Philosophical Magazine and Journal of Science* 26.156 (1913), pp. 1024–1034. DOI: [10.1080/14786441308635052](https://doi.org/10.1080/14786441308635052). eprint: <https://doi.org/10.1080/14786441308635052>. URL: <https://doi.org/10.1080/14786441308635052>.
- [213] H.G.J. Moseley M.A. “LXXX. The high-frequency spectra of the elements. Part II”. In: *The London, Edinburgh, and Dublin Philosophical Magazine and Journal of Science* 27.160 (1914), pp. 703–713. DOI: [10.1080/14786440408635141](https://doi.org/10.1080/14786440408635141). eprint: <https://doi.org/10.1080/14786440408635141>. URL: <https://doi.org/10.1080/14786440408635141>.
- [214] Carpenter. *XAS measurement near Fe K edge illustrating the three regions of a typical X-ray Absorption Fine Structure (XAFS) spectrum*. URL: <https://www.cei.washington.edu/education/science-of-solar/xray-absorption-near-edge-spectroscopy-xanes/>.
- [215] Grant Bunker. “Theory”. In: *Introduction to XAFS: A Practical Guide to X-ray Absorption Fine Structure Spectroscopy*. Cambridge University Press, 2010, 106–133. DOI: [10.1017/CB09780511809194.005](https://doi.org/10.1017/CB09780511809194.005).
- [216] D. C. Koningsberger and Roelof Prins. *X-Ray Absorption : Principles, Applications, Techniques of EXAFS, SEXAFS, and XANES*. Vol. 92. New York - Wiley, 1998. DOI: [10.1002/bbpc.19890930232](https://doi.org/10.1002/bbpc.19890930232).
- [217] A. Krol, C. S. Lin, Z. H. Ming, C. J. Sher, Y. H. Kao, C. T. Chen, F. Sette, Y. Ma, G. C. Smith, Y. Z. Zhu, and D. T. Shaw. “X-ray-absorption studies of Y-Ba-Cu-O and Bi-Sr-Ca-Cu-O films at oxygen K edge by means of fluorescence and total electron yield: A comparison of two techniques”. In: *Phys. Rev. B* 42.4 (Aug. 1990), pp. 2635–2638. DOI: [10.1103/PhysRevB.42.2635](https://doi.org/10.1103/PhysRevB.42.2635).

- [218] Frank De Groot. "Core level spectroscopy of solids. CRC Press, Boca Raton". In: (Mar. 2008). DOI: [10.1201/9781420008425](https://doi.org/10.1201/9781420008425).
- [219] R. W. FINK, R. C. JOPSON, HANS MARK, and C. D. SWIFT. "Atomic Fluorescence Yields". In: *Rev. Mod. Phys.* 38 (3 July 1966), pp. 513–540. DOI: [10.1103/RevModPhys.38.513](https://doi.org/10.1103/RevModPhys.38.513). URL: <https://link.aps.org/doi/10.1103/RevModPhys.38.513>.
- [220] WALTER BAMBYNEK, BERND CRASEMANN, R. W. FINK, H. U. FREUND, HANS MARK, C. D. SWIFT, R. E. PRICE, and P. VENUGOPALA RAO. "X-Ray Fluorescence Yields, Auger, and Coster-Kronig Transition Probabilities". In: *Rev. Mod. Phys.* 44 (4 Oct. 1972), pp. 716–813. DOI: [10.1103/RevModPhys.44.716](https://doi.org/10.1103/RevModPhys.44.716). URL: <https://link.aps.org/doi/10.1103/RevModPhys.44.716>.
- [221] J. H. Hubbell, P. N. Trehan, Nirmal Singh, B. Chand, D. Mehta, M. L. Garg, R. R. Garg, Surinder Singh, and S. Puri. "A Review, Bibliography, and Tabulation of K, L, and Higher Atomic Shell X-Ray Fluorescence Yields". In: *Journal of Physical and Chemical Reference Data* 23.2 (1994), pp. 339–364. DOI: [10.1063/1.555955](https://doi.org/10.1063/1.555955). eprint: <https://doi.org/10.1063/1.555955>. URL: <https://doi.org/10.1063/1.555955>.
- [222] M. Abbate, J. B. Goedkoop, F. M. F. de Groot, M. Grioni, J. C. Fuggle, S. Hofmann, H. Petersen, and M. Sacchi. "Probing depth of soft x-ray absorption spectroscopy measured in total-electron-yield mode". In: *Surface and Interface Analysis* 18.1 (1992), pp. 65–69. DOI: <https://doi.org/10.1002/sia.740180111>. eprint: <https://onlinelibrary.wiley.com/doi/pdf/10.1002/sia.740180111>. URL: <https://onlinelibrary.wiley.com/doi/abs/10.1002/sia.740180111>.
- [223] M. O. Krause. "Atomic radiative and radiationless yields for K and L shells". In: *Journal of Physical and Chemical Reference Data* 8.2 (Apr. 1979), pp. 307–327. DOI: [10.1063/1.555594](https://doi.org/10.1063/1.555594).
- [224] David Attwood. *Soft X-Rays and Extreme Ultraviolet Radiation: Principles and Applications*. Cambridge University Press, 1999. DOI: [10.1017/CB09781139164429](https://doi.org/10.1017/CB09781139164429).

- [225] G. Schütz, W. Wagner, W. Wilhelm, P. Kienle, R. Zeller, R. Frahm, and G. Materlik. "Absorption of circularly polarized x rays in iron". In: *Phys. Rev. Lett.* 58 (7 Feb. 1987), pp. 737–740. DOI: [10.1103/PhysRevLett.58.737](https://doi.org/10.1103/PhysRevLett.58.737). URL: <https://link.aps.org/doi/10.1103/PhysRevLett.58.737>.
- [226] A. S. Schlacter and W. W. Wilhelm. *New Directions in Research with Third-Generation Soft X-Ray Synchrotron Radiation sources*. Vol. 254. Springer Science, 1994, pp. 220–221. ISBN: 978-94-010-4375-5.
- [227] Gerrit Laan and Adriana Figueroa. "X-ray magnetic circular dichroism-A versatile tool to study magnetism". In: *Coordination Chemistry Reviews* 277 (Oct. 2014). DOI: [10.1016/j.ccr.2014.03.018](https://doi.org/10.1016/j.ccr.2014.03.018).
- [228] B. T. Thole, P. Carra, F. Sette, and G. van der Laan. "X-ray circular dichroism as a probe of orbital magnetization". In: *Phys. Rev. Lett.* 68 (12 Mar. 1992), pp. 1943–1946. DOI: [10.1103/PhysRevLett.68.1943](https://doi.org/10.1103/PhysRevLett.68.1943). URL: <https://link.aps.org/doi/10.1103/PhysRevLett.68.1943>.
- [229] Paolo Carra, B. T. Thole, Massimo Altarelli, and Xindong Wang. "X-ray circular dichroism and local magnetic fields". In: *Phys. Rev. Lett.* 70 (5 Feb. 1993), pp. 694–697. DOI: [10.1103/PhysRevLett.70.694](https://doi.org/10.1103/PhysRevLett.70.694). URL: <https://link.aps.org/doi/10.1103/PhysRevLett.70.694>.
- [230] Gerrit van der Laan. "Line shape of 2p magnetic-x-ray-dichroism spectra in 3d metallic systems". In: *Phys. Rev. B* 55 (13 Apr. 1997), pp. 8086–8089. DOI: [10.1103/PhysRevB.55.8086](https://doi.org/10.1103/PhysRevB.55.8086). URL: <https://link.aps.org/doi/10.1103/PhysRevB.55.8086>.
- [231] C. T. Chen, Y. U. Idzerda, H.-J. Lin, N. V. Smith, G. Meigs, E. Chaban, G. H. Ho, E. Pellegrin, and F. Sette. "Experimental Confirmation of the X-Ray Magnetic Circular Dichroism Sum Rules for Iron and Cobalt". In: *Phys. Rev. Lett.* 75 (1 July 1995), pp. 152–155. DOI: [10.1103/PhysRevLett.75.152](https://doi.org/10.1103/PhysRevLett.75.152). URL: <https://link.aps.org/doi/10.1103/PhysRevLett.75.152>.
- [232] Ruqian Wu, Dingsheng Wang, and A. J. Freeman. "First principles investigation of the validity and range of applicability of the x-ray magnetic circular dichroism sum rule". In: *Physical Review Letters* 71.21 (Nov. 1993), pp. 3581–3584. DOI: [10.1103/PhysRevLett.71.3581](https://doi.org/10.1103/PhysRevLett.71.3581).

- [233] Ruqian Wu and A. J. Freeman. "Limitation of the magnetic-circular-dichroism spin sum rule for transition metals and importance of the magnetic dipole term". In: *Physical Review Letters* 73.14 (Oct. 1994), pp. 1994–1997. DOI: [10.1103/PhysRevLett.73.1994](https://doi.org/10.1103/PhysRevLett.73.1994).
- [234] J. Stöhr and H. König. "Determination of spin- and orbital-moment anisotropies in transition metals by angle-dependent x-ray magnetic circular dichroism". In: *Physical Review Letters* 75.20 (Nov. 1995), pp. 3748–3751. DOI: [10.1103/PhysRevLett.75.3748](https://doi.org/10.1103/PhysRevLett.75.3748).
- [235] Gerrit van der Laan. "Microscopic origin of magnetocrystalline anisotropy in transition metal thin films". In: *Journal of Physics Condensed Matter* 10.14 (Apr. 1998), pp. 3239–3253. DOI: [10.1088/0953-8984/10/14/012](https://doi.org/10.1088/0953-8984/10/14/012).
- [236] Reiko Nakajima, J. Stöhr, and Y. U. Idzerda. "Electron-yield saturation effects in L-edge x-ray magnetic circular dichroism spectra of Fe, Co, and Ni". In: *Phys. Rev. B* 59.9 (Mar. 1999), pp. 6421–6429. DOI: [10.1103/PhysRevB.59.6421](https://doi.org/10.1103/PhysRevB.59.6421).
- [237] Philippe Ohresser, Edwige Otero, Fadi Choueikani, Stefan Stanescu, F Deschamps, L Ibis, Thierry Moreno, F Polack, Bruno Lagarde, F Marteau, F Scheurer, L Joly, Jp Kappler, B Muller, and Ph Saintavit. "Polarization characterization on the DEIMOS beamline using dichroism measurements". In: *Journal of Physics: Conference Series* 425 (Mar. 2013), p. 212007. DOI: [10.1088/1742-6596/425/21/212007](https://doi.org/10.1088/1742-6596/425/21/212007).
- [238] L. Joly, B. Muller, E. Sternitzky, J.-G. Faullumel, A. Boulard, E. Otero, F. Choueikani, J.-P. Kappler, M. Studniarek, M. Bowen, and P. Ohresser. "Versatile variable temperature insert at the DEIMOS beamline for *in situ* electrical transport measurements". In: *Journal of Synchrotron Radiation* 23.3 (May 2016), pp. 652–657. DOI: [10.1107/S1600577516002551](https://doi.org/10.1107/S1600577516002551). URL: <https://doi.org/10.1107/S1600577516002551>.
- [239] B. L. Henke, E. M. Gullikson, and J. C. Davis. "X-Ray Interactions: Photoabsorption, Scattering, Transmission, and Reflection at $E = 50\text{--}30,000$ eV, $Z = 1\text{--}92$ ". In: *Atomic Data and Nuclear Data Tables* 54.2 (July 1993), pp. 181–342. DOI: [10.1006/adnd.1993.1013](https://doi.org/10.1006/adnd.1993.1013).

- [240] Rachid Belkhou, Stefan Stanescu, Sufal Swaraj, Adrien Besson, Milena Ledoux, Mahdi Hajlaoui, and Didier Dalle. “HERMES: A soft X-ray beamline dedicated to X-ray microscopy”. In: *Journal of synchrotron radiation* 22 (July 2015), pp. 968–979. DOI: [10.1107/S1600577515007778](https://doi.org/10.1107/S1600577515007778).
- [241] Andrew D. Kent and Daniel C. Worledge. “A new spin on magnetic memories”. In: *Nature Nanotechnology* 10.3 (Mar. 2015), pp. 187–191. DOI: [10.1038/nnano.2015.24](https://doi.org/10.1038/nnano.2015.24).
- [242] B. G. Park, J. Wunderlich, X. Martí, V. Holý, Y. Kurosaki, M. Yamada, H. Yamamoto, A. Nishide, J. Hayakawa, H. Takahashi, A. B. Shick, and T. Jungwirth. “A spin-valve-like magnetoresistance of an antiferromagnet-based tunnel junction”. In: *Nature Materials* 10.5 (May 2011), pp. 347–351. DOI: [10.1038/nmat2983](https://doi.org/10.1038/nmat2983).
- [243] Jiacheng Shi, Victor Lopez-Dominguez, Francesca Garesci, Chulin Wang, Hamid Almasi, Matthew Grayson, Giovanni Finocchio, and Pedram Amiri. “Electrical manipulation of the magnetic order in antiferromagnetic PtMn pillars”. In: *Nature Electronics* 3 (Feb. 2020). DOI: [10.1038/s41928-020-0367-2](https://doi.org/10.1038/s41928-020-0367-2).
- [244] Nityan Nair, Eran Maniv, Caolan John, Spencer Doyle, J. Orenstein, and James Analytis. “Electrical switching in a magnetically intercalated transition metal dichalcogenide”. In: *Nature Materials* 19 (Feb. 2020), pp. 1–5. DOI: [10.1038/s41563-019-0518-x](https://doi.org/10.1038/s41563-019-0518-x).
- [245] Matthias Muenks, Peter Jacobson, Markus Ternes, and Klaus Kern. “Correlation-driven transport asymmetries through coupled spins in a tunnel junction”. In: *Nature Communications* 8, 14119 (Jan. 2017), p. 14119. DOI: [10.1038/ncomms14119](https://doi.org/10.1038/ncomms14119). arXiv: [1605.02798](https://arxiv.org/abs/1605.02798) [[cond-mat.mes-hall](https://arxiv.org/abs/1605.02798)].
- [246] Eufemio Moreno-Pineda, Clément Godfrin, Franck Balestro, Wolfgang Wernsdorfer, and Mario Ruben. “Molecular Spin Qudits for Quantum Algorithms”. In: *Chemical Society Reviews* 47 (Nov. 2017). DOI: [10.1039/C5CS00933B](https://doi.org/10.1039/C5CS00933B).
- [247] M. Ormaza, P. Abufager, B. Verlhac, N. Bachellier, M. L. Bocquet, N. Lorente, and L. Limot. “Controlled spin switching in a metallocene molecular junction”. In: *Nature Communications* 8, 1974 (Dec. 2017), p. 1974. DOI: [10.1038/s41467-017-02151-6](https://doi.org/10.1038/s41467-017-02151-6).

- [248] Amandine Bellec, Jérôme Lagoute, and Vincent Repain. “Molecular electronics: Scanning tunneling microscopy and single-molecule devices”. In: *Comptes Rendus Chimie* 21 (July 2018). DOI: [10.1016/j.crci.2018.06.001](https://doi.org/10.1016/j.crci.2018.06.001).
- [249] Sujoy Karan, Carlos García, Michael Karolak, David Jacob, Nicolás Lorente, and Richard Berndt. “Spin Control Induced by Molecular Charging in a Transport Junction”. In: *Nano Letters* 18.1 (Jan. 2018), pp. 88–93. DOI: [10.1021/acs.nanolett.7b03411](https://doi.org/10.1021/acs.nanolett.7b03411).
- [250] Shichao Yan, Deung-Jang Choi, Jacob A. J. Burgess, Steffen Rolf-Pissarczyk, and Sebastian Loth. “Control of quantum magnets by atomic exchange bias”. In: *Nature Nanotechnology* 10.1 (Jan. 2015), pp. 40–45. DOI: [10.1038/nnano.2014.281](https://doi.org/10.1038/nnano.2014.281).
- [251] Alexander Ako Khajetoorians, Jens Wiebe, Bruno Chilian, Samir Lounis, Stefan Blügel, and Roland Wiesendanger. “Atom-by-atom engineering and magnetometry of tailored nanomagnets”. In: *Nature Physics* 8.6 (June 2012), pp. 497–503. DOI: [10.1038/nphys2299](https://doi.org/10.1038/nphys2299).
- [252] Ben Warner, Fadi El Hallak, Henning Prüser, John Sharp, Mats Persson, Andrew J. Fisher, and Cyrus F. Hirjibehedin. “Tunable magnetoresistance in an asymmetrically coupled single-molecule junction”. In: *Nature Nanotechnology* 10.3 (Mar. 2015), pp. 259–263. DOI: [10.1038/nnano.2014.326](https://doi.org/10.1038/nnano.2014.326). arXiv: [1510.02204](https://arxiv.org/abs/1510.02204) [[cond-mat.mes-hall](https://arxiv.org/abs/1510.02204)].
- [253] Junhyeon Jo, Jinho Byun, Jaeyeong Lee, Daeseong Choe, Inseon Oh, Jungmin Park, Jin Mi-Jin, Jaekwang Lee, and Jung-Woo Yoo. “Emergence of Multispininterface and Antiferromagnetic Molecular Exchange Bias via Molecular Stacking on a Ferromagnetic Film”. In: *Advanced Functional Materials* 30 (Jan. 2020). DOI: [10.1002/adfm.201908499](https://doi.org/10.1002/adfm.201908499).
- [254] Srijani Mallik, Stefan Mattauch, Manas Dalai, Thomas Brückel, and Subhankar Bedanta. “Effect of magnetic fullerene on magnetization reversal created at the Fe/C60 interface”. In: *Scientific Reports* 8 (Apr. 2018). DOI: [10.1038/s41598-018-23864-8](https://doi.org/10.1038/s41598-018-23864-8).

- [255] K. Bairagi, A. Bellec, V. Repain, C. Fourmental, C. Chacon, Y. Girard, J. Lagoute, S. Rousset, L. Le Laurent, A. Smogunov, and C. Barreteau. “Experimental and theoretical investigations of magnetic anisotropy and magnetic hardening at molecule/ferromagnet interfaces”. In: *Phys. Rev. B* 98.8, 085432 (Aug. 2018), p. 085432. DOI: [10.1103/PhysRevB.98.085432](https://doi.org/10.1103/PhysRevB.98.085432).
- [256] Suman Mundlia, Saurabh Chaudhary, Lakshman Peri, Archit Bhardwaj, Janmey Jay Panda, Satyaki Sasmal, and Karthik V. Raman. “Robust Monolayer Exchange-Bias Effect in Molecular Crane-Pulley Response at Magnetic Surface”. In: *Physical Review Applied* 14.2, 024095 (Aug. 2020), p. 024095. DOI: [10.1103/PhysRevApplied.14.024095](https://doi.org/10.1103/PhysRevApplied.14.024095).
- [257] Timothy Moorsom, Shoug Alghamdi, Sean Stansill, Emiliano Poli, Gilberto Teobaldi, Marijan Beg, Hans Fangohr, Matt Rogers, Zabeada Aslam, Mannan Ali, B. J. Hickey, and Oscar Cespedes. “ π -anisotropy: A nanocarbon route to hard magnetism”. In: *Phys. Rev. B* 101.6, 060408 (Feb. 2020), p. 060408. DOI: [10.1103/PhysRevB.101.060408](https://doi.org/10.1103/PhysRevB.101.060408).
- [258] Cynthia Fourmental, Amandine Bellec, Vincent Repain, Jérôme Lagoute, Cyril Chacon, Yann Girard, Sylvie Rousset, Yannick J. Dappe, Alina Vlad, Andrea Resta, Yves Garreau, and Alessandro Coati. “Deep metallic interdiffusion in a model ferromagnetic/molecular system”. In: *Physical Review Materials* 3.8, 083603 (Aug. 2019), p. 083603. DOI: [10.1103/PhysRevMaterials.3.083603](https://doi.org/10.1103/PhysRevMaterials.3.083603).
- [259] Mirko Cinchetti, V. Alek Dediu, and Luis E. Hueso. “Activating the molecular spinterface”. In: *Nature Materials* 16.5 (May 2017), pp. 507–515. DOI: [10.1038/nmat4902](https://doi.org/10.1038/nmat4902).
- [260] Michał Studniarek, Salia Cherifi-Hertel, Etienne Urbain, Ufuk Halisdemir, Rémi Arras, Beata Taudul, Filip Schleicher, Marie Hervé, Charles-Henri Lambert, Abbass Hamadeh, Loïc Joly, Fabrice Scheurer, G. Schmerber, Victor Costa, B. Warot-Fonrose, Cecile Marcelot, Olivia Mauguin, Ludovic Largeau, Florian Leduc, and Martin Bowen. “Modulating the Ferromagnet/Molecule Spin Hybridization Using an Artificial Magnetoelectric”. In: *Advanced Functional Materials* 27 (Jan. 2017). DOI: [10.1002/adfm.201700259](https://doi.org/10.1002/adfm.201700259).

- [261] Maciej Misiorny, Michael Hell, and Maarten Wegewijs. "Spintronic magnetic anisotropy". In: *Nature Physics* 9 (Oct. 2013), pp. 801–805. DOI: [10.1038/nphys2766](https://doi.org/10.1038/nphys2766).
- [262] Wei Pan, Nai-You Jih, Chien-Cheng Kuo, and Minn-Tsong Lin. "Coercivity enhancement near blocking temperature in exchange biased Fe/FexMn1x films on Cu(001)". In: *Journal of Applied Physics* 95 (June 2004), pp. 7297–7299. DOI: [10.1063/1.1652415](https://doi.org/10.1063/1.1652415).
- [263] Tomás Bucko, J. Hafner, Sébastien Lebègue, and János Ángyán. "Improved Description of the Structure of Molecular and Layered Crystals: Ab Initio DFT Calculations with van der Waals Corrections". In: *The journal of physical chemistry. A* 114 (Oct. 2010), pp. 11814–24. DOI: [10.1021/jp106469x](https://doi.org/10.1021/jp106469x).
- [264] J. MacLaren, T. Schulthess, W. Butler, Roberta Sutton, and Michael McHenry. "Electronic structure, exchange interactions, and Curie temperature of FeCo". In: *Journal of Applied Physics* 85 (Apr. 1999), pp. 4833–4835. DOI: [10.1063/1.370036](https://doi.org/10.1063/1.370036).
- [265] S. Javaid, M. Bowen, S. Boukari, L. Joly, J. B. Beaufrand, Xi Chen, Y. J. Dappe, F. Scheurer, J. P. Kappler, J. Arabski, W. Wulfhekel, M. Alouani, and E. Beaupaire. "Impact on Interface Spin Polarization of Molecular Bonding to Metallic Surfaces". In: *Physical Review Letters* 105.7, 077201 (Aug. 2010), p. 077201. DOI: [10.1103/PhysRevLett.105.077201](https://doi.org/10.1103/PhysRevLett.105.077201).
- [266] K. O'Grady, Luis Fernandez-Outon, and G. Vallejo-Fernandez. "A New Paradigm for Exchange Bias in Polycrystalline Thin Films". In: *Journal of Magnetism and Magnetic Materials* 322 (Apr. 2010), pp. 883–899. DOI: [10.1016/j.jmmm.2009.12.011](https://doi.org/10.1016/j.jmmm.2009.12.011).
- [267] Zouhair Sefrioui. "All-Manganite Tunnel Junctions with Interface-Induced Barrier Magnetism". In: *APS March Meeting Abstracts*. Vol. 2011. APS Meeting Abstracts. Mar. 2011, p. L17.001.
- [268] F. Y. Bruno, M. N. Grisolia, C. Visani, S. Valencia, M. Varela, R. Abrudan, J. Tornos, A. Rivera-Calzada, A. A. Ünal, S. J. Pennycook, Z. Sefrioui, C. Leon, J. E. Villegas, J. Santamaria, A. Barthélémy, and M. Bibes. "Insight into spin

- transport in oxide heterostructures from interface-resolved magnetic mapping". In: *Nature Communications* 6, 6306 (Feb. 2015), p. 6306. DOI: [10.1038/ncomms7306](https://doi.org/10.1038/ncomms7306).
- [269] Vincent Baltz, Aurelien Manchon, M. Tsoi, Takahiro Moriyama, T. Ono, and Y. Tserkovnyak. "Antiferromagnetic spintronics". In: *Reviews of Modern Physics* 90 (Feb. 2018). DOI: [10.1103/RevModPhys.90.015005](https://doi.org/10.1103/RevModPhys.90.015005).
- [270] Yu-Ao Chen, Qiang Zhang, Teng Chen, Wen-Qi Cai, Liao Shengkai, Jun Zhang, Kai Chen, Juan Yin, Jianyu Wang, Zhu Chen, Sheng-Long Han, Qing Yu, Ken Liang, Fei Zhou, Xiao Yuan, Mei-Sheng Zhao, Tian-Yin Wang, Xiao Jiang, Liang Zhang, and Xian-Min Jin. "An integrated space-to-ground quantum communication network over 4,600 kilometres". In: *Nature* 589 (Jan. 2021). DOI: [10.1038/s41586-020-03093-8](https://doi.org/10.1038/s41586-020-03093-8).
- [271] Han-Sen Zhong, Hui Wang, Yu-Hao Deng, Ming-cheng Chen, Li-Chao Peng, Yi-Han Luo, Jian Qin, Dian Wu, Xing Ding, Yi Hu, Peng Hu, Xiao-Yan Yang, Hao Li, Li Yuxuan, Xiao Jiang, Lin Gan, Guangwen Yang, L. You, and Jian-Wei Pan. "Quantum computational advantage using photons". In: *Science (New York, N.Y.)* 370 (Dec. 2020), pp. 1460–1463. DOI: [10.1126/science.abe8770](https://doi.org/10.1126/science.abe8770).
- [272] Armen Allahverdyan, Roger Balian, and Th Nieuwenhuizen. "Maximal work extraction from finite quantum systems". In: *Europhysics Letters (epl)* 67 (Aug. 2004), pp. 565–571. DOI: [10.1209/epl/i2004-10101-2](https://doi.org/10.1209/epl/i2004-10101-2).
- [273] Gianluca Francica, Felix Binder, Giacomo Guarnieri, Mark Mitchison, J. Goold, and Francesco Plastina. "Quantum Coherence and Ergotropy". In: *Physical Review Letters* 125 (Oct. 2020). DOI: [10.1103/PhysRevLett.125.180603](https://doi.org/10.1103/PhysRevLett.125.180603).
- [274] James Millen and André Xuereb. "Perspective on quantum thermodynamics". In: *New Journal of Physics* 18.1 (Jan. 2016), p. 011002. DOI: [10.1088/1367-2630/18/1/011002](https://doi.org/10.1088/1367-2630/18/1/011002). URL: <https://doi.org/10.1088/1367-2630/18/1/011002>.
- [275] Amikam Levy, Lajos Diósi, and Ronnie Kosloff. "Quantum flywheel". In: *Phys. Rev. A* 93 (5 May 2016), p. 052119. DOI: [10.1103/PhysRevA.93.052119](https://doi.org/10.1103/PhysRevA.93.052119). URL: <https://link.aps.org/doi/10.1103/PhysRevA.93.052119>.

- [276] Felix C Binder, Sai Vinjanampathy, Kavan Modi, and John Goold. “Quanta-cell: powerful charging of quantum batteries”. In: *New Journal of Physics* 17.7 (July 2015), p. 075015. DOI: [10.1088/1367-2630/17/7/075015](https://doi.org/10.1088/1367-2630/17/7/075015). URL: <https://doi.org/10.1088/1367-2630/17/7/075015>.
- [277] Michele Campisi and Rosario Fazio. “The power of a critical heat engine”. In: *Nature Communications* 7 (June 2016), p. 11895. DOI: [10.1038/ncomms11895](https://doi.org/10.1038/ncomms11895).
- [278] C L Latune, I Sinayskiy, and F Petruccione. “Collective heat capacity for quantum thermometry and quantum engine enhancements”. In: *New Journal of Physics* 22.8 (Aug. 2020), p. 083049. DOI: [10.1088/1367-2630/aba463](https://doi.org/10.1088/1367-2630/aba463). URL: <https://doi.org/10.1088/1367-2630/aba463>.
- [279] Vasco Cavina, Andrea Mari, and Vittorio Giovannetti. “Slow Dynamics and Thermodynamics of Open Quantum Systems”. In: *Proceedings* 12 (July 2019), p. 19. DOI: [10.3390/proceedings2019012019](https://doi.org/10.3390/proceedings2019012019).
- [280] Wolfgang Niedenzu, Victor Mukherjee, Arnab Ghosh, A. Kofman, and Gershon Kurizki. “Quantum engine efficiency bound beyond the second law of thermodynamics”. In: *Nature Communications* 9 (Jan. 2018). DOI: [10.1038/s41467-017-01991-6](https://doi.org/10.1038/s41467-017-01991-6).
- [281] Zhu Ma, Juan Zhao, Xu Wang, and Junsheng Yu. “Effect of bulk and planar heterojunctions based charge generation layers on the performance of tandem organic light-emitting diodes”. In: *Organic Electronics* 30 (Mar. 2016), pp. 136–142. DOI: [10.1016/j.orgel.2015.12.020](https://doi.org/10.1016/j.orgel.2015.12.020).
- [282] Piotr Blonski and Adam Kiejna. “Calculation of surface properties of bcc iron”. In: *Vacuum* 74 (May 2004), pp. 179–183. DOI: [10.1016/j.vacuum.2003.12.118](https://doi.org/10.1016/j.vacuum.2003.12.118).
- [283] Noam Erez, Goren Gordon, M. Nest, and Gershon Kurizki. “Thermodynamic control by frequent quantum measurements”. In: *Nature* 452 (May 2008), pp. 724–7. DOI: [10.1038/nature06873](https://doi.org/10.1038/nature06873).
- [284] Stefano Gherardini, Francesco Campaioli, Filippo Caruso, and Felix Binder. “Stabilizing open quantum batteries by sequential measurements”. In: *Physical Review Research* 2 (Jan. 2020). DOI: [10.1103/PhysRevResearch.2.013095](https://doi.org/10.1103/PhysRevResearch.2.013095).

- [285] Marlan Scully, Kimberly Chapin, Konstantin Dorfman, Moochan Kim, and Anatoly Svidzinsky. "Quantum heat engine power can be increased by noise-induced coherence". In: *Proceedings of the National Academy of Sciences of the United States of America* 108 (Aug. 2011), pp. 15097–100. DOI: [10.1073/pnas.1110234108](https://doi.org/10.1073/pnas.1110234108).
- [286] A.L. Allred. "Electronegativity values from thermochemical data". In: *Journal of Inorganic and Nuclear Chemistry* 17.3 (1961), pp. 215–221. ISSN: 0022-1902. DOI: [https://doi.org/10.1016/0022-1902\(61\)80142-5](https://doi.org/10.1016/0022-1902(61)80142-5). URL: <https://www.sciencedirect.com/science/article/pii/0022190261801425>.
- [287] Guo-Xing Miao, Markus Münzenberg, and Jagadeesh Moodera. "Tunneling path toward spintronics". In: *Reports on Progress in Physics* 74 (Feb. 2011), p. 036501. DOI: [10.1088/0034-4885/74/3/036501](https://doi.org/10.1088/0034-4885/74/3/036501).
- [288] Marc Warner, Salahud Din, Igor Tupitsyn, Gavin Morley, A Stoneham, Jules Gardener, Zhenlin Wu, Andrew Fisher, Sandrine Heutz, Christopher Kay, and Gabriel Aeppli. "Potential for spin-based information processing in a thin-film molecular semiconductor". In: *Nature* 503 (Oct. 2013). DOI: [10.1038/nature12597](https://doi.org/10.1038/nature12597).
- [289] Katharina Bader, Mario Winkler, and Joris van Slageren. "Tuning of Molecular Qubits: Very Long Coherence and Spin-Lattice-Relaxation Times". In: *Chem. Commun.* 52 (Feb. 2016). DOI: [10.1039/C6CC00300A](https://doi.org/10.1039/C6CC00300A).
- [290] Matteo Atzori and Roberta Sessoli. "The Second Quantum Revolution: Role and Challenges of Molecular Chemistry". In: *Journal of the American Chemical Society* 141 (June 2019). DOI: [10.1021/jacs.9b00984](https://doi.org/10.1021/jacs.9b00984).
- [291] J. Teixeira, J. Ventura, Joao Araujo, João Sousa, Piotr Wisniowski, and Paulo Freitas. "Tunneling processes in thin MgO magnetic junctions". In: *Applied Physics Letters* 96 (July 2010), pp. 262506–262506. DOI: [10.1063/1.3458701](https://doi.org/10.1063/1.3458701).
- [292] Matthew Rispoli, Alexander Lukin, Robert Schittko, Sooshin Kim, M. Tai, Julian Leonard, and Markus Greiner. "Quantum critical behaviour at the many-body localization transition". In: *Nature* 573 (Sept. 2019), pp. 1–6. DOI: [10.1038/s41586-019-1527-2](https://doi.org/10.1038/s41586-019-1527-2).

-
- [293] B Roche, P Roulleau, T Jullien, Y. Jompol, I. Farrer, David Ritchie, and D.C. Glattli. “Harvesting dissipated energy with a mesoscopic ratchet”. In: *Nature communications* 6 (Apr. 2015), p. 6738. DOI: [10.1038/ncomms7738](https://doi.org/10.1038/ncomms7738).
- [294] Edward Bormashenko. “Entropy, Information, and Symmetry; Ordered Is Symmetrical, II: System of Spins in the Magnetic Field”. In: *Entropy* 22 (Feb. 2020), p. 235. DOI: [10.3390/e22020235](https://doi.org/10.3390/e22020235).
- [295] Kevin A. van Hoogdalem, Mathias Albert, Pascal Simon, and Daniel Loss. “Proposal for a Quantum Magnetic RC Circuit”. In: *Physical Review Letters* 113 (3 July 2014), p. 037201. DOI: [10.1103/PhysRevLett.113.037201](https://doi.org/10.1103/PhysRevLett.113.037201). URL: <https://link.aps.org/doi/10.1103/PhysRevLett.113.037201>.